Lead-free Solders for High-Reliability Applications: High-Cycle Fatigue Studies

By

Nathan Barry

A thesis submitted to
The University of Birmingham
for the degree of
DOCTOR OF ENGINEERING

Department of Metallurgy and Materials
School of Engineering
The University of Birmingham
23 October 2008

Abstract

The use of lead (Pb) in solders for electronic connections is now extensively restricted in Europe, with its use likely to be phased out completely in the medium term. Although Pb-free solders have been the subject of much research, little investigation has been carried out into their reliability for applications exposed to vibration in service. Aerospace applications, which have service lives measured in decades, are of particular pertinence. The present work shows the development and validation of a method for testing small, model solder joints in high-cycle fatigue. The tests are conducted using common equipment yet provide fast results and objective comparisons between solders without the influence of PCBs or components, which typically obscure the solders' intrinsic contribution. S-N diagrams are presented which compare the performance of traditional Sn-Pb solder to that of Pb-free alloys at room and high temperatures and with copper and nickel substrates. It is found that in all situations the Pb-free alloys offer lower lifetimes to failure than the traditional Sn-Pb, an unexpected result when considering the inferior mechanical properties of the latter. The large disparity at room temperatures and with copper substrates is significantly reduced by elevated temperatures and by soldering to nickel substrates. In order to investigate these results, a number of techniques are employed. In addition to extensive fractography, the damping capacity of the solders is investigated and a scanning acoustic microscope is used in conjunction with resonant decay tracking of specimens to study the crack propagation paths prior to complete failure. The analysis of results focuses on the possible causes for this performance difference, drawing on existing soldering literature and wider engineering principles. It is concluded that the overall pattern of results presents contradictory evidence for the contribution of various factors, such as yield strength or interfacial adhesion, which are hard to reconcile. It is thought likely that more numerous fatigue initiation sites in the Pb-free alloys are responsible to some degree for their lower cycles to failure, although more research into the effect of substrate and interfacial intermetallics is necessary to determine the mechanism by which these influence the results, in the absence of relevant fractographic evidence.

Dates of work

The research in this thesis was carried out between July 2004 and March 2007 at Goodrich Engine Control Systems (York Road), Birmingham.

Previous publication

Parts of the work contained herein were published in Soldering & Surface Mount Technology (2007) Vol 19 No. 2 pp 29 – 38.

Acknowledgements

I would like to thank the following people particularly for their direct input to this project and their advice and support throughout:

Prof. Ian P. Jones (University of Birmingham)
Terry Hirst (Goodrich)
Ian Fox (Goodrich)

I would also like to thank others for their help on a practical, academic or personal level:

Christina Paradiso
Paul Stanley
Lesley Tomkins
Dave Price
Toby Forrester
John Lane
Dr. A Dasgupta
Dr. M Osterman
Dr. D. Barker
Dr. M. Al-Bassyiounni
Jordi Rosich
Adrian Griffiths
Richard Harris
Peter Lindsey
Robin Hogg
Michael Booth
Milos Dusek
Steve McBride
David Cuff
Michael Jameson
Chris Hardy
Alan Jones
Tom Finch
Dr. H. Dong
Andrew Ward
Bob Plant
Andrew Stiles
James Robins
Ian Nicholson
Chris Gartside
Romart Tooling Ltd.
Goodfellow Ltd.
Sensors UK Ltd.

.

Sponsoring Company

The work for this thesis was conducted at, and with the full support of, Goodrich Engine Control Systems (York Road site) in Birmingham, UK. The author's thanks go to Goodrich for the funding of this EngD project and the support of all its staff in conducting the experimental work.

Goodrich Corporation, a *Fortune* 500 company, is a global supplier of systems and services to aerospace, defense and homeland security markets. With one of the most strategically diversified portfolios of products in the industry, Goodrich serves a global customer base with significant worldwide manufacturing and service facilities. For more information visit http://www.goodrich.com.

Nomenclature

Term	Definition
Pb	Lead
Sn	Tin
Ag	Silver
Cu	Copper
Au	Gold
Bi	Bismuth
Sb	Antimony
Zn	Zinc
IMC	Inter-Metallic Compound
HCF	High-Cycle Fatigue
SAC	Sn-Ag-Cu alloy
PCB	Printed Circuit Board
T_m	Melting temperature
CTE	Coefficient of Thermal Expansion
TEM	Transmission Electron Microscope

Contents

List of Figures

1. Introduction

The toxicity of the heavy metallic element lead (Pb) has led in recent decades to increasing efforts to restrict its use. Following the banning of Pb in paints, fuels and plumbing applications throughout the majority of the world, all of which can be demonstrated to present a direct risk to human health, scrutiny has turned to its less prominent uses in industry. These include the universal use of Pb in the electronics industry as a constituent of solder, used to join electronic devices. The first administrative region of the world to actively legislate against Pb use in electronics has been the European Union, which has introduced the RoHS [1] and WEEE [2] directives. These directives target the electrical and electronic equipment industry and are designed respectively to outlaw many harmful substances from use and make the producers of electrical and electronic goods responsible for their safe disposal or recycling at the end of their lives. The directives came into force in all member states in July 2006 and similar legislation is planned in China and Korea.

Although some research into Pb-free solder alloys has been taking place in the past two decades, this regulatory pressure has greatly accelerated its pace in both industry and academia. Initial research concentrated mainly on identifying elements and alloys which could potentially replace Pb. This process was largely complete by the latter stages of the 1990s, as demonstrated by the review paper of Miric and Grusd [3] in 1997 to which few significant alloy advances can be added. While in the early stages of this research the mechanical properties of such alloys were the primary concern, in recent years the actual choice of alloys by manufacturers switching to Pb-free solders has been increasingly influenced by both cost and processability concerns. While these factors are key for mass-

market manufacturers of consumer goods, for the military, aerospace, medical and other 'mission-critical' industries, reliability is the most important consideration.

Scientific test data and empirical knowledge of soldering with traditional tin-lead solder have accumulated over many decades to the point where its behaviour in the short and long term is well-understood and documented. This is not the case for Pb-free solders where even the alloy with the most use, tin-silver, has only been in service for the last decade in a few electronic applications. There is thus a lack of data on the long-term reliability of the common Pb-free alloys which needs to be addressed before the aforementioned high-reliability industries can safely adopt any change in solder.

One major limiting factor in the selection of a Pb-free alloy is that the entire electronics manufacturing industry is accustomed to the low melting point of the eutectic tin-lead alloy (183 ºC) and components are designed to withstand soldering temperatures associated with this. Any rise in the processing temperature of PCBs will have adverse effects on component reliability whilst a decrease in melting point (and hence maximum service temperature) is unacceptable since there is already pressure to increase service temperatures in many applications. This narrow window of melting points restricts research to a handful of alternative alloys based on tin (Sn) with other elements added.

Alongside the temperature requirements, there are a number of metallurgical and mechanical properties of Sn-Pb which an alternative alloy has to rival in order for it to be a successful replacement. The ways in which these properties can be investigated divide broadly into two categories; empirical tests on PCBs or real soldered components, or carefully-controlled tests

on bulk or miniature solder specimens. These methods often yield different results and a particular lack of research exists into the high-cycle fatigue of Pb-free solders via either one. Electronics in high-reliability applications often experience vibration in service, subjecting them to the small, fluctuating loads of high-cycle fatigue. They could also be simultaneously subject to elevated or lowered temperatures. Scientific tests in the high-cycle fatigue regime are hard to conduct at small size scales and the aim of the present work is to reconcile the features of both approaches in a new testing method and thus compare the performance of Pb-free alloys to Sn-Pb in a repeatable and meaningful way.

1.1. Objectives

This work was designed to achieve objective research into the high-cycle fatigue performance of Sn-Pb versus Pb-free solders under a number of test conditions relevant to the aerospace industry and to examine the metallurgical reasons for any differences seen. A key challenge in this objective was to overcome the limitations of typical solder research and to develop a method of testing which provided such objective results. The overall aim was to provide the high-reliability electronic industries with knowledge useful when considering any move away from Sn-Pb solder and the resultant implications for reliability.

2. Literature survey

A review and summary of the state-of-the-art on Pb-free solders and their vibration or high-cycle fatigue is presented, noting the lack of literature on the latter.

2.1. Soldering definitions and review

The term "solder" refers to a group of metal alloys which melt at relatively low temperatures and whose purpose is to form a joint between two other, possibly dissimilar, materials. The distinction between soldering and brazing is only the temperature at which the joining operation takes place; lower than approximately 400 ºC in the former case. Both these techniques involve a 'filler' metal which in the molten state adheres to the two substrates to be joined, then freezes to form a permanent joint, as opposed to welding where the substrates themselves are melted to fuse together. Being a 'filler' material, the adhesion of a solder to its substrates is critical. The most common alloy system in soldering is that of tin (Sn) and lead (Pb) [note – lead will henceforth be referred to as Pb to avoid confusion with electrical leads]. Their relative proportions in a binary alloy can be varied to give melting points up to that of pure Pb (327.5 ºC) but the most important ratio is 63Sn/37Pb (weight %), which is the eutectic point [note - all compositions henceforth given in weight % unless otherwise specified]. This eutectic mixture melts sharply at 183 ºC and is used universally to join wires and components in electronic circuits and assemblies, manually or by automated processes [4]. The term Sn-Pb will refer to this eutectic 63Sn/37Pb alloy henceforth unless otherwise specified.

2.1. Useful properties of Sn-Pb

One of the primary qualities of Sn-Pb is its low melting point, which allows soldering to be carried out with basic skills, minimal operating risks and without expensive equipment. Perhaps even more importantly, this low melting point allows small and sensitive passive and active electronic components to be joined together by the soldering process without heat damage. Complementing this fundamental quality is the ductility of Sn-Pb, which displays an elongation commonly reaching 100 % and in some cases super-plasticity after deformation at high temperatures [5]. This ductility allows Sn-Pb solder joints to accommodate thermal and mechanical strains; especially important when joining fragile and brittle electronic components. Although a weak alloy by common engineering standards, with Young's Modulus values of around 30 GPa [6] and a yield strength with common lower and upper reported values of 19 and 45 MPa [6, 7], this ability of Sn-Pb to absorb plastic deformation has been relied upon in general soldering practice and incorporated into design guidelines for PCBs (Printed Circuit Boards).

2.2. Replacement of Pb

From the perspective of the electronics industry, it would be desirable if a move to Pb-free solder could be achieved by a 'drop-in replacement' alloy; one that could replicate the pertinent physical properties of Sn-Pb and allow existing manufacturing practices and equipment to be used without alteration. It quickly became clear that this would not be the case and that no one element or alloy could replace Pb in this manner. Although a Pb-free alloy, Sn-3.5Ag, is mentioned in Hedges [8] (1960) as a recognised solder for certain applications, it was not until the 1990s that serious investigations into that alloy and others with regard to replacing Sn-Pb began to take place. In 1998 a paper by Miric et al.[3]

summed up the most likely candidate alloys for replacement of Sn-Pb. It can be seen from this review that it had already been established that Sn continued to be the only viable base metal on which to base solder alloys, with the exception of special low-melting point applications. Sn achieves this position because it the only metallic element which in its molten state forms bonds with a variety of other (electrically important) metals such as Cu, Ni, Ag, Au and Zn at temperatures below their melting points and below that which would cause damage to electrical components. The addition of Pb to Sn to create traditional solder was historically due to the very low cost of Pb coupled with the reduction in melting point for mixtures at or near the eutectic point of this alloy system [8].

2.3. Metallurgy of Sn

2.3.1. Crystallographic properties

Attention should then focus on the metallurgy of Sn since it comprises the matrix of all of the Pb-free alloys studied in the present work. Sn has two allotropes, referred to as 'white tin' (beta phase, metallic) and 'grey tin' (alpha phase, semiconductor). The overwhelmingly common form of Sn is the beta phase, which is stable at temperatures from 13 ºC to its liquidus at 231.9 ºC. Below 13 ºC the alpha phase is the one which is thermodynamically stable but it is rarely encountered in real life; henceforth all references to Sn will be to the beta phase unless otherwise stated. The structure of β-Sn is body centred tetragonal with lattice parameters $a = b = 0.5820$ nm and $c = 0.3175$ nm[9]. This c/a ratio of 0.546 gives rise to highly anisotropic behaviour in Sn. Tests on single crystals of Sn reported by Hedges [8] give Young's modulus values ranging from 26.3 MPa in the [110] direction to 84.8 MPa in the [001] direction. Fine-grained polycrystalline Sn is reported to have a Young's modulus

of 44.3 MPa in the same source, although a figure of 49.9 MPa is given in Smithells [7] and other values above and below this are stated in the literature.

2.3.2. Mechanical properties

Pure Sn also has very poor mechanical properties at room temperature – for example a tensile strength of only 11 MPa [8] and a hardness of 3.9 HB [7] – but it should be noted that this is largely due to its low melting point relative to common engineering metals such as Al, Ni or steel. Ductility is the exception to this, with tensile elongations of 53 % possible at room temperature [10]. The creep, hardness and tensile properties of Sn are very sensitive to alloying additions and particularly loading rates and therefore discussion of these properties for pure Sn is of little importance; they shall be addressed in reference to actual Pb-free alloys in due course.

2.3.3. Chemical properties

Chemically, Sn is a relatively inert metal which does not react with air, water, nitrogen, hydrogen or weak electrolytes [8] and Sn-rich alloys display largely similar traits. A stable oxide layer ($Sn0_2$) is slowly grown during ageing in air but this compound (known as 'dross' in the soldering industry) forms rapidly as a skin on Sn-based solders when molten. Chemical fluxes are used to counteract this and ensure good wetting of surfaces. Tin tends to form intermetallic compounds rather than solid solutions, although it does take into solution small amounts of univalent metals such as Cu, Ag and Au [11, 12]. Neighbouring elements to Sn in the periodic table such as In, Sb and Bi do however have appreciable solid solubility in [13], and form eutectic mixtures with, it. All these elements have been experimented with,

along with others, in the quest to replace Pb in solders and the alloys which have been suggested and studied in the literature are now discussed.

2.4. Review of alloying elements and their effects

The main Pb-free solder alloys at the present time in terms of literature study and industrial use are Sn-0.7Cu, Sn-3.5Ag and variants of Sn-Ag-Cu. However, before describing the alloy systems used in the present work, a mention should be given of alternative alloys which are not included in the study. A significant proportion of Pb-free alloys in current commercial use are those whose melting point is designed to approximate that of Sn-Pb as closely as possible [14]. The reasoning behind this is to avoid drastic changes to existing PCB assembly production lines and processes, and to ensure that damage is not caused to components by overheat [6, 13, 15, 16]. Bi is widely studied in the context of both a binary eutectic with Sn and a ternary addition to the Sn-Ag system. The Sn-Bi binary, with eutectic composition Sn-57Bi, offers an attractively low melting point of 138 ºC [17]; however, although performing well under thermo-mechanical cycling [3], its melting point is too low to be considered for use in high reliability sectors. When added to the Sn-Ag binary alloy system [18-20], Bi is known to provide solid solution strengthening to the Sn matrix [19] resulting in significant hardness and tensile strength increases [19, 21]. Bi additions are also purported to improve the wetting performance of Sn-based alloys [19], although Harrison et al. [13] disagree with this finding. There are however two significant reliability issues surrounding the use of Bi in a Pb-free solder. Firstly there is a processing concern that a Bi-containing solder could accidentally be mixed with or otherwise exposed to traditional Sn-Pb solder. The danger of this situation is illustrated by examination of the ternary phase diagram of Sn-Pb-Bi [22] where a eutectic point at 96 ºC is present. A low melting point phase of this

composition has been shown to occur in Sn-Bi solders contaminated with Pb [23] and the Sn-Ag alloy system has been proven susceptible to forming low-melting point Sn-Ag-Pb phases at grain/colony boundaries [24]. The other issue with addition of Bi to the Sn-Ag binary system is that of degradation of reliability under low-cycle fatigue conditions which was reported by Kariya et al. [25] and Kanchanomai et al. [20]. These issues made the selection of any Bi-containing alloys contentious for the high-reliability sector, where significant performance benefits would be needed to outweigh the risks of Pb contamination, at least while Sn-Pb use persists. Another alloy system not included in this study is that of Sn-Zn. With a eutectic point at 199 ºC at a composition of Sn-9Zn, this alloy and its variants are naturally attractive due to their melting points being closer to Sn-Pb than many others. However, the use of Zn results in a solder that oxidises and corrodes [3, 14, 26] in addition to possessing poor vibrational fatigue resistance [27], thought to be due to brittle Sn-Zn intermetallics. They also require aggressive fluxes for soldering, the residues of which are a long-term corrosion risk.

Sb is sometimes added to Sn-Ag or Sn-Ag-Cu solders for similar reasons to Bi, although it can be used in isolation with Sn to create a solid solution, high-temperature melting point alloy (T_m ~ 240 ºC) with composition Sn-5Sb [14]. When used as a low-quantity alloying addition (<1 %) to existing binary or ternary alloys, it gives improvements in tensile strength [28] and fatigue resistance, although in higher quantities it can lead to embrittlement of joints [29] and its effects on wettability are unclear [13]. Sb is also considered to be a toxic element [3] and in light of a lack of information in the literature on the effects of its addition at the time the present work was commenced, no alloys containing it were selected.

A range of other Pb-free solders using elements such as Au, In and Al is described in the literature but they are generally for specialist (either high or low-melting point *c.f.* Sn-Pb)

soldering applications and not applicable to a study on high-reliability solders for general electronics assembly use.

2.5. Pb-free alloys for high reliability

The Pb-free alloy system predominantly studied in the literature and seen as the leading candidate to replace Sn-Pb is the ternary Sn-Ag-Cu system, often abbreviated to 'SAC' in the industry. This is a development of the Sn-3.5Ag eutectic alloy in which the additional Cu is designed to add mechanical strength through formation of intermetallic particles and to reduce the dissolution of Cu substrates by lowering the Cu concentration gradient across the solder/substrate interface [30]. Research still continues into Sn-3.5Ag and results are often applicable to Sn-Ag-Cu in some areas.

2.5.1. Sn-Ag-Cu

In the ternary Sn-Ag-Cu system there exists a eutectic whose exact composition is still disputed – researchers have claimed it to be Sn-3.5Ag-0.9Cu at 217.2 ºC (Loomans et al. [31] and Moon et al. [12]), Sn-4.7Ag-1.7Cu at 217 ºC (Miller et al. [32]) and Sn3.9Ag-0.9Cu [NEMI]. The industry appears to have designated the commercial alloy Sn-3.8Ag-0.7Cu (referred to as SAC 387) as the 'nominal' eutectic. A eutectic composition as opposed to one with a melting (or 'pasty') range is especially desirable for modern reflow soldering since solidification of solder at either end of small, light electrical components at different rates can result in them shifting from their desired positions [33]. Since the initial research to identify the eutectic composition of Sn-Ag-Cu, focus has progressively shifted to hypo-eutectic forms of the alloy such as Sn-3.0Ag-0.5 Cu (referred to as SAC305) in the industry. This is partially due to the reported tendency of Sn-3.8Ag-0.7Cu to form large (>100 μm)

intermetallic plates which could affect joint integrity [34] but mainly to a desire to save money due to the considerable cost of including silver in an alloy. The debate over which particular Sn-Ag-Cu composition is superior is clouded by many factors; the regime under which they are tested, whether the tests are on PCB assemblies or on bulk solder samples, and whether the performance metric is the ultimate lifetime of the solder joints or their success rates in mass production, for example. The best perspective to take is perhaps encapsulated by the findings of Nurmi et al. [35] which were that although differences were found between hypo-eutectic, eutectic and hyper-eutectic Sn-Ag-Cu compositions under thermal cycling reliability tests, these differences were minor when compared with the response of Sn-Pb solder. Other researchers have reached similar conclusions [14, 36]. The alloy/s which will eventually become established in the marketplace will therefore probably be those which provide a performance in the main failure mode (which is thermo-mechanical fatigue) deemed acceptable at minimum cost, a trend which will favour the lower Ag content compositions. The aim of the present work is therefore not to compare small variations of Pb-free alloys to one another but to fill a gap in the current knowledge of Pb-free research which is of interest to the high-reliability sector. The properties of Sn-Ag-Cu in its various compositions have been covered extensively in the literature so a summary of the salient points presented. The phase diagrams for Sn-Ag, Sn-Cu and isotherms from the ternary Sn-Ag-Cu diagrams are referenced in Appendices 7.1 – 7.3.

Moon et al. [12] studied the thermodynamics of the ternary Sn-Ag-Cu eutectic extensively. The case of the nominal eutectic Sn-Ag-Cu alloy cooling from, for example, 240 ºC results firstly in a binary eutectic forming, which is $L \rightarrow Ag_3Sn + Cu_6Sn_5$. These intermetallic phases are discussed in more detail later. Nucleation of the primary Sn phase requires an undercooling of around 20 ºC, which often results in a dendritic Sn network. Thus the typical

microstructure of eutectic or near-eutectic Sn-Ag-Cu consists of regions of primary Sn phase interspersed with 'pseudo-eutectic' regions of Sn + Ag_3Sn + Cu_6Sn_5 [12, 30, 37]. Typical sizes of the intermetallic phases are between 0.1 and 5 μm for both types although there is understandably some variation with composition and cooling rates. In terms of basic monotonic tensile properties, there is a wide variation in the data reported for Sn-Ag-Cu (and indeed Sn-Pb). This scatter is explained by Plumbridge et al. [6] as being a function of factors such as bulk versus micro sized samples, large strain rate dependence, thermal history and the general lack of consistency of test methodology for a material that is not used for general engineering purposes. In analysing any more advanced topic of material behaviour such as low or high-cycle fatigue, reference to the basic tensile properties is important. Yield stress and ultimate tensile strength for solders tend to be very close because highly plastic behaviour (little or no work hardening) is commonly observed.

Source	Solder	Temp. (ºC)	Strain rate (s^{-1})	E (GPa)	Yield Stress (MPa)	Tensile strength (MPa)	Ductility %	Notes
Plumbridge[6]	Sn-Ag-Cu	-10	1.0E+00	-	-	96	-	Open Uni. Tests, bulk cylindrical specimens, as-cast, rapidly cooled
	Sn-Pb	-10	1.0E+00	-	-	84	-	
	Sn-Ag-Cu	-10	1.0E-02	-	-	72	-	
	Sn-Pb	-10	1.0E-02	-	-	67	-	
	Sn-Ag-Cu	75	1.0E+00	-	-	51	-	
	Sn-Pb	75	1.0E+00	-	-	37	-	
	Sn-Ag-Cu	75	1.0E-02	-	-	34	-	
	Sn-Pb	75	1.0E-02	-	-	16	-	
Kim et al.[38]	Sn-3.0Ag-0.5Cu	75	3.5E-03	-	38	43	35	Bulk samples cooled 8deg/s, 2x4.5mm section, 100deg/30min heat treat
Shohji et al.[21]	Sn-3.5Ag-0.75Cu	20	1.0E-03	-	-	41	35	Bulk, 10mm dia,
	Sn-Pb	20	1.0E-03	-	-	38	90	
	Sn-3.5Ag-0.75Cu	100	1.7E-03	-	-	30	30	
	Sn-Pb	100	1.7E-03	-	-	25	125	
CALCE TMM[14]	Sn-3.9Ag-0.6Cu	20	1.0E+00	18.2	70	-	-	Micro specimens, obtained in shear (converted to tensile), approx 3x1x0.18 mm
	Sn-Pb	20	1.0E+00	18	70	-	-	
Motorola Corp. (in CALCE)[14]	Sn-3.8Ag-0.7Cu	25	1.0E-03	-	-	37	-	Bulk 0.5x4mm room age 7 days
		100	1.0E+00	-	-	20	-	
Li et al.[28]	Sn-3.5Ag-0.7Cu	25	1.0E-04	-	-	33	-	10x1.5x0.2 mm specimens, aged 24 hr at 60 ºC
		25	1.0E-02	-	-	45	-	
		75	1.0E-04	-	-	27	-	
		75	1.0E-02	-	-	40	-	

Table 2.1. Selected tensile properties of Sn-Ag-Cu and Sn-Pb solders

The published creep behaviour data for Sn-Ag-Cu alloys show even more variation. The intermetallic particles in this alloy system are responsible for significant performance differences between different compositions in creep tests [39, 40], although these differences are superimposed on the large variations already present in the reported data due to the lack of a consistent test methodology, as discussed previously. In particular, a disparity in creep testing results arising just from size effects is reported by Villain et al. [41]. Since solders reside at high homologous temperatures even in ambient conditions (e.g. $T/T_m = 0.65$ for

Sn-Pb and 0.61 for Sn-3.8Ag-0.7Cu at 25 ºC), creep mechanisms are much more active in solders than for other engineering metals. Chiefly, power law creep (dislocation dominated, sensitive to temperature and applied stress) and possibly Nabarro-Herring creep (lattice diffusion and hence temperature-controlled) will be the mechanisms in question for solders over their typical operating temperatures [6, 42]. Shohji et al. [21] have performed an investigation into the tensile and creep properties of Sn-Ag based solders, using cast bulk specimens of solder with diameter 10 mm. A power law exponent, *n*, of around 11 was found for the Sn-Ag-Cu solder, with an activation energy of 47.3 kJ/mol, using the following equation (valid for a single creep mechanism over varying stress or temperature):

$\dot{\varepsilon} = A(\sigma)^n \exp\left(\frac{-Q}{RT}\right)$ where *A*, *n*, are experimental constants, $\dot{\varepsilon}$ is the steady-state creep rate, *Q* is the creep activation energy, *T* is absolute temperature and *R* the universal gas constant. The authors compare this figure to that of 102 kJ/mol for the self-diffusion of Sn and hypothesise that a dislocation core diffusion process is instead dominating over the strain range tested (10^{-4} – 10^{-2} s^{-1}). At both ambient and elevated temperatures, Sn-Ag-Cu is demonstrated to have creep rupture life superior to that of Sn-Pb by more than an order of magnitude at low strain rates, although the gap narrows at higher strain rates and the situation may reverse if the trends continue. Work in the University of Maryland by the CALCE centre has established a micro shear test method for solder joints which can test intrinsic solder properties with sub-micron precision [43]. Some results generated by this test method are reported [14] for Sn-Pb and Sn-3.9Ag-0.6Cu. In agreement with the work of Shohji et al. the Sn-Ag-Cu alloy is shown to have low creep rates compared to Sn-Pb at low applied stresses but this advantage disappears at higher stresses where a reversal of order takes place (the crossover point depending on temperature). Finally, Guo et al. [44] studied the effect of Ni, Cu and Ag concentrations in Sn-Ag based alloys and concluded that creep performance

was significantly influenced by Ag and possibly Ni content, although activation energy and creep constitutive equation data were not reported.

2.5.2. Sn-Cu and Sn-Cu-Ni

Another alloy system, the binary eutectic Sn-Cu, is also prominent in Pb-free research although not to the same extent as Sn-Ag-Cu. It has a eutectic point at 0.7 % Cu and 227 ºC (Appendix 7.1). This alloy, henceforth referred to as Sn-Cu, is generally reported to have similar mechanical performance to that of Sn-Pb, lacking the strength of the more popular Sn-Ag-Cu. Its main attraction to the soldering industry is its low cost by virtue of having no precious or expensive alloying additives [45]. This feature is behind its use as a wave soldering alloy where large quantities of bulk solder are required and maintenance of precise alloy compositions is problematic. Wave soldering was traditionally used to solder only through-hole components, which typically show extremely low rates of mechanical failure due to the compliance of their legs (or leads) and their high degree of attachment to the PCB. This means solder mechanical performance is not paramount in wave soldering. Despite this, Sn-Cu has been demonstrated to have reasonable thermo-mechanical fatigue performance when used to solder surface mount components; in some circumstances greater than that of Sn-Pb or Sn-Ag-Cu [46]. Sn-Cu consists of a pure β-Sn matrix with dispersed Cu_6Sn_5 particles [45], often sited on grain boundaries [14]. One study reports a yield stress of 27.5 MPa at room temperature, compared to 32.5 and 47.1 MPa for Sn-Pb and Sn-3.8Ag-0.7Cu respectively. In isothermal low-cycle fatigue tests on bulk specimens it was found to have slightly superior performance to Sn-Pb, in one of the very few objective studies devoted to it in the literature [47]. Since the wetting performance of Sn-Cu has been reported to be deficient [48], an addition of around 0.05 % Ni is used in a commercial alloy to improve this

and reputedly improve the uniformity of microstructure by reducing primary Sn dendrite growth [49]. This alloy is referred to as Sn-Cu-Ni.

2.6. Intermetallic compounds

Intermetallic compounds, whilst a factor in the integrity of Sn-Pb joints, play an even larger role in the integrity of Pb-free solders. This increased influence is due to the inclusion of intermetallics in Pb-free solders as important strengthening particles in addition to their presence as an interfacial layer between solder and substrate. The two roles are discussed separately in the forthcoming section.

2.6.1. Interfacial intermetallic layers

The adhesion between solder and substrate is crucial to the integrity of a joint and is a reason why testing of bulk solder specimens cannot replicate the conditions experienced by, and the failure modes seen in, actual solder joints. The most common substrate for electronic solders to be used with is Cu. Cu finds wide use in electronics due to its excellent conductivity and Sn-based solders readily wet it. Other potential, wettable, substrates are Ni or Ni/Fe alloys, Ag and Au, which are commonly coated over Cu contacts. Intermetallic compounds (IMCs) are created when a molten solder wets either Cu or such alternative substrates. They form while the solder is in a molten state but continue to grow in the solid state at room temperatures as well as elevated ones via a mechanism which requires diffusion. The interfacial adhesions between solder/IMC and IMC/substrate therefore constitute a large part of the integral strength of a solder joint and can indeed be a limiting factor in it. The kinetics of such layer growths obey the following relationship [5]:

$x = x_0 + At^n \exp\left(\frac{-Q}{RT}\right)$ where x is the layer thickness at a given time and temperature, x_0 is the initial layer thickness formed in the molten state, t = time, A, n = constant, T = absolute temperature, R = universal gas constant and Q is the activation energy in kJ/mol. In general, solder intermetallic layer growths display parabolic growth rates, where $n = 0.5$. This indicates a diffusion-controlled process in which the growth rate slows with time as the layer becomes thicker and it becomes harder for atoms to diffuse across the layer to form additional compound.

2.6.2. Identities of interfacial intermetallic compounds

The identities of the IMCs Sn forms with alloying elements and substrates are well established in both Sn-Pb and Pb-free solders. Numerous studies have been published on the subject of Pb-free solder IMC growth, morphology and stoichiometry [30, 45, 50-52].

In the most common case of soldering to a Cu substrate, the main compound formed is Cu_6Sn_5, referred to as the η-phase. After ageing in the solid state a further compound, Cu_3Sn (ε-phase) appears. This phase grows between Cu_6Sn_5 and the Cu substrate and is reported to appear after ageing at 120 ºC but not 100 ºC [45]. Where Ni is present either as a substrate coating or in the solder itself, it can diffuse into Cu_6Sn_5 compounds at the interface or elsewhere to form a $(Cu,Ni)_6Sn_5$ structure where Ni atoms, being of a similar atomic diameter to Cu, can substitute into the structure up to levels of over 4 at.% [45]. In the case of Ni substrates either Ni_3Sn_4 or $(Cu,Ni)_6Sn_5$ can be formed between them and Sn-based solders, depending on the amount of Cu present in the solder [50, 53, 54] – in most cases a bi-layer of the two compounds forms. The technique in which Ni is electro-deposited on the surface of Cu substrates necessitates a significant P content which can vary although it is in the region of 15 at.%. This is responsible for forming very thin layers of additional compounds [30]

such as Ni_3P which are so thin they are hard to resolve or identify in the SEM. Such additional compounds have been suspected of causing reliability problems in Pb-free solders, especially under shock loading conditions [26, 55].

2.6.3. Effect of interfacial intermetallic layers on reliability

The influence of Cu-Sn and Ni-Sn IMC layers on the integrity of joints is well documented in the literature but an attempt to generalise their effects could be misleading. This is due to the multitude of ways in which the solder/IMC/substrate interface can be tested, with different studies examining different aspects of its integrity. Examples of this are adhesive failures of IMC/solder interfaces [38], thermo-mechanical fatigue IMC interactions [46, 56, 57], diffusion voiding [58] and vibration-induced IMC failures [59]. It is generally accepted that excessive IMC layer growth after ageing or thermal cycling (where the hot portion of the cycle is responsible for growth) is deleterious to solder joint integrity [5, 60]. Most studies report the phenomenological aspects of IMC-related joint failure and appear to overlook the underlying metallurgical reasons. While the adhesion of IMC layers to solder at an atomic level has not been studied to the author's knowledge, several factors which could influence this have been reported.

IMC	Structure	a	b	c	Ref.
Cu_6Sn_5	Monoclinic, face-centred	11.0225	7.2824	9.8272	Larsson[61]
Cu_3Sn	Orthorhombic	5.4900	4.3200	4.7400	Burkhardt[62]
Ag_3Sn	Orthorhombic	5.9680	4.7802	5.1843	
Ni_3Sn_4	Monoclinic, face-centred	12.2200	4.0550	5.2150	Nowtony[63]

Table 2.2. Crystallographic data for common Sn-based IMCs (measurements in Angstroms)

Table 2.2 shows crystallographic data for common Sn-based IMCs. None of the compounds share the b.c.t. structure of Sn and as such it is unlikely any coherency exists between them and Sn solder matrices. The densities of the compounds Cu_6Sn_5, Cu_3Sn and Ni_3Sn_4 are reported to be greater than those of the pure metals they form from. Thus the formation of

these compounds will lead to volumetric stresses which could weaken the bond between them and the solder. To the author's knowledge, no research specifically on this effect has been undertaken. Another possible factor concerning IMC layers is the CTE mismatch between them, solder and substrate. However, from what little research appears to have been conducted in this area, the CTE of the common IMCs do not appear to be significantly different from that of either Sn or Cu, certainly less than the difference between the two pure metals themselves [64]. The influence of the IMC layer upon failure; notably its roughness is studied by Varghese and Dasgupta [65], who build on earlier analytical work by Suo and Hutchinson[66] in understanding fracture involving intermetallic layers. Suo and Hutchinson established that the actual stress intensity around a planar crack in a bimetal interface is a function of Mode I (tensile) and Mode II (shear) loading. Varghese and Dasgupta extend this to the interface between Sn-Pb solder and an intermetallic layer. They found that with decreasing interfacial roughness (as would be expected in an aged interface), the strain energy release rate was lowered. That is to say, smoother interfaces are predicted to present less resistance to crack growth.

2.6.4. Role of intermetallic particles in solders

A number of elements demonstrate beneficial hardening effects when taken into solid solution by Sn but some fall under the scope of RoHS restrictions on toxicity grounds, such as Cd and As. Thus the formation of second phase particles in the soft Sn matrix is key to increasing its strength. Second phase, usually harder, particles added to a metallic matrix strengthen the material by impeding dislocation motion [42]. Generally dispersed particles force dislocations to bow around them in an Orowan mechanism, which requires an increase in energy, depending on particle spacing, size and shape [42]. Hedges [8] shows the increase

in hardness imparted to Sn by various common intermetallic second phase particles. Among the particles performing best are those of $FeSn_2$ and Ag_3Sn, in contrast to a fairly weak effect for the common Cu_6Sn_5. Fe is traditionally considered a 'contaminant' in soldering, however, and its presence can lead to poor solder joints [8]. Although it was stated earlier that intermetallic coherency with Sn is unlikely, Hedges hypothesizes that a degree of matrix coherency is present with many of these intermetallic particles due to their strengthening effect not being repeated when refractory material particles (e.g. SiC) of similar dimensions are added instead. Recent research into additions of nanopowders to solders would seem to support this, with 'foreign' TiO_2 dispersions showing only slight increases in microhardness compared to equivalent-volume Cu additions which formed the Cu_6Sn_5 compound [67]. Any coherency effect is uncertain due to lack of specific research in this regard.

2.6.5. Intrinsic intermetallic properties

Nano-indentation techniques have been applied to measure the Young's moduli and hardness of the common Cu_6Sn_5, Cu_3Sn, Ag_3Sn and Ni_3Sn_4 compounds, usually in-situ in a solder. The extremely small volume of material tested by nano-indentation ensures that porosity or matrix effects are minimised. The reported values are shown below and show modulus and hardness values much greater than that of Sn-3.5Ag solder (measured as 51.7 GPa and 0.50 GPa respectively in Jang et al.'s work [68]).

IMC	E values reported (GPa)	Hardness values reported (GPa)	Ref.
Cu_6Sn_5	125, 112.3, 124	6.10, 5.9	[64, 68-70]
Cu_3Sn	136, 134.2, 143	5.69, 6.5	[64, 68-70]
Ag_3Sn	78.9, 48.5, 86	1.04, 3.0	[69-71]
Ni_3Sn_4	142, 152	8.40	[64, 68]

Table 2.3. Modulus and hardness values reported for common solder IMCs

These intermetallic phases are commonly described in soldering literature as 'brittle' [30]. One fracture toughness study of Sn-Pb solder joints [72] shows a definite decrease in fracture toughness as failure switches from bulk solder to Cu-Sn IMC layers, but the decrease is not severe considering the ductility of the bulk solder that the intermetallics are compared to. A more objective study of the fracture toughness values of Cu_6Sn_5 and Cu_3Sn gives figures of 2.36 and 2.85 MPa$\sqrt{m}$ respectively [73] which is comparable to that of alumina (Al_20_3) and well below the range of common engineering Al or steel alloys [74].

2.6.6. Influence of IMC particles on solder deformation and fracture behaviour

The role of intermetallic particles in the deformation and fracture behaviour of lead-free solders has been the subject of a number of studies although with the caveat of very different testing regimes being used. Often research is separated into mechanistic studies of creep/tensile regimes or phenomenological studies of observed cracking behaviour of intermetallic-containing solders. Fatigue crack growth testing by Zhao et al. [75] found that in cyclic-dependent regimes, Ag_3Sn phases contributed to strength although they were redundant in slower-cycled time-dependent regimes. This interpretation probably illustrates the danger of drawing conclusions concerning intermetallic strength contributions based on observations of fracture surfaces, for the majority of the literature on the creep strength of Sn-Ag based alloys instead shows a high degree of intermetallic dependence in time-dependent (creep) tests. The fact that cracks do not directly interact with intermetallic particles does not mean that the particles have not altered the time or manner in which crack features have been allowed to develop through the microstructure. For example, Lee and Subramanian [40] found that Cu_6Sn_5 and $(Cu,Ni)_6Sn_5$ particles located on grain boundaries improved the creep and thermo-mechanical properties of Sn-Ag solders, postulated to be via

grain boundary pinning. Choi et al. [76] and Wade at al. [39] also found heavy modification of creep properties by intermetallic particles. An extremely thorough paper by Kerr and Chawla [77] demonstrates the imposition of a threshold stress (over which the stress exponent increases greatly) in deformation of Sn-based solders due to Ag_3Sn particles restricting dislocation movement, over a range of temperatures. Direct TEM observation of dislocations bowing around such particles and after creep deformation is shown. Kim et al. [78] observe that large (~100 μm) Ag_3Sn platelets initiate failure in shear tests and Ding et al. [79] investigate Ag_3Sn contributions to fracture behaviour at different strain rates but in general the detailed role of particles in mechanical failure of any kind is scarcely reported. This is probably due to many studies concentrating on the effect of intermetallic layers and the role they play in failure instead.

2.6.7. Intermetallics: Summary

Intermetallic compounds both as solder/substrate interfacial layers and strengthening particles have been shown to have a major influence on the properties of prominent Pb-free solders. The intermetallic compounds found in solders have been found to be much harder and stiffer than their Sn or Sn-Pb matrix with a corresponding decrease in fracture toughness, although the relationship between this and bulk solder properties is not fully explored in the literature. The role of interfacial intermetallic layers has been shown to be complex, with many factors surrounding their effect on joint reliability, although in most cases smaller intermetallic layers clearly demonstrate a positive effect on reliability. Finally, the role of intermetallics in particle reinforcement form has been discussed and shown to make the time-dependent mechanical properties of the alloys which include them significantly different

from the traditional Sn-Pb alloy, such as introducing threshold stresses in deformation behaviour and radically altering creep exponents.

2.7. Causes of solder joint failure

There are many process issues which affect the formation and integrity of solder joints, such as wetting, flux composition, reflow temperatures and cooling rates. It is beyond the scope of the present work to comment on these issues; a review is given by Harrison et al. [13]. However, once a solder joint has been satisfactorily formed, its failure can principally occur by one of two processes.

2.7.1. Low-cycle fatigue / thermo-mechanical fatigue

A solder joint must accommodate strains imposed upon it by the differential thermal expansions of the materials or components it is attached to. Thermal excursions in electronics are common due not only to power cycles (i.e. current-carrying components being switched on and off) but also external environment changes in the case of aeronautical or automotive use. A simple derivation of these strains is given by Plumbridge et al. [6]. They consist partially of the local mismatch in CTE (Coefficient of Thermal Expansion) between solder and substrate, but more importantly a longer-range leverage effect from multiple solder joints being sited along the length of components with different CTE from that of the PCB. These strains, most commonly in shear mode, can therefore reach over 10 %, which greatly exceeds the elastic behaviour limit of most metals. These cyclic thermal strains cause so-called thermo-mechanical fatigue (TMF). It is generally accepted that this method

of failure, which involves a thermal cycle in phase with a mechanical strain cycle (thermo-mechanical fatigue) is responsible for the majority of field failures of solder joints. The behaviour of Sn-Pb under this type of loading is well-studied, having been the subject of extensive reports over recent decades. Frear et al. [5] (1990) sum up the state of current understanding of Sn-Pb failure behaviour.

2.7.2. High-cycle fatigue

The high-cycle fatigue of Sn-Pb is a subject rarely studied in the literature and although a text on testing electronic equipment for vibration has been produced by Steinberg [80], the focus of the book, written before the Pb-free era, is on the contribution of PCB and component specifics to vibration failure as opposed to the intrinsic properties of the Sn-Pb solder joints themselves. Despite this, high-cycle fatigue is considered by the USAF to be responsible for 20 % of electronic failures in aircraft systems [81, 82], with 55 % attributed to thermal effects and the remainder to environmental factors.

2.8. Solder fatigue testing methods

2.8.1. LCF / TMF testing

Although knowledge of Pb-free alloys in this area has accelerated considerably over the last decade, they are still under-characterised compared to Sn-Pb, in terms of both phenomenological materials knowledge and empirical field experience. The literature over this period reflects the co-existence of two different means of solder reliability testing which are sometimes difficult to reconcile. One is the empirical method, which involves soldering complete PCB assemblies populated with components and subjecting them to thermal cycles, which provokes thermo-mechanical fatigue [13, 37, 48, 56]. These cycles are unlikely

represent true service conditions due to the time-dependent nature of both Pb and Pb-free solder properties.

The other way in which thermo-mechanical fatigue can be tested for is by testing bulk or micro solder specimens of standard geometry rather than 'real' joints. While this method would seem at the outset to be a more scientific and objective test of material properties, having isolated some variables inherent in the soldering process, there is debate as to the validity of this type of testing and whether it can be used to compare Pb to Pb-free solders and predict service life. One of the main reasons is that it is technically difficult to achieve a thermal cycle in phase with a mechanical one, certainly when trying to test specimens of a representative size. Most researchers choose instead to conduct isothermal testing [20, 83-85] and either ignore the thermal aspect or use techniques such as strain range partitioning [86] to separate the time-dependent and time-independent variables and to model damage. A review of many different low-cycle fatigue models and their applicability to real solder joints has been undertaken by Lee et al. [87]. It has been found that even internal CTE differences within a solder joint can be responsible for cracking and damage during thermal cycling, without an external applied strain. This has been observed in the case of Sn-Pb [88] where the different CTE of Sn and Pb phases are responsible and also in Sn-Ag-Cu, where the anisotropic CTE of Sn itself correlates with damage.

2.8.2. HCF testing

It is apparent that most literature on solder reliability refers to performance under relatively slow, low-cycle ($< 10^4$ cycles) fatigue conditions, whether imposed thermally, mechanically or both. Some literature exists examining high-cycle fatigue conditions (i.e. elastic strains only and lifetimes $>10^4$ cycles), which are usually referred to as vibration tests in the

soldering industry since they will only be encountered if the service life of the product involves external vibrations. While the term vibration does not strictly mean low-stress, high-cycle fatigue conditions, in the context of soldering research this is what it refers to. One of the main limitations of vibration testing as practised by most soldering researchers is that it involves the testing of PCB assemblies populated with components in order to determine their reliability under vibratory conditions. The precise conditions experienced by an individual solder joint vary hugely with the type of component it is attaching, its position on the PCB and the vibration loading imposed on it. Each of these factors can be responsible for large variations in joint stress. For example, the response of PCBs to vibration depends on their size, stiffness, clamping conditions and, critically, test frequency. Thus the local bending stresses on a solder joint are affected by the global response of the PCB it is attached to. It is perhaps for reasons such as these that much vibration reliability testing is confined to the laboratories of companies whose electronic products are affected by vibration. Since the variation in stress condition for a given solder joint is higher than for an equivalent joint tested in thermo-mechanical fatigue, for example, the results of such vibration tests are unlikely to be applicable to other PCB assemblies. In recent years, with the spread of electronics into increasing numbers of products and the introduction of Pb-free solders into mainstream research, the focus must move towards intrinsic solder material performance under vibratory conditions. While experiments into this have been conducted at the CALCE centre (University of Maryland), the work is unpublished and still pertains to soldered components on PCBs, albeit simple, well-characterised ones.

2.9. Review of current literature on solder HCF or vibration testing

What follows is a review of the current state of research into not only Pb versus Pb-free vibration performance but also mechanistic understanding of the performance of both solder types. There is, as of yet, no comprehensive comparison published of the high-cycle fatigue properties of Pb-free solders versus Sn-Pb.

2.9.1. Mechanistic issues

Possibly the most thorough study of fatigue in Pb-free solders conducted so far is that of Zhao et al. [75] in 2001. The work only relates to the Sn-3.5Ag binary alloy (although its results are comparable to earlier work by the same authors on Sn-Pb [89]) but the results should be reasonably applicable to the Sn-Ag-Cu ternary system. The work is principally a fatigue crack propagation study testing small notched compact tension (CT) specimens machined from bulk solder (dimensions 39 x 50 x 6 mm). It was found that the results of the fatigue crack growth tests, conducted between 0.1 and 10 Hz, could be separated into two groups which fit two different fracture mechanics parameters; ΔJ (large plastic zone conditions) and C^* (creep-affected crack growth). At high frequencies and low R ratios, cyclic-dependent crack growth behaviour was observed to fit the ΔJ parameter and transgranular cracking was observed in the microstructure. At lower test frequencies and high R ratios the data fitted the C^* parameter and the cracking behaviour was predominantly intergranular. These results demonstrate that the period of loading affects whether or not creep processes influence the cracking behaviour. Indications of recrystallisation were also observed near cracks in the creep-dominated, slower tests. Plotted against results from

similar Sn-Pb tests, it was found that in the cyclic-dependent regime Sn-3.5Ag proved to be of superior performance.

Two pieces of research by Basaran et al. [90] and Zhao et al. [91], one a modelling exercise and one a real test, postulate that contrary to general belief strains in solder joints under vibration do not remain entirely elastic. In the former case a damage mechanics model of Sn-Pb joints indicates a highly non-linear response of shear strain (with increased damage due to creep interaction) in joints at high acceleration and low frequency. It should be noted that the model used was based specifically on two-phase Sn-Pb microstructures. The study by Zhao et al. [91] attempts to verify this result by experiments on Sn-Pb BGA (Ball Grid Array) components, measuring strain fields optically with Moiré interferometry. The results appear to show that over 100 ºC and for low (<1 kHz) frequencies, inelastic strains occurred. This seems to indicate that a longer period of loading (as in Basaran's results) can allow time-dependent processes (i.e. creep) to contribute to the damage process. However in the author's view there is an oversight in the methodology employed in the tests related to the 'zeroing' method which is meant to account for CTE mismatches at elevated temperatures; whether the plastic strain fields recorded were the result of vibration or not is in question.

Kanchanomai et al. [92] conducted a detailed study of the Mode I (tensile) fatigue cracking behaviour of Sn-Pb solder with respect to its interface with Cu substrates. The (tetragonal) solder joint volume used was approximately 25 x 6 x 5 mm and tests were conducted at room temperature with R = 0.1 and a frequency of 10 Hz. Specimens were notched and fatigued to give a consistent pre-crack. The data fitted that of the cyclic-dependent regime identified by Zhao et al., with transgranular crack growth and a similar ΔJ threshold value. As crack lengths approached half way through the section, the path of damage switched from the bulk solder to the IMC/solder interface. FE modelling of different a/W ratios (a = crack length

and W = specimen width) showed that in the early stages of crack growth the plastic zone around the crack tip was small, but at $a/W = 0.46$ the plastic zone was much larger and debonded the interface with the Cu substrate. It was not reported exactly which interface was responsible for adhesive failure in the work.

2.9.2. Test comparisons

Illustrations of 'traditional' vibration testing studies are given by Kim et al. [82], Wang et al. [93], Che et al. [94] and Tu et al. [59], usually studying one type of surface-mount component joint (e.g. BGA or flip-chip). Failure characteristics and crack paths are generally studied by retrospective cross-sectioning and the effects of IMC layers are often analysed. The results from tests such as these are highly component and joint-shape specific. A slightly more detailed study is undertaken by Liu et al. [95] who characterise the crack growth due to vibration in (Sn-Pb) BGA solder joints by an optical method, although it should be noted that as with some other studies, the joints themselves have to be cut in half initially before this method can be applied! The authors attempt to fit crack growth to the Paris Law (details of which are described elsewhere [96]) and predict life, with reasonable success. In that study the lifetimes spent in crack initiation and stable crack growth were 15 % and 60 % respectively. Stam and Davitt [36] have conducted vibration tests on a range of component and substrate coatings, comparing the reliability of Sn-Pb to that of Sn-3.8Ag-0.7Cu. They found that the difference between the solder types was less significant than the component type or substrate coating (e.g. Cu or Ni). This illustrates the disadvantages of testing complete PCB assemblies if the desire is to compare intrinsic solder performance. Still testing solder joints on PCB assemblies but in a simplified and more uniform manner, Osterman and Barker [97] report the findings of Sn-Pb versus Sn-3.0Ag-0.5Cu solders under

vibration loading. It was found that for lower stresses, Sn-3.0Ag-0.5Cu outperformed Sn-Pb whilst at higher stresses the situation was reversed. The crossover point for this change was between 10^4 and 10^5 cycles. Due to the similar power law exponents (represented as gradients on an S-N diagram) the absolute values for lifetimes of the solders were, however, largely similar.

2.9.3. HCF summary

The work to date on vibration of components with Pb-free joints has been reviewed and found to be lacking in objectivity and scope. Work has been done on the fatigue crack propagation of a limited selection of solder alloys such as Sn-3.5Ag, which was found to behave elastically in response to a 10 Hz fatigue test; decreasing frequency was shown to result in increasingly plastic behaviour. Other experimental work concentrates on particular components and does not isolate the intrinsic contribution of the solder to the fatigue results. Finally, modelling studies exist offering some insight into the degree of creep interaction in high-cycle fatigue but only for Sn-Pb.

2.10. Resonant testing and decay

2.10.1. Theory of resonant decay

A background to mechanical vibrations is given elsewhere [98]. The natural frequencies of a mechanical (or in fact any) system are those at which the undamped response of the system tends to infinity; that is, the output response (e.g. displacement) is magnified compared to the input. There is one natural, or resonant, peak for every degree of freedom in the system. All real mechanical systems possess some degree of damping, which broadens and attenuates the resonant frequency peaks but does not appreciably alter their value in most situations with

stiff materials, e.g. metals. For a simple, one-degree-of-freedom system such as a mass attached to a spring, the natural frequency, f_0, (in Hz) can be found analytically by an equation of the form $f_0 = \frac{1}{2\pi}\sqrt{\frac{k}{m}}$

where *k* represents spring stiffness and m the mass. Natural frequencies of systems with more than two degrees of freedom are complex to determine analytically since they involve finding the eigenvalues of large stiffness matrices, a task more suited to computers. In the case of a simple beam rather than a spring, the stiffness can be simply represented by $\frac{EA}{L}$, where *E* is Young's Modulus, *A* is cross-sectional area and *L* is length. It can be seen that a change in stiffness will result in a change to f_0. If a beam is cracked, for example, its effective area *A* will decrease and the natural frequency will lower. This result is exploited widely to determine, for instance, the structural health of bridges [99] and rotating shafts [100]. The damping capacity of a structure or material is a measure of its ability to absorb energy when vibrated (elastically strained). When considering the most simple, one-degree-of-freedom system, δ is defined as the natural logarithm of the ratio of two successive amplitude peaks: $\delta = \ln\left(\frac{x_p}{x_{p+1}}\right)$. For most practical situations, $\delta \approx 2\pi\alpha$ where α is the viscous damping ratio of the system [98]. Viscous damping is not strictly appropriate to intrinsic material damping; a structural damping factor, η, should be used instead. When a one-degree-of-freedom system undergoes forced harmonic (sinusoidal) vibration, $\eta = \frac{\Delta f}{f}$ where Δf is the half-power bandwidth (width of the response curve at -3 dB of the maximum of the peak) and f is the frequency at which maximum amplitude is reached. The value of η

can therefore be easily determined experimentally by subjecting the system to a swept range of input frequencies, identifying peaks and measuring their widths.

2.10.2. Literature on resonant decay test methodology

In the wider field of engineering, numerous studies have utilised resonant frequency drops to monitor and predict cracking and failure behaviour of material specimens under fatigue. George et al. [101] produced a bi-axial stress state in steel, Al and Ti alloy plates by analysing the resonant frequencies and displacement fields at resonance and then subjecting them to vibration at those frequencies. An electrodynamic shaker was used to provide excitation and the methodology of detecting cracks by resonant frequency decay was demonstrated. Bedewi and Kung [102] provide a more detailed example of how resonant frequency decay can be utilised to gauge damage in material specimens. They used plates of composite graphite/epoxy material subjected to cyclic bending loads at 19 Hz. At set intervals, fatigue testing was stopped and small impacts from a hammer-like actuator were used to excite the natural frequencies of the plates, allowing a frequency analysis to be conducted. The researchers in this case concentrated on the 5^{th} and 6^{th} resonant frequencies identified as well as the damping ratios at these frequencies. They found that by normalising the cycles to failure against total life and measured resonant frequency against initial resonant frequency, a reasonable 'master curve' could be assembled which described the frequency decay of multiple specimens. They investigated retrospectively whether the lifetime could have been predicted accurately at 25 % progress of the test and found that after 25 % test progress the remaining life could be predicted with an error of 13 % for one particular resonant frequency. The damage to notched steel plate specimens during tensile high-cycle fatigue loading was studied by Giannoccaro et al. [103]. Again using impact excitation at

fixed intervals to determine resonant frequencies, they discovered that different resonant frequencies provided varying qualities of life indication. When normalising with respect to lifetime however, they found that a distinct 'knee' could be seen in the ensemble data for multiple specimens at around 90 % of life, after which resonant decay was rapid.

2.10.3. Literature on solder resonant testing

Chuang et al. [104] and Song et al. [27] at the National Cheng-Kung University, Taiwan, have studied the fatigue of model solder specimens under resonant fatigue conditions. In both cases the specimens (bulk solder plates) form part of the test system itself, being mechanically vibrated in a bending mode with weights added to accelerate failure. The natural frequencies of the solder plates were determined and the vibration applied at the fundamental (lowest) resonant frequency to maximise displacement.

As test cycles accumulate in a specimen, its natural frequency decays as stiffness is lost due to a crack propagating through the section. In these tests the driving frequency was not adjusted to account for this, meaning that displacement amplitude decreased throughout. These tests can therefore be considered to be neither under load nor displacement control, making conventional fatigue damage parameters such as Coffin-Manson or Basquin [105] inapplicable. However, they represent an interesting reflection of real life vibration performance since the elastic properties of the solders themselves have an exaggerated importance to the test results; chiefly their damping capacity. Pb is noted for its high damping capacity and finds use in protecting large building structures from earthquake vibrations [106]. It would be intuitive to suggest that Sn-Pb solder has a higher damping capacity than mainly Sn-based alloys due to its Pb content. This could lower the effective stress seen by components soldered to a PCB with Sn-Pb solder compared to a Pb-free alloy

due to increased energy absorption and concomitant strain amplitude decrease. Song et al. compared the experimentally-measured logarithmic decrement, δ, of Sn-Pb to that of various Pb-free solders. They found to the contrary; that Sn-rich solders such as Sn-0.7Cu and Sn-3.5Ag demonstrated higher δ values than Sn-Pb. However, when test conditions were such that the natural damping behaviour of the solder became dominant, Sn-Pb lasted the longest before failure. The precise failure mechanisms found are hard to ascertain from the paper but it would seem that the Sn-Cu and Sn-Ag solders fail by cracks propagated transgranularly through the matrix while Sn-Pb shows a mixture of this mechanism and phase separation. The regime of fatigue studied appears to be the 'transition' range between around 10^3 and 10^5 cycles, where general elastic or plastic strains could be present, clouding the analysis somewhat.

2.10.4. Resonant decay summary

The method of using the resonant frequency and damping properties of test specimens to assess their damage during fatigue is well-established in theory and experiment. Fatigue specimens have been shown to behave similarly when their normalised frequency decay is considered. Some relevant research has been carried out on solders, showing longer fatigue lifetimes for Sn-Pb compared to that of Sn-Ag, but only without strain amplitude control. These tests also only refer to bulk specimens and do not extend to the true high-cycle regime.

2.11. Scanning Acoustic Microscopy

The use of ultrasonic sound reflections to detect objects or features inside them has been experimented with since the early 20th century [107]. Techniques using such ultrasonic sound have found wide use in the medical industry and for non-destructive testing (NDT) of

metals, particularly the detection of cracks or flaws in pipe work. Towards the end of the 20th century, the scanning acoustic microscope (SAM) was developed; an instrument which focuses acoustic waves (in the MHz – GHz frequency range) and transmits them through a coupling medium (usually water) to a specimen, detecting signals that are reflected back. The operating principles and practice of such a machine are set out by Briggs [108]. Similarly to an optical microscope, the resolution of a SAM is inversely proportional to the sound frequency used and is of the order of one wavelength. Resolutions depend on the material under study and the coupling fluid used, but using water range from approximately 1.2 mm in steel at 5 MHz to <0.2 μm at 4.2 GHz in silicon [108]. In the electronics industry, the SAM has found extensive use in the detection of flaws such as delamination and voids in integrated electronic circuits or chips [6, 109]. Failure rates of clusters of solder joints [110] and their voiding levels [111] have also been studied with a SAM but the cracking behaviour of individual joints has not been studied with such a method, to the author's knowledge. Used in its most common C-Scan mode, the SAM responds to changes in acoustic impedance of the sample as a function of depth through it. The acoustic impedance, Z, of a material is the product of its density and longitudinal sound wave transmission speed. The reflection, R, of the acoustic signal by an interface between two substances with differing impedances is given by Briggs [108] as: $R = \frac{Z_2 - Z_1}{Z_2 + Z_1}$

An internal fatigue crack in a solder joint and or a crack between the joint and its intermetallic layer would give rise to such a reflection since the impedance difference between a metal and air (or a vacuum) is large. If a scan across the surface area of a planar solder joint is conducted, an image can be formed of any such reflections arising from discontinuities in the joint. The depth of the features can be gauged from recording the time-of-flight of the acoustic signal and calibrated against known sound propagation speeds.

2.12. Summary

In summary then, the background to the Pb-free issue in soldering has been discussed, with reference to the challenges which it presents to the reliability of solder joints, particularly for aerospace applications. The modes of failure of solder joints have been described and the heavy concentration of existing literature on low cycle and thermo-mechanical fatigue testing, to the exclusion of high-cycle fatigue, has been noted. The metallurgy of the main Pb-free alloy systems has been studied, noting the common Sn matrix and intermetallic reinforcements in contrast to the eutectic Sn-Pb alloy. Whilst in general the candidate Pb-free solder alloys are found to have superior mechanical strength to Sn-Pb, accounting for their superiority in many LCF or TMF tests, the ways in which this might affect high-cycle fatigue can not be inferred. The lack of on objective and authoritative HCF test, or even test method, for Sn-Pb versus Pb-free solders is clear in the literature. The opportunity to undertake an objective series of tests which develop understanding in this area is thus demonstrated.

3. Experimental Method

3.1. Solders

The solders used in the present work are given below (all compositions weight %):

Solder	Name	Nominal Composition	Supplier	Sn	Ag	Cu	Co	Ni	Pb	Fe	Sb	Bi
A[1]	Sn-Pb	Sn-37Pb	Alpha Metals	62.1	0.02	0.04	-	0.004	bal	0.003	0.04	0.01
B[2]	Sn100C	Sn-0.7Cu-0.05Ni	DKL Metals	99.4	<0.001	0.63	<0.01	0.05	0.02	<0.01	0.01	-
C[2]	SAC387	Sn-3.8Ag-0.7Cu	DKL Metals	95.6	3.7	0.6	<0.01	<0.01	0.08	<0.01	0.02	-
D[2]	SAC305	Sn-3.0Ag-0.5Cu	Alpha Metals	96.6	3.0	0.48	<0.01	<0.01	0.04	<0.01	0.02	-
E[3]	Innolot	Sn-3.8Ag-0.7Cu-3Bi-1.4Sb-0.15Ni	Henkel Multicore	91	3.8	0.7	-	0.15	-	-	1.4	3.0

Table 3.1. Compositions of solders used in the present work

[1]Figures given as an example of typical compositional analysis of traditional wave solder used in electronics manufacturing

[2] Compositional analysis conducted by Tin Technology Ltd on actual solder samples from present work. Trace element levels determined by ICP-AES. Accuracy levels:
Sn,Ag: ± 0.2 %
Cu: ± 0.05 %
Co,Ni,Pb,Sb: ± 0.01 %

[3] Figures given by alloy suppliers

All solders were supplied in solid form except solder E which was supplied as a paste (solder micro-balls in a viscous flux suspension). The flux content of this paste was burnt off by raising it above the solder liquidus until only bulk metal remained.

3.2. High-cycle fatigue (HCF) test development

3.2.1. Design concept

A number of prototype systems were tried in pursuit of the final design presented here. They were all based around the concept of performing a fast fatigue test on a small model solder

joint without needing specialised machinery which is capable of applying strains with a range of under a micron. It was identified that electromechanical shakers used in vibration testing of PCBs on Goodrich premises could apply high vibration forces at high speeds without large displacements. Instead of attempting to clamp both ends of a model solder joint and strain them both minutely and accurately, a dynamic approach could be pursued, using the inertia of a large mass to multiply the force on a small joint when subject to vibrations. For simplicity and for mechanical reasons of concentricity (more easily understood later) only a cylindrical, rod-type solder joint specimen was considered. Early attempts at such a system proved that an electromechanical shaker could be used in conjunction with 'dead' weight applied to the end of a test specimen in order to conduct a fatigue test on a solder joint sandwiched between two Cu rods. The theoretical risk that failure would instead occur due to forces not in the direction of vibration proved unfounded, even when using parts whose construction tolerances were less than ideal. The prototype tests established sensible lower limits on the specimen dimensions attainable while eliminating a number of ideas on how to clamp the specimens in the shaker due to cost, re-usability and trueness. The final design incorporates three main elements – model solder joints constructed by a multi-stage process, holders which clamp the joints and include a mass whose inertia creates stress on them under vibration, and a fixture which accepts the holders and allows them to be vibrated on an electrodynamic shaker.

3.2.2. Solder joint construction

The solder joints are constructed by filling with solder the gap between two axially-aligned cylindrical copper rods with a diameter of 2.50 mm. The rods were manufactured by EDM (Electro-Discharge Machining) to ensure maximum trueness; these were found to be far

superior to those made by more conventional lathe machining. Testing the actual diameters of the rods showed they have a diameter deviation no more than 0.08 mm from the nominal 2.50 mm. To create the solder joint, two rods are assembled in a stainless steel 316 fixture that aligns them end-to-end and, when the desired gap between the ends has been set, clamps them in place very accurately (Figure 3.1).

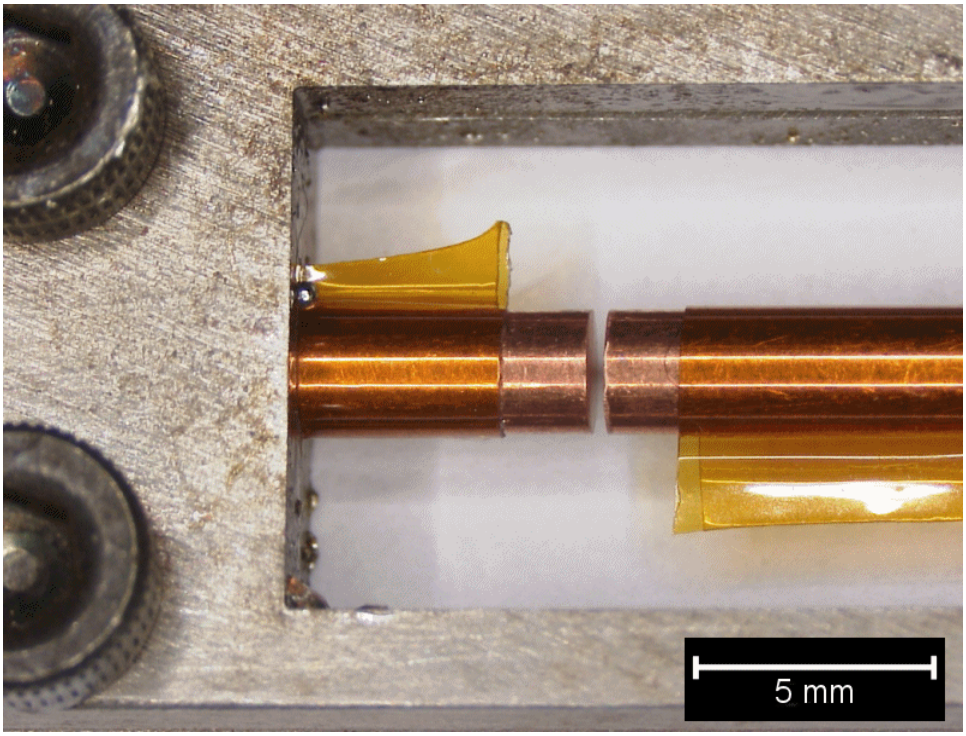

Figure 3.1. Stainless steel assembly block holding two halves of Cu rod prior to soldering

The gap between the ends is set at a nominal 350 microns; this figure is picked essentially by judgement and experience, knowing that too close a gap would hinder solder filling and too wide a gap in proportion to the diameter would give a convex solder joint geometry which is not desired. In practise the gap is set by using a compound optical microscope to line up the ends of the rods in the fixture. A tolerance of ± 20 microns is allowed at this stage due to practicality and the fact that this dimension is not critical to the determination of tensile stresses. The ends of the rods as-manufactured have good orthagonality to their long axes but their surfaces are too rough for acceptable soldering. Therefore before soldering they are

faced off with 1200 then 2500 grit abrasive paper using the same alignment fixture as before on a circular grinding wheel. This surface is further prepared just before use by dipping for 5 s in a dilute nitric acid solution then rinsing with water to remove any oxide layer or contamination. The final preparation stage before soldering is to coat the rods with polyamide ('Kapton') tape which resists solder (as seen in Figure 3.1). Only the surfaces to be soldered are left exposed. This ensures that when immersed in a solder bath the majority of the rod is not wetted by the solder.

3.2.3. Soldering operation

The method of soldering the rods is immersion in a bath of molten solder. Two separate tabletop baths were used; one for all Pb-free alloys and one for Sn-Pb in order to avoid contamination. The temperatures of the baths were maintained at between 260 and 270 °C for the Pb-free bath and 250 to 260 ºC for the Sn-Pb bath. These temperatures take commercial bath soldering temperatures (250-260 ºC) as a basis and increase them slightly for Pb-free to reflect the higher liquidus temperature of these alloys. Initial experiments showed that these temperatures were the lowest permissible before wetting began to suffer and joints did not form properly. During the soldering operation, the rod/fixture assembly has flux (Alpha RMA 615-15) applied from a dripper bottle to the soldering surfaces. The assembly is then dipped in the soldering pot for 25 s. Upon withdrawing the assembly, it is immediately placed onto a heatsink. The heatsink is necessary to counteract the large thermal mass of the stainless steel fixture holding the rods. The solder joint remains molten for approximately another five seconds, giving a total liquidus time of 30 s which is comparable to that of an automated reflow soldering operation. Temperature logging of this

cooling process reveals that the joint cools down at approximately 3 °C/s which is also comparable to that of a commercial joint.

3.2.4. Post-soldering treatments

This soldering process leaves a joint with a 'bulge' of excess solder. This is polished off by hand to leave a cylindrical solder joint flush with the copper rods (Figure 3.2).

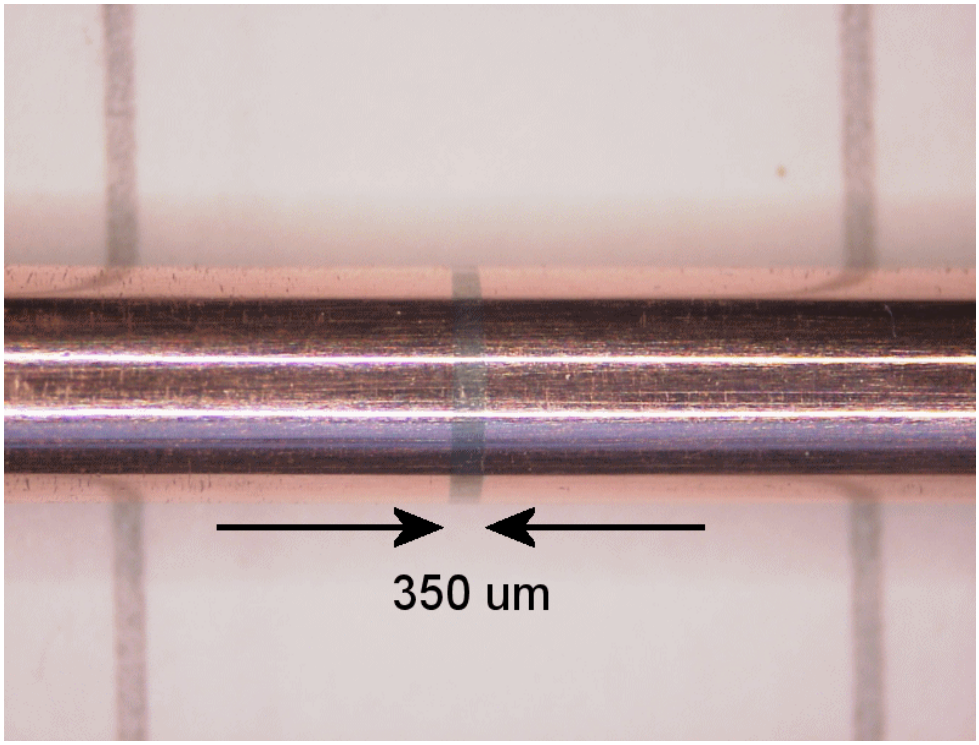

Figure 3.2. Soldered and polished Cu rod incorporating solder joint

The polishing process utilises progressively finer grit papers (320, 600, 1200, 2500, 4000) until a visibly scratch-free finish is achieved. The completed rods are then stored at 125 °C for 24 hr in order to relieve stresses induced during the assembly stages and also to simulate the effect of product 'burn-in' temperature cycles. These temperature cycles are meant to catch early product failures before delivery and their excursions to 125 °C or higher will have the effect of extra solid-state growth of IMC layers and grain or precipitate growth.

3.2.5. Ni coating of Cu substrates

Further rods were coated with Ni and Au by Invotec Ltd, who manufacture PCBs. This process is commonly applied to the Cu pads on a PCB to preserve their solderability and inhibit intermetallic layer growth and 'leaching' of the Cu by the solder during solid state ageing. A ~6 μm layer of Ni was electroplated onto the Cu substrate, which was followed by a very thin 'flash' coating of Au, in the region of 100 nm thick. Au has an extremely low rate of oxidation and presents a highly wettable surface for the solder. It is however quickly dissolved by Sn upon soldering and the underlying Ni forms the intermetallic compound layer which bonds the solder to the substrate. The chemistry of the Ni plating operation results in a significant P (phosphorus) content being present, as noted in Chapter 2.

3.2.6. Vibration fixture

The fixture is custom-made, bolts onto a range of shakers and allows up to eight specimens to be shaken in the vertical (Z) direction at one time. Its detailed design is contained in Appendix 7.4. It is constructed from aluminium (as are most vibration test fixtures) for weight reasons, but retains very thick webs and flanges to transmit force with minimal losses and overall is as compact as possible for the same reason. It is shown schematically in Figure 3.3 and photographically in Figure 3.4.

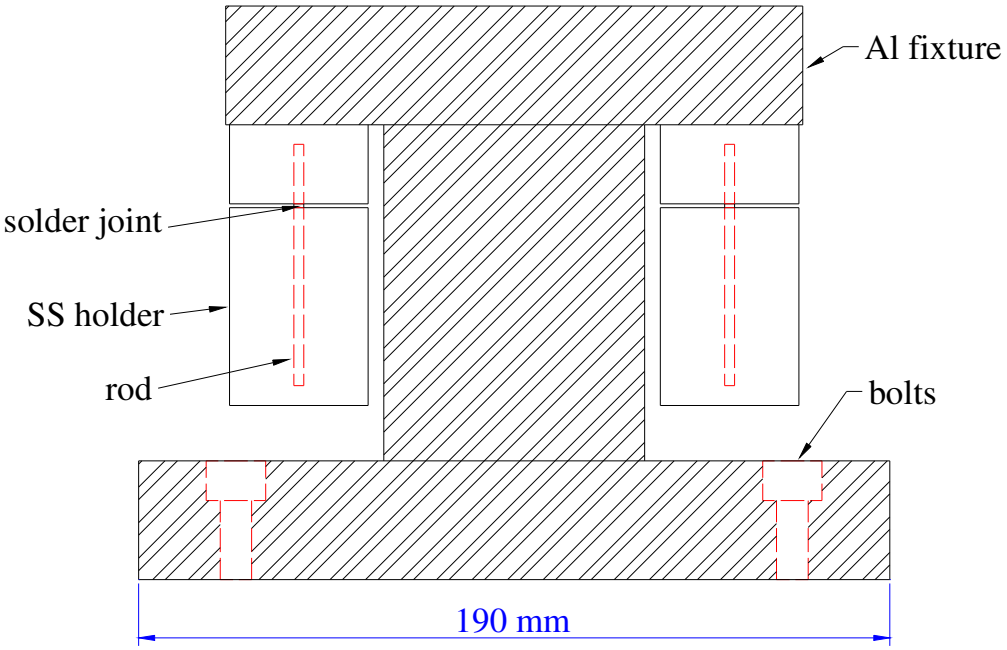

Figure 3.3. Schematic representation of fixture used to achieve high-cycle fatigue testing in the present work

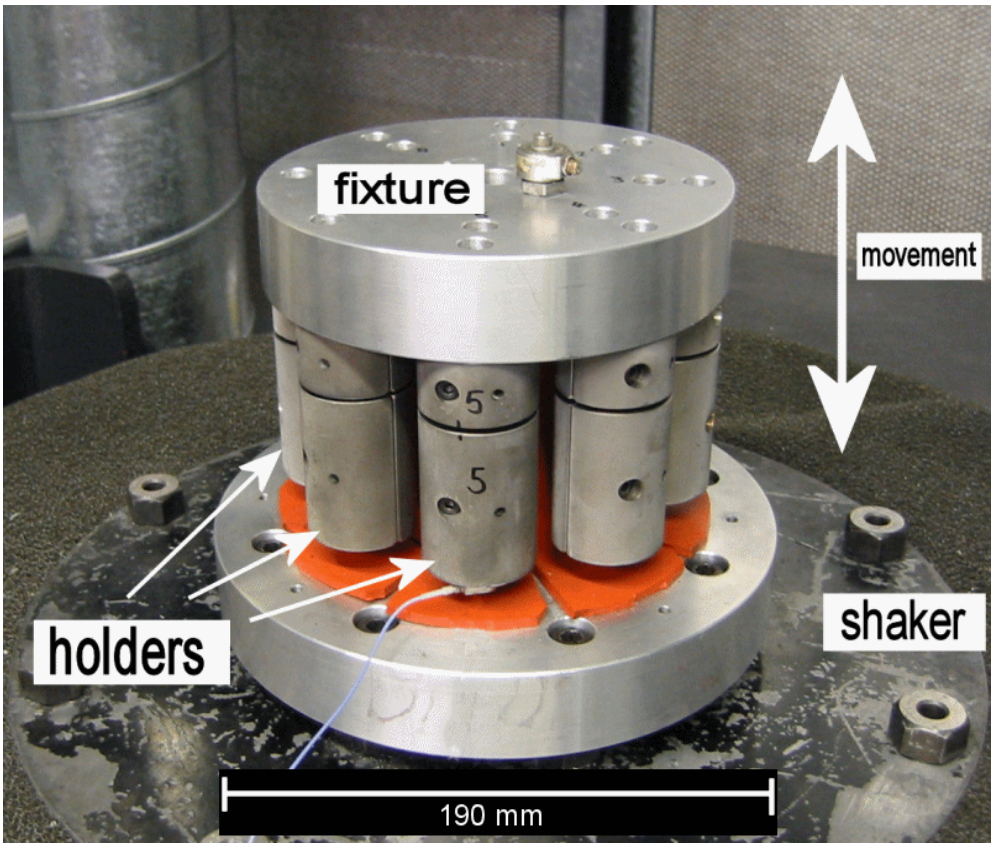

Figure 3.4. High-cycle fatigue testing fixture, mounted to electro-dynamic shaker, containing stainless steel holders and Cu rods joined by solder

Bolted to the upper flange of the fixture are up to eight equi-spaced stainless steel 316 cylinders with a diameter of 35 mm. (Appendix 7.5). Each cylinder is designed to hold one solder joint specimen vertically through its long axis. To this end, the cylinders have a central 2.50 mm bore machined by EDM. They are also split in two other directions as shown in Figure 3.5.

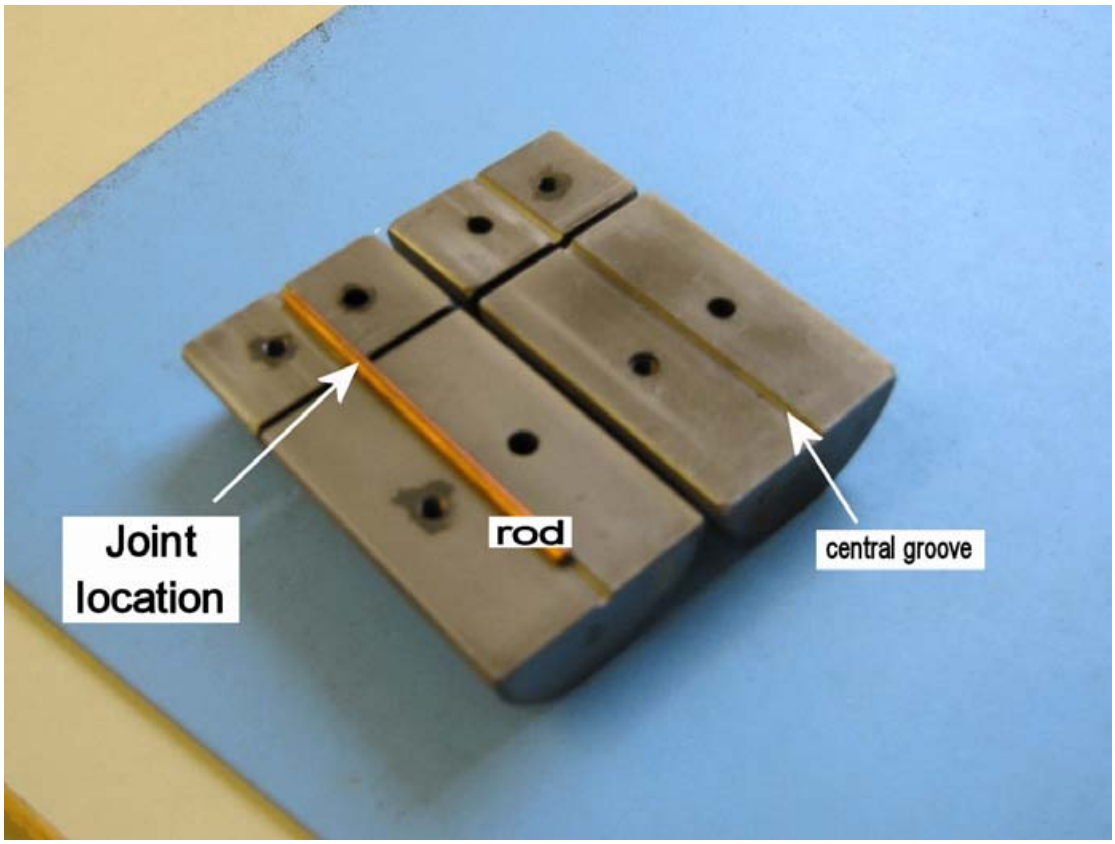

Figure 3.5. Stainless steel cylinder containing Cu rod in central bore

to allow the rods to be inserted and bolted tight. The presence of bolts holes and splits in a cylinder slightly disturb its concentricity as the mass is now no longer uniformly distributed with respect to all radial directions from cylinder's centre. This is detrimental to the dynamic performance of the cylinders as it could worsen lateral vibrations. However the small magnitude of any imbalance is more then compensated for by the swiftness and reliability of the clamping it provides as compared to alternative methods such as grub screws, gluing or threaded rods and holders. The internal and external surfaces of the cylinders were plasma

nitrided by the surface engineering group of the Metallurgy and Materials Department at the University of Birmingham, in order to harden them against repeated clamping and bolting damage.

3.2.7. Test methodology

To conduct a test run, a batch of eight soldered rods are inserted into the eight steel holders described previously, so that the joint sits between the two halves of the holder. As shown in Figure 3.3, the holders are bolted into the fixture so that the larger end of the holder is free-hanging with only the solder joint to take its weight. During testing, the fixture is vibrated in the vertical (Z) direction, creating an alternating tensile then compressive stress in the solder joint due to the inertia of the mass attached to it. The force on the joint is simply determined by Newton's 2nd Law; $F = ma$; and transformed to stress by dividing by the area of the joint. A static force of 1 g multiplied by the mass of the lower holder (0.367 kg) is exerted on the joints due to gravity. This results in a slight offset from zero of the mean of the stress cycle. With test accelerations ranging from approximately 20 to 50 g, this represents only 1–2.5 % of the dynamic stress range and is disregarded. As the cycles of stress accumulate, a fatigue crack will initiate then advance through the solder joint, eventually causing failure. When this occurs, the lower half of the holder drops into a padded compartment keeping the two fracture surfaces away from each other while the remaining specimens continue to be cycled. Each holder is connected to one channel of a simple data logger which measures electrical continuity and registers a voltage change when the two halves separate. This data is reviewed after all specimens have failed and the times to failure noted and converted to cycles to failure by multiplying by test frequency. If any specimen had not failed after 5×10^8 cycles (approximately 10 days' continuous testing), the test was halted and the specimen was

considered a ‘runout’. Unless otherwise stated, all tests were conducted at ambient temperatures, which in the room used corresponded to around 25 ºC.

3.2.8. Control system and resonance determination

Since the aim of the present work is to replicate as closely as possible the uniformity achieved with a conventional material test machine, a test frequency was chosen which would avoid resonant behaviour of any part of the system, thus ensuring that failure occurred due only to axial loading and at the amplitudes calculated. To determine this test frequency, both experimental and finite element work was conducted. Experimentally, initial test runs were conducted on a Ling 805 electrodynamic shaker controlled by a Data Physics vibration control software/hardware system. The drive input to the shaker is a sinusoidal waveform whose amplitude is controlled in a closed-loop configuration by feedback from an accelerometer mounted to the top of the fixture. The accelerometers used varied from test to test but were all Endevco models which vary capacitance in response to acceleration, a feature which is less sensitive to cable interference than voltage output. In addition to the control accelerometer mounted to the fixture, a second accelerometer was used to determine the response of the holder to a range of input frequencies. Mounting an accelerometer on the side of the holder was attempted in order to assess the off-axis response. However this was not ideal as the accelerometer’s mass, although small, contributed to the response when mounted in this way, moving it to different locations was problematic and its output signal was very small. Therefore a different instrument was used to measure the response; a laser vibrometer (Polytec CLV1000) which can make non-contact velocity measurements of a surface from any angle. The laser vibrometer output signal is differentiated in software to provide a direct acceleration reading.

3.3. Finite element modal analysis

In parallel with this experimental work, a finite element analysis of the rod/holder system was conducted using ANSYS Workbench 9.0. A single rod and holder were modelled in three dimensions using elastic, isotropic elements with the appropriate material constants for copper, stainless steel and tin (representing Pb-free solder). Material constants are given in Table 3.2. The bolts, holes and splits in the cylinder were not modelled for reasons of simplicity. Perfect constraint was assumed at the rod/holder interface and also at the top surface of the holder to represent being bolted to the fixture. A modal analysis of this system was conducted to identify the first six natural frequencies of the system. The displacement contours of the modes identified by the analysis are shown in Figure 3.6 and their frequencies are given in Table 3.3.

Material	E (GPa)	Poisson ratio
Steel	200	0.30
Copper	120	0.35
Solder 1 (Sn-Pb)	30	0.40
Solder 2 (Pb-free)	50	0.36

Table 3.2. Material properties used for FE analyses

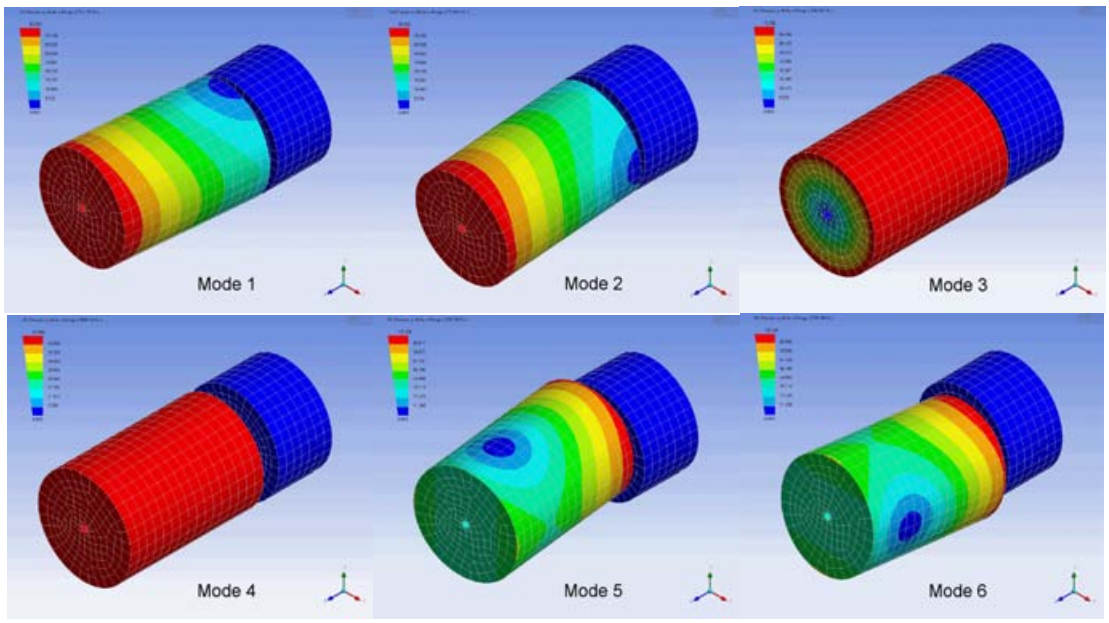

Figure 3.6. Displacement contours of first six resonant modes of rod/holder system predicted by FEA

Mode	Frequency (Hz)
1	73
2	74
3	154
4	3,060
5	3,250
6	3,262

Table 3.3. Frequencies of first six resonant modes of rod/holder system predicted by FEA

Modes 1 and 2 are close in frequency and show the propensity for lateral 'wobbling' low down in the frequency range. Mode 3 is the torsional rotation of the lower holder about the Z axis while Mode 4 is the axial stretching of the rod along the Z axis due to the mass of the lower holder. Modes 5 and above deviate from simple harmonic motion.

3.4. Experimental modal analysis

In comparison to these predicted results, the results of the experimental modal analysis are presented. The frequency response of the Ling 805 shaker is 10 – 3000 Hz. Sweeping the drive frequency through this range showed the response of the holder obtained from training the laser vibrometer on positions of maximum displacement as predicted by the finite element model, at appropriate angles. These responses are presented in Figure 3.7.

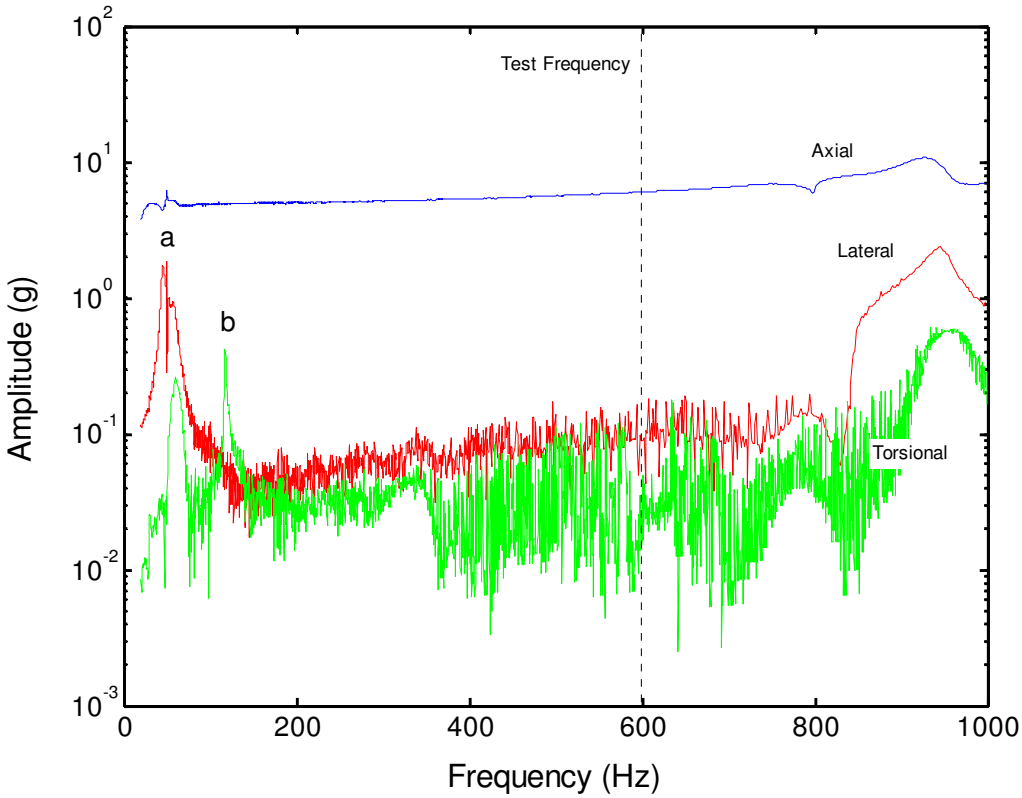

Figure 3.7. Experimental resonance testing results showing response of rod/holder through frequency range of 10 Hz to 1 kHz with 5 g sinusoidal input waveform. Letters a and b indicate the location of modes 1/2 and 3 respectively.

The lateral bending and torsional modes are identified in the graph by correlation with the FEA results. These identities were further checked by varying the angle and position of the laser vibrometer to verify that it obtained the strongest signals in the directions expected for each requisite mode. Their lower experimental values compared to FEA are expected because the constraints in the FEA model are perfect, whereas in reality more flexibility between components exists, lowering the stiffness and hence resonant frequencies of the system. This suggests that in practise, Modes 4-6 probably lie within the frequency range of the Ling 805 shaker. In the range above 1 KHz, however, numerous and high-amplitude resonant peaks were found in the response of both the holder and the general fixture it was mounted to, making identification of the modes relative to FEA modelling impractical and

running tests near those frequencies hazardous. It was hence decided to restrict the frequency range of interest to 10-1000 Hz, as displayed in Figure 3.7. A test frequency of 600 Hz was selected on the judgement that it was far away from any resonant peaks yet would still achieve fast testing speeds. This is within the range of frequencies generated by a jet engine [112].

3.5. Finite element stress analysis

In addition to the modal analysis described previously, the stresses on the solder joint were modelled in order to calibrate test acceleration level to solder joint stress. The same analysis parameters as before were used but with the addition of a static pressure on the lower face of the lower holder. The value of this pressure was chosen to create a force on the solder joint equal to that of the peak dynamic force created by the inertia of the holder mass during acceleration. Thus a 'snapshot' of the stresses at the peak of the acceleration sine wave is obtained. Stress in the solder volume in uniaxial tension at 1 g is given by:

Force = mass (holder) * acceleration

= 0.367 kg * 9.81 ms^{-2}

= 3.600 N

Stress = force / area (solder joint)

= 3.600 / (π * 0.00125 $m^{2)}$

= 0.733 MPa

Two analyses were run; one with appropriate Young's Modulus and Poisson's Ratio values for Sn-Pb and one with values representing pure Sn. Sn is deemed an appropriate reference to use because all the Pb-free solders in the present work are overwhelmingly constituted of it and both Young's Modulus and Poisson's Ratio are both properties of the parent matrix and

do not change with small additions of alloying elements [42]. Properties for pure Sn are taken from Smithells [7] while the Young's Modulus value used for Sn-Pb is that reported by Plumbridge et al. [6] from acoustic pulse methods.

The results of the modelling for solders with elastic moduli of 30 and 50 GPa are shown in Figure 3.8 and Figure 3.9 respectively.

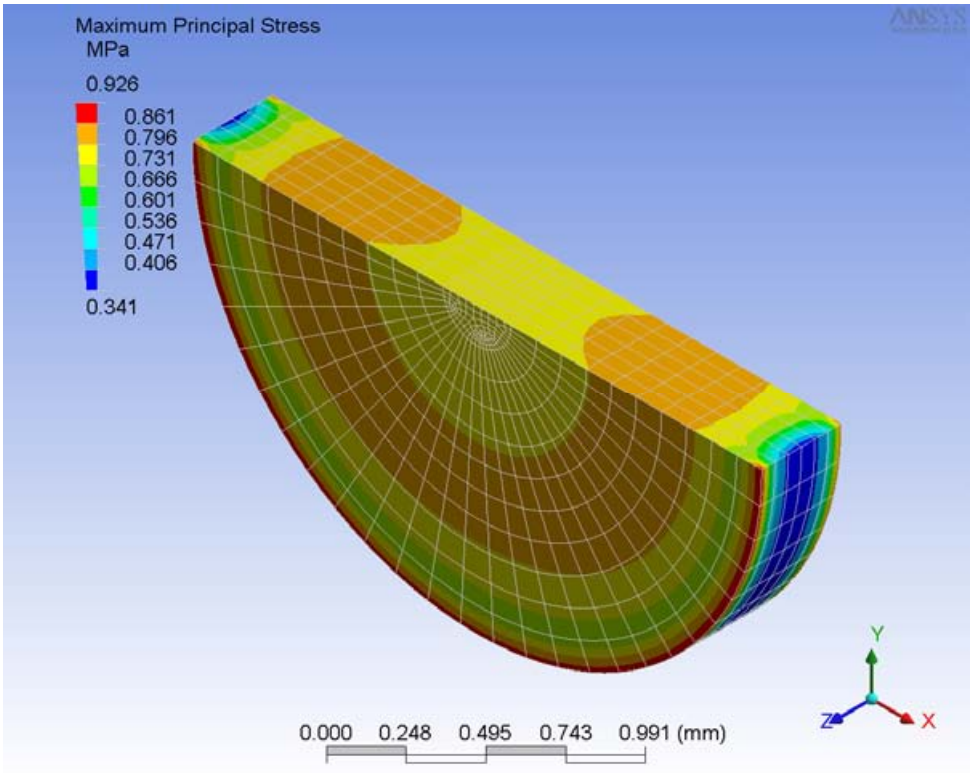

Figure 3.8. Section through solder joint showing calculated maximum principal stresses at 1 g acceleration for 30 GPa solder (Sn-Pb)

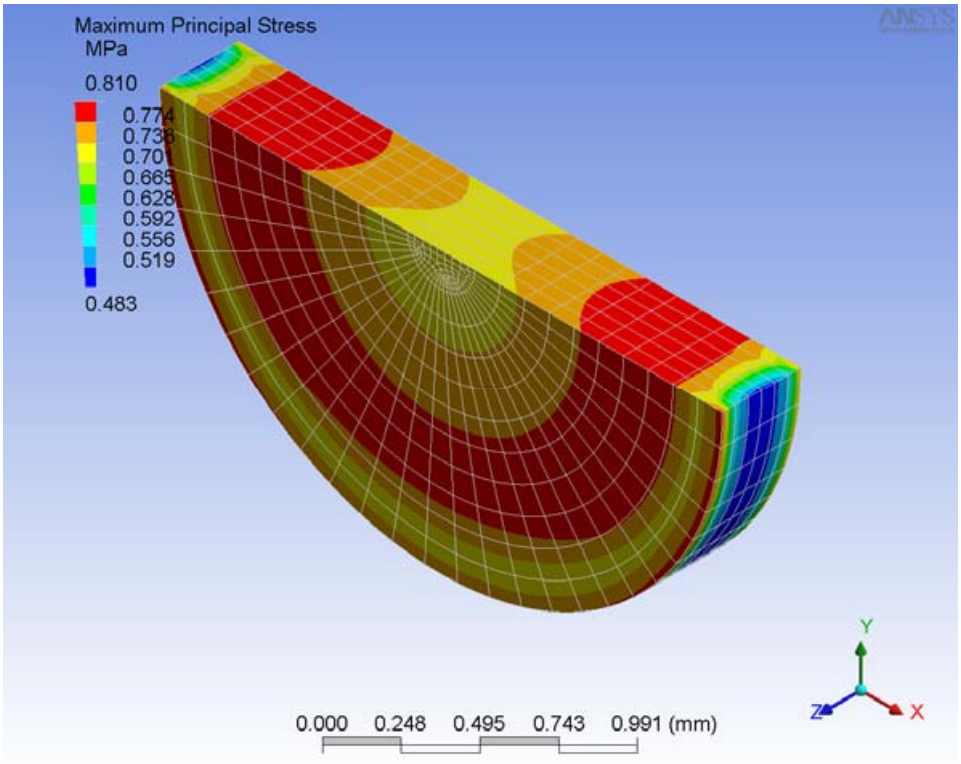

Figure 3.9. Section through solder joint showing calculated maximum principal stresses at 1 g acceleration for 50 GPa solder (Pb-free)

The maximum principal stress directions in both cases were exclusively in the Z direction. Minimum principal stresses were also examined and found to be diminutive compared to the former. Although there are local areas of high and low stresses around the circumference of the solder joint, the stresses are relatively uniform in the bulk of the joint. Thus it is deemed reasonable to take the mean of all nodal maximum principal stresses over the volume of the joint to arrive at calibration factors of 0.74 MPa/g and 0.77 MPa/g for Pb-free and Sn-Pb solders respectively. These figures are used henceforth to translate test accelerations into solder joint stress values. These values are referred to as 'nominal stresses' because it is recognised that they are an average and will also experience slight variation due to physical tolerances and test conditions.

3.6. Elevated temperature tests

Elevated temperature tests were conducted by utilising a shaker built into a thermal cycling chamber. After all the holders had been inserted and the data-logging cables connected, the chamber was set to 100 ºC and left for around an hour to allow all parts of the apparatus to attain this temperature. All other methodology was as reported earlier in the chapter.

3.7. Damping capacity tests

The damping capacities of three solders; Sn-Pb, Sn-Cu-Ni and SAC305 were investigated by examining the width of their resonant peaks. The first two resonant peaks of the system, occurring approximately between 40-55 Hz, are characterised earlier in the chapter and were selected for examination due to their large amplitude. As before, a laser vibrometer was used to measure the off-axis response of a joint/holder system over the range of frequencies in question. The HCF apparatus was installed in a combined shaker + temperature cycling

chamber as in the elevated temperature tests, with the laser aimed through a port hole in the chamber (Figure 3.10 and Figure 3.11).

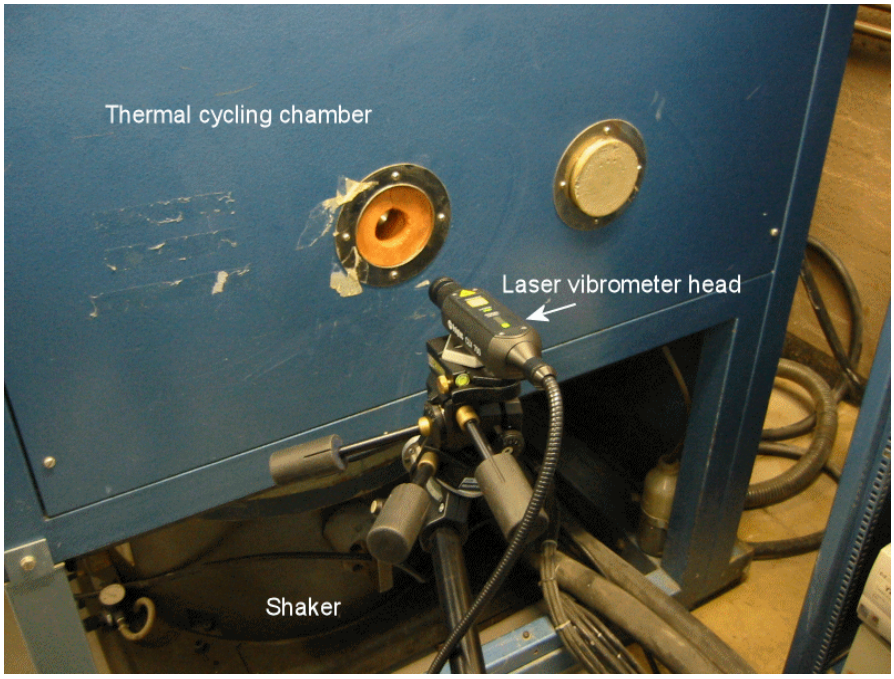

Figure 3.10. Laser vibrometer aimed through port hole in thermal cycling chamber for resonant decay testing

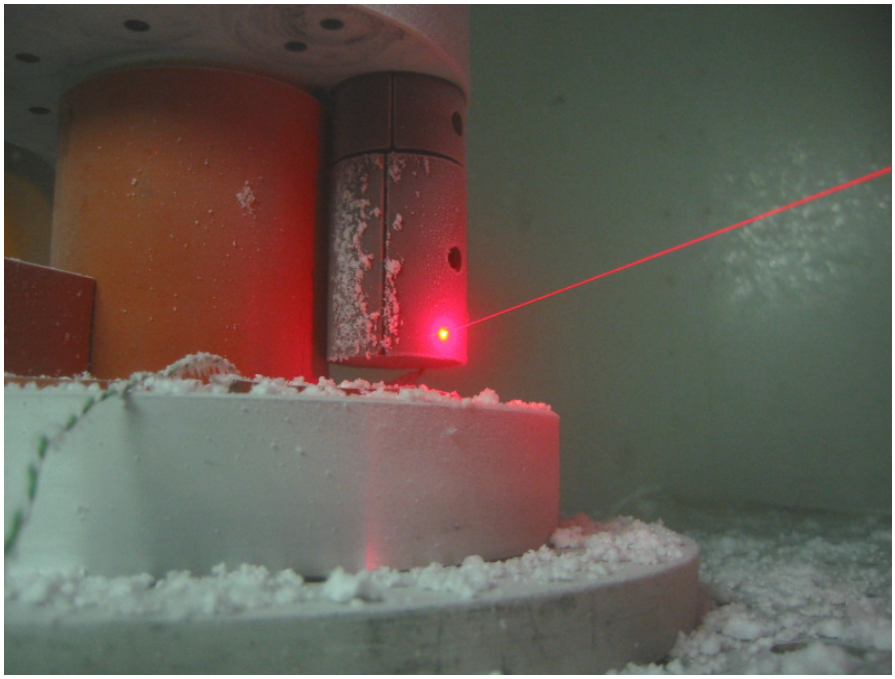

Figure 3.11. Laser vibrometer beam aimed through chamber hole onto holder/fixture at -50 ºC (beam visualisation from LNO_2 vapour)

Frequency sweeps at 1 g acceleration were conducted at temperatures ranging from -50 to +100 ºC, with the temperature of the test fixture established from a thermocouple mounted to it. At low temperature extremes the fixture was left to stand for several minutes to allow dissipation of the liquid nitrogen vapour (used to cool the chamber) which obscured the laser beam. The data were smoothed in Matlab using the Savitzky-Golay algorithm, which preserves peak amplitude and precision, and plotted using a spline interpolant fit. Q values were calculated from the spline curve using the approximation given by Lalanne et al.[98] as the inverse of the damping factor η.

3.8. Resonant frequency decay tests

In order to track the resonant frequency decay of the rod/holder system, the following procedure was followed. Instead of vibrating continually until failure, selected rods underwent individual tests which were halted at regular intervals (commonly 10 – 20 s) and a survey of the resonant frequencies of the system conducted at each interval, using the laser vibrometer in lateral positions as previously. The frequencies were recorded and when they began to drop significantly, the intervals were shortened and the tests continued until the desired decay had been achieved. Empirically-based judgement was used as to when to reduce the intervals and by how much, experience being gained from initial testing of a number of SAC387 rods which were superfluous to requirements. It was quickly found that cracking and hence resonant frequency decay of the rods was confined overwhelmingly to the final 5 – 10 % of the life of the specimens, whereupon decay materialised very quickly. This necessitated very short intervals of testing in the final stages; down to 0.05 s or 30 cycles of stress. Occasionally the judgements failed and the rods broke unintentionally, in

which case the result was simply recorded as standard. Approximately 25 rods were assigned to resonant decay testing; of these, 19 attempts were successful in halting tests before final failure. Rods made with various solders were used; generally those with Ni coatings. They were chosen from batches assigned to the highest-stress (40 or 45 g) and hence shortest-duration tests for practicality reasons. The frequency sweeps used during test intervals to determine resonant peaks were set at a level of -40 dB from the main test amplitude, to avoid causing actual damage to the solder joints while ensuring sufficient signal strength for the laser to operate with. Upon successfully halting a test, the intact rod was carefully removed from its holder and the majority of its excess length cut off. The remaining rod stub was then held in the assembly fixture (Figure 3.1) to help grind it down on a rotating grinding wheel in a controlled manner. An example of such a stub is shown in Figure 3.12.

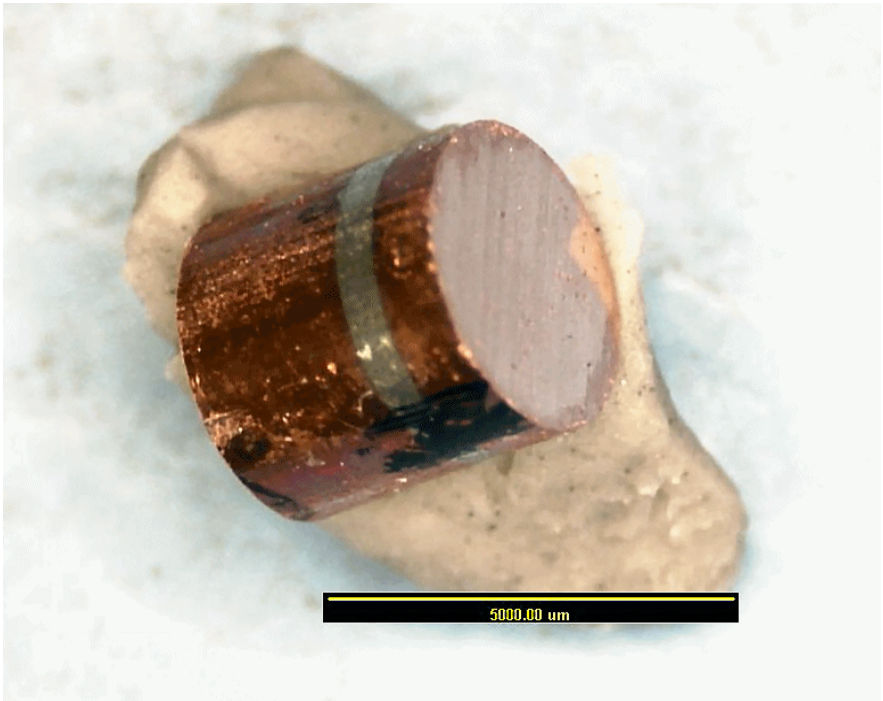

Figure 3.12. Solder joint/rod stub ground down for SAM examination

3.9. Acoustic Microscopy

A Scanning Acoustic Microscope (SAM) was utilised to investigate the cracking behaviour of HCF solder joint specimens cycled almost to a point of failure, as described previously. The mechanisms giving rise to contrast in SAM images as well as the operating principles of the machines are covered extensively by Briggs [108]. The system, loaned by Ultrasonic Sciences Ltd (USL), was equipped with a 20 MHz pulse generator and a range of transducer probes operating at between 35 and 50 MHz. HCF joint stubs were prepared as above and placed on a metal plate in the operating water tank of the SAM. The orientation of joints was noted and reversed in cases where imagining was inconclusive, to establish at what depth features of interest lay in the solder joint. Images are presented as greyscale micrographs representing a raster scan over the area of the joint, typically at a speed of 0.01 mm/s. Since the edges of a solid are ill-defined in a SAM due to scattering of acoustic energy, a white circle is superimposed on the images in software. The circle represents the physical outline of the specimen, having a diameter matched to it (measured by Vernier callipers) and calibrated by comparison to the scale bar created by the SAM software. The SAM software also includes a calibration for depth which is based on the time-of-flight of signals through materials of a known acoustic wave propagation velocity. The library included with the software suggests a figure of 4650 m/s for copper; this was adjusted to 4370 m/s after calibration against the thickness of joint specimens determined optically as described previously. Subsequently each image displays a gate depth, indicating the start of the electronic ‘gate’ in mm, and a gate width, representing how far past this start the signals continue to be collected from. Hence only a ‘slice’ or x-y plane of the solder joint is imaged – usually also the plane in greatest focus. Brightness and contrast of images were adjusted in software to optimise details and boost dim images originating from weaker reflections. All

rods used for resonance testing and SAM imaging possessed Ni coatings, with the exception of rods 214 & 215 (SAC387) and all Innolot joints, which used uncoated Cu rods.

3.10. X-ray imaging

X-ray inspection of some HCF solder joints was carried out by Tin Technology Ltd in St. Albans, TRW in Shirley and TWI in Port Stanley. All three companies utilised modern X-ray microfocus machines with beam voltages of approximately 110-160 kV in order to detect voids in untested joints. A number of part-tested joints, prepared as in the resonant decay method description, were also X-rayed to help correlate features seen (e.g. voids) with those found using the SAM.

3.11. Microscopy

Solder joint specimens cross-sectioned for metallography were generally prepared in the following manner:

1. Set in cold-curing epoxy resin
2. Desired material removed by grinding on rotating wheels with fresh grit papers in the order 80, 240, 320, P600/1200 at around 150 rpm
3. Polished on rotating wheels with cloths impregnated with 6 then 1 μm diamond paste at no more than 120 rpm
4. 20-30 second polish with 0.02 μm colloidal silica solution

The final, alkaline-based, colloidal polish also has an etching effect on Sn-based solders; Sn is consumed but Pb and intermetallics are not. The resultant surface relief gives clear microstructural contrast under both light and electron microscopes. Light microscopy was conducted in Goodrich laboratory facilities using a typical compound microscope under

polarised light. Cross-polarising was used to give grain orientation contrast and DIC (Differential Interference Contrast) prisms were occasionally used to enhance the contrast of microstructural features. Electron microscopy was predominantly carried out at the University of Birmingham using JEOL 6060, Philips XL-30 or JEOL 7000F scanning electron microscopes (SEM). For cross-sections set in epoxy, specimens were generally gold coated by plasma sputtering for 3 minutes to avoid surface charging in the SEM. Energy-Dispersive X-ray (EDX) spectroscopy was conducted in-situ by Oxford INCA systems for elemental analysis. Electron Back-Scattered Diffraction (EBSD) is a relatively new technique for phase identification and crystallographic orientation studies in the SEM and is described by Watt [113]. The technique was used in the JEOL 7000F, equipped with a field-effect electron gun and an Oxford Crystal EBSD detector system. Samples were polished with extreme care and left uncoated – charging was addressed by coating any exposed epoxy surface with silver-loaded paint. Samples were inclined at 70º to horizontal and accelerating voltages of 20 – 25 kV were used.

3.12. IMC layer thickness measurements

To determine the thickness of IMC layers, an image measurement method was employed on SEM images of the requisite areas. Using a manually-guided line-detection algorithm in the Paint Shop Pro 9.0 software program, the IMC layers were traced around and all pixels enclosed by them turned to white (brightness value 255) while all other pixels were set to black (brightness value 0) as in Figure 3.13. This black & white image was saved to disk whereupon a simple Matlab script was used to count the numbers of black and white pixels

and divide by image width to give an average thickness. This thickness was converted from pixels to microns with the calibration information from the image itself using its overlaid scale marker. Results from between six and nine images spread across different joints were averaged to give the final figures for each solder and substrate type.

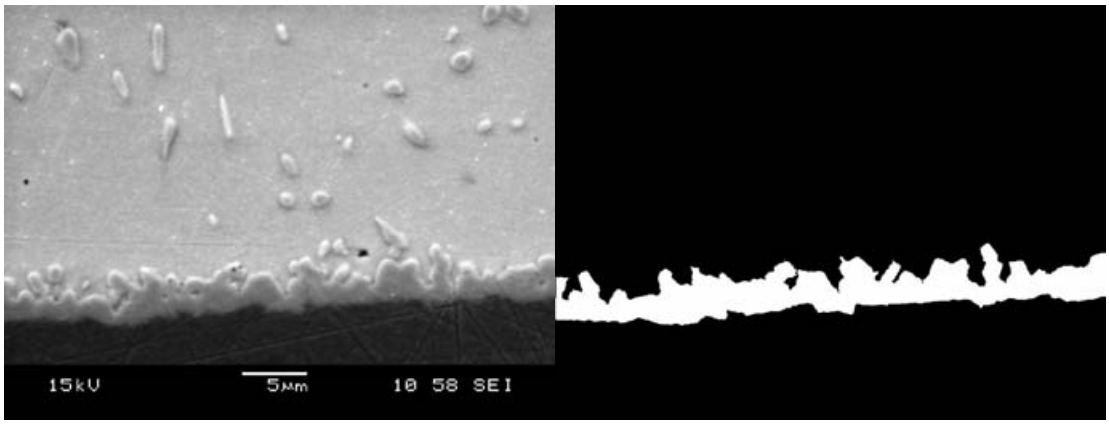

Figure 3.13. Electron micrograph (left) of IMC layer and accompanying black & white processed image for pixel counting to transform into layer thickness measurement

3.13. Tensile testing

Five specimens of each of the following types of solder: Sn-Pb, Sn-Cu-Ni, SAC305 and Innolot were constructed by the same experimental procedure described previously. They were subjected to monotonic tensile tests in an electric screw-driven polymer testing machine, chosen for its low load capability. A test speed equating to a strain rate of 2.4 s^{-1} was used for all tests, to approximate the strain rate experienced by the HCF solder joints during testing. This is difficult to establish in the case of the dynamic HCF tests since the loading waveform is sinusoidal and hence strain rate is continuously varying. However a linear approximation yields a strain rate of around 1 s^{-1} experienced by the joints under dynamic HCF loading. The actual strain rate of the tensile specimens will necessarily be less than the nominal 2.4 s^{-1} figure due to much strain being absorbed by the Cu rods that the solder is attached to. Cross-head extension was measured along with test load (converted to

nominal stress) and the results saved electronically to be plotted later. Fracture surfaces were kept for SEM examination.

3.14. High-speed video capture

It was deemed necessary in the early stages of developing the HCF test method to establish whether the failures were due only to tensile/compressive fatigue failure and not affected by torsional, bending or other modes of vibration predicted by FEA and confirmed by experimental modal analysis. Reducing test frequency to a level where cycling was slow enough to be observed by the human eye was not possible for two reasons. Firstly, the acceleration capability of the shaker decreases with frequency due to it needing more displacement to maintain the same acceleration; there is a physical displacement limit of the machine which would make this unachievable in most cases. Reduction in test frequency would also bring the testing down into the range of undesired resonances (Figure 3.7) which could interfere with results. Therefore a high-speed video camera (Olympus I-Speed monochrome) was hired in order to capture the motion of the system at the point of joint failure. A frame rate of 3000 fps was selected, giving 5 video frames per vibration cycle. With suitable lighting, three solder joints were fatigued to failure whilst recording video of the joint through a close-focusing lens. The camera records ten seconds of video up to the point at which it is triggered; in this case manually upon seeing that the solder joint had broken.

4. Results

4.1. Microstructure notes

The reported microstructures of both Sn-Pb and Pb-free solders have been discussed in Chapter 2, with the exception of the Innolot alloy which is not the subject of any published work at the time of writing. Microstructures obtained in the present work are presented from polished cross-sections of actual HCF joints following the preparation method outlined in Chapter 3 and subject to the soldering and heat treatment procedures outlined therein.

4.1.1 Sn-Pb

Figure 4.1 shows a typical Sn-Pb microstructure obtained in the present work with alternate Sn-rich and Pb-rich lamellar phases of length scale ~5 μm present. A less-magnified view Figure 4.2 shows variation in the distribution of these phases throughout the joint. This is consistent with un-aged Sn-Pb microstructures widely reported elsewhere [5]. Pb precipitation within the Sn-rich phases is a common phenomenon due to the reduction in mutual solubility of Sn and Pb upon cooling to room temperature and is shown in Figure 4.3. The grain structure of eutectic Sn-37Pb is typically of the same order as the Sn and Pb phase size (~5 μm in the present work), although larger-scale 'colonies' of similar orientation exist throughout a joint which are sometimes misleadingly called grains. These colonies can be distinguished by cross-polarised light microscopy (Figure 4.4). As expected, a Cu_6Sn_5 layer is present at the interface between the Cu rods in the present study and the Sn-Pb solder used Figure 4.5. The mean thickness of this layer in the present work was 1.34 μm which is in line with published data [30]. Any Cu_3Sn layer beneath the Cu_6Sn_5 layer was, if present, too thin to be detectable by FEG-SEM examination. In the case of Ni-coated Cu rods, a thinner (0.72 μm) dual-compound layer was found Figure 4.6. Adjacent to the Ni substrate a Ni-rich

and P-containing compound was identified, while between this layer and the solder, EDX analysis showed a Ni-Sn compound. Exact compositions are hard to determine due to the small size of these layers and the spatial resolution of EDX in the SEM (Figure 4.7, Figure 4.8, Table 4.1). Published work [26, 114] suggests that they could be Ni_3P and Ni_3Sn_4 respectively, although TEM examination would be necessary to determine this.

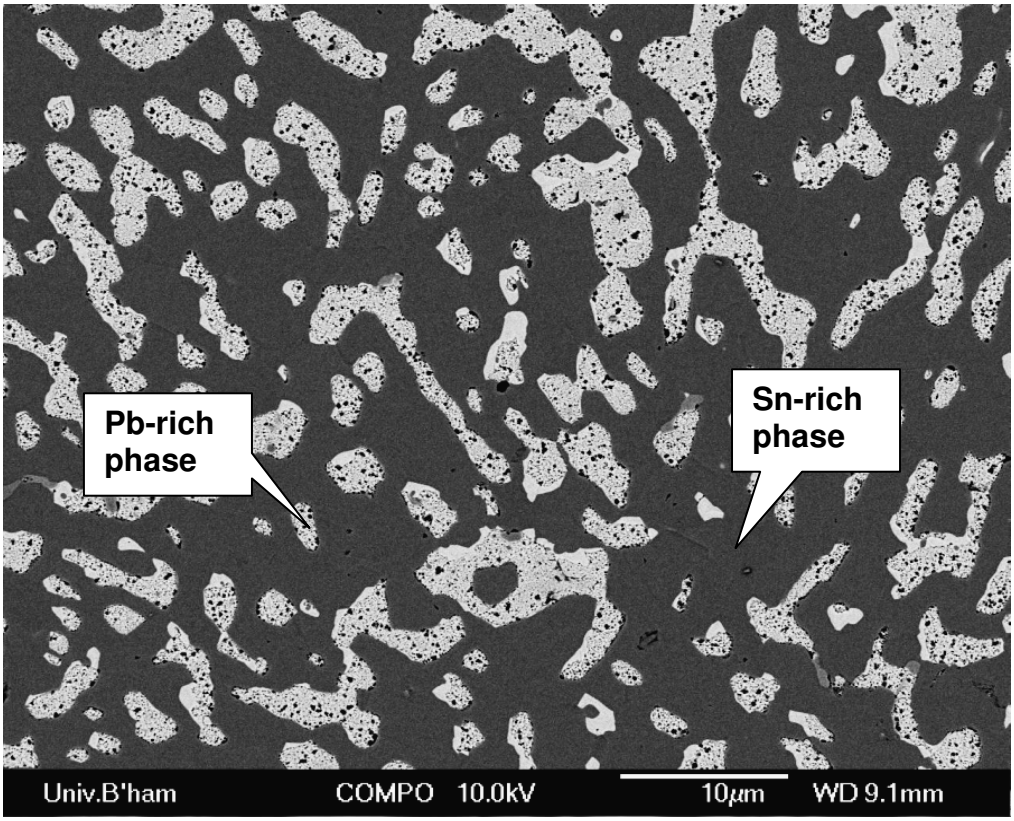

Figure 4.1. Backscattered electron micrograph of typical Sn-Pb microstructure as found in joint (2000x mag.)

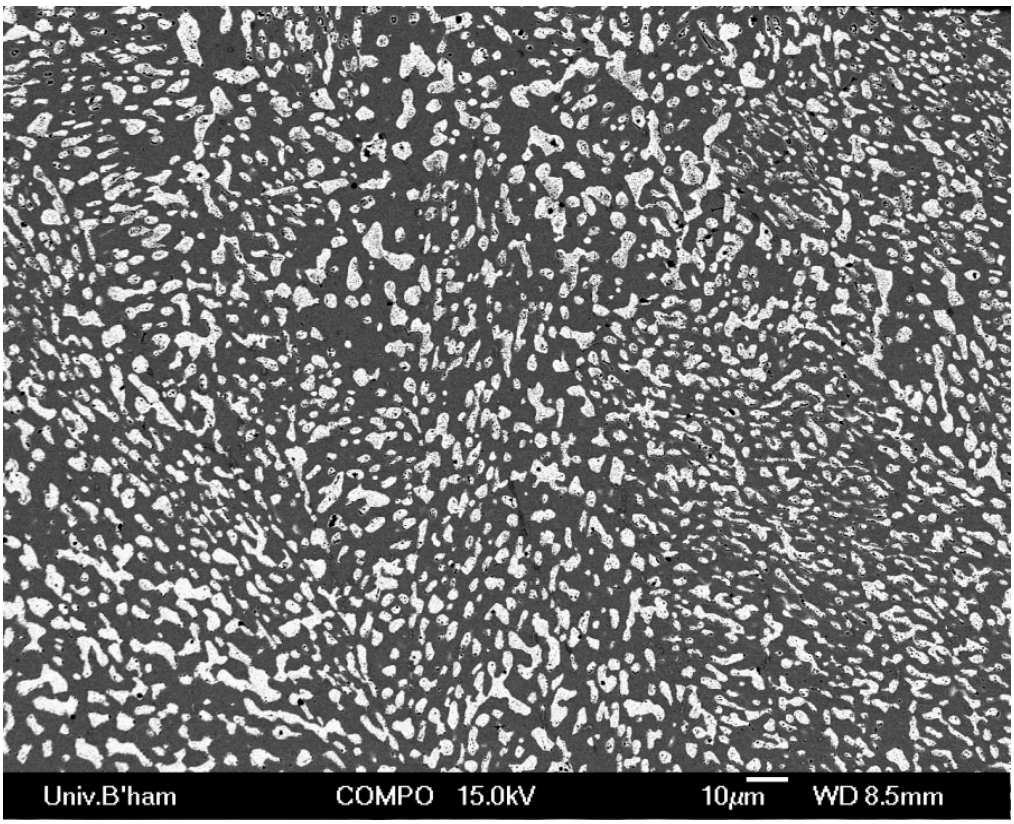

Figure 4.2. Backscattered electron micrograph of typical Sn-Pb microstructure as found in joint (500x mag.)

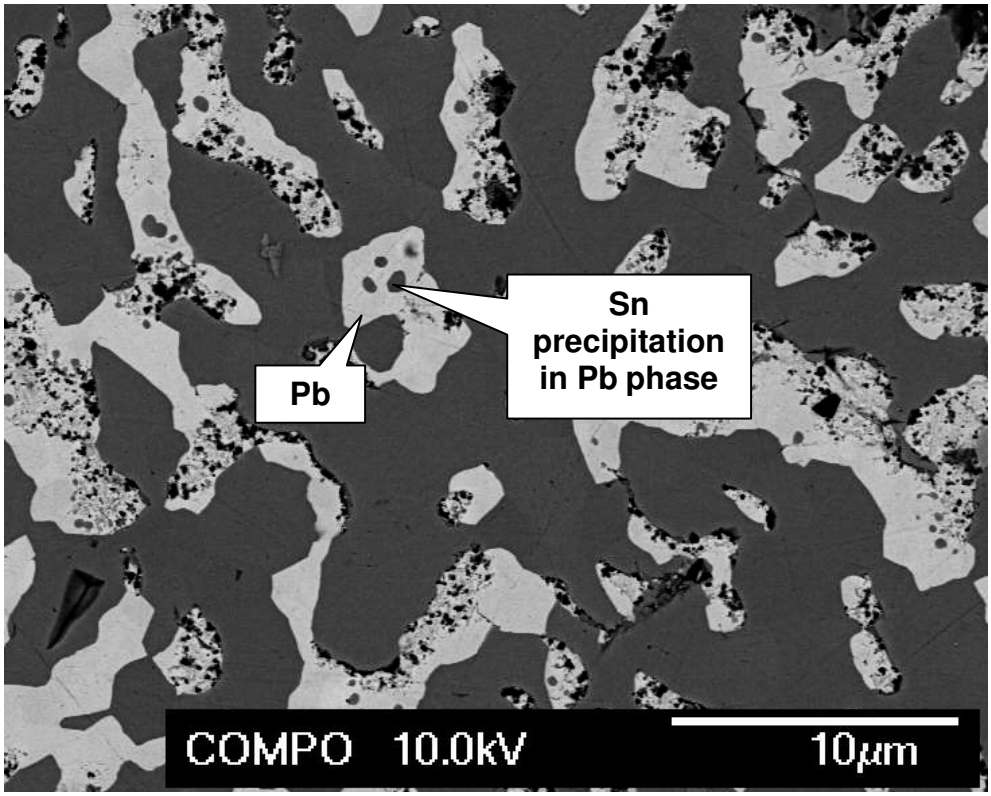

Figure 4.3. Backscattered electron micrograph of Sn-Pb microstructure showing Sn precipitation in Pb-rich phases

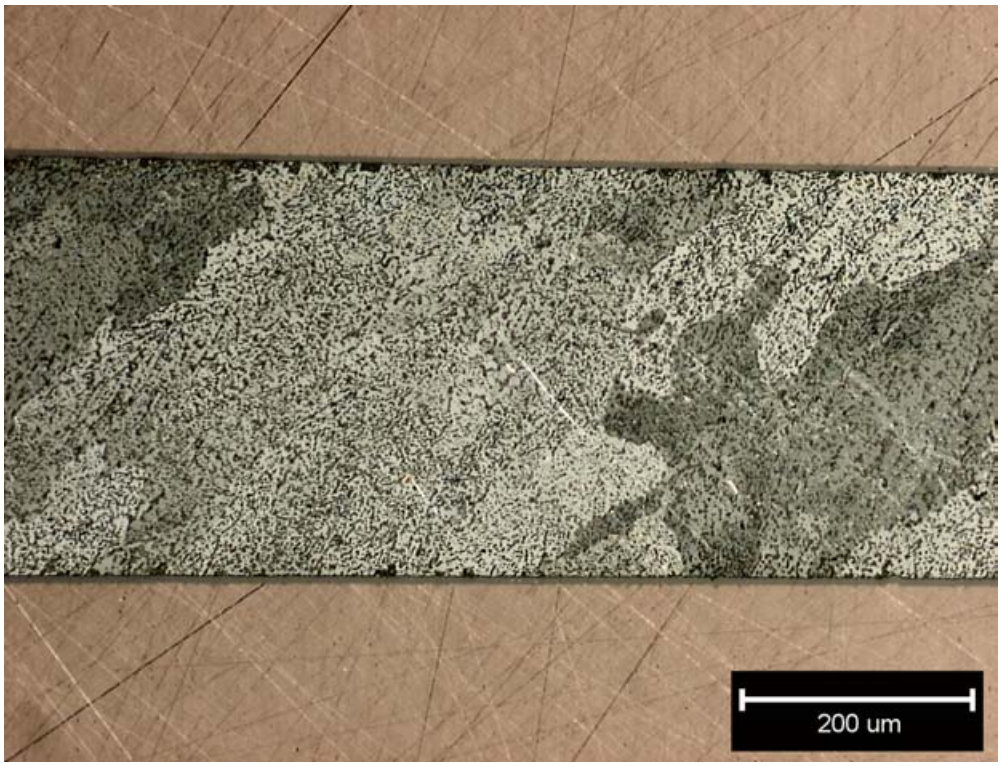

Figure 4.4. Optical micrograph of Sn-Pb microstructure using cross-polarised light, showing different colonies (contrast from crystal orientation)

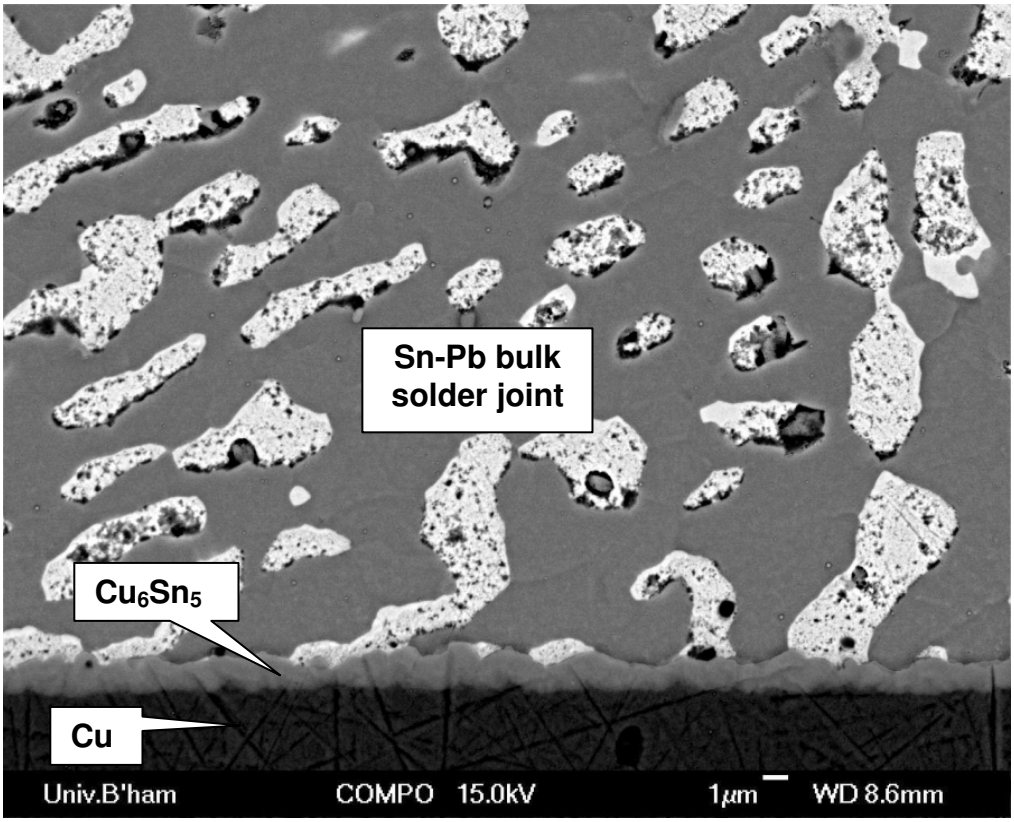

Figure 4.5. Backscattered electron micrograph of cross-sectioned HCF solder joint (Sn-Pb) showing Cu substrate, Cu_6Sn_5 intermetallic layer and bulk solder

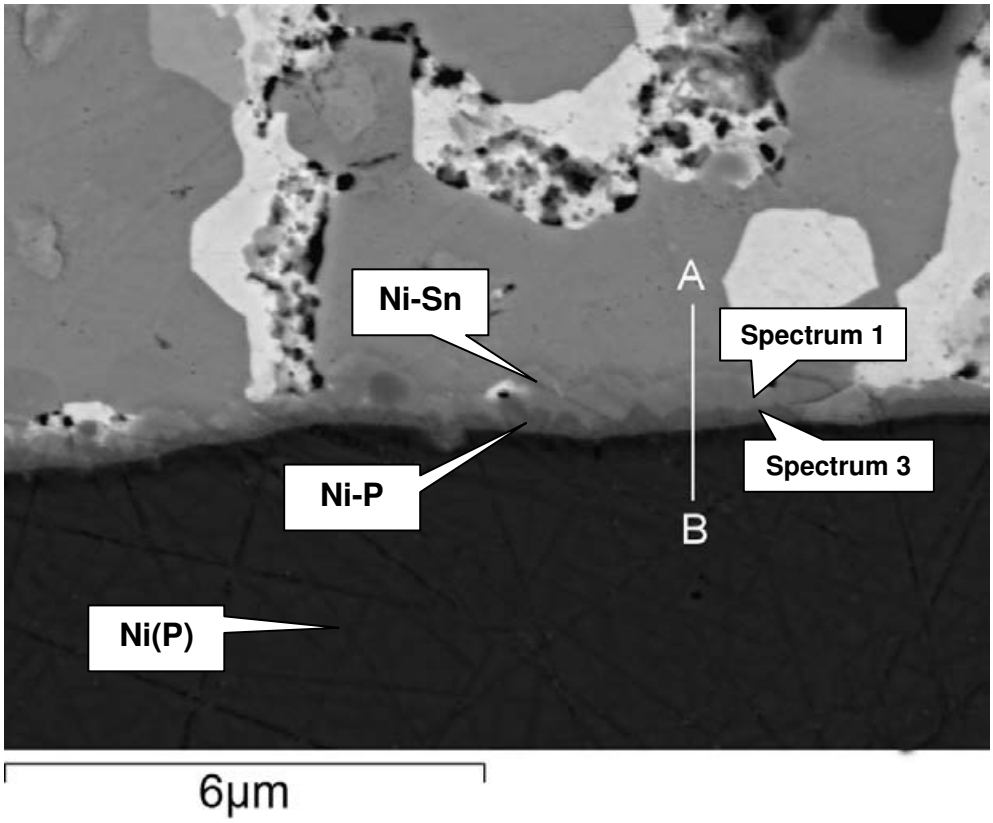

Figure 4.6. Backscattered electron micrograph of cross-sectioned HCF joint; Sn-Pb soldered to Ni substrate showing dual compound IMC layer

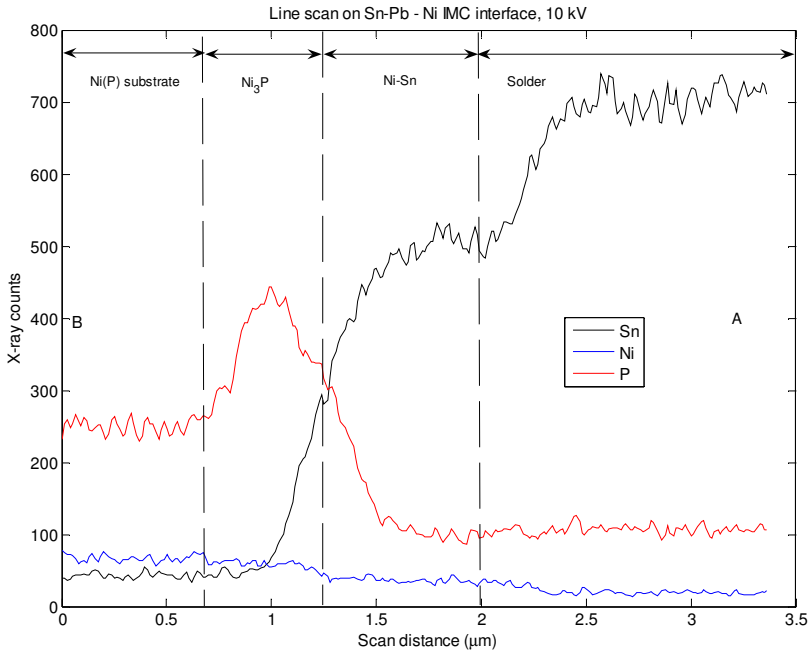

Figure 4.7. EDX line scan along section BA from Figure 4.6 showing distributions of Sn, Ni and P at 10 kV accelerating voltage to achieve high spatial resolution

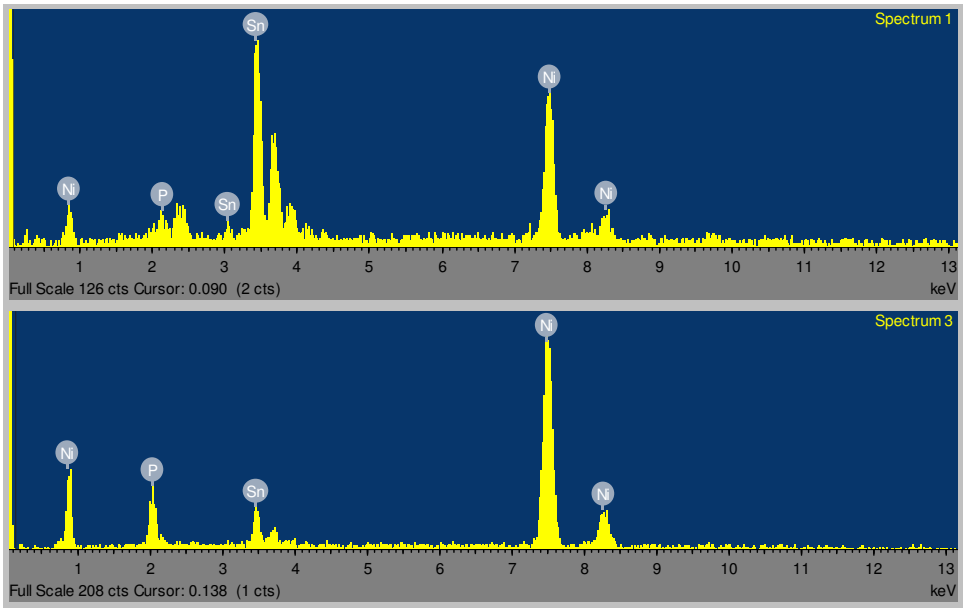

Figure 4.8 – EDX spectra 1 and 3 from Figure 4.6

Element	Spectrum 1		Spectrum 3	
	wt.%	at.%	wt.%	at.%
P	0.03 ± 0.61	0.08	60.1 ± 0.65	11.39
Ni	49.99 ± 1.68	66.86	83.47 ± 1.07	83.42
Sn	49.98 ± 1.68	33.06	10.52 ± 0.92	5.20

Table 4.1. Tabulated X-ray counts for spectra 1 and 3 from Figure 4.6 with accelerating voltage 20 kV to stimulate higher characteristic energy lines of Ni (although analysis volume subsequently enlarges)

4.1.2 Sn-Cu-Ni

Figure 4.9 represents a typical Sn-Cu-Ni microstructure as found in the present work. This alloy is a commercial modification of the Sn-0.7Cu eutectic alloy which itself is the subject of few studies. Therefore microstructural comparisons are difficult to come by although one is provided by Wu and Huang [115]. The amount of Ni added to Sn-0.7Cu to produce the alloy in question is not commercially disclosed but was found to be only 0.05 % in the present work. The purpose of this addition is for the Ni atoms to aid heterogeneous nucleation of the Cu_6Sn_5 phase upon freezing of the alloy, thus giving a finer and more even dispersion of particles in the Sn matrix compared to the un-modified eutectic [49]. In the present work this aspiration was realised to some degree, with network-like eutectic regions being present in some cases (Figure 4.10) although absent in others (Figure 4.11, which showed an even dispersion of Cu_6Sn_5 particles). Interfacial intermetallic layers found when soldering to Cu (Figure 4.12) and Ni (Figure 4.13) substrates are shown. The small constituent amount of Ni in the solidified Sn-Cu-Ni microstructure is distributed chiefly in the interfacial IMC layer after soldering to either Cu or Ni substrates (Figure 4.14 - 4.18). Negligible amounts of Ni were found in the bulk solder Cu_6Sn_5 precipitates in both cases. The thickness of the IMC layer ($(Cu,Ni)_6Sn_5$) for Sn-Cu-Ni on a Cu substrate was significantly higher (4.16 μm) than for the other solders in the study but in line with published results by Nishikawa et al. [51]. When soldering Sn-Cu-Ni to Ni substrates, a $(Cu,Ni)_6Sn_5$ layer is expected [116] and while the accuracy of EDX in SEM, as before, is insufficient to identify positively the interfacial compound, the significant Cu counts shown in Figure 4.18 suggest that $(Cu,Ni)_6Sn_5$ is present in this case.

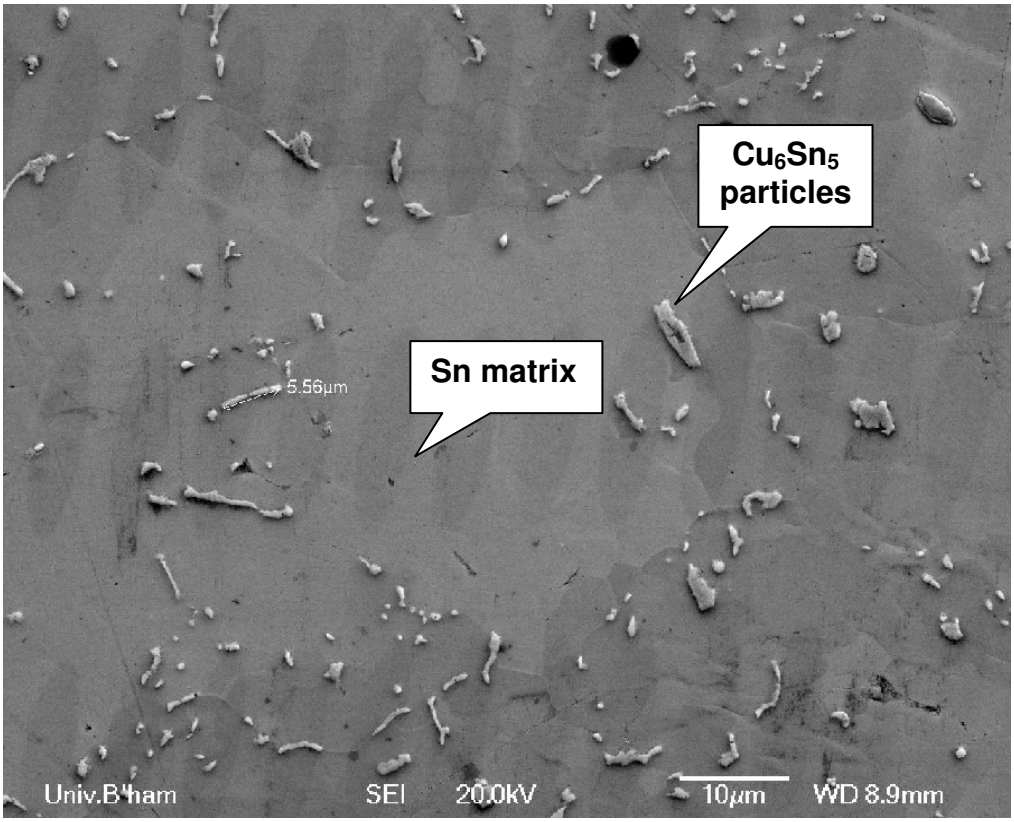

Figure 4.9. Secondary electron micrograph of typical Sn-Cu-Ni microstructure as found in HCF joint (note: elliptical darkened regions are surface contamination as a result of electron beam dwell during scans and should be ignored)

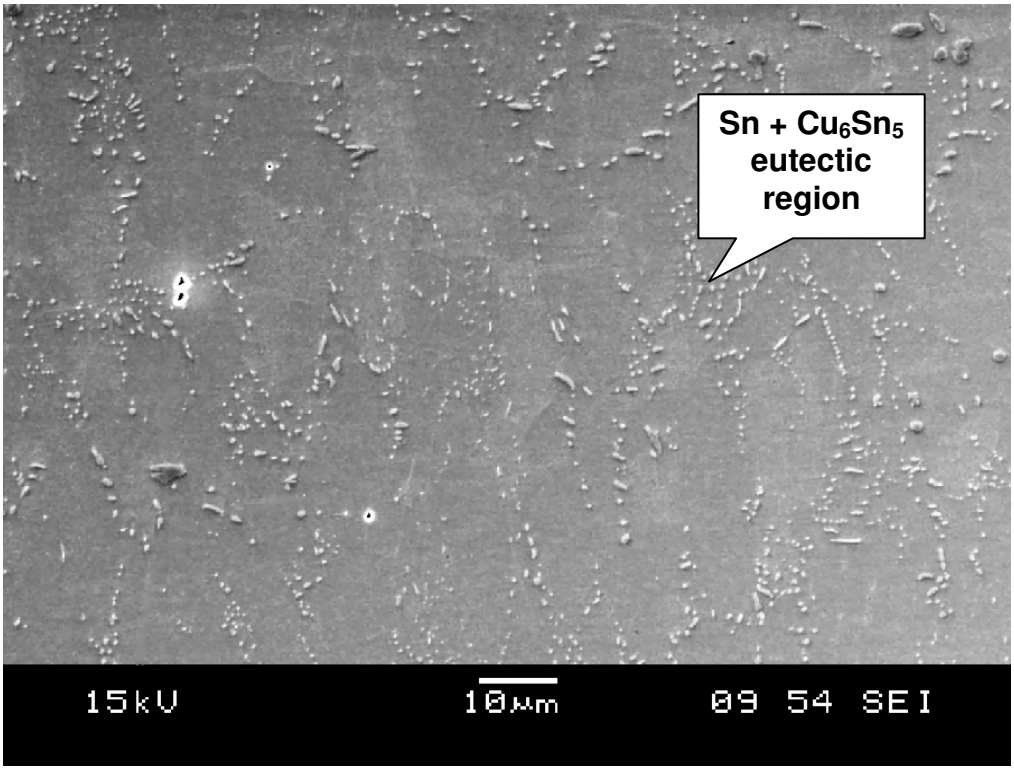

Figure 4.10. Secondary electron micrograph of typical Sn-Cu-Ni microstructure at lower resolution (1000x mag.) showing eutectic regions of Sn + Cu_6Sn_5 in Sn matrix

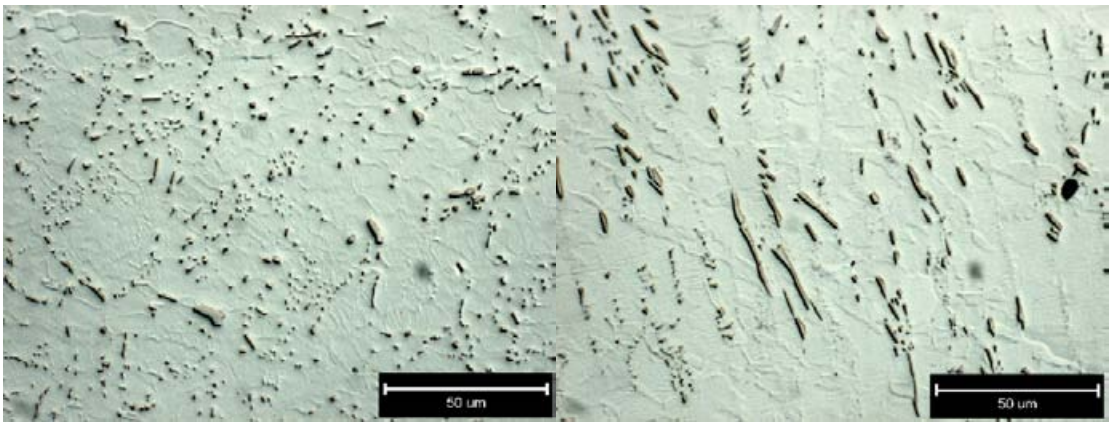

Figure 4.11. Optical DIC micrographs of alternative Sn-Cu-Ni microstructure showing dispersed Cu_6Sn_5 particles with no eutectic regions (500x mag.)

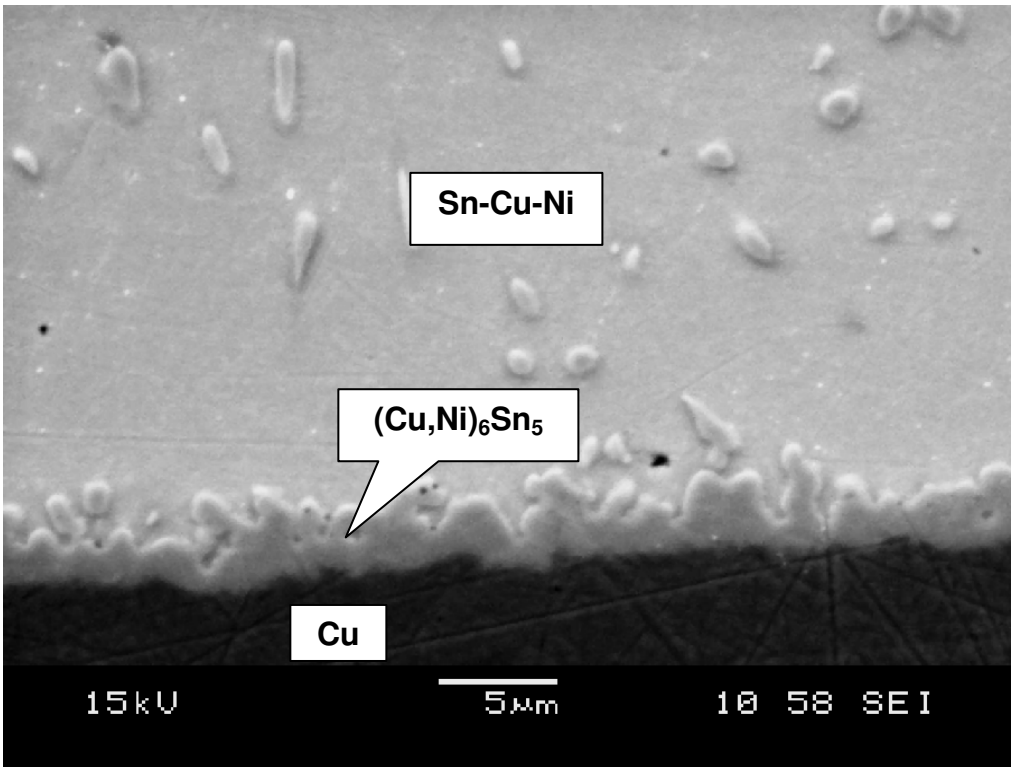

Figure 4.12. Backscattered electron micrograph of $(Cu,Ni)_6Sn_5$ IMC layer found when soldering Sn-Cu-Ni to Cu substrate (3000x mag.)

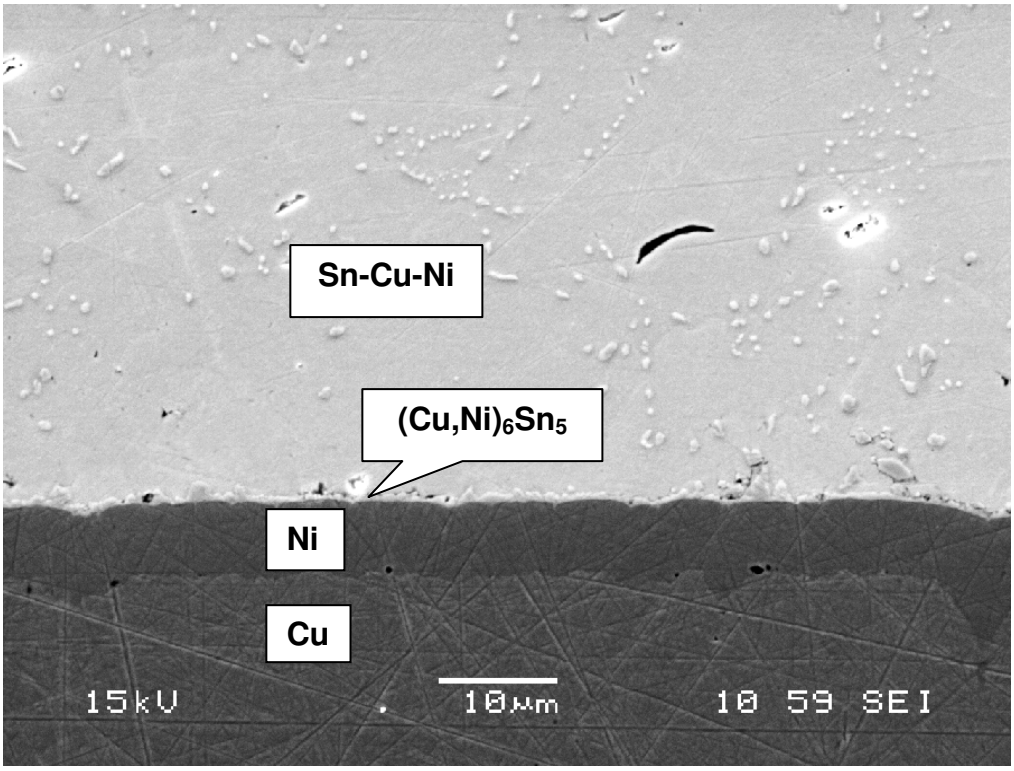

Figure 4.13. Secondary electron micrograph of $(Cu,Ni)_6Sn_5$ IMC layer found when soldering Sn-Cu-Ni to Ni substrate (3000x mag.)

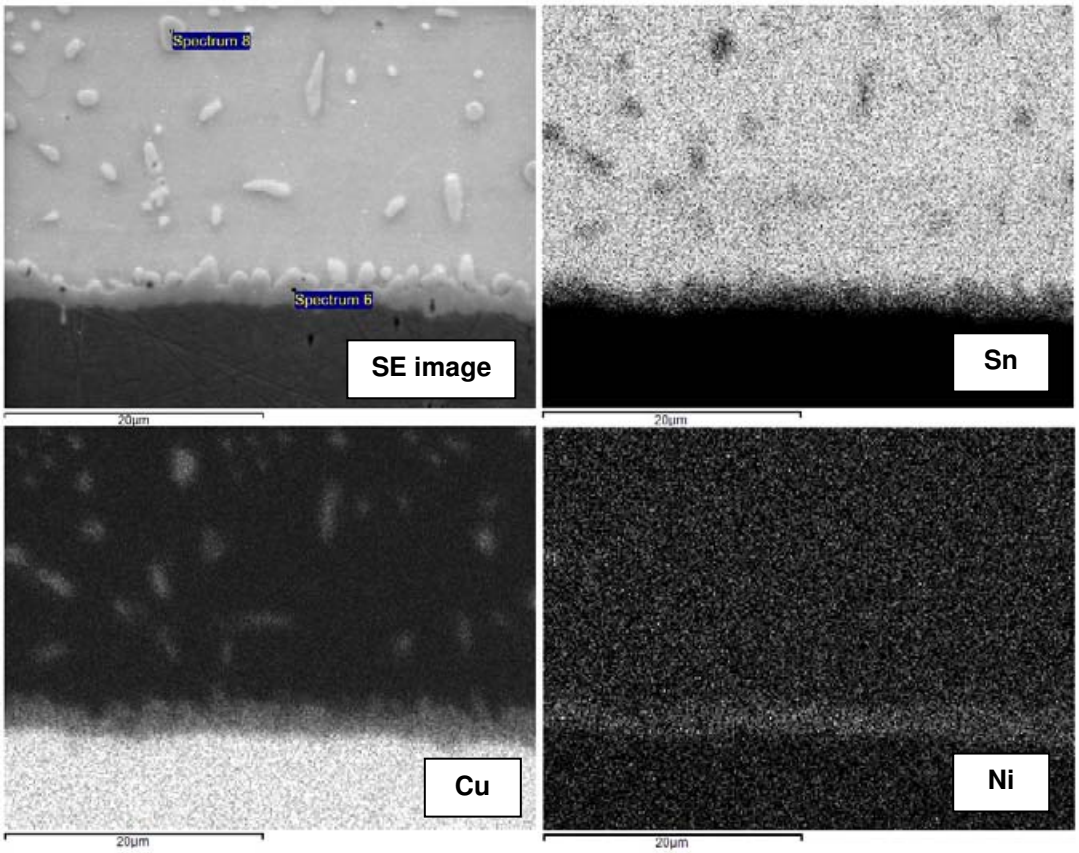

Figure 4.14. Secondary electron image and accompanying EDX elemental distribution maps of Sn-Cu-Ni interfacial microstructure as soldered to Cu substrate

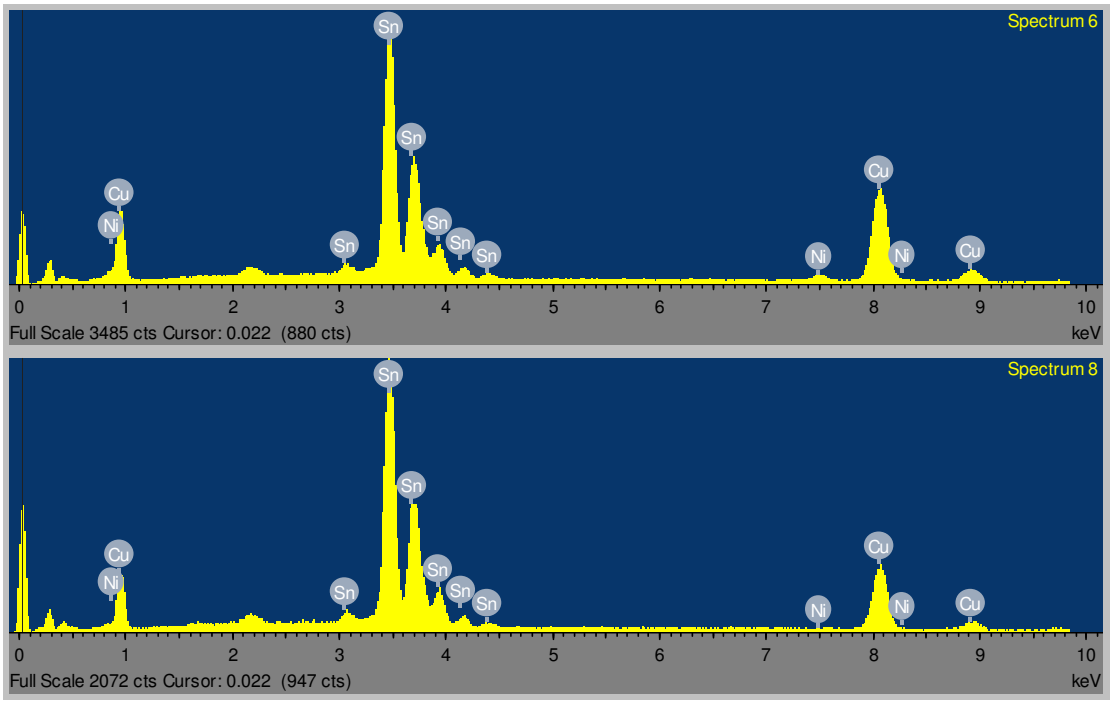

Element	Spectrum 6		Spectrum 8	
	wt.%	at.%	wt.%	at.%
Sn	65.14 ± 0.25	49.91	75.35 ± 0.32	62.07
Cu	33.24 ± 0.25	47.58	24.63 ± 0.31	37.90
Ni	1.62 ± 0.12	2.51	0.02 ± 0.12	0.03

Figure 4.15. X-ray spectra and tabulated X-ray counts for spectra 6 and 8 Figure 4.14

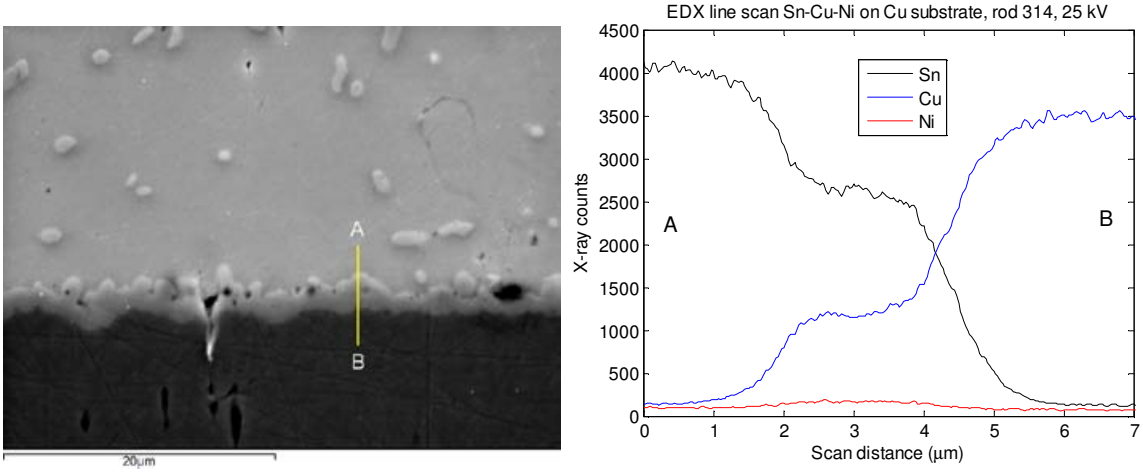

Figure 4.16. Secondary electron image of Sn-Cu-Ni microsection as soldered to Cu substrate and associated EDX line scan over IMC layer

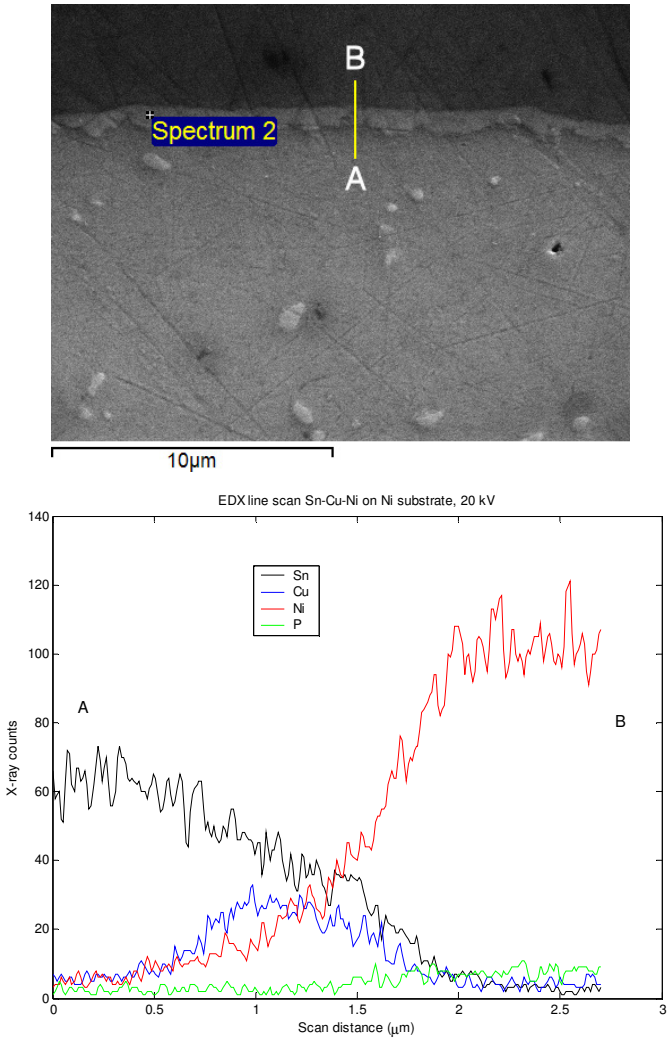

Figure 4.17. Secondary electron image of Sn-Cu-Ni microsection as soldered to Ni substrate and associated EDX line scan over IMC layer

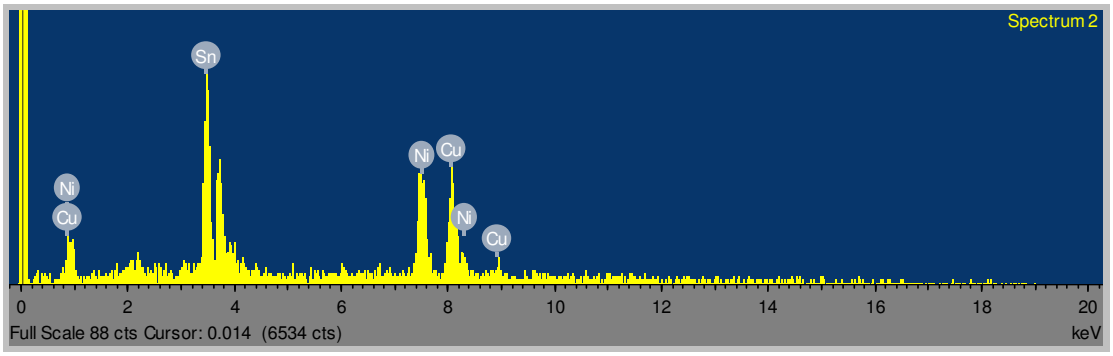

Element	wt.%	at.%
Sn	40.19 ± 1.99	25.73
Cu	31.79 ± 2.14	38.01
Ni	28.02 ± 2.00	36.26

Figure 4.18. X-ray spectra and tabulated X-ray counts for spectrum 2 from Figure 4.17

4.1.3 SAC305

A typical SAC305 microstructure from the present work is shown in Figure 4.19. Similarly to many other reports [12, 37, 117], this consists of a pure Sn matrix with small, often needle or rod-shaped Ag_3Sn precipitates and larger, dispersed Cu_6Sn_5 precipitates. The variation in size of the Ag_3Sn particles is shown in Figure 4.20 and is from around 0.1 to 2 μm. Cu_6Sn_5 precipitates tend to be larger (2-3 μm) and more angular in appearance. A typical distribution of particles, highlighted by EDX mapping, is shown in Figure 4.21. In the majority of microstructures seen in the present work, eutectic Sn + Ag_3Sn regions or networks were found (Figure 4.22, Figure 4.23). These were often oriented in the direction of heat flow during solidification which in the case of the present work runs parallel to the long axis of the Cu rods. Similarly to Sn-Pb, solidified SAC305 contains colonies of grains orientated in the same direction which can extend to several hundred microns in size. Without cross-polarised light the boundaries between such colonies are often invisible since the morphology does not change. The eutectic Sn + Ag_3Sn regions sometimes encircle individual Sn grains (Figure 4.24) but with a different orientation from them and can be shown to constitute distinct crystallographic regions (Figure 4.25) as opposed to an area of matrix containing a high density of Ag_3Sn particles. Intermetallic compound layers formed with SAC305 on Cu and Ni substrates are shown in Figure 4.26 and Figure 4.27 respectively. In the present work their average thicknesses were found to be 0.96 ± 0.43 and 1.62 ± 0.30 μm respectively which is in line with expectations [30]. The identity of the IMC layer in the case of a Cu substrate is well established in the literature as Cu_6Sn_5 and this was confirmed by EDX analysis in the present work (Figure 4.28). There is not a clear precedent in the literature on which one can rely for the identification of the IMC layer when soldering Sn-Ag-Cu solders to Ni substrates. The amount of Cu present in the solder can affect whether an $(Ni,Cu)_3Sn_4$

or $(Cu,Ni)_6Sn_5$ compound forms. This sensitivity to Cu levels is studied by Han et al. [53] and Luo et al. [50], where it would appear that there is a transition between the two compound types; the $(Cu,Ni)_6Sn_5$ compound occurring with higher Cu concentrations and $(Ni,Cu)_3Sn_4$ with lower. A study by Zeng et al. [26] puts this critical Cu concentration at 0.6 % based on thermodynamic calculations. This would indicate that the compounds formed in the present work (with 0.5 %Cu present) are more likely to be $(Ni,Cu)_3Sn_4$. The EDX results presented in Figure 4.29 – 4.31 give conflicting evidence for the existence of either compound. Spectrum 3 appears to suggest $(Cu,Ni)_6Sn_5$, with the atomic ratio of Sn found (0.39) close to the stoichiometric ratio of 0.43. However, Spectrum 4 shows an atomic Sn content of 0.56 which is close to the stoichiometric value of 0.57 for $(Ni,Cu)_3Sn_4$. It could be considered that a bi-layer of the two compounds is present as described by Ho et al. [118]. The spatial resolution of EDX in SEMs coupled with the small thickness of the layer limits the reliability of these readings, since large adjacent areas of Ni and Sn exist which will almost certainly be contributing to the X-ray counts. The situation of SAC305 soldered to Ni substrates can also result in very thin (<0.2 μm) nano-crystalline Ni-P compound layers [26] in addition to Ni-Cu-Sn compounds. These were not detected in the present work, possibly due to the aforementioned SEM/EDX limitations.

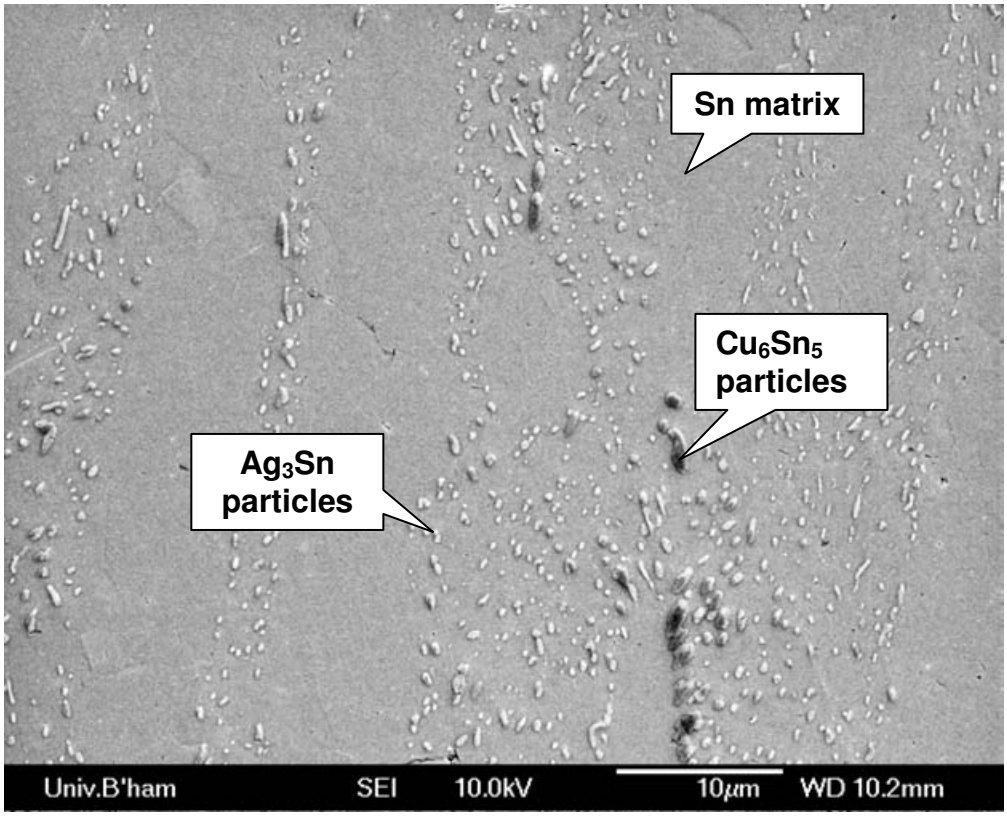

Figure 4.19. Secondary electron micrograph of typical SAC305 microstructure as found in joint (2000x mag.)

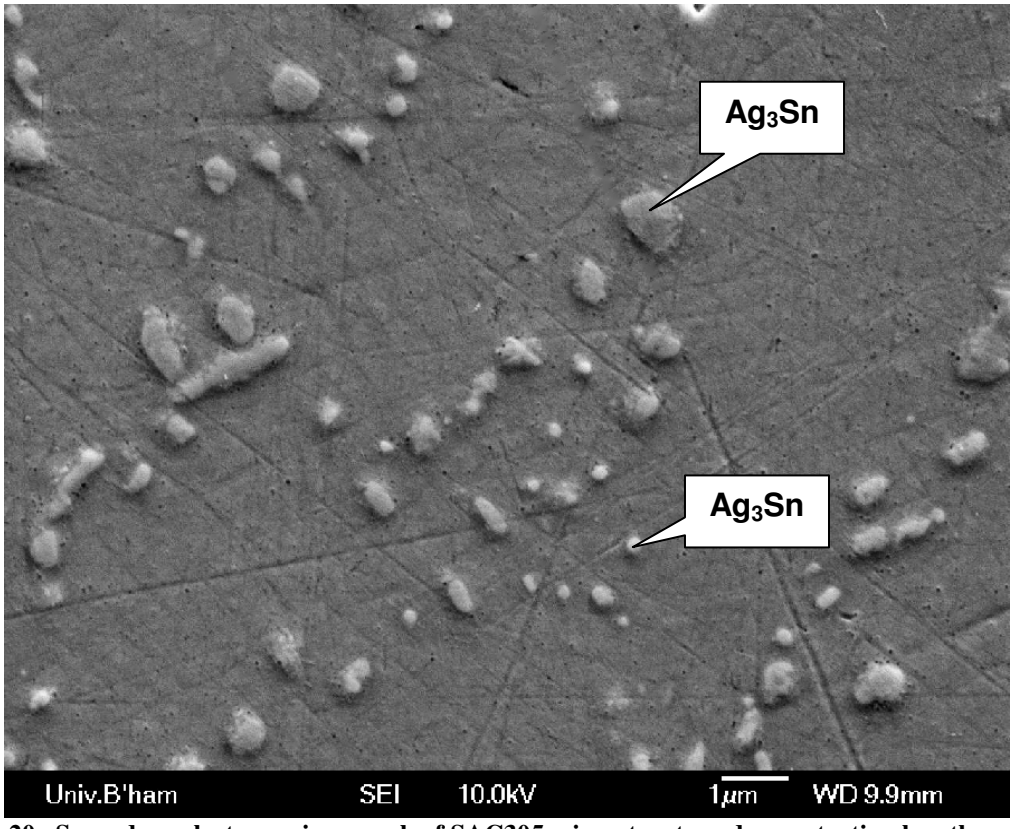

Figure 4.20. Secondary electron micrograph of SAC305 microstructure demonstrating length scales of Ag_3Sn particles (8000x mag.)

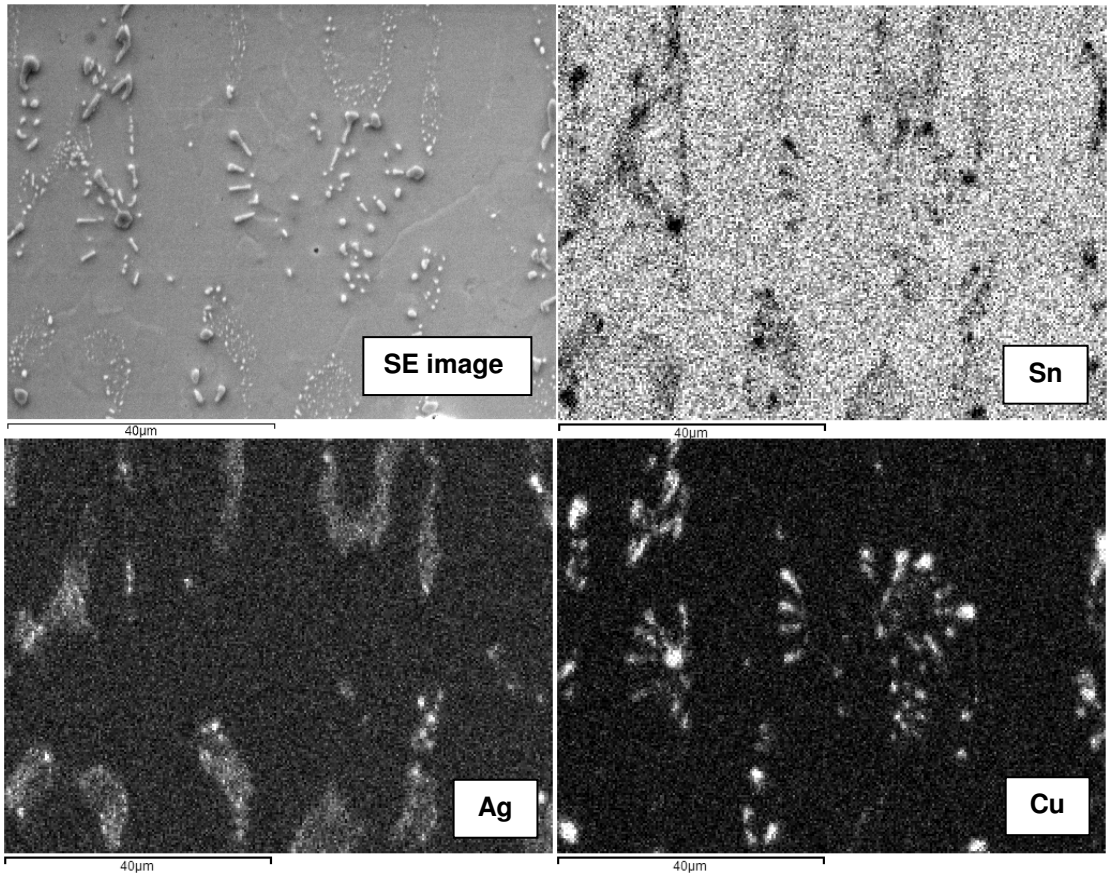

Figure 4.21. EDX elemental distribution maps of SAC305 microstructure at 25 kV accelerating voltage, rod 345

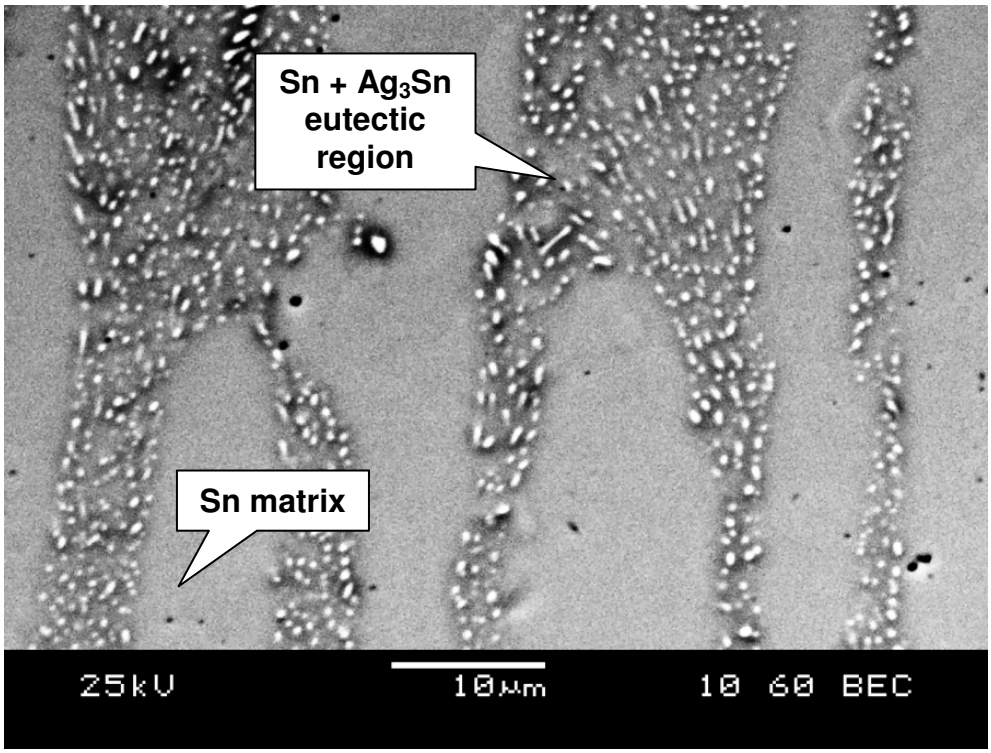

Figure 4.22. Backscattered electron micrograph of SAC305 microstructure showing common eutectic Sn + Ag_3Sn networks in pure Sn matrix (2000x mag.)

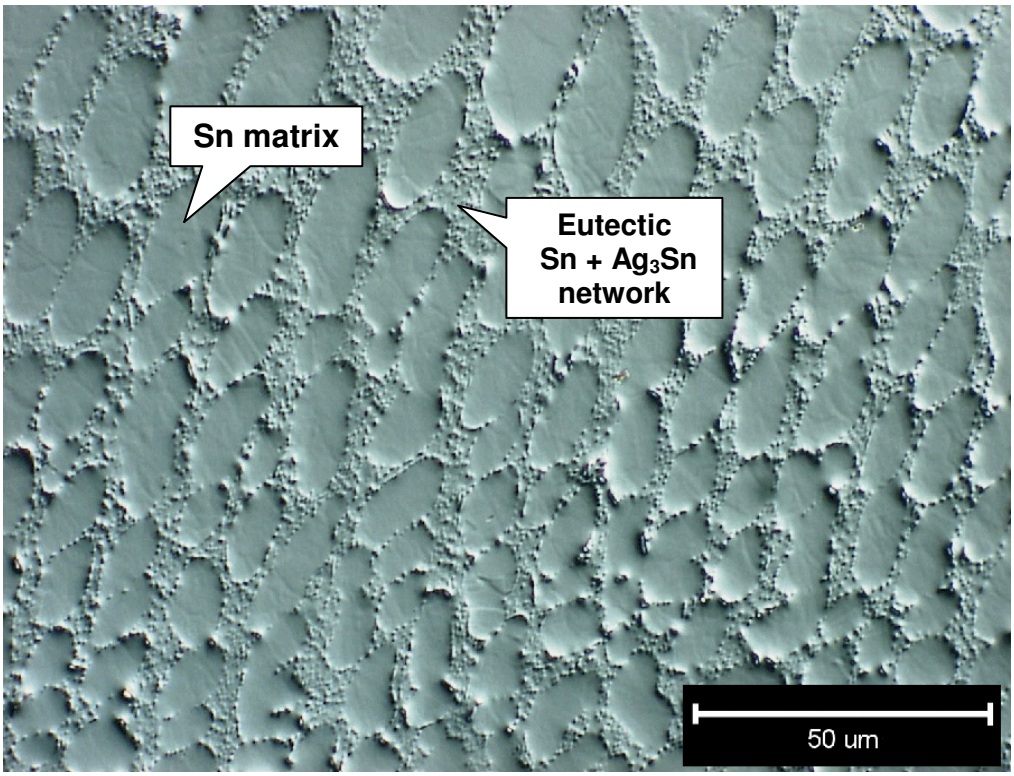

Figure 4.23. Optical DIC micrograph of common SAC305 microstructure at lower resolution (500x mag.) showing Sn + Ag_3Sn eutectic network in Sn matrix

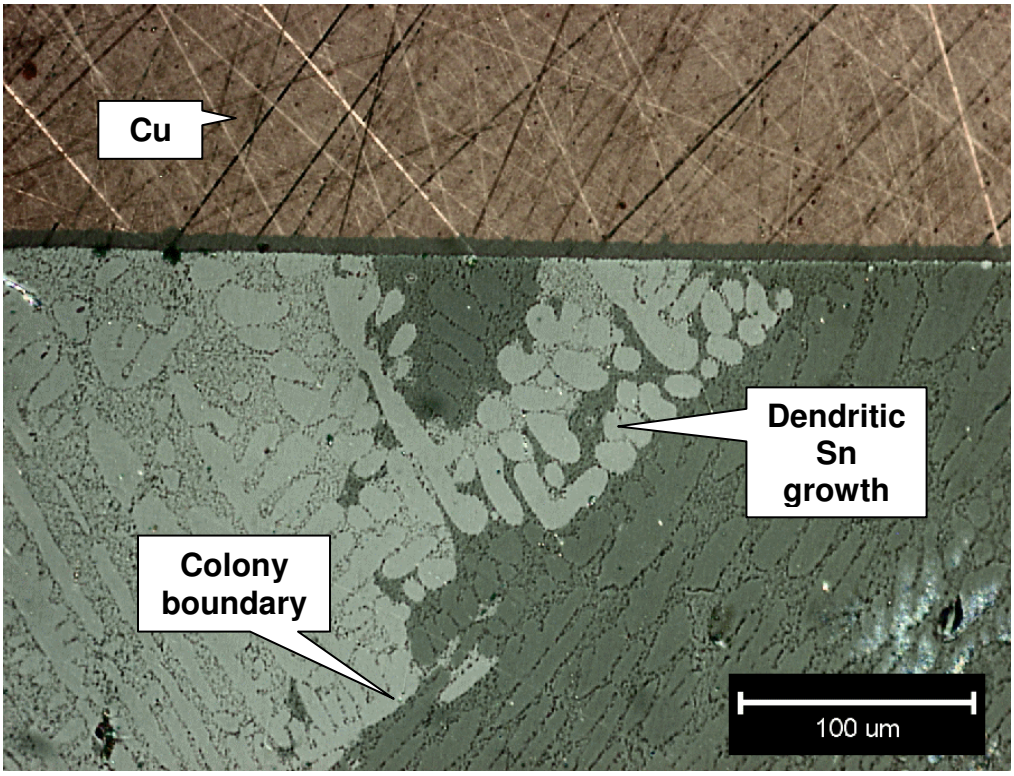

Figure 4.24. Cross-polarised optical micrograph of SAC305 microstructure – contrast from crystal orientation – showing directional solidification and dendritic growth of Sn

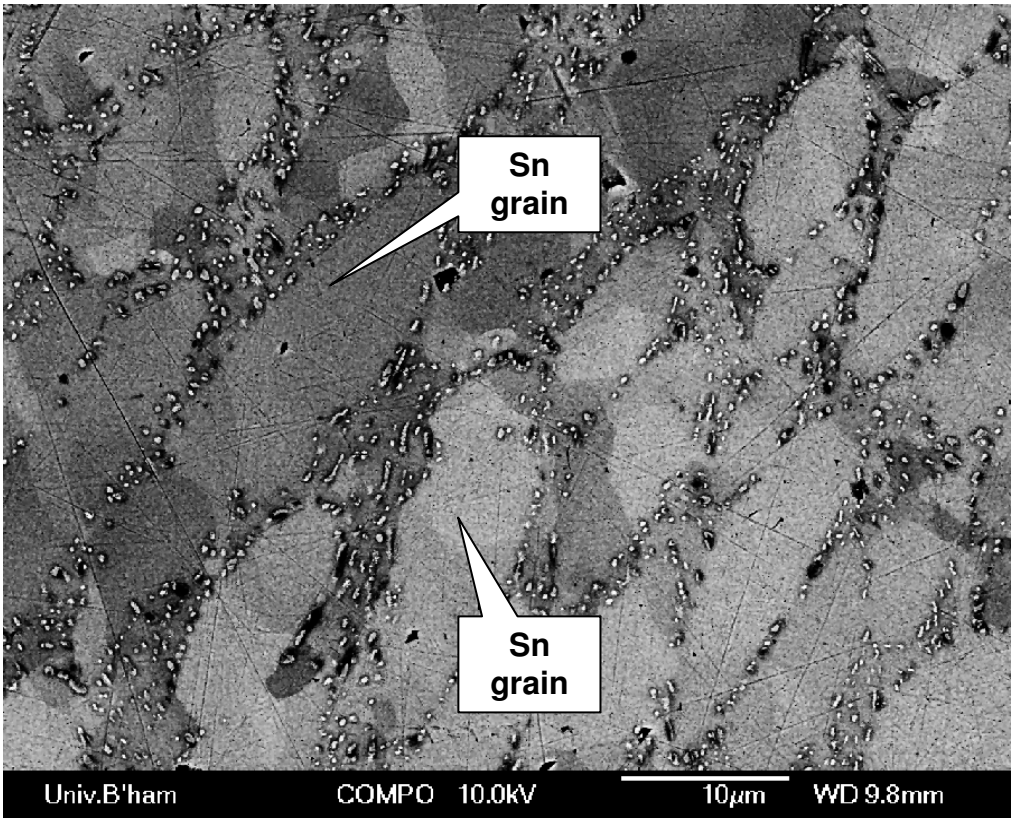

Figure 4.25. Electron micrograph of SAC305 microstructure – contrast from backscattered electrons under unusual conditions – showing grain structure

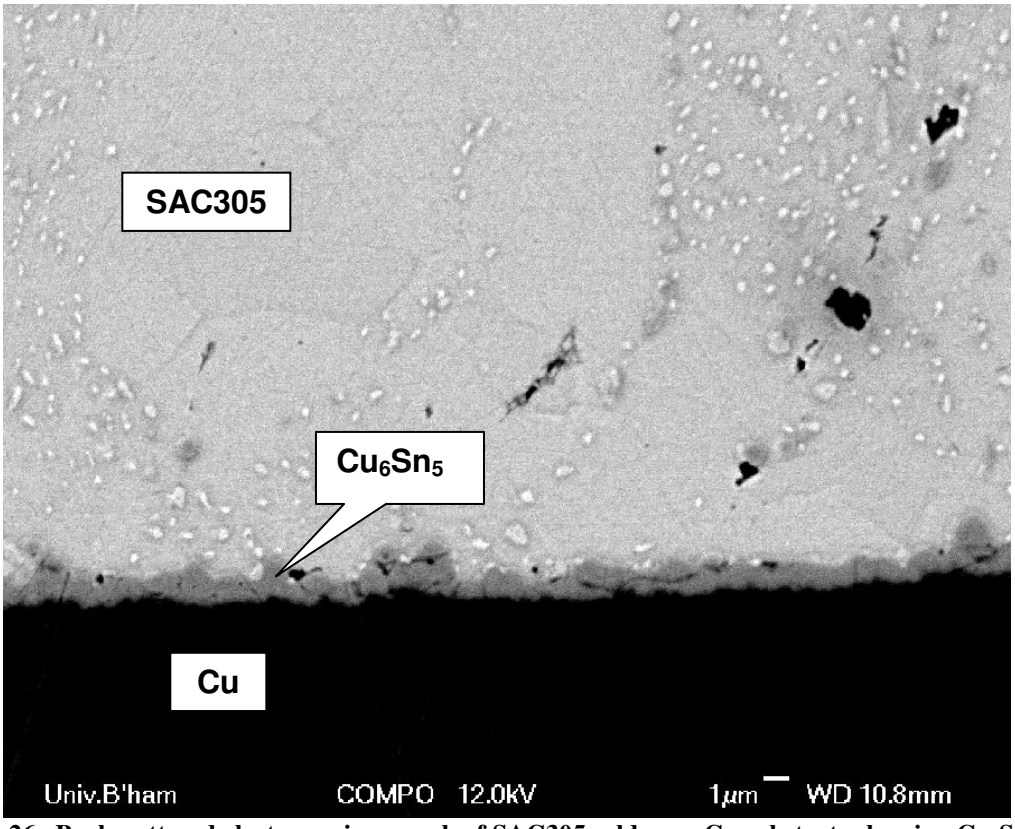

Figure 4.26. Backscattered electron micrograph of SAC305 solder on Cu substrate showing Cu_6Sn_5 IMC layer (3000x mag.)

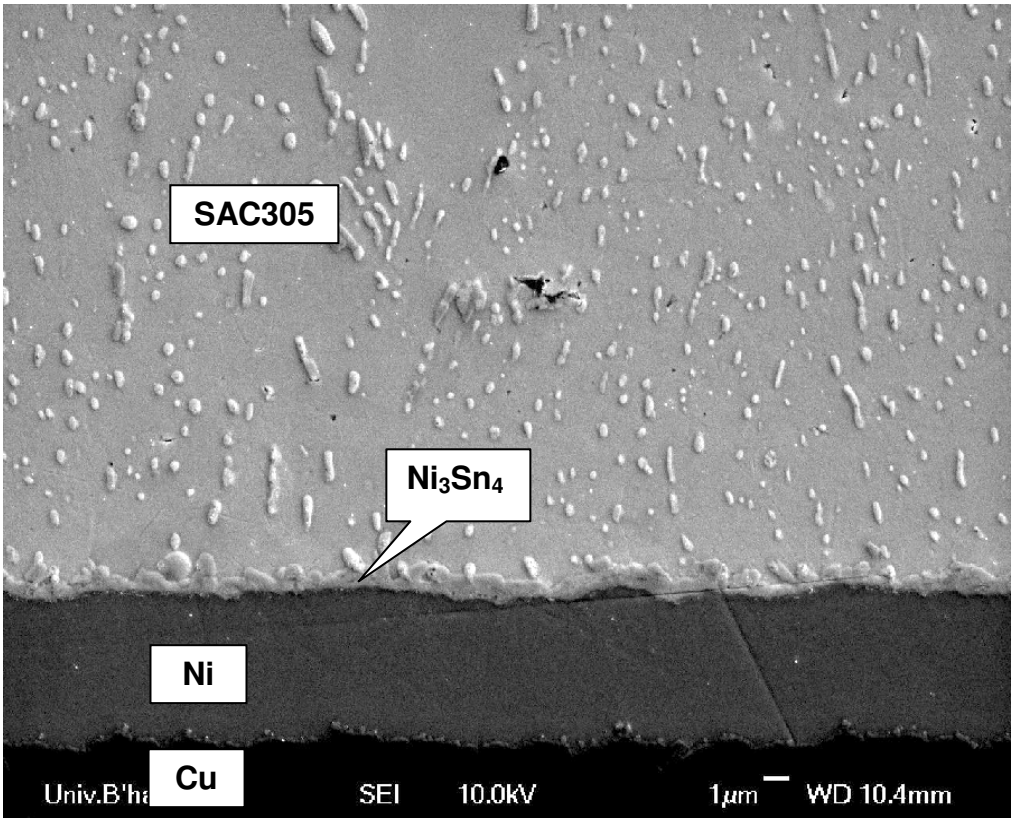

Figure 4.27. Secondary electron micrograph of SAC 305 solder on Ni substrate showing Ni-Sn IMC layer (3000x mag.)

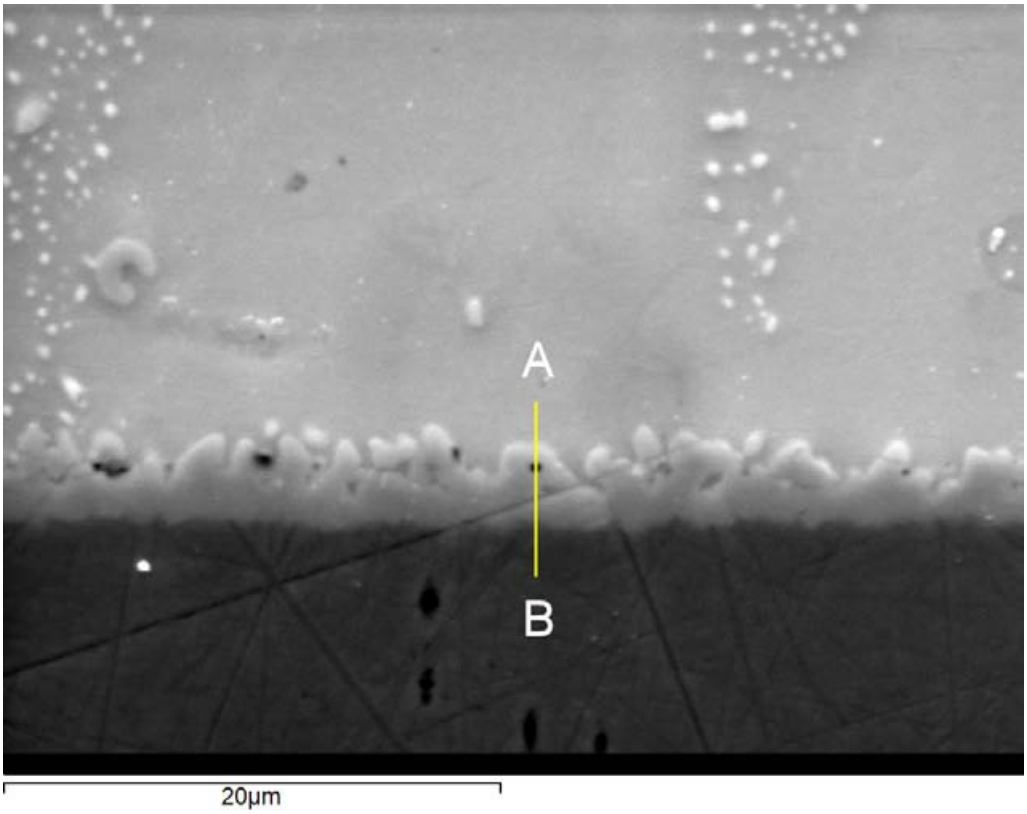

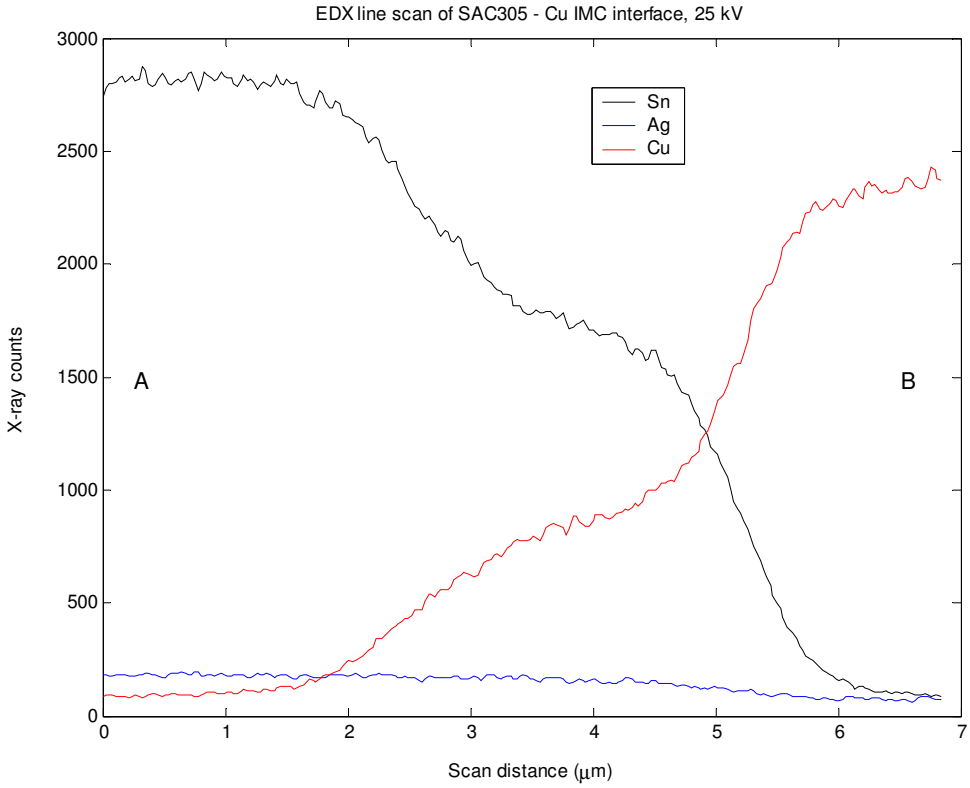

Figure 4.28. Secondary electron image and accompanying EDX elemental line scan of IMC interface formed between SAC305 solder and Cu substrate (accelerating voltage 25 kV)

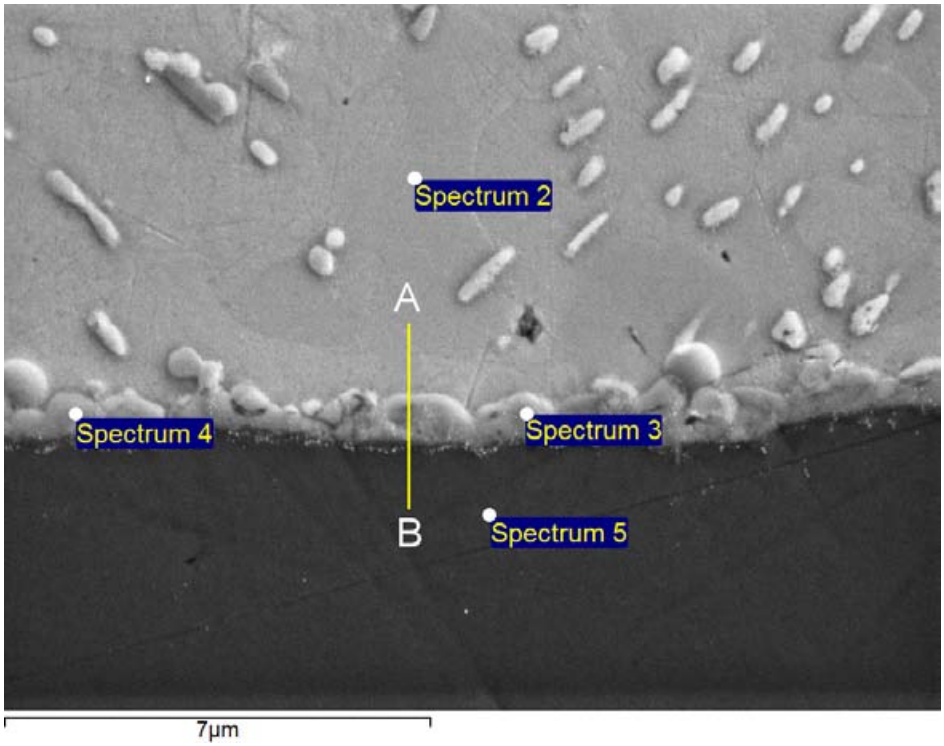

Figure 4.29. Secondary electron micrograph of SAC305 IMC layer as soldered to Ni substrate (8,000x mag.)

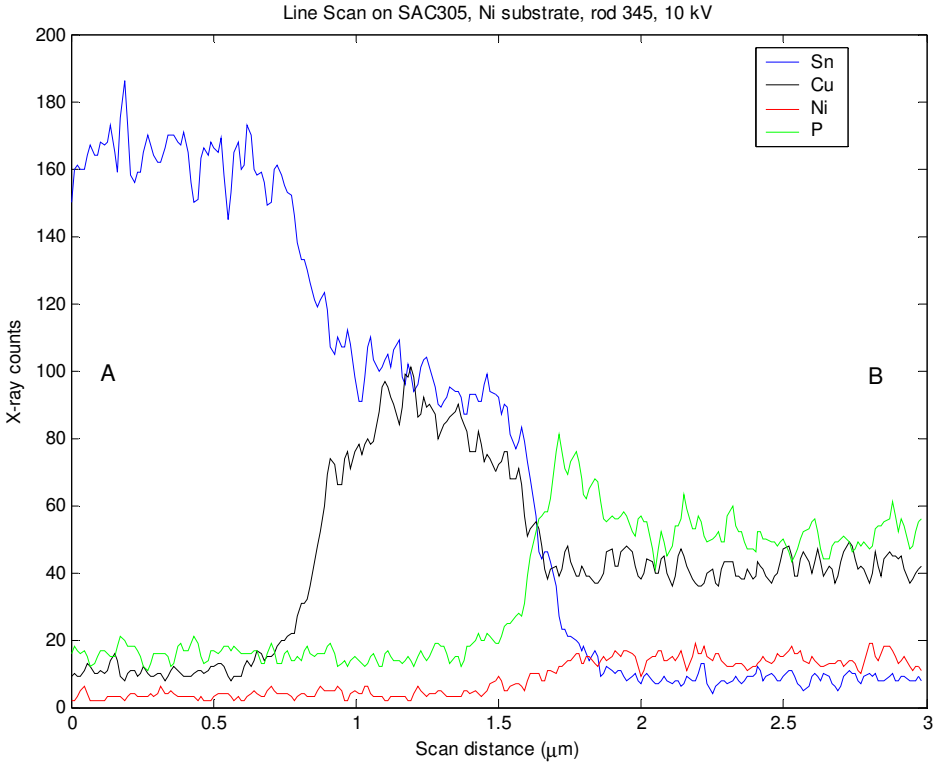

Figure 4.30. EDX line scan along AB of Figure 4.29 showing Sn, Cu, Ni and P distributions at 10 kV accelerating voltage for improved spatial resolution

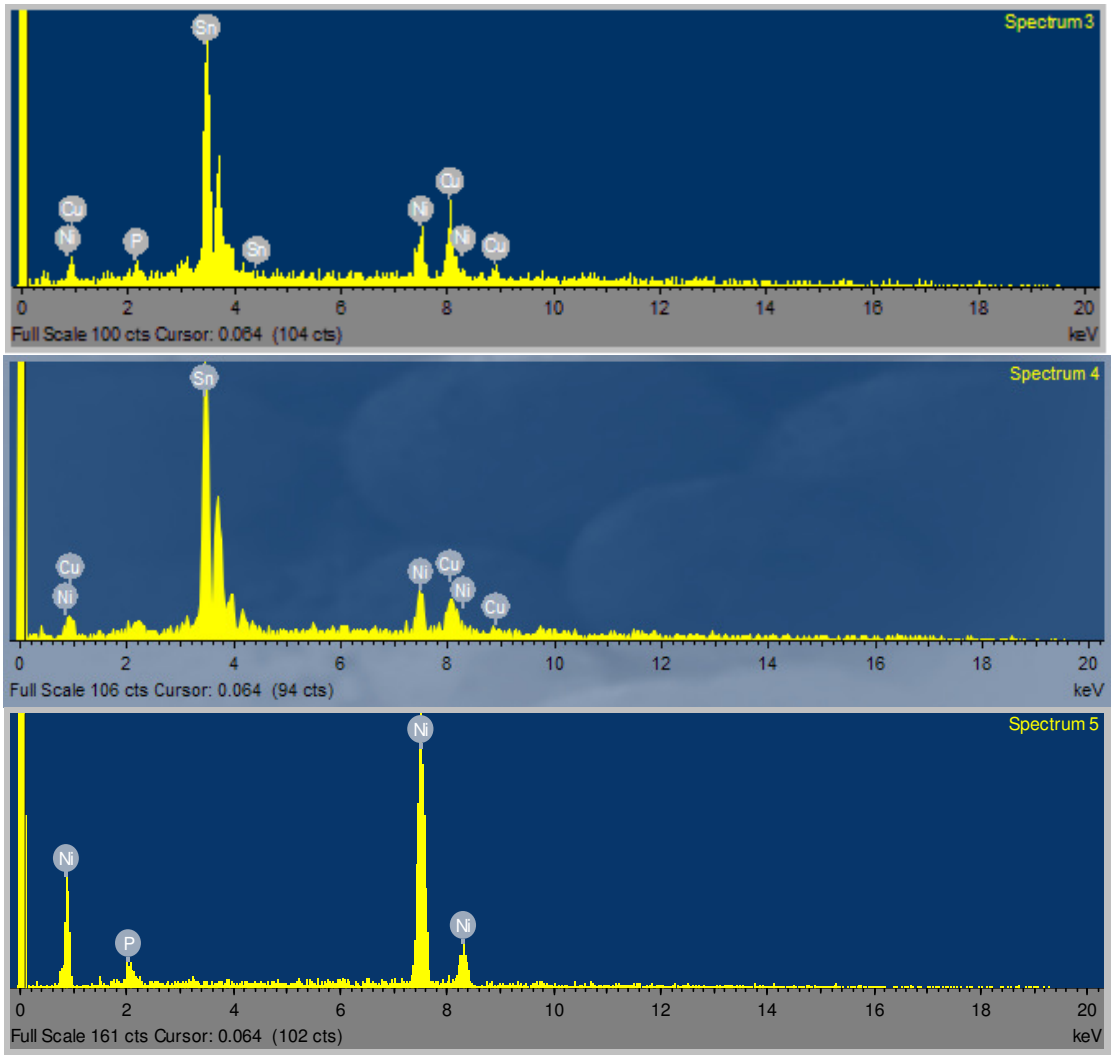

Element	Spectrum 3		Spectrum 4		Spectrum 5	
	wt.%	at.%	wt.%	at.%	wt.%	at.%
P	-	-	-	-	7.80 ± 0.70	13.82
Ni	14.87 ± 2.05	21.31	15.75 ± 1.81	24.96	92.20 ± 0.70	86.18
Sn	55.04 ± 2.45	39.00	71.01 ± 2.48	55.66	-	-
Cu	15.04 ± 1.25	39.96	13.24 ± 2.26	19.38	-	-

Figure 4.31. X-ray spectra and tabulated X-ray counts for positions 3-5 on Figure 4.29 at 20 kV accelerating voltage for improved stimulation of higher energy lines

4.1.4 SAC387

SAC387 was only used for a few a few early tests with Cu substrates. All comments on SAC305 microstructure can be considered relevant to SAC387.

4.1.5 Innolot

The microstructure of the as-yet-unpublished Sn-3.8Ag-0.7Cu-3Bi-1.4Sb-0.15Ni Innolot alloy is depicted in Figure 4.32 – 4.34. Although based on the eutectic Sn-3.8Ag-0.7Cu, the microstructure of Innolot shows marked differences from this. While limited areas of Sn + Ag_3Sn 'eutectic' exist (Figure 4.33), they are not joined up into networks as in the plain Sn-Ag-Cu alloys. Large (frequently > 10 μm) $(Cu,Ni)_6Sn_5$ precipitates populate the microstructure (Figure 4.33) and pure Bi particles of 2 - 3 μm dimensions precipitate out from the matrix in small, isolated clusters (Figure 4.34, Figure 4.36). IMC X-ray mapping (Figure 4.36) shows that the elements which have appreciable solid solubility in Sn (Bi and Sb) are found only in the matrix, not in any IMCs. Ni is present in the $(Cu,Ni)_6Sn_5$ particles and an IMC layer is found when soldered to Cu (Figure 4.37, Figure 4.38). This layer is slightly thicker than that of Sn-Pb or SAC305 at 2.92 ± 0.78 μm and has a more planar appearance. It is positively identified by EDX (Figure 4.39) and EBSD (Figure 4.40, Figure 4.41) as $(Cu,Ni)_6Sn_5$ from the atomic ratios. Large Ag_3Sn structures emanating from this layer were common among all Innolot joints. Tests by a member of the consortium responsible for the development of the alloy show that it solidifies over a much wider temperature range than SAC387 (Figure 4.43), with a solidus of 206 ºC and a liquidus of around 219 ºC. Cross-sectioning and polishing the Innolot alloy specimens proved to be significantly easier than the other alloys in the present work; consequently the EBSD technique (which requires a very flat and smooth surface) was successfully applied to a

specimen joint to confirm the identification of its intermetallic compounds (Figure 4.40 and Figure 4.41).

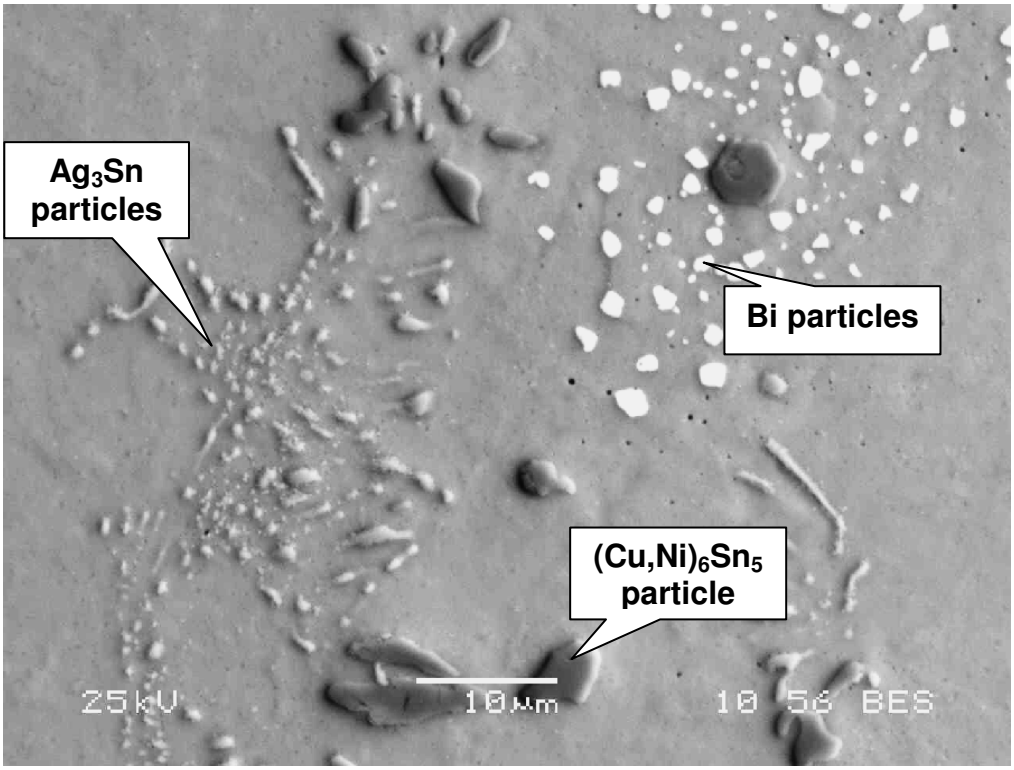

Figure 4.32. Backscattered electron micrograph of Innolot microstructure (1800x mag.)

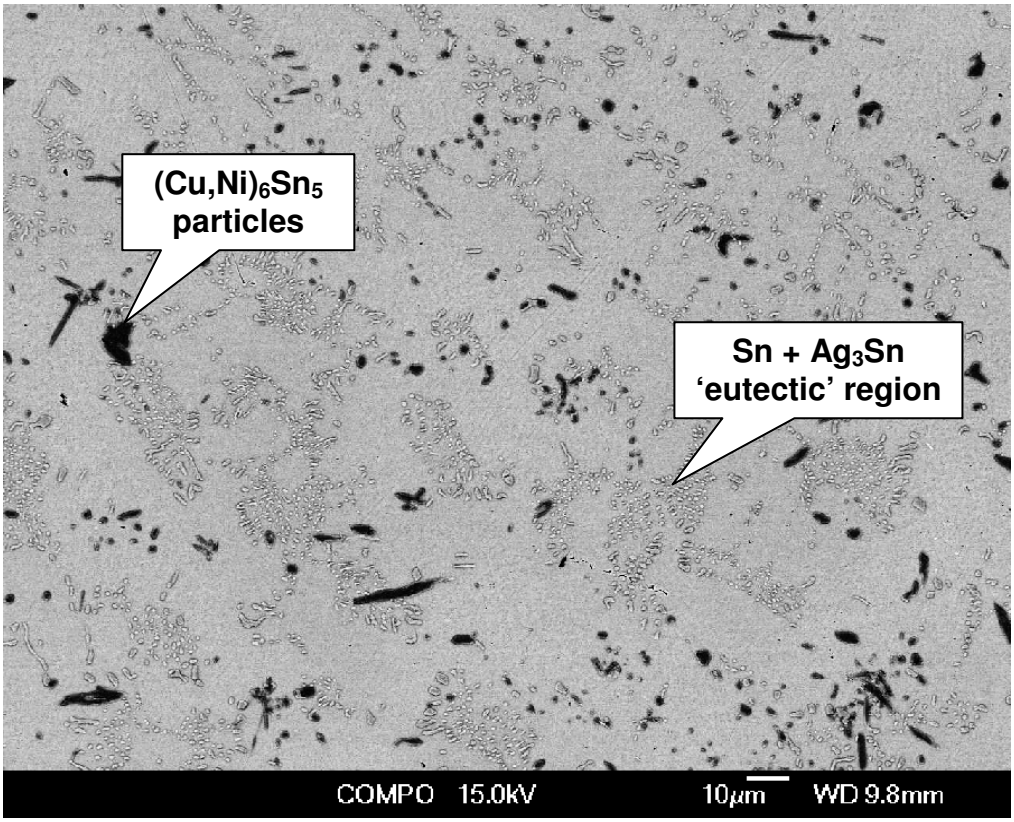

Figure 4.33. Backscattered electron micrograph of typical Innolot microstructure showing scattered $(Cu,Ni)_6Sn_5$ particles with angular morphology (dark) and semi-dispersed 'eutectic' regions of Sn + Ag_3Sn (500x mag.)

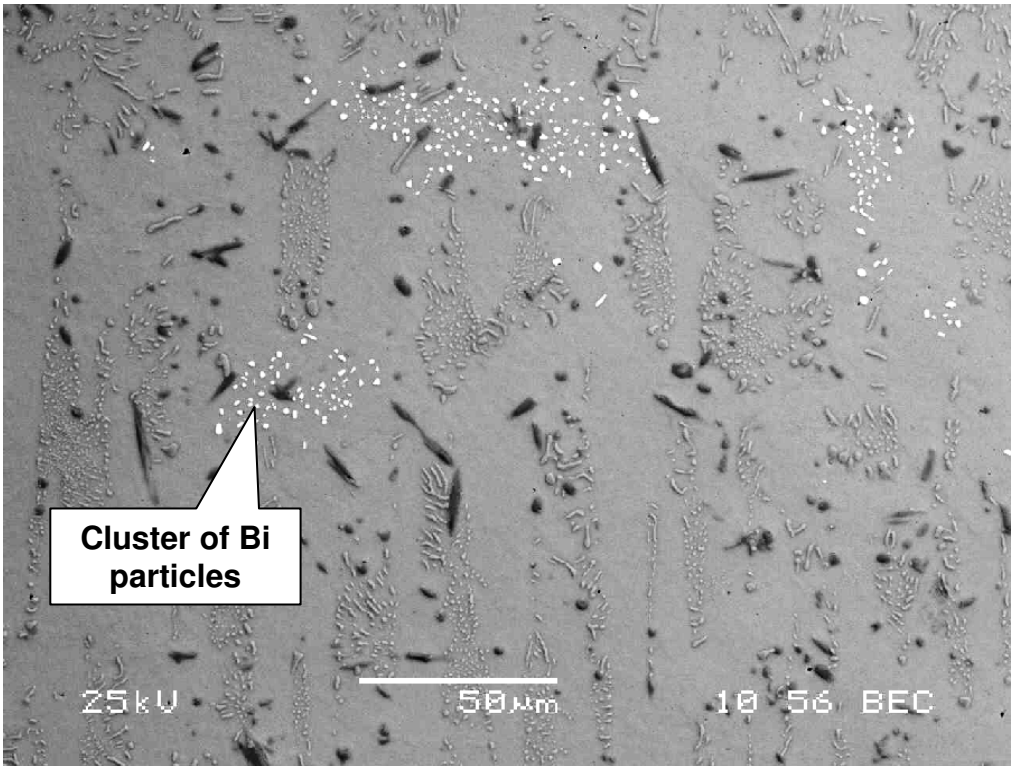

Figure 4.34. Backscattered electron micrograph of alternative Innolot morphology showing clusters of pure Bi particles (500x mag.)

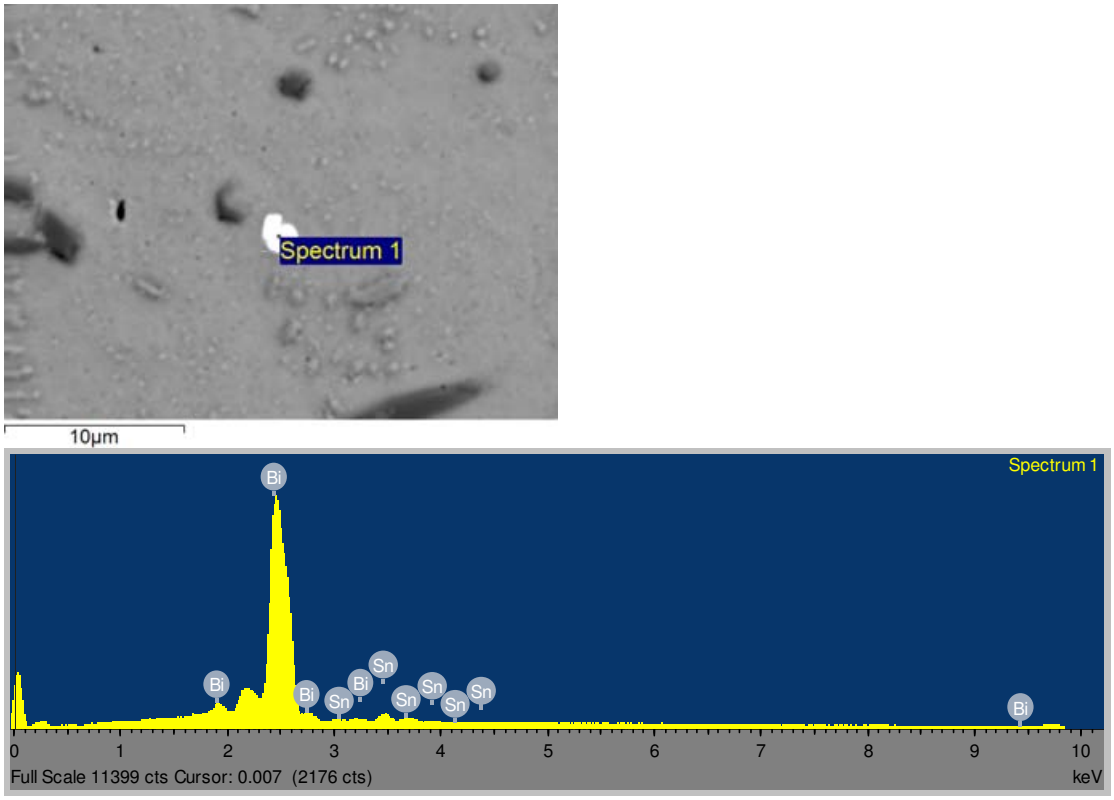

Figure 4.35. Backscattered electron micrograph, X-ray spectrum and tabulated X-ray counts for white particle found in Innolot microstructure (accelerating voltage 25 kV)

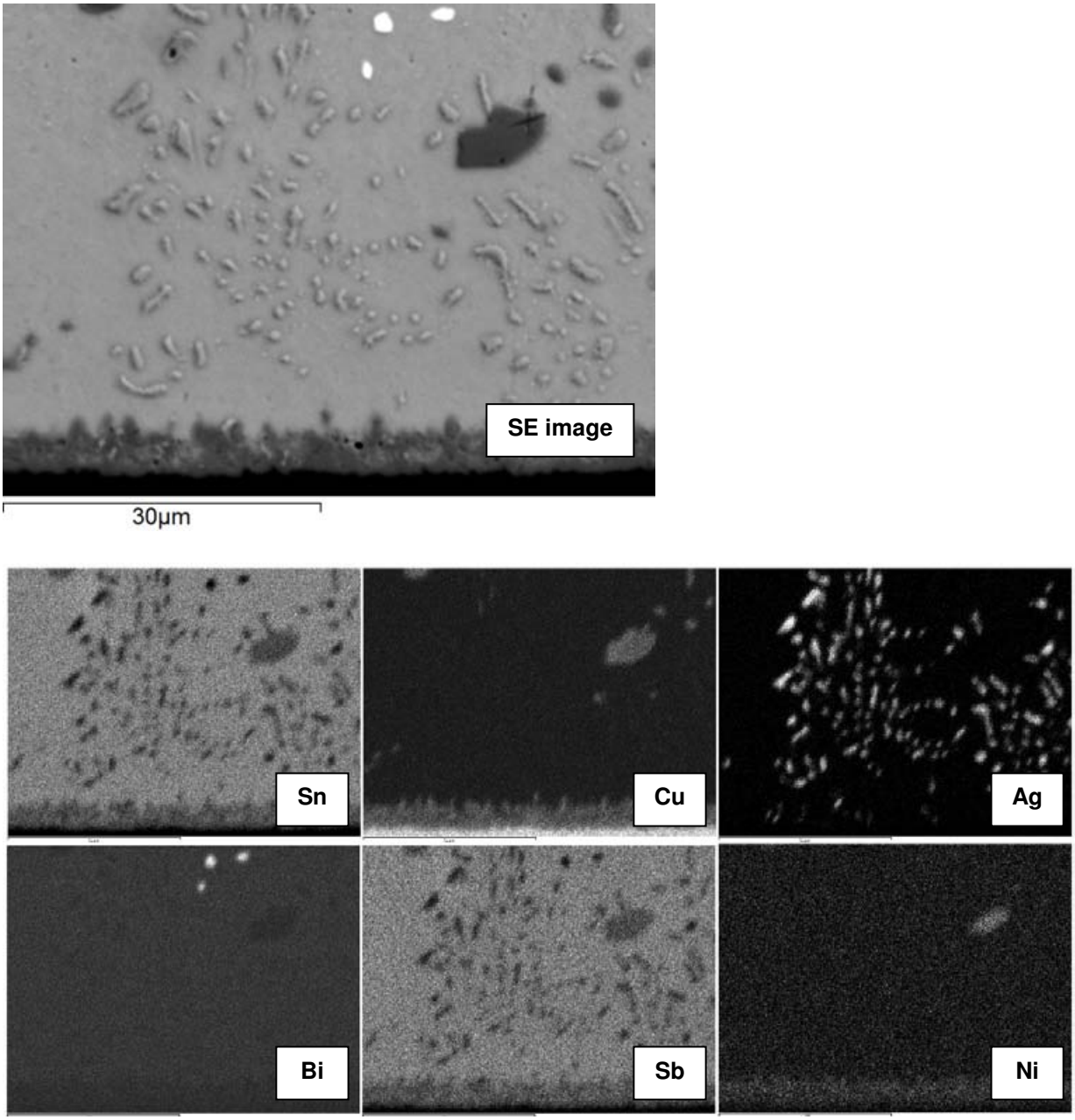

Figure 4.36. Secondary electron image and accompanying EDX elemental distribution maps for example Innolot microstructure and IMC layer as soldered to Cu substrate (25 kV accelerating voltage)

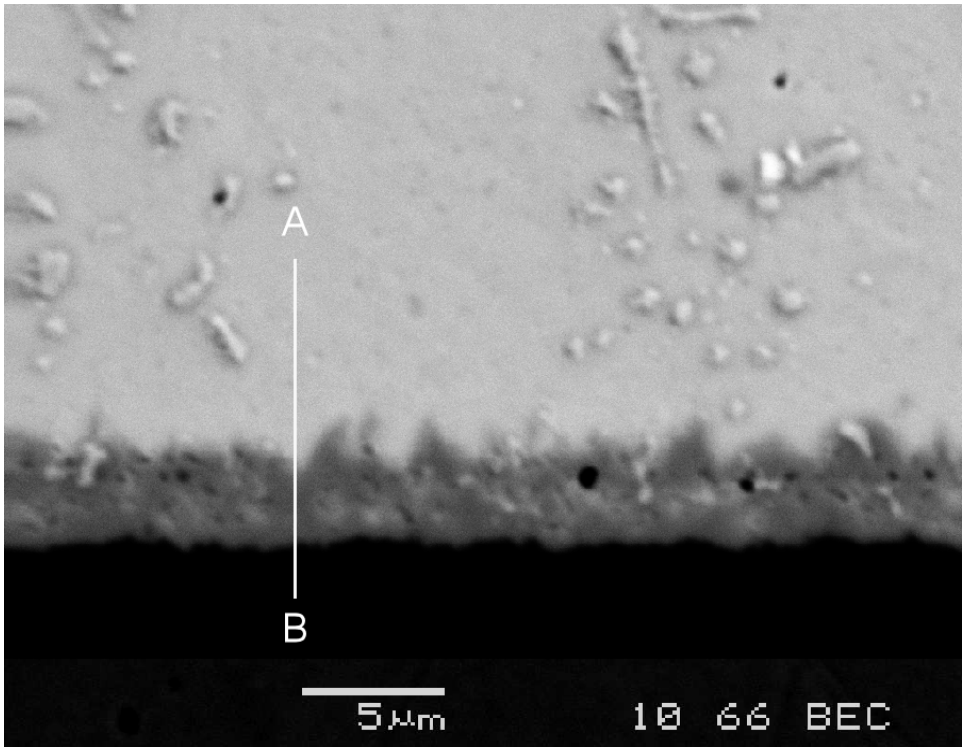

Figure 4.37. Backscattered electron micrograph of Innolot IMC layer as soldered to Cu substrate

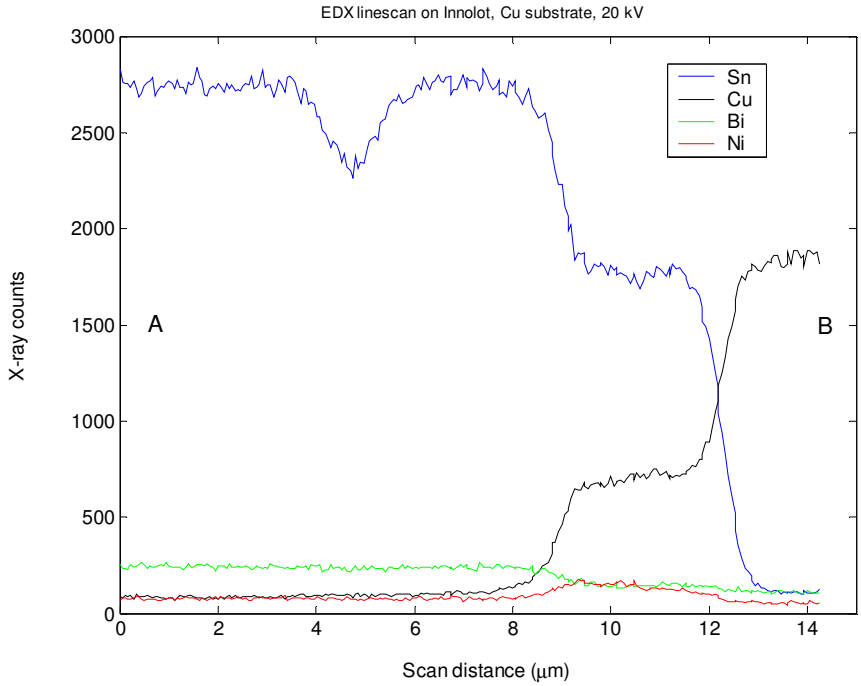

Figure 4.38. EDX line scan along AB from Figure 4.37 showing Sn, Cu, Bi and Ni distributions (accelerating voltage 20 kV)

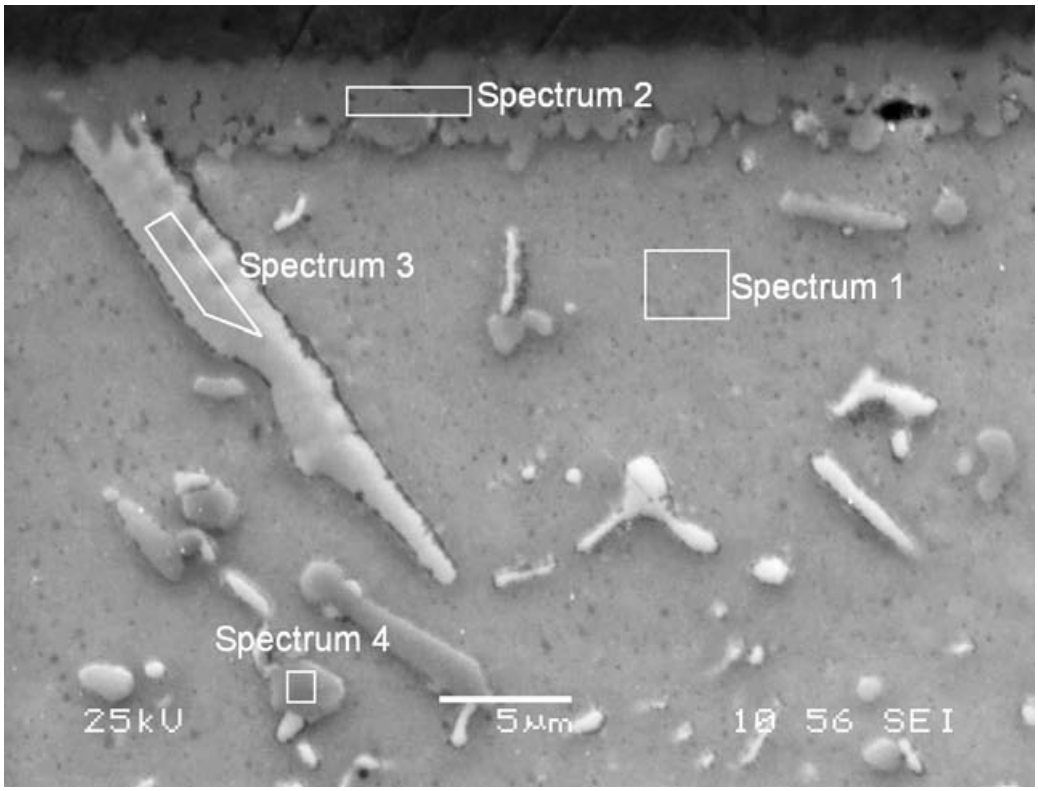

Figure 4.39. Secondary electron micrograph of Innolot microstructure showing large IMC particle nucleating from IMC layer as soldered to Cu substrate

Spectrum 1		
Element	**wt.%**	**at.%**
Sn	97.02 ± 0.84	98.29
Bi	2.98 ± 0.84	1.71

Spectrum 2		
Element	**wt.%**	**at.%**
Ni	3.43 ± 0.49	5.17
Cu	35.20 ± 0.92	49.05
Sn	61.37 ± 0.95	45.78

Spectrum 3		
Element	**wt.%**	**at.%**
Ag	72.39 ± 1.46	74.26
Sn	27.61 ± 1.46	25.74

Spectrum 4		
Element	**wt.%**	**at.%**
Ni	5.46 ± 1.32	8.36
Cu	30.51 ± 2.09	43.16
Sn	64.03 ± 2.20	48.48

Tabulated X-ray counts for spectra 1-4 regions in above micrograph

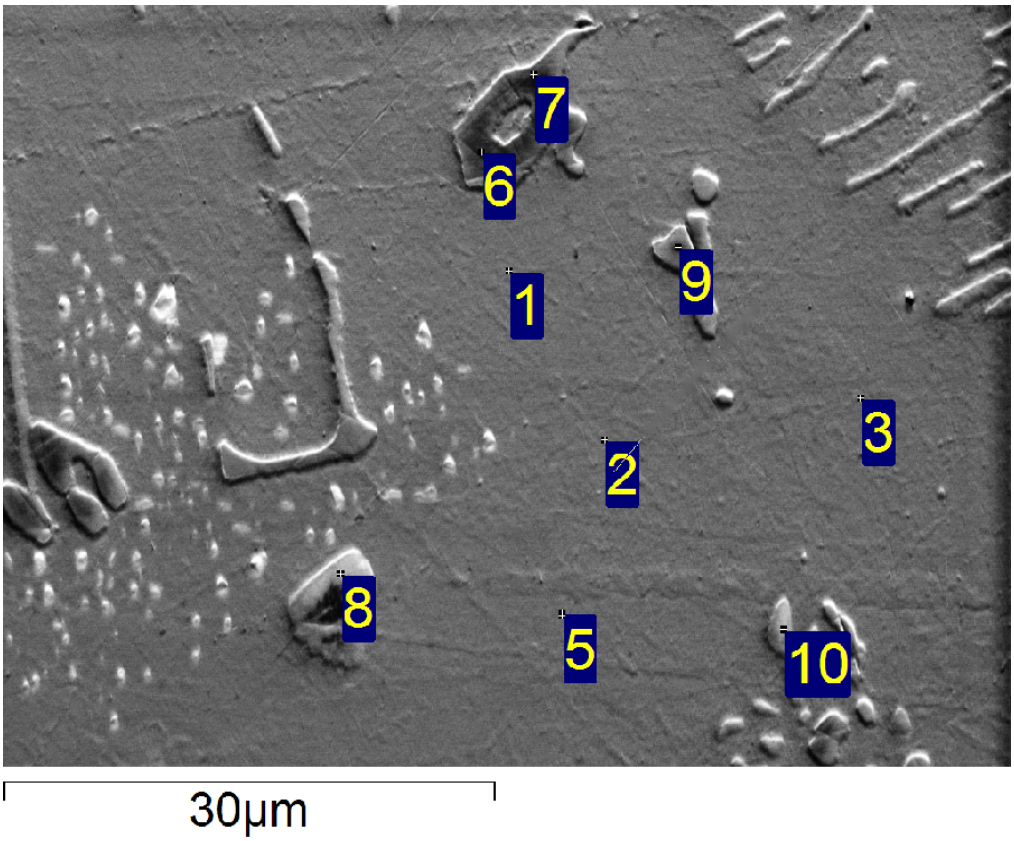

Figure 4.40. Secondary electron image of Innolot microstructure as found in HCF joint – markers represent positions of EBSD point analyses shown below

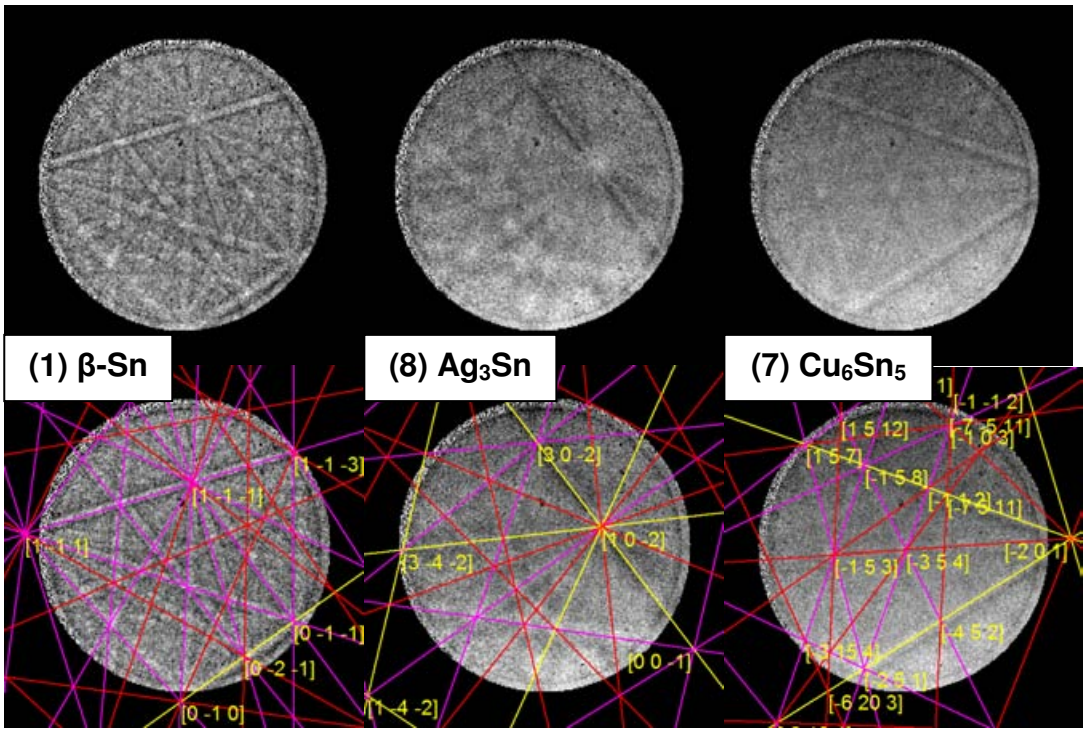

Figure 4.41. EBSD patterns from respective positions in Figure 4.40 with software Kikuchi line indexing shown in lower row of images

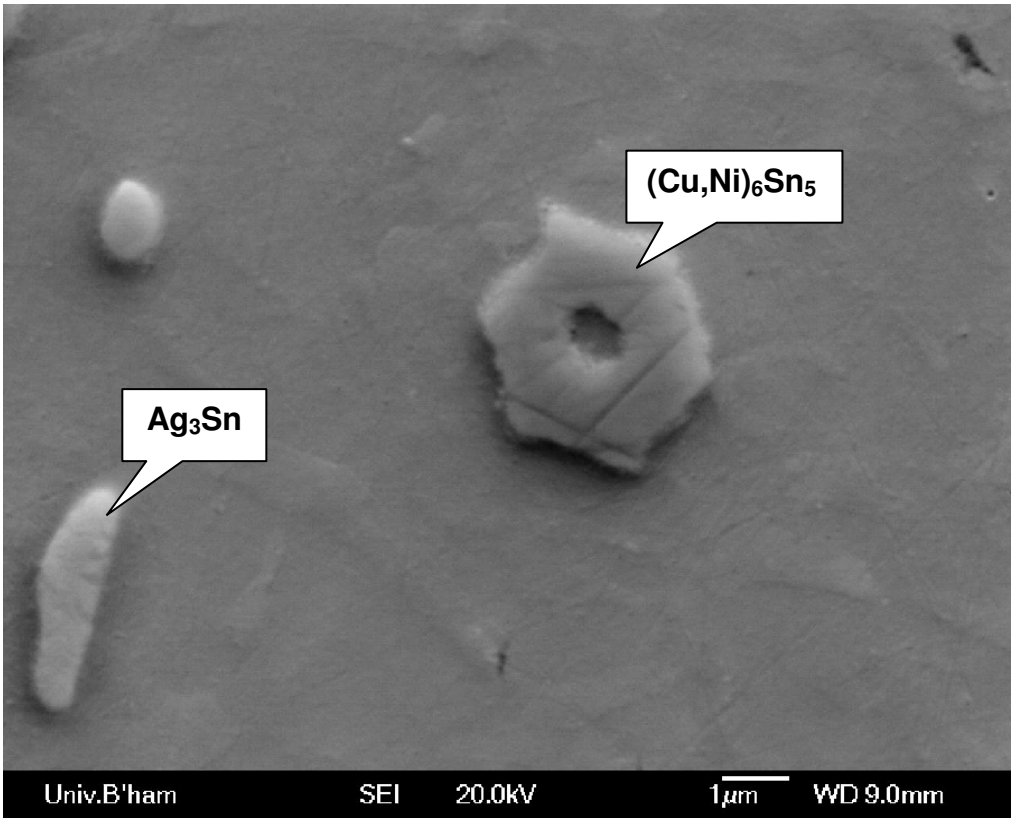

Figure 4.42. Secondary electron micrograph of Ag-Sn and Cu-Sn particles found in Innolot solder demonstrating smooth and angular (often hexagonal) morphologies respectively

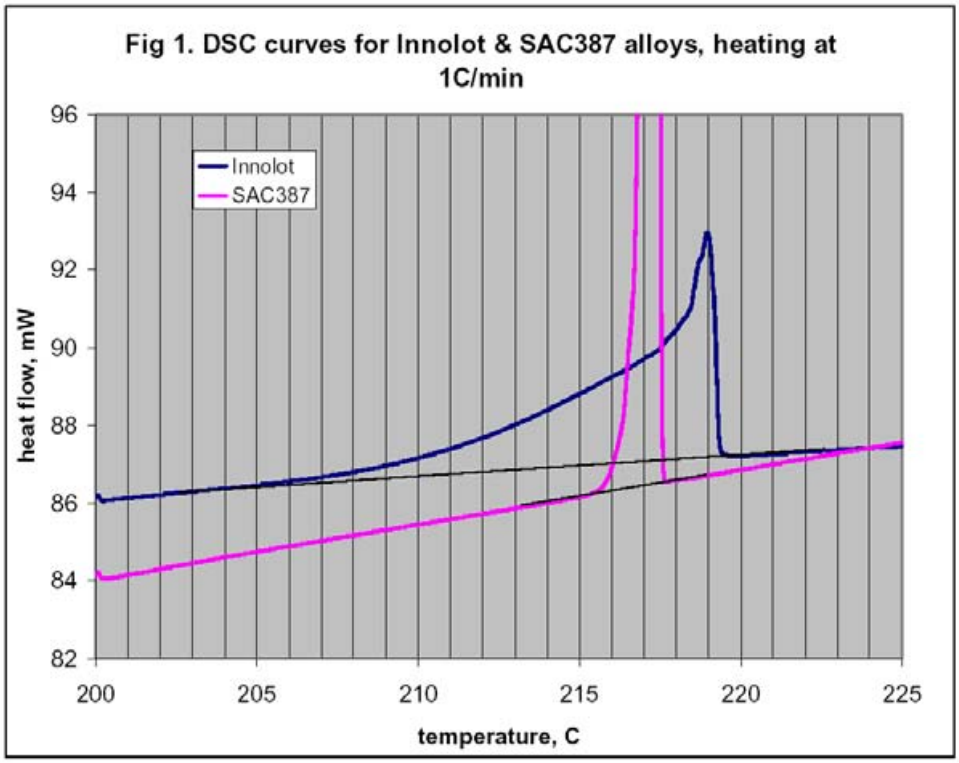

Figure 4.43. DSC curve for Innolot alloy in comparison to SAC387

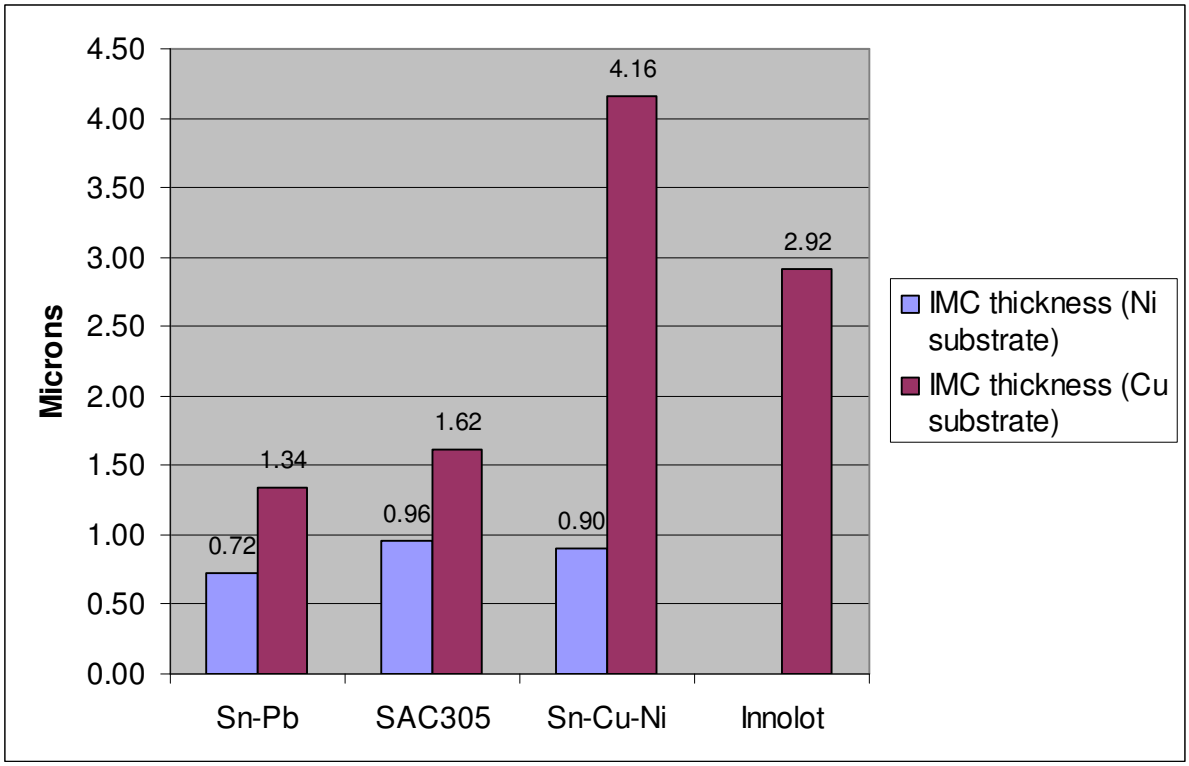

Figure 4.44. Mean thicknesses of interfacial intermetallic compounds for solders in the present work as determined by image analysis of micrographs

4.2. High-cycle fatigue results

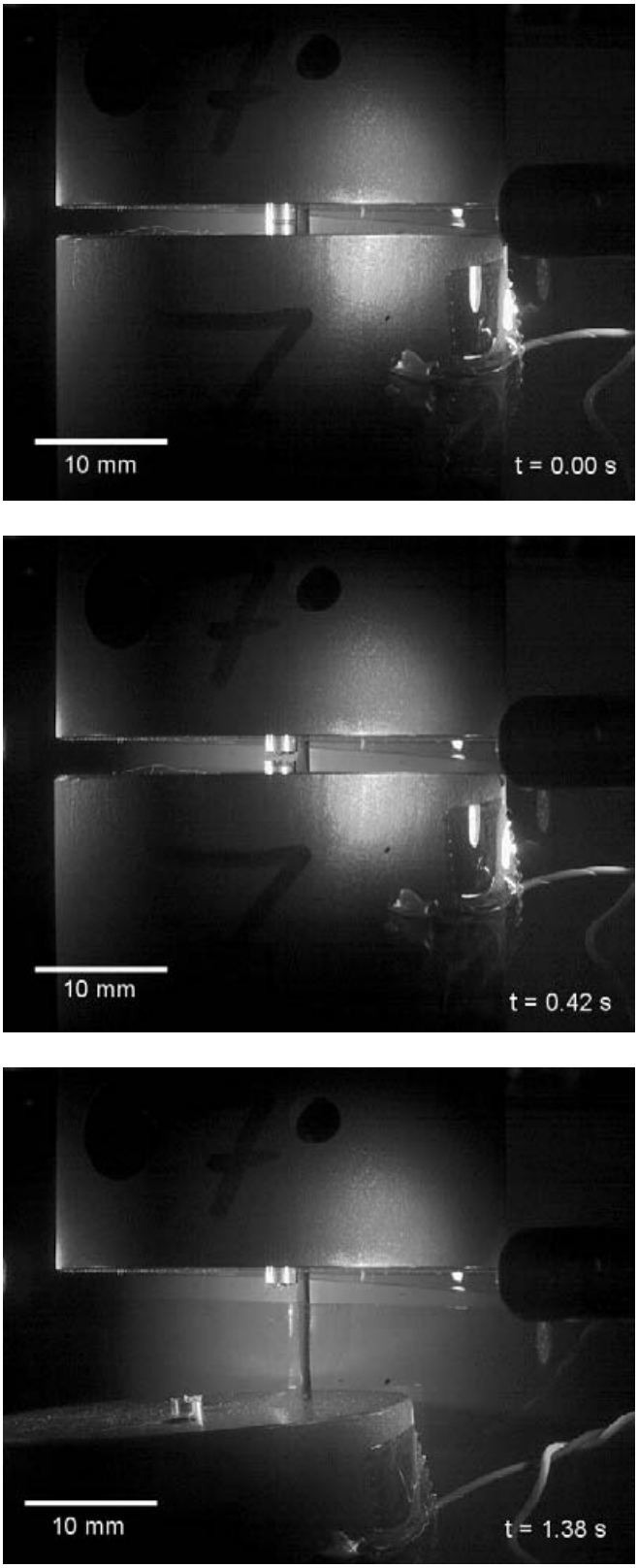

Figure 4.45. Frames of video from high-speed video capture showing progress of failure of solder joint under 600 Hz vibration at 25 ºC

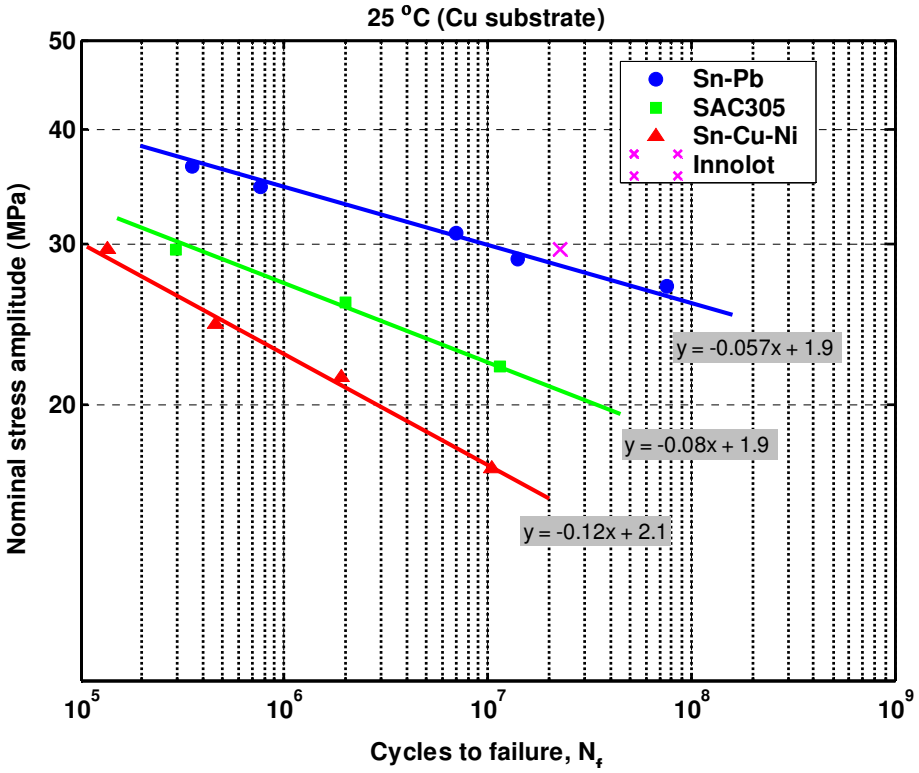

Figure 4.46. Nominal stress amplitude vs. cycles to failure for solder joints on Cu substrates subjected to fatigue loading at 25 ºC and 600 Hz

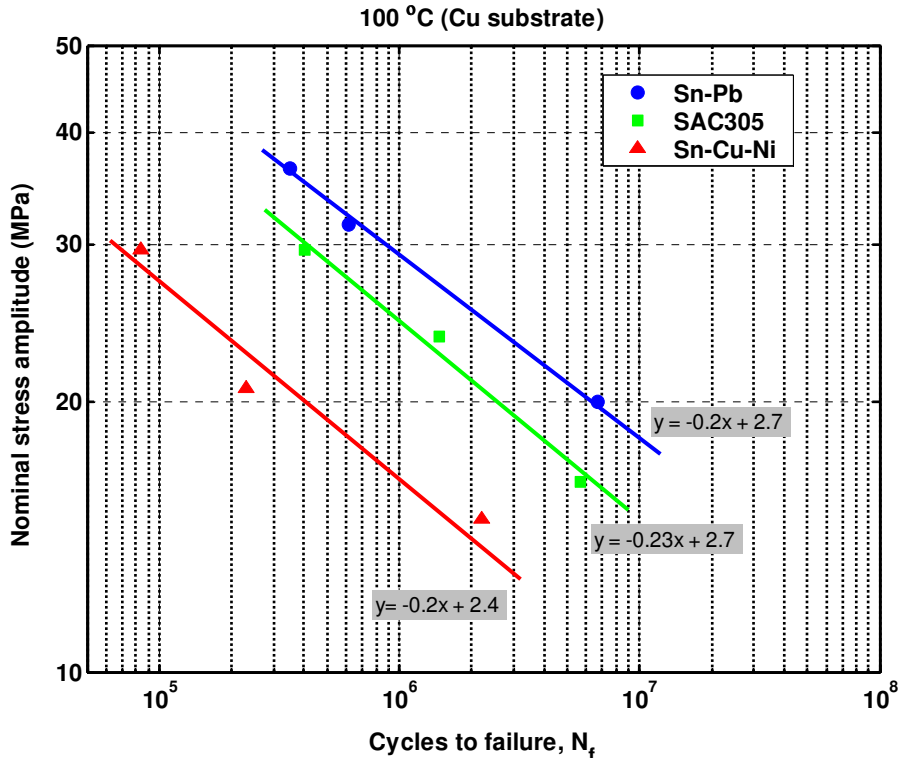

Figure 4.47. Nominal stress amplitude vs. cycles to failure for solder joints on Cu substrates subjected to fatigue loading at 100 ºC and 600 Hz

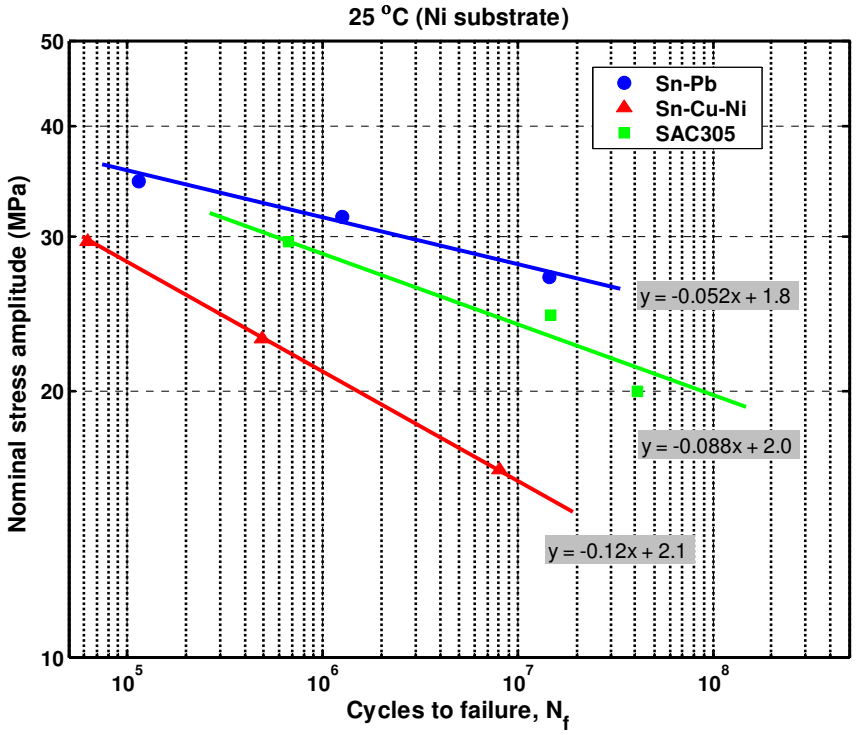

Figure 4.48. Nominal stress amplitude vs. cycles to failure for solder joints on Ni substrates subjected to fatigue loading at 25 °C and 600 Hz

Solder	g level	Nominal stress amplitude (MPa)	Mean cycles to failure	Standard deviation	Coefficient of variation
Sn-Pb	47.3	36.4	510,375	552,141	1.08
Sn-Pb	45	34.7	770,850	334,378	0.43
Sn-Pb	40	30.8	7,004,250	5,837,311	0.83
Sn-Pb	37.5	28.9	14,143,500	14,971,282	1.06
Sn-Pb	35	27	75,445,500	59,213,722	0.78
Sn-Cu-Ni	40	29.6	135,500	52,537	0.39
Sn-Cu-Ni	35	25.9	456,525	350,867	0.77
Sn-Cu-Ni	29	21.5	1,917,975	1,102,110	0.57
Sn-Cu-Ni	23	17	10,534,500	9,860,789	0.94
SAC305	40	29.6	241,560	157,837	0.65
SAC305	35	25.9	2,004,087	1,884,798	0.94
SAC305	29.8	22.1	11,556,000	7,221,848	0.62
Innolot	29.6	21.9	22,672,125	39,658,452	1.75

Table 4.2. Tabulated statistical results for solders fatigued to failure at 600 Hz, 25 °C on Cu substrates

	Sn-Pb		Sn-Cu-Ni		SAC305	
	b	**1/b**	**b**	**1/b**	**b**	**1/b**
25 ºC, Cu substrate	-0.057	-17.5	-0.120	-8.3	-0.080	-12.5
100 ºC, Cu substrate	-0.200	-5.0	-0.200	-5	-0.230	-4.3
25 ºC, Ni substrate	-0.052	-19.2	-0.120	-8.3	-0.088	-11.4

Table 4.3. Tabulated fatigue constants and their inverse for solders at all tested conditions

Figure 4.46 shows the stress-life results for 4 solders tested at ambient temperatures and soldered to uncoated Cu rods. Each data point represents the mean cycles to failure of up to eight specimens (with a minimum of 5 unless otherwise noted) tested using the experimental method developed in this work. All data in Figure 4.46 fit well to a straight line when plotted in log-log space. The equations of the linear fits as determined by Matlab are displayed on the graph. It can be seen that the performance order of the alloys in increasing merit is Sn-Cu-Ni > SAC305 > Sn-Pb > Innolot, although the data set for Innolot is not sufficient to form more than one point (as explained later). Using the linear fit coefficients to calculate interpolated lifetimes, it can be demonstrated that the lifetime ratios of the solders at a nominal cyclic stress amplitude of 29 MPa are approximately 1 : 1.4 : 229 for Sn-Cu-Ni : SAC305 : Sn-Pb at ambient temperatures. The exponent, *b*, of the Basquin equation $\sigma_a \left(N_f\right)^b = C$, which is the gradient of the linear fit in log-log space, is shown for the solders in Table 4.3. The solder with the best performance, Sn-Pb, also has the shallowest gradient, *b*, of -0.057 meaning it has the greatest sensitivity to stress. In contrast, the worst performing solder, Sn-Cu-Ni, has the steepest gradient (*b* = -0.12).

The results for Sn-Pb, SAC305 and Sn-Cu-Ni on Cu substrates tested at 100 ºC are shown in Figure 4.47, with the Basquin coefficients presented in Table 4.3. The merit order of performance is the same as that of the data at 25 ºC but, at the higher temperature, SAC305 is significantly closer to the top-performing Sn-Pb than before. The gradients of the linear fits to the respective solders' data are much more similar at 100 ºC than at 25 ºC, and overall lifetimes are significantly reduced at the higher temperature. The performance ratios of Sn-Cu-Ni : SAC305 : Sn-Pb are approximately 1 : 5 : 32 at 100 ºC and σ_a = 29 MPa. An S-N graph of results obtained at 25 ºC with joints soldered to Ni-coated Cu rods is shown in Figure 4.48. The results are similar to those obtained at 25 ºC on uncoated Cu rods in terms of the performance merit order and linear fit gradients but the additional step of Ni coating appears to improve the performance of the Sn-Cu-Ni and SAC305 joints while hindering that of the Sn-Pb joints. This effect is illustrated more clearly by plotting all results on the same axes, as shown in Figure 4.49. The lifetime ratios of Sn-Cu-Ni : SAC305 : Sn-Pb are approximately 1 : 6 : 15 at 25 ºC with Ni substrates. The performance deficit of the Pb-free solder alloys compared to traditional Sn-Pb solder is thus reduced with Ni substrates at ambient temperature. While the linear fits to the averaged data points in log-log space are good for Sn-Cu-Ni and Sn-Pb in Figure 4.48, the fit to SAC305 is poor. One could consider these data as representing either a straight line with higher than usual scatter, or two distinct lines with different gradients. More data would be needed to justify either approach with more certainty. In the present work the decision has been taken to treat the data as conforming to a single linear fit; this is partly due to the data for SAC305 on Ni substrates comprising slightly fewer specimens than average, meaning that the scatter is probably higher, and partly based on the established behaviour of materials in high-cycle fatigue [96] which tends towards gradients becoming shallower rather than steeper at very high lifetimes.

A number of high-cycle fatigue failure results (25 ºC, Cu substrate) are not presented in the main results due to their isolated nature but they are nevertheless of interest and are shown in Figure 4.50. One batch of eight specimens using SAC387 solder was constructed and tested; their average lifetime is shown to be close to that of SAC305. A batch of eight SAC305 specimens were tested at σ_a = 18.7 MPa as part of the main test regime but two of the joints did not fail after 5 x 10^8 cycles (runouts). This meant that the mean life to failure could not be plotted for this batch; the individual data points are instead displayed. It would appear that the endurance limit has been approached for SAC305 – a stress level below which no failures occur. It was initially decided to test the Innolot alloy at similar stresses to SAC305 – a decision based on their similar metallurgy. However, testing at σ_a = 18.7 and 24.4 MPa resulted in a number of runouts, as indicated in Figure 4.50. A further batch of eight specimens was tested at σ_a = 29.6 MPa, which did yield eight failures. The remaining batch of specimens were tested at σ_a = 33.3 MPa in the resonant frequency decay study described in Chapter 3. Due to issues described later, only two of these specimens were found to be in a cracked state (and therefore their failure imminent). Therefore, although the mean of these two results is plotted, it is recognised that two specimens do not represent a sufficient quantity with which to plot a data point used to obtain a gradient. It should also be noted that the Innolot alloy, when considering the σ_a = 29.6 MPa batch which produced eight failures, demonstrated a very large scatter of lifetimes – the standard deviation of this batch was almost twice the mean lifetime, higher than any other batch for any solder (Table 4.2). It was found when examining the fracture surfaces of this batch that none of them contained significant voids or other defects and in fact the fracture surfaces were all very similar, in contrast to the other alloys.

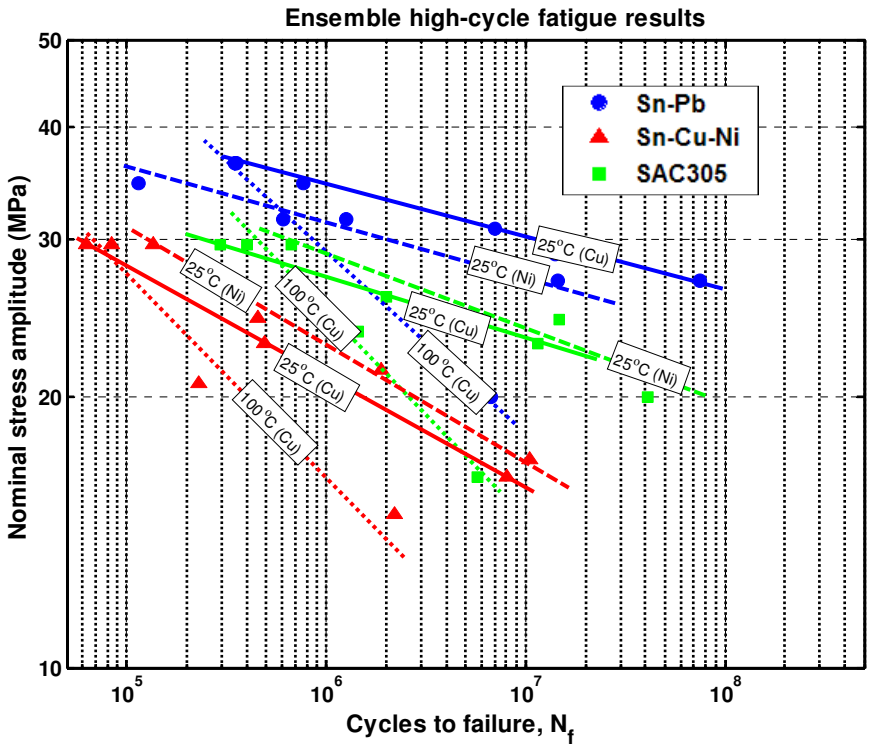

Figure 4.49. Nominal stress amplitude vs. cycles to failure for solder joints on both Cu and Ni substrates, at ambient and elevated temperatures, subjected to fatigue loading at 600 Hz

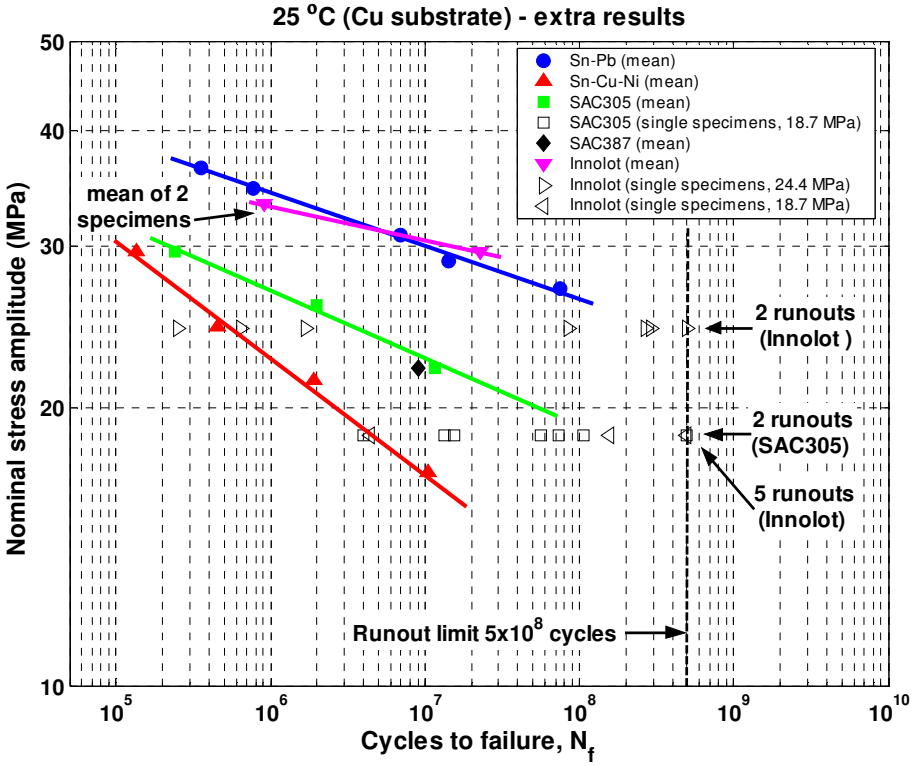

Figure 4.50. Nominal stress amplitude vs. cycles to failure for solder joints on Cu substrates subjected to fatigue loading at 25 ºC and 600 Hz including incomplete SAC305, SAC387 and Innolot data where complete curves could not be plotted due to omissions or runouts (machine turned off before failure because of time constraints)

4.3. Resonant decay behaviour

The effect of increasing specimen damage throughout the high-cycle fatigue lifetime on frequency response is shown in Figure 4.51. Up to seven resonant frequencies were identified in most specimens as candidates for damage tracking. However, the 3rd of these (in ascending numerical order) was sometimes undetectable, and Figure 4.52 shows that the highest three were clearly system resonant frequencies (such as those of the shaker or fixture) since they do not change with specimen damage. The 4th frequency did decay with specimen damage but was unpredictable compared with the lowest two frequencies. Figure 4.53 presents a comparison between the 1st, 2nd and 3rd resonant frequency decays of SAC387 rods over their lifetimes, showing that the smoothest and strongest response was that of the 2nd resonant frequency, identified in Chapter 3 as a bending mode of the rod/holder system. Henceforth the 2nd resonant frequency was used for tracking purposes in all results. Progressive fatigue crack damage as measured by the decrease in 2nd resonant frequency is used to compare Sn-Pb, Sn-Cu-Ni and SAC305 solders in Figure 4.54, with corresponding fractographs shown in Figure 4.55. It can be seen that the when normalising the frequency drop with respect to its initial value and normalising the cycles to failure with respect to the final value, the crack damage of all three solders follows a very similar pattern. Steady but slow decays in the 2nd resonant frequency are seen throughout the majority of their lifetimes, with a significant downturn seen at around 0.90 of the failure time. Failure occurs swiftly after this point for these alloys, with final $f/f_{initial}$ values between approximately 0.80 and 0.90 recorded (around 5 – 10 Hz below initial in terms of absolute value). An unsoldered Cu 'dummy' rod was tested by way of a comparison and showed that approx 1 Hz (or ~0.02 of a typical normalised initial frequency) was lost over 10 minutes of cycling at 600 Hz. This loss is attributed to settling in and slight relaxation of the clamping system.

Figure 4.56 – 4.61 show the resonant frequency decay results for all specimens successfully fatigued to a set $f/f_{initial}$ value of between 0.90 and 0.97 with tests halted before failure, grouped by solder. It should be noted that the lifetime scales of each specimen are actually slightly different, since they were halted before failure (which would be the true lifetime value of 1.0) at different points but in all cases apart from Innolot, the difference will be only of the order of 1 %. The Innolot alloy displayed distinctly different resonant decay behaviour from the other alloys. Usually when two successive drops in frequency were detected at regular intervals during a fatigue test, the period between resonant frequency assessments was shortened in case failure was imminent. When testing the Innolot alloy, this strategy did not prove relevant, with progressive frequency drops recorded throughout its life and little evidence of drastic frequency drops towards the end of its lifetime. This behaviour is recorded in Figure 4.59. In fact, four Innolot specimens which were cycled until $f/f_{initial}$ values of 0.90 – 0.93 were achieved were actually undamaged when subsequently cross-sectioned and examined with microscopy. Specimens of all other solders displayed significant cracking at similar $f/f_{initial}$ values.

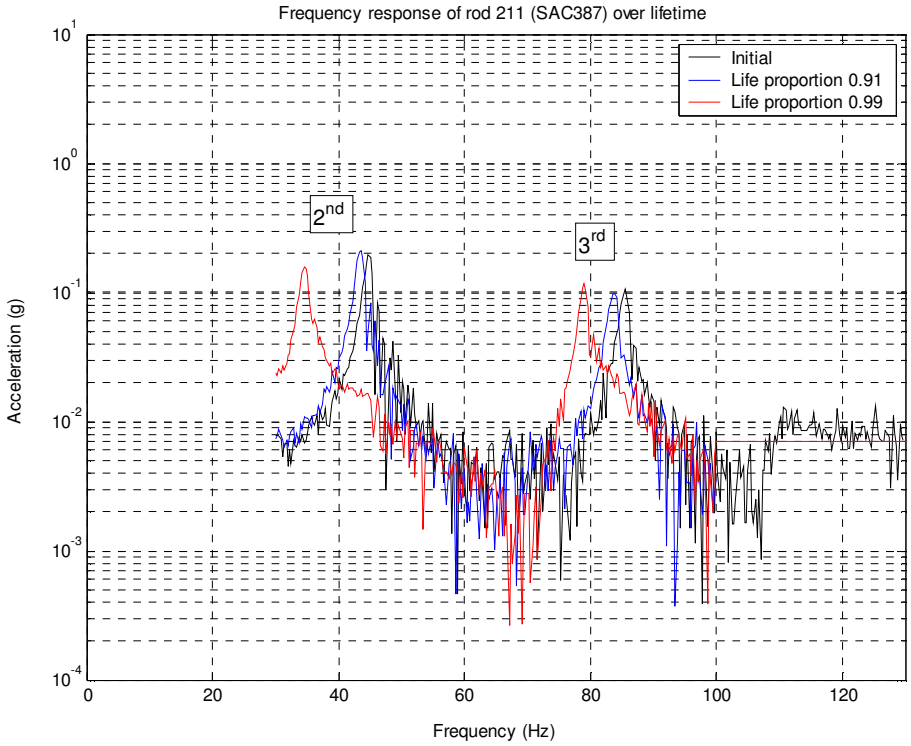

Figure 4.51. Example frequency response of rod/holder system at various stages of life throughout a fatigue test – note greater frequency shift of 2nd resonant frequency *c.f.* 3rd

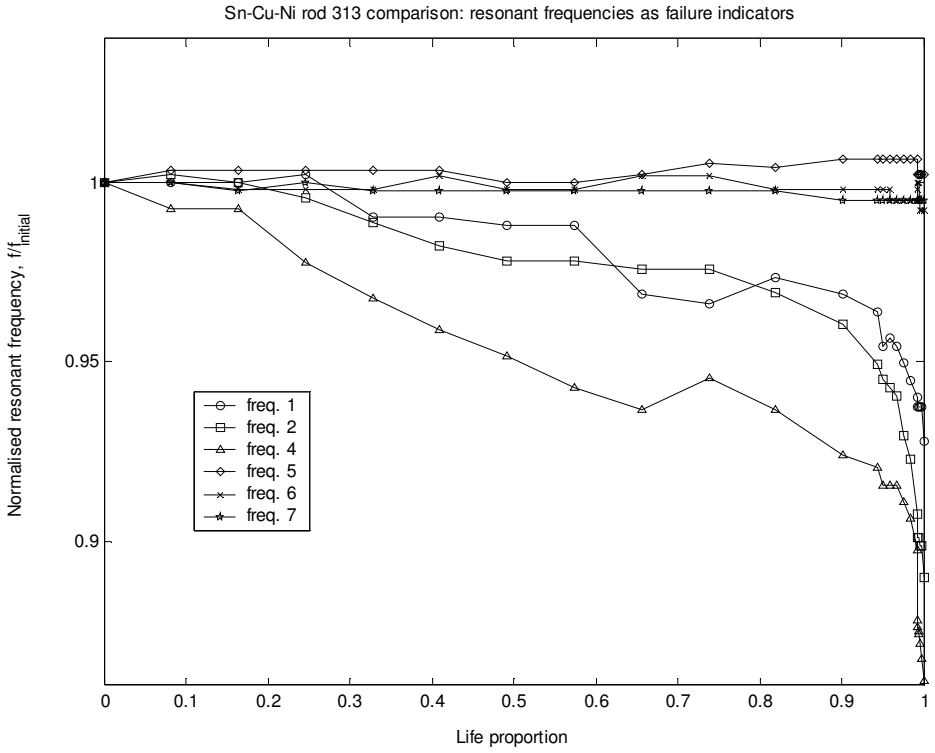

Figure 4.52. Normalised resonant frequencies vs. life proportion for Sn-Cu-Ni rod showing suitability of each frequency as a damage indicator (fatigued to failure at σ_a = 29.6 MPa, 25 ºC and 600 Hz)

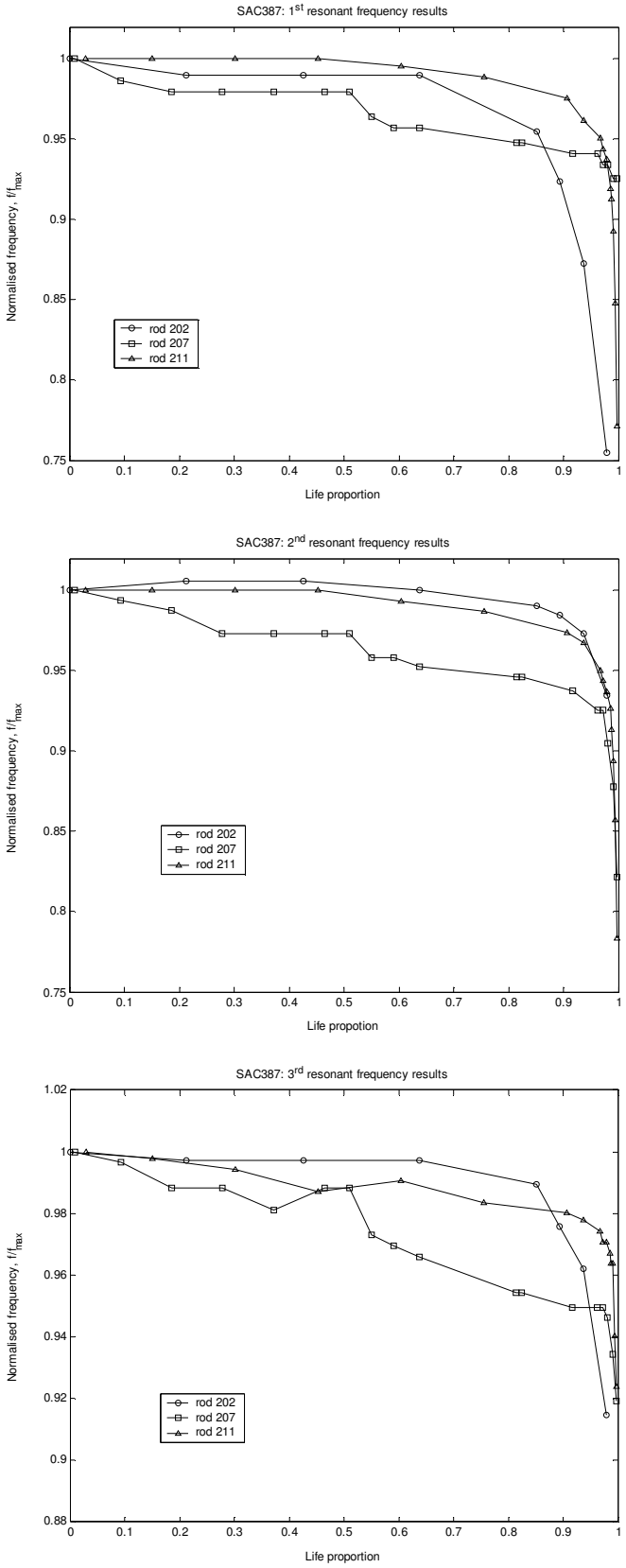

Figure 4.53. Comparison of first (lowest) three experimentally measured resonant frequencies of selected SAC387 rods as indicators of damage (fatigued to failure at σ_a = 29.6 MPa, 25 ºC and 600 Hz)

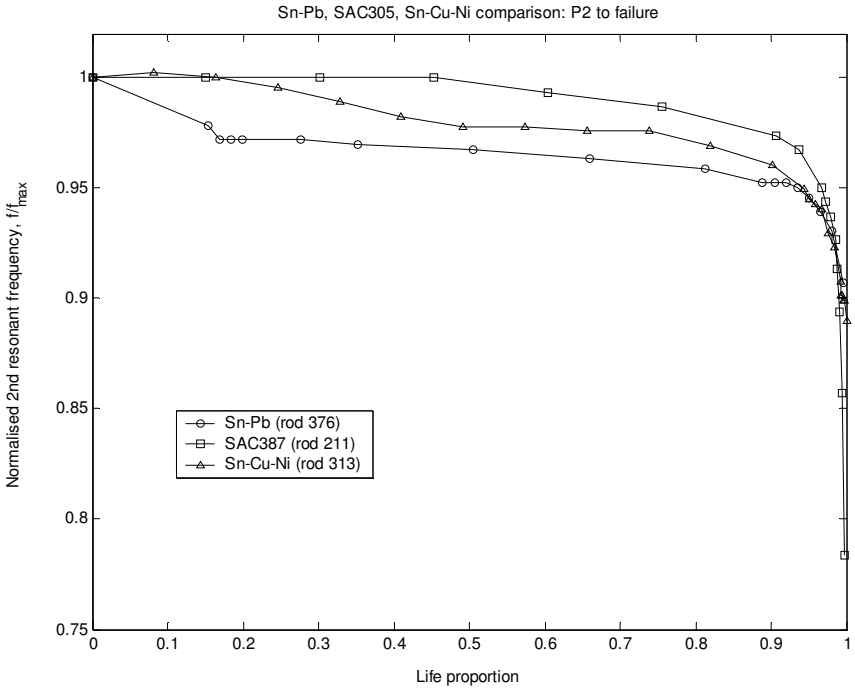

Figure 4.54. Comparison of damage indication provided by tracking 2nd resonant frequency of rod/holder system over lifetime of three different solder joint types. Tests conducted at 25 ºC, 600 Hz; joints fatigued to complete failure

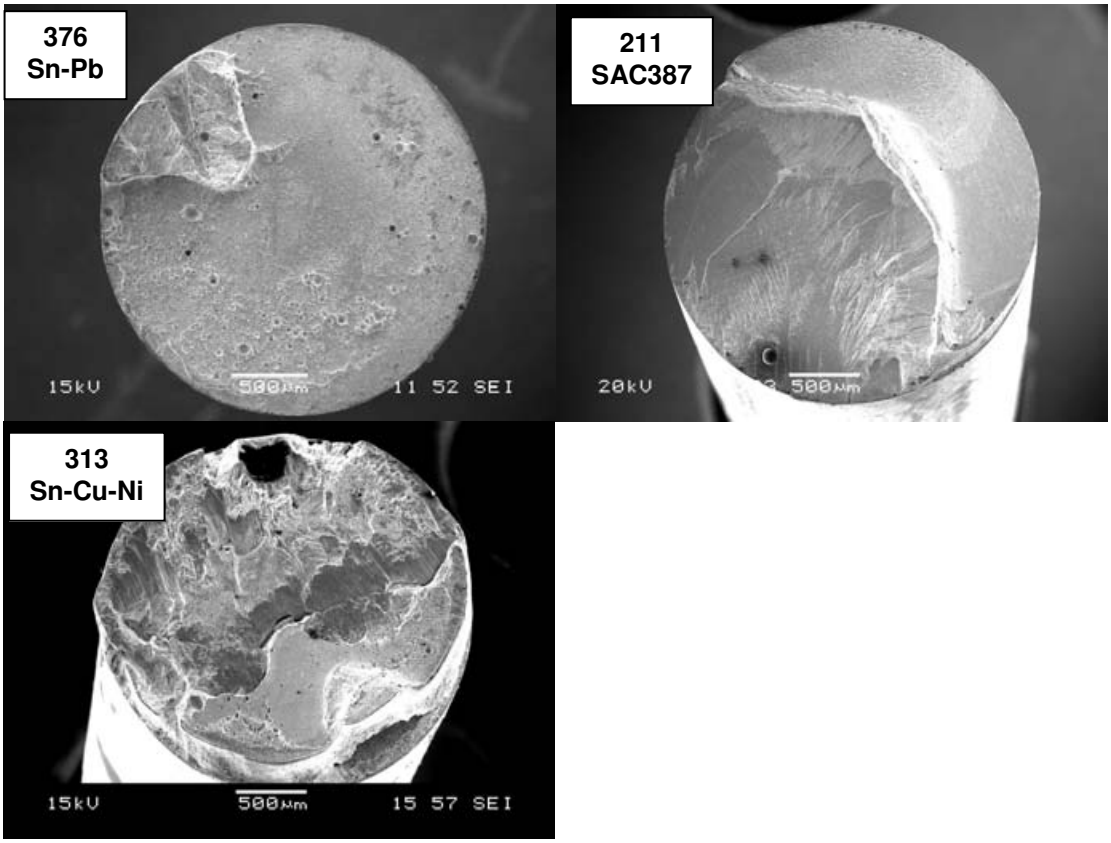

Figure 4.55. Electron micrographs of macroscopic fracture surfaces of joints whose resonant frequencies are tracked to failure in Figure 4.54 showing how different fracture paths can correspond to similar resonant decay plots

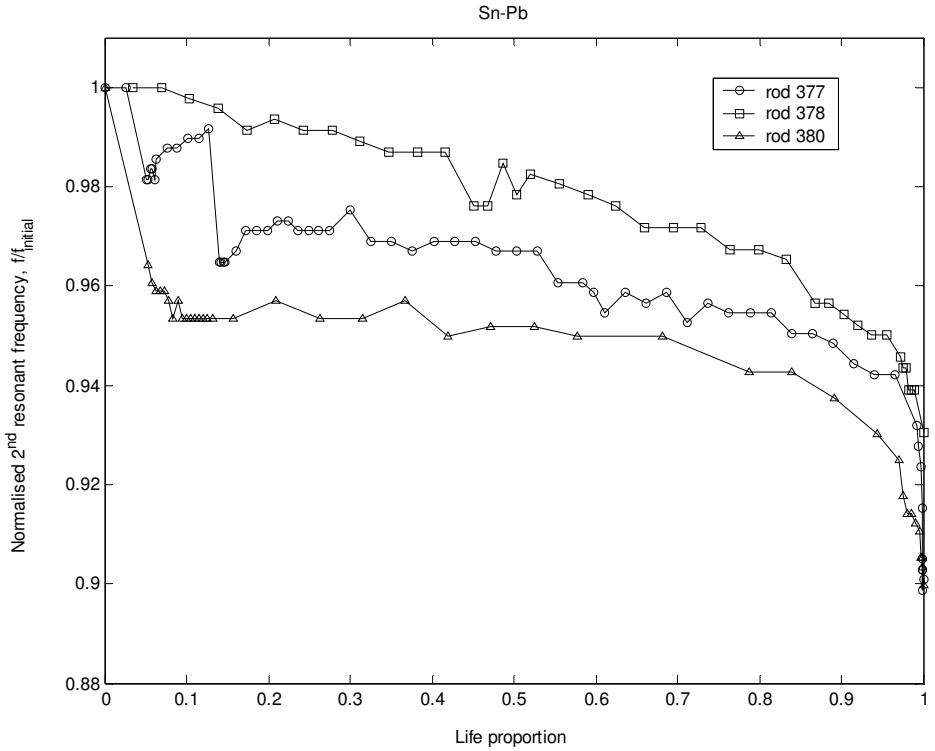

Figure 4.56. Normalised 2nd resonant frequency vs. life proportion for Sn-Pb solder joints on Ni substrates fatigued to $f/f_{initial}$ values of between 0.90 and 0.93 at 25 ºC and 600 Hz

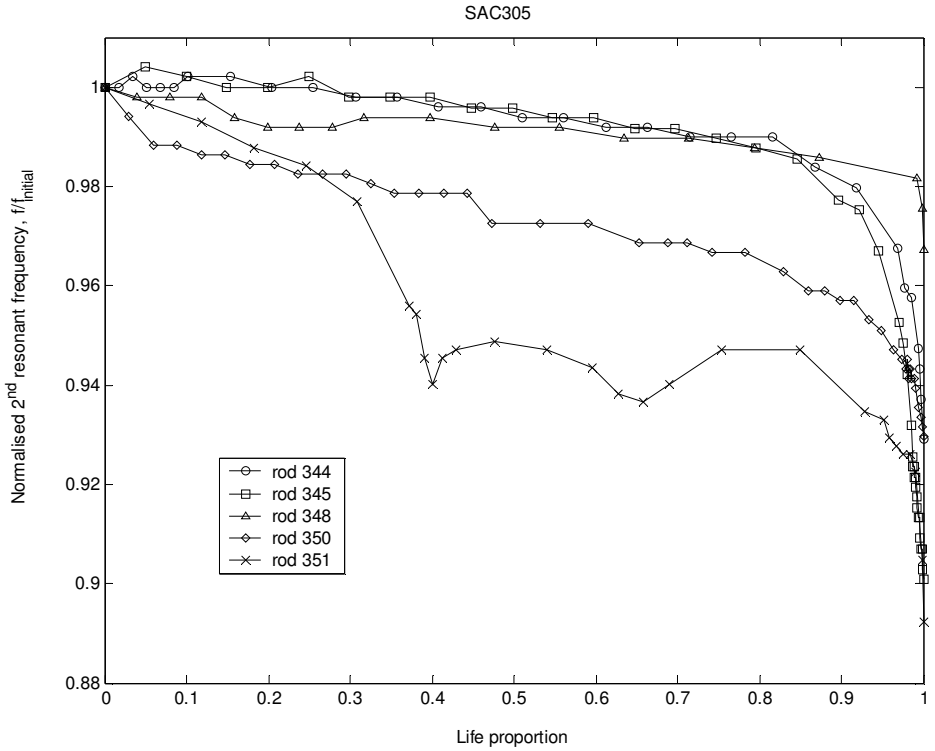

Figure 4.57. Normalised 2nd resonant frequency vs. life proportion for SAC305 solder joints on Ni substrates fatigued to $f/f_{initial}$ values of between 0.90 and 0.97 at 25 ºC and 600 Hz

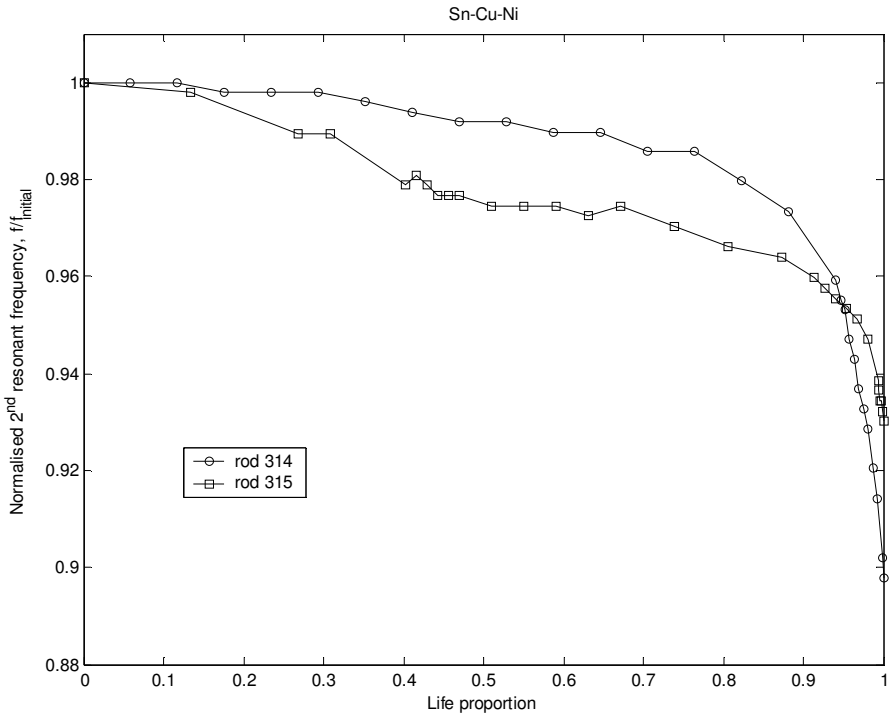

Figure 4.58. Normalised 2nd resonant frequency vs. normalised lifetime for Sn-Cu-Ni solder joints on Ni substrates fatigued to $f/f_{initial}$ values of between 0.90 and 0.93 at 25 ºC and 600 Hz

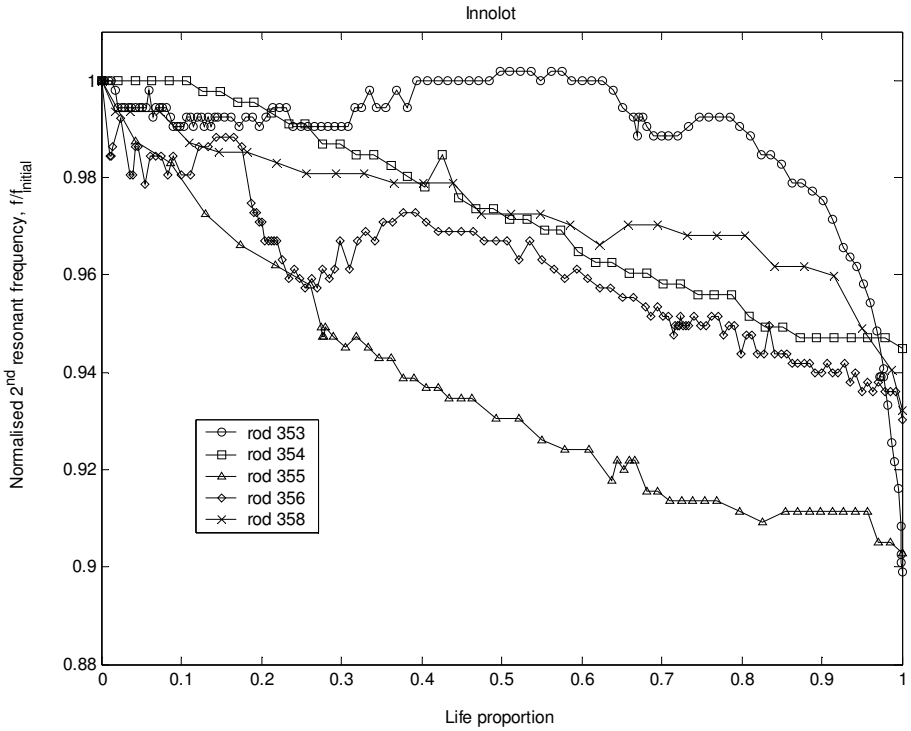

Figure 4.59. Normalised 2nd resonant frequency vs. normalised lifetime for Innolot solder joints on Cu substrates fatigued to $f/f_{initial}$ values of between 0.90 and 0.94 at 25 ºC and 600 Hz

4.4. Fracture behaviour in high-cycle fatigue

The fracture surfaces of many of the solder joint specimens fatigued to failure by the method set out in Chapter 3 were examined in the SEM. It should be remembered that a high-cycle fatigue fracture surface is formed by two distinct processes – the initiation and growth of a dominant fatigue crack followed by general plastic collapse, or 'overstress failure', as the intact area of the specimen decreases until the material's yield stress is exceeded in the remaining section. The analysis of which fracture surface features corresponded to which process often proved to be challenging in the present work, not least because there is the interface between the solder and substrate to consider. The analysis is addressed later in the chapter, aided by the results of the resonant decay studies. Principally, it was found that the fracture surfaces in the present work could be classified into two groups; bulk failure (through the solder) and interfacial failure (along the interface between solder and substrate). These two types are illustrated in Figure 4.60. However, the majority of the Innolot fracture surfaces conformed to a 'shallow notch' type appearance; one which was characteristic only to this alloy (see Figure 4.61). The proportions of different fracture types found are visualised in Figure 4.62 – 4.67, further broken down into 25 ºC (Cu substrate), 100 ºC (Cu substrate) and 25 ºC (Ni substrate). In the case of the baseline Sn-Pb solder, it is found that the majority of failures are interfacial at ambient temperatures on Cu substrates, whereas elevated temperatures and Ni substrates produce a greater proportion of bulk failures, although the interfacial mode is still dominant (Figure 4.62). A different case is seen for Sn-Cu-Ni, whose fracture surfaces are overwhelmingly characterised by bulk failure, especially with Ni substrates (Figure 4.63). Interfacial failures are the dominant type (82 %) at 25 ºC on Cu substrates for SAC305, although elevated temperatures and Ni substrates decrease this proportion to roughly half of the total failures (Figure 4.64). The Innolot alloy failed with a characteristic shallow notch appearance in 90 % of cases (Figure 4.65).

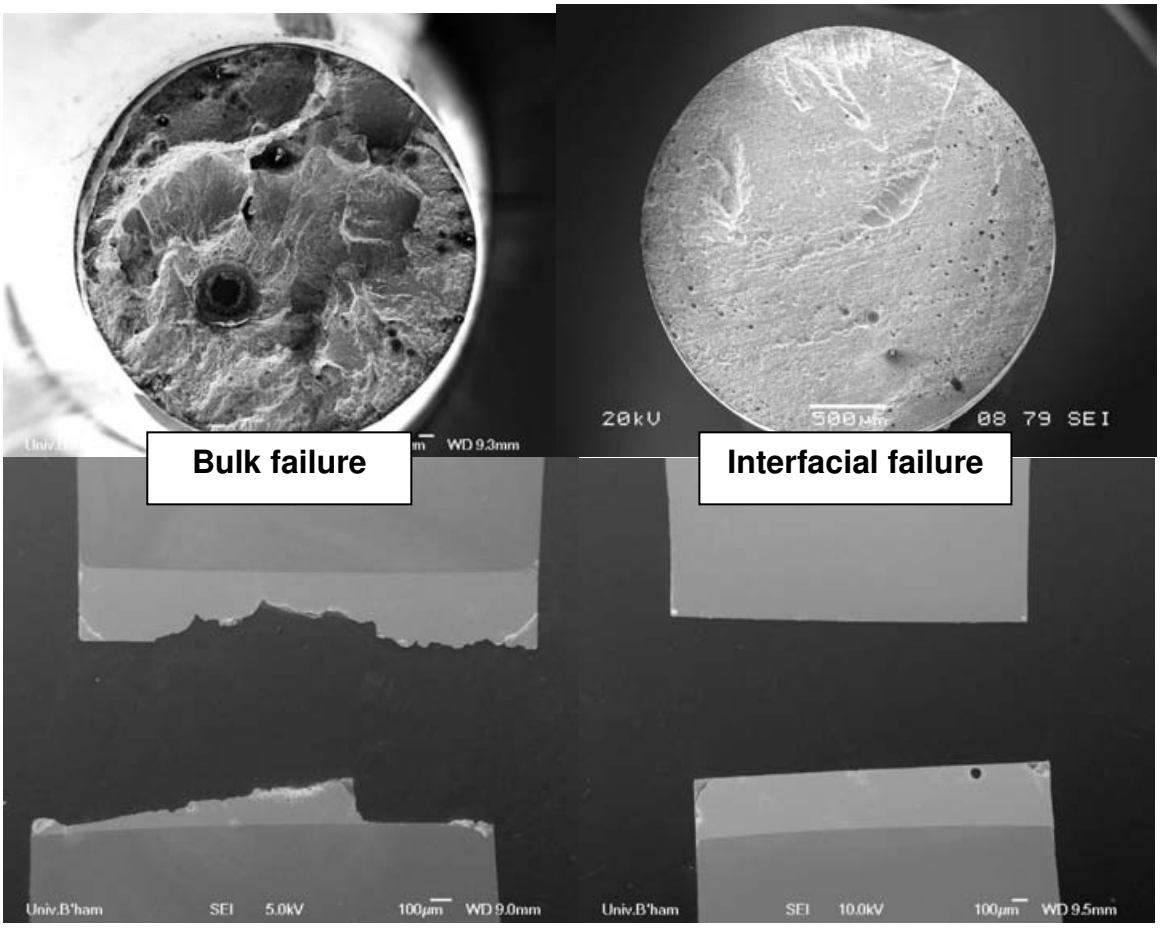

Figure 4.60. Examples of bulk (left) and interfacial (right) fracture surfaces in plan view (top) and cross-section (bottom) found in Sn-Pb, Sn-Cu-Ni and SAC305 joints after high-cycle fatigue

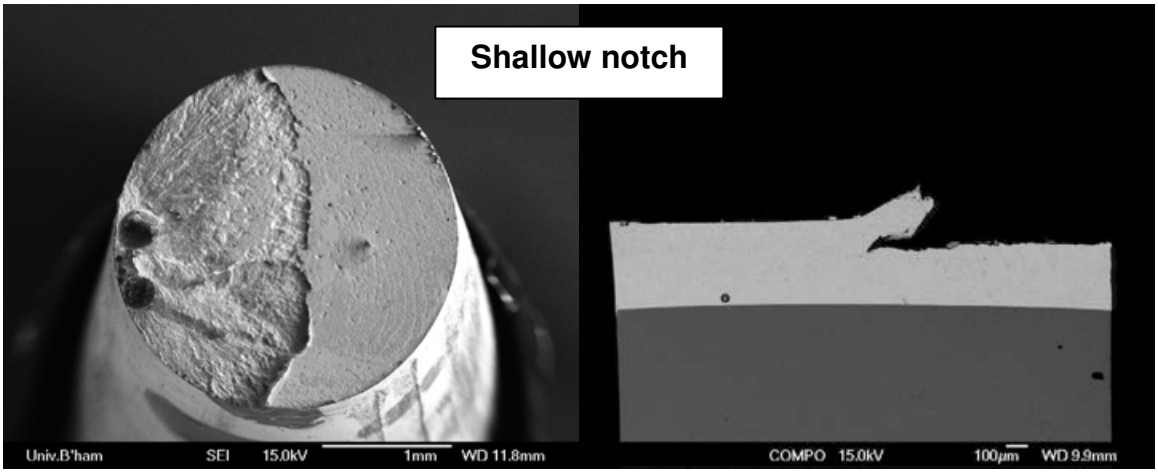

Figure 4.61. Example of shallow notch fracture surface appearance found in 90 % of Innolot joints after high-cycle fatigue

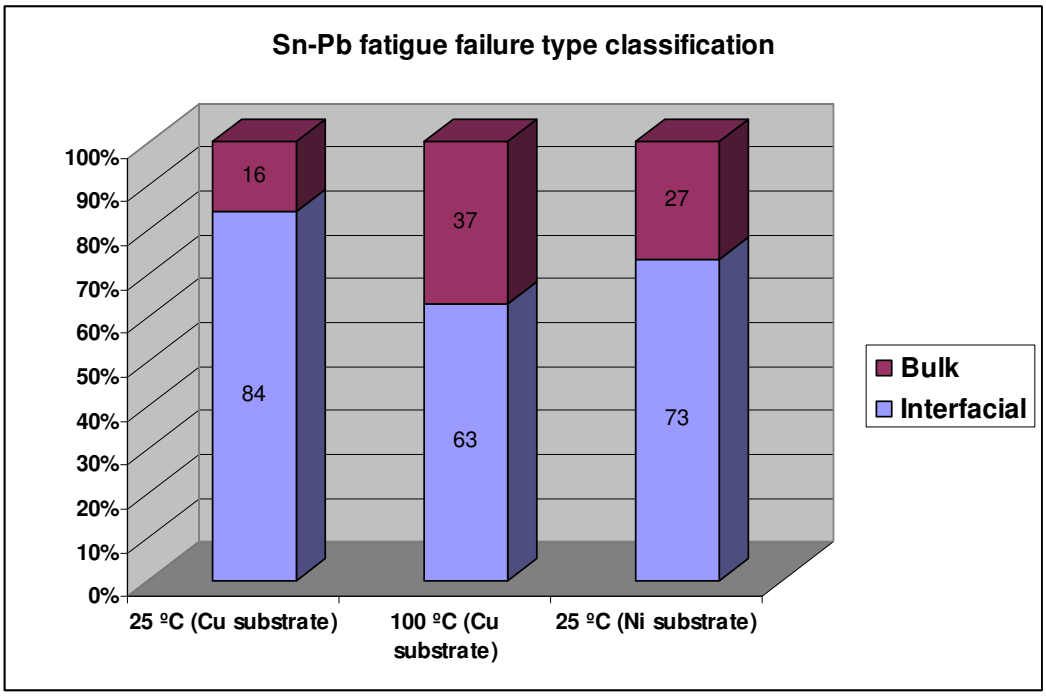

Figure 4.62. Sn-Pb fatigue failure type classifications

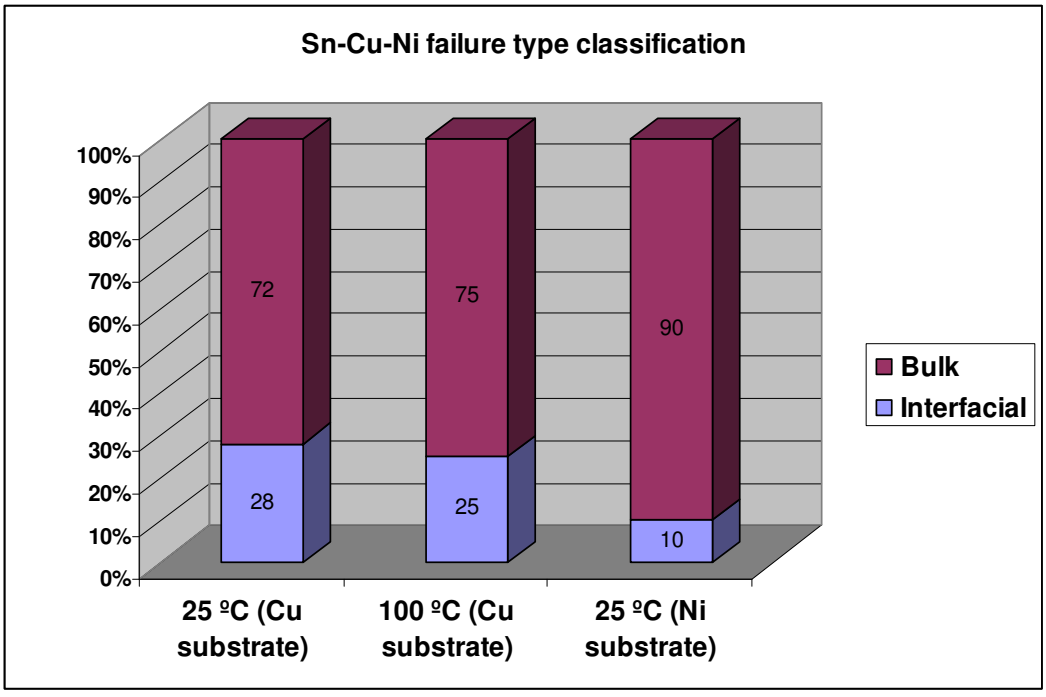

Figure 4.63. Sn-Cu-Ni fatigue failure type classifications

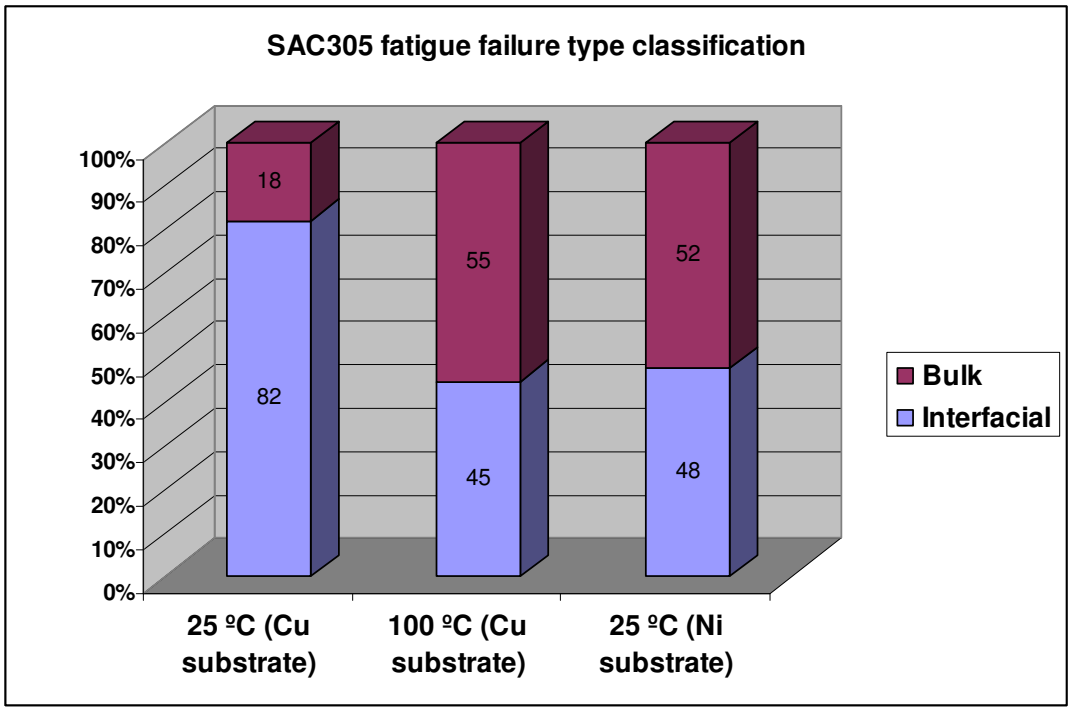

Figure 4.64. SAC305 fatigue failure type classifications

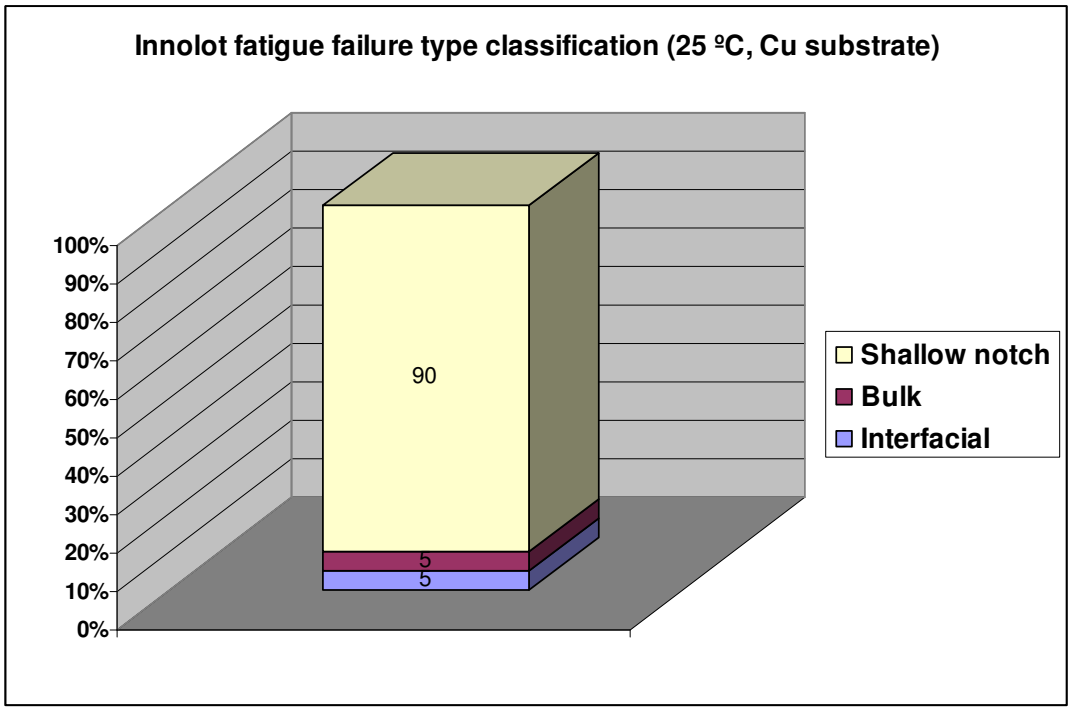

Figure 4.65. Innolot fatigue failure type classification

4.5. Detail of interfacial failures

It should be noted that the term 'interfacial' failure is a broad classification that encompasses a range of features. One major point of note is that many of the interfacial failures found did not occur completely across one interface as in Figure 4.60 but instead occurred across opposing interfaces of the joint, meeting in a distinct 'shelf' at some point across the section (Figure 4.66). It was decided to class these failures in the interfacial group despite the existence of a crack path through the bulk (the 'shelf') since the crack path along ~100 % of the joint area is the dominant feature in both. In some fracture surfaces of both these interfacial types were situations where the solder volume was peeling away from one or both interfaces despite the primary crack path being elsewhere (Figure 4.67). This behaviour indicates that interfacial failure was imminent along both interfaces, one crack having reached the critical size slightly before the other. The other important point regarding interfacial failures is to clarify the exact path that cracks were found to take.

The interface between solder and substrate actually comprises two interfaces: solder/IMC and IMC/substrate. It was rare for a crack path to be found along the latter interface but less rare for the former. In the majority of cases, however, the crack did not take a path along either of these interfaces. Instead, it took a path parallel to the interface but in the solder itself, around 5 – 20 μm from the IMC layer. Examples of this are shown in Figure 4.68 and Figure 4.69 for different solders. This behaviour was found with both Cu and Ni substrates. The less common situation of clean separation between solder and IMC layer is nevertheless shown in Figure 4.70. Whether this separation occurred during the primary fatigue crack growth or during the final overstress failure is not obvious as this stage but is discussed later.

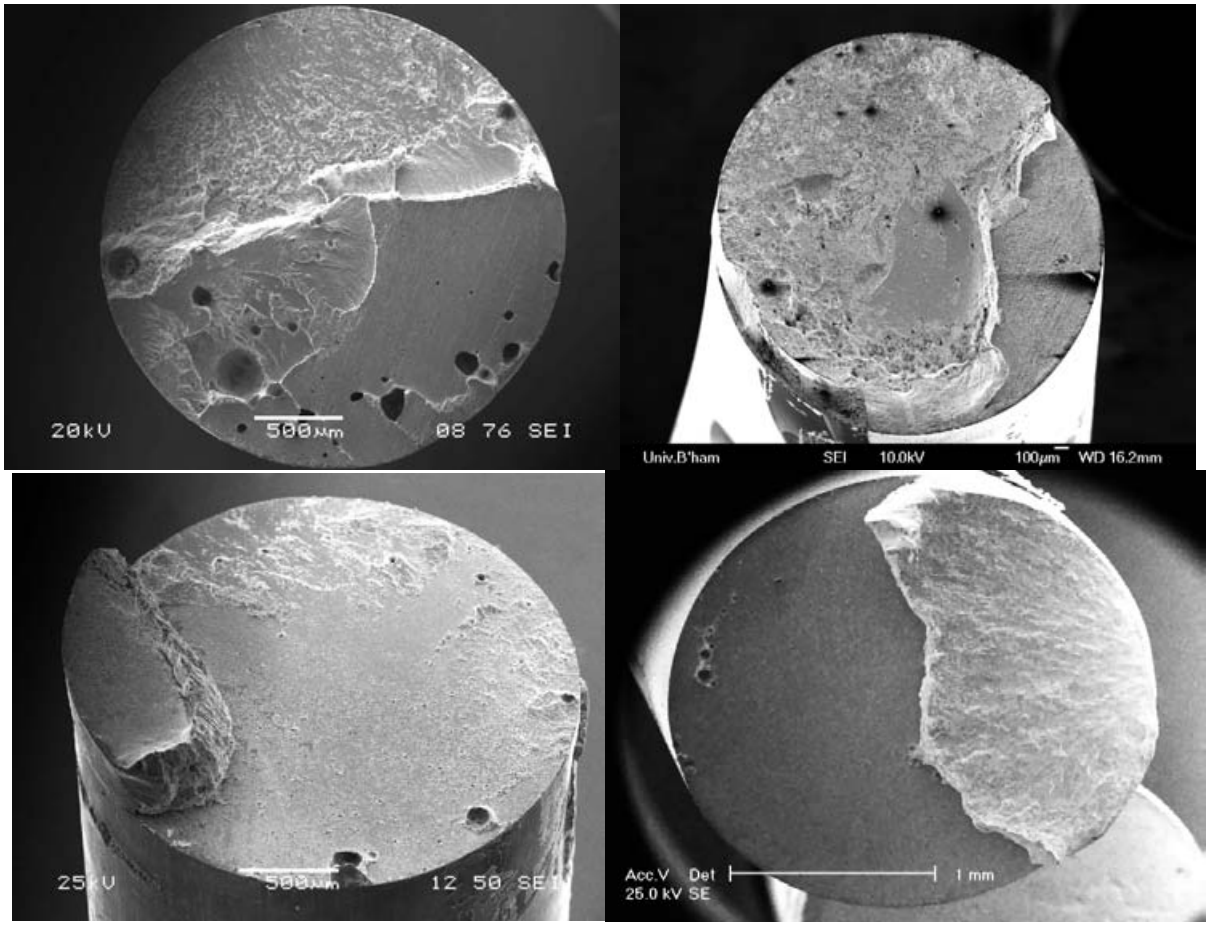

Figure 4.66. Secondary electron micrographs of interfacial failures from a variety of solders showing interfacial failure across both interfaces, meeting in a shelf feature at various distances across different joints

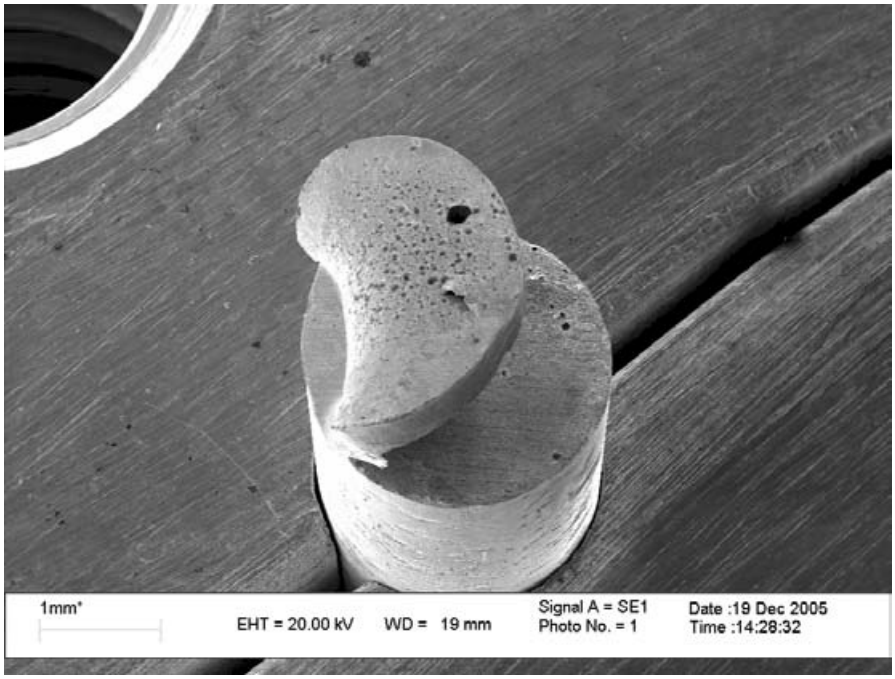

Figure 4.67. Secondary electron micrograph of solder peeling away from interface

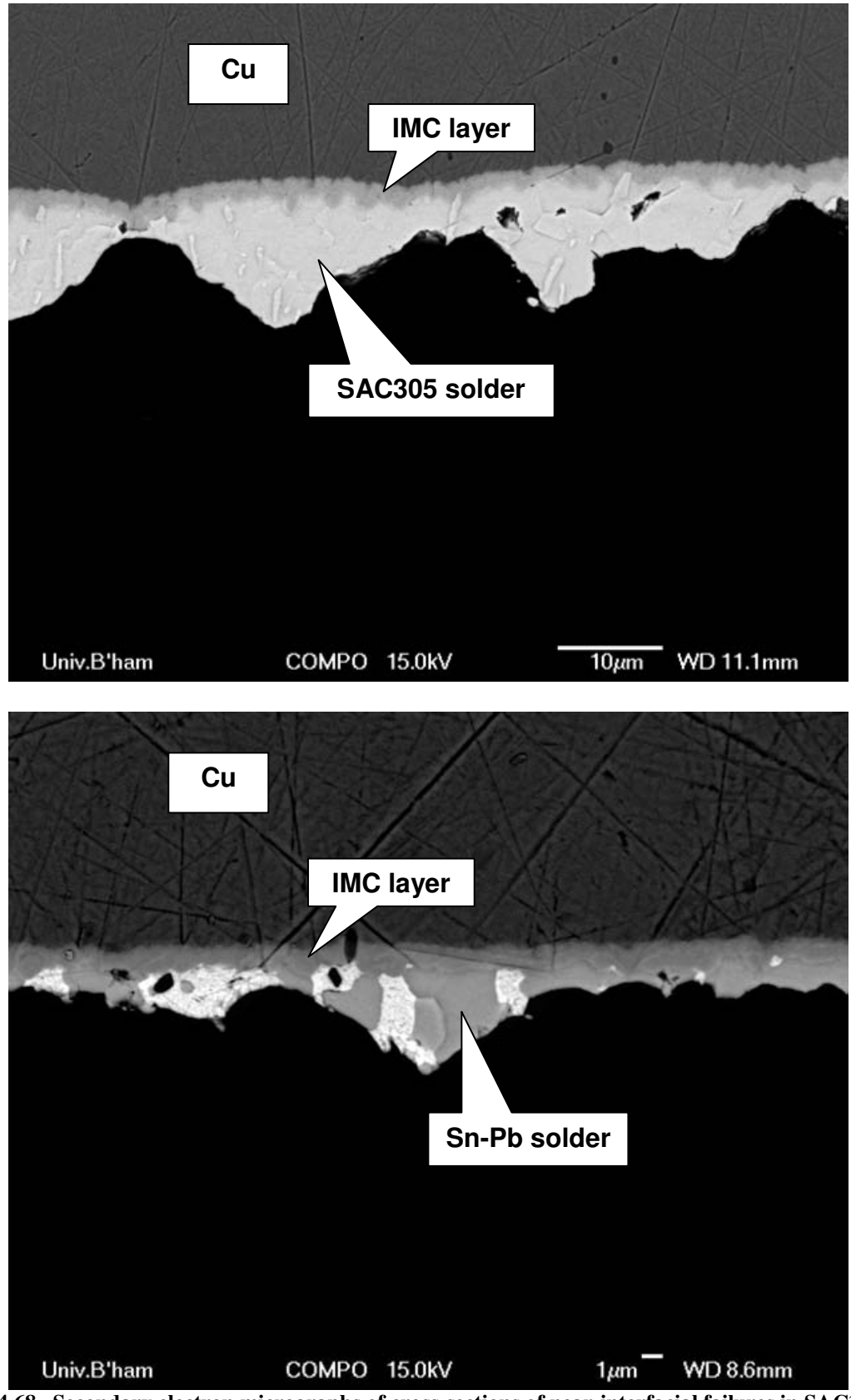

Figure 4.68. Secondary electron micrographs of cross-sections of near-interfacial failures in SAC305 (top) and Sn-Pb (bottom) showing failure parallel to interface leaving a thin layer of solder over IMC layer

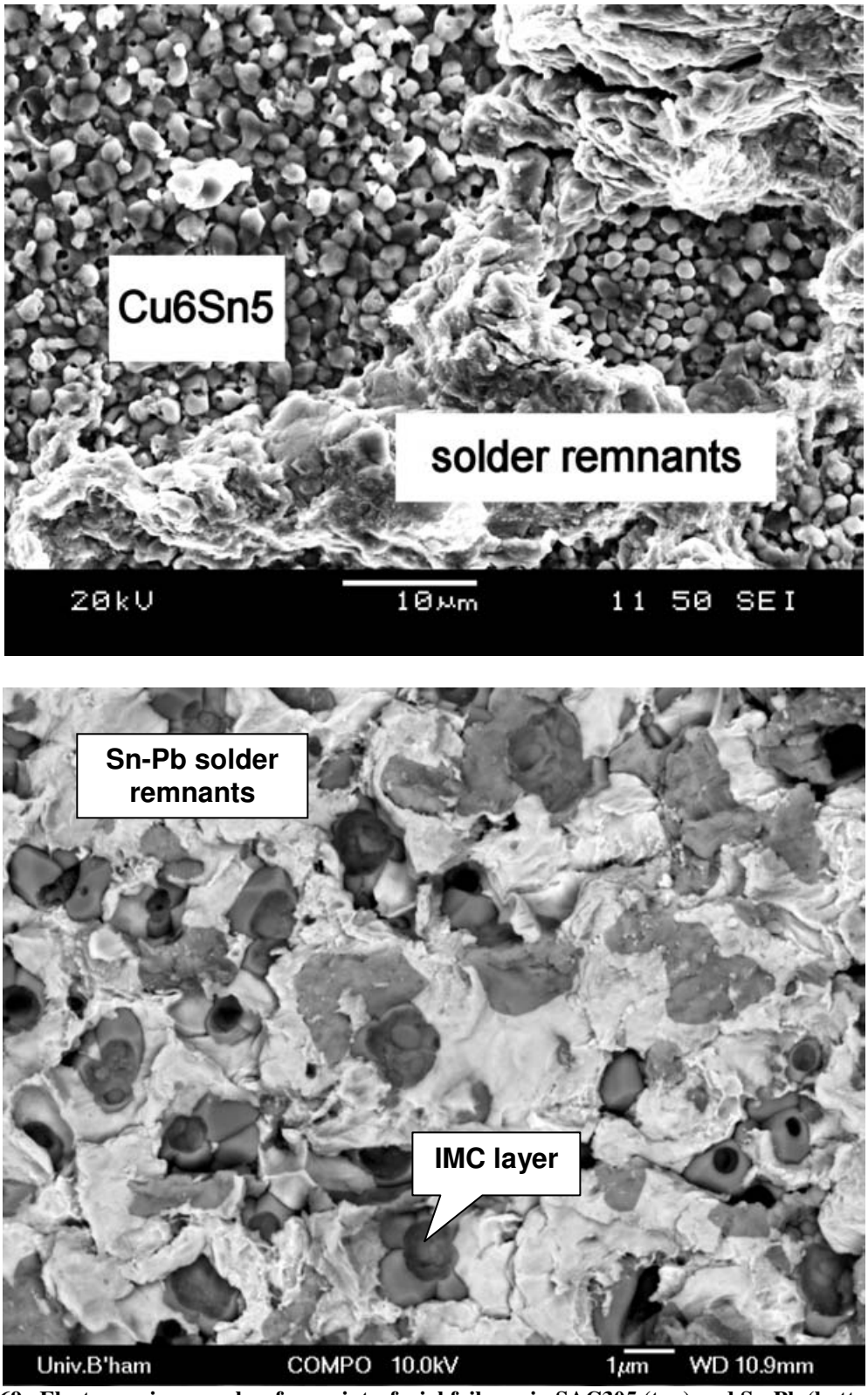

Figure 4.69. Electron micrographs of near-interfacial failures in SAC305 (top) and Sn-Pb (bottom) solder; view looking down on fracture surface. Large patches of thin solder layer left over IMC layer

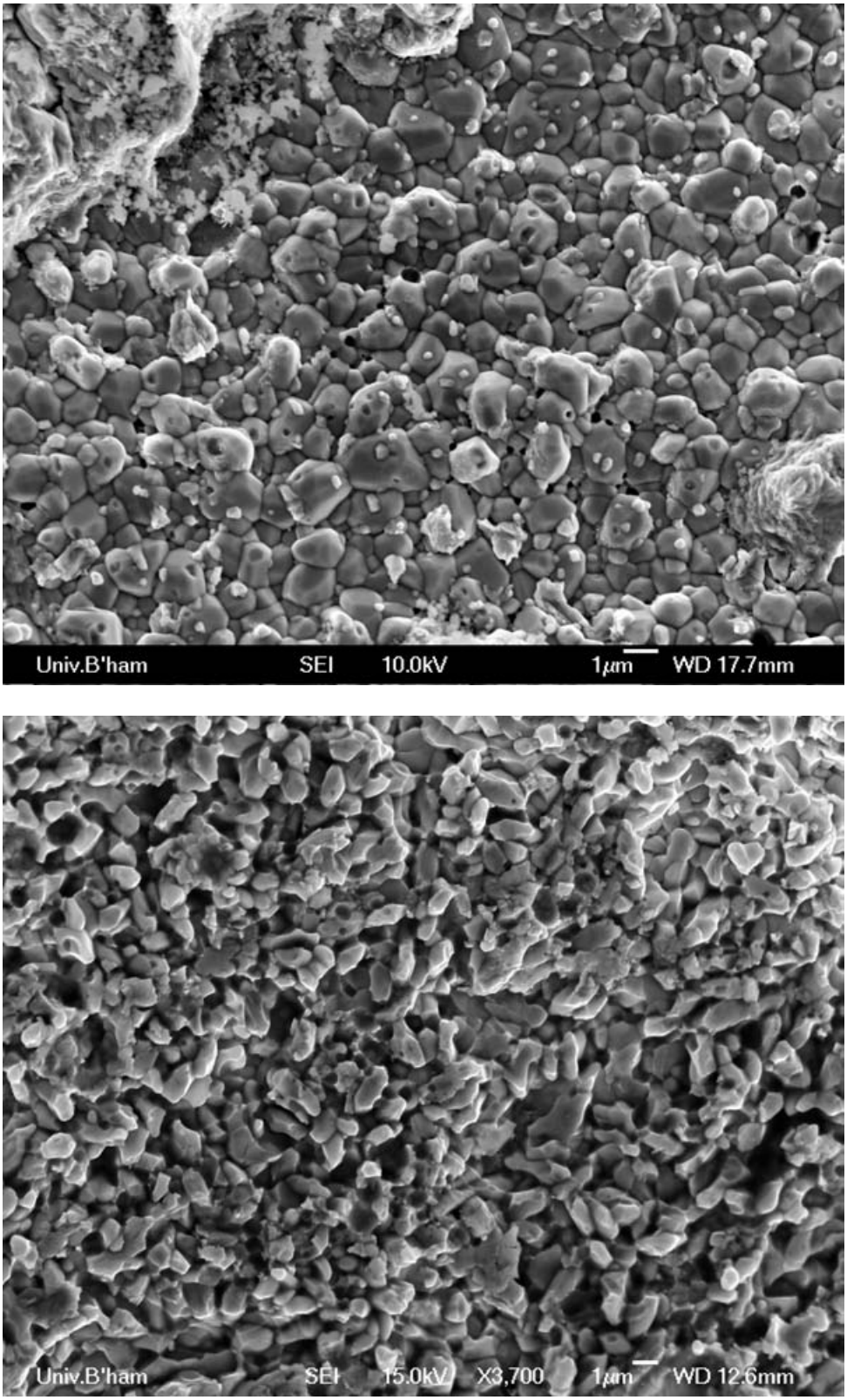

Figure 4.70. Secondary electron micrographs of exposed IMC layers left on HCF fracture surfaces of SAC305 (top) and Sn-Cu-Ni (bottom) showing clean separation

4.6. Interpretation of fracture surfaces

Initial fatigue crack growth areas are assumed to be represented by relatively sharp surface features with little evidence of plasticity. Fast/unstable crack growth areas, occurring when the cracked portion of the joint reaches a critical area and the effective stress is increasing with each stress cycle, are assumed to be represented by striations (clear, stepped parallel surface markings) or less clear repetitive markings. Overstress is assumed to be characterised by either very clean IMC/solder separation (for reasons discussed later) or very ductile microstructural features such as dimples from void coalescence.

4.6.1 HCF fracture surface features of Sn-Pb

The majority of Sn-Pb fracture surfaces showed failure at or near the solder/IMC interface at 25 ºC. In these cases, the fracture surfaces tended to show fine dimples (Figure 4.71), which are networks of circular ridges of solder protruding normal to the solder/IMC interface of approximately 2 to 20 μm in diameter. Often, when this dimpled solder layer is thin enough, the underlying IMC layer can be seen in the centre of the dimples where it seems the dimples have coalesced, leaving voids in their centres (Figure 4.72). In specimens tested at 25 ºC where bulk failure was instead found, the general appearance of the fracture surfaces was ductile (rounded rather than sharp features) and relatively featureless (Figure 4.73), with a texture or morphology dimensionally similar to the grain size of Sn-Pb (~5 μm) and little evidence of intergranular separation. In the small region of bulk failure (the 'ridge') connecting the two interfacial fracture surfaces in the manner described previously, fracture was again lacking in any evidence of failure along slip planes or other features pertaining to crystal orientation, showing instead a complex, ductile surface morphology (Figure 4.74).

The fracture surfaces of Sn-Pb HCF joints tested at 100 ºC show similar features to those from room temperature tests. Figure 4.75 and Figure 4.76 show a near-interfacial type failure at this elevated temperature which again displays a dimpled morphology. The increase in temperature does not appear to make one phase (Sn-rich or Pb-rich) more responsible than the other for the coalescence of these dimples (Figure 4.76). The features observed with Ni substrates for Sn-Pb were largely similar to those observed with Cu substrates (Figure 4.77).

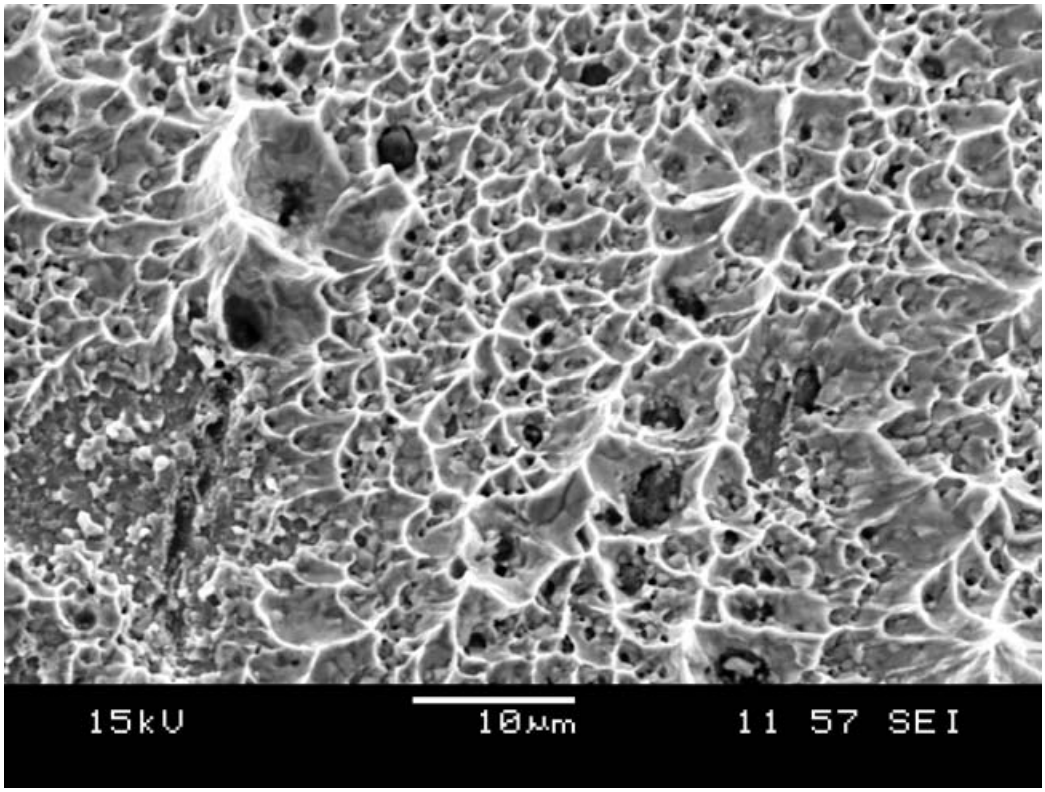

Figure 4.71. Secondary electron micrograph of typical Sn-Pb interfacial HCF fracture surface showing dimples of approximately 5 µm diameter

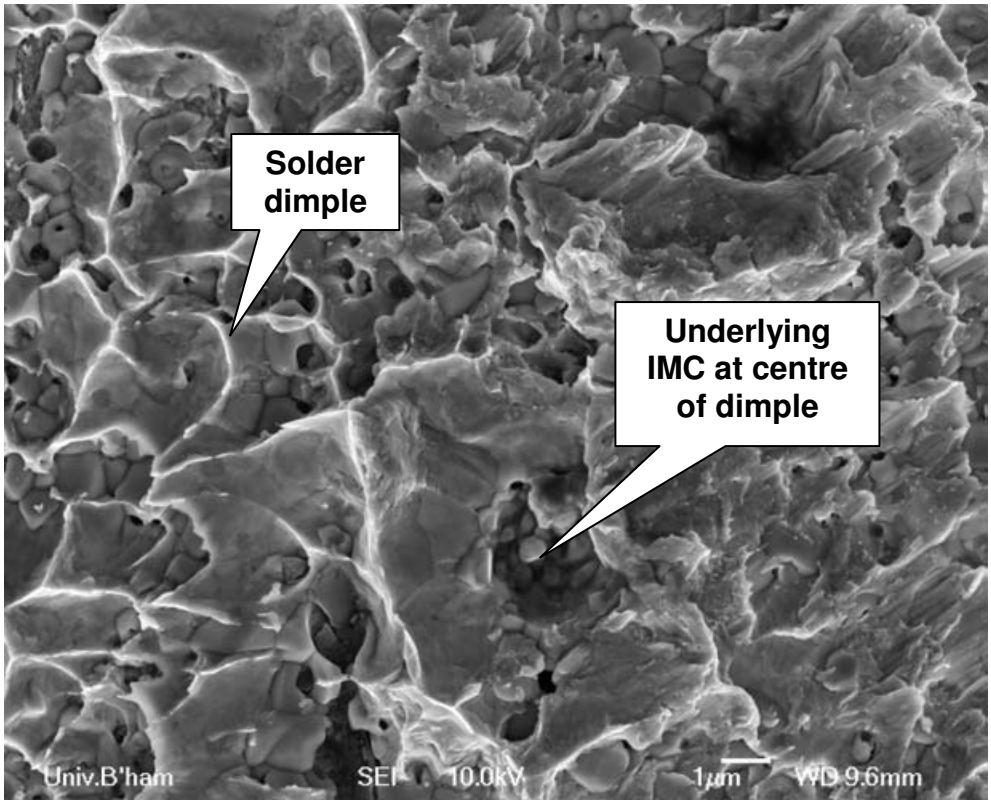

Figure 4.72. Secondary electron micrograph of typical interfacial Sn-Pb HCF fracture surface showing dimples of solder with underlying IMC layer revealed by voids developing in their centres

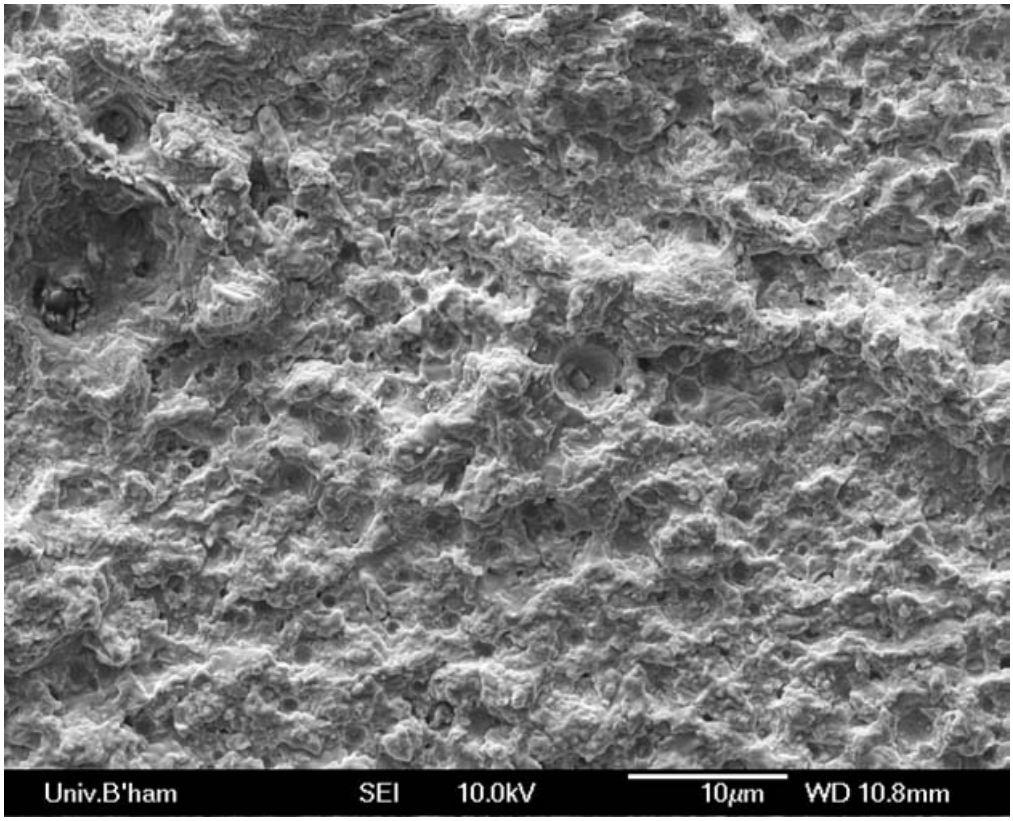

Figure 4.73. General appearance of Sn-Pb HCF fracture surface when cracking occurs through the bulk solder rather than close to the interface

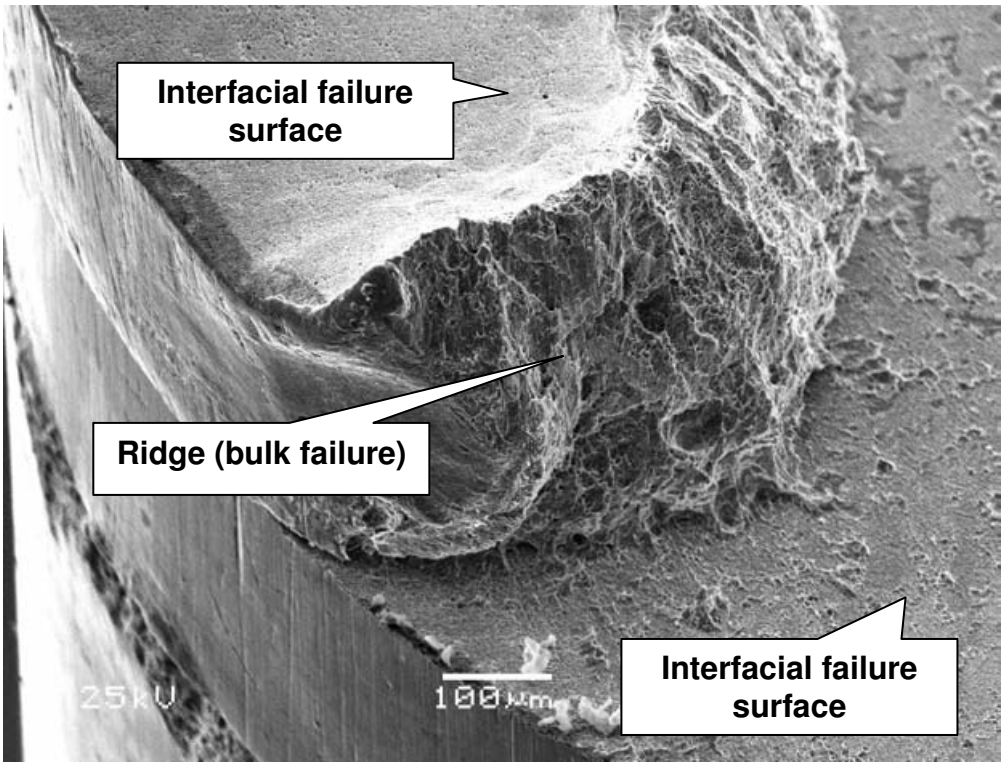

Figure 4.74. Appearance of bulk failure ridge linking opposing interfacial HCF Sn-Pb fracture surfaces

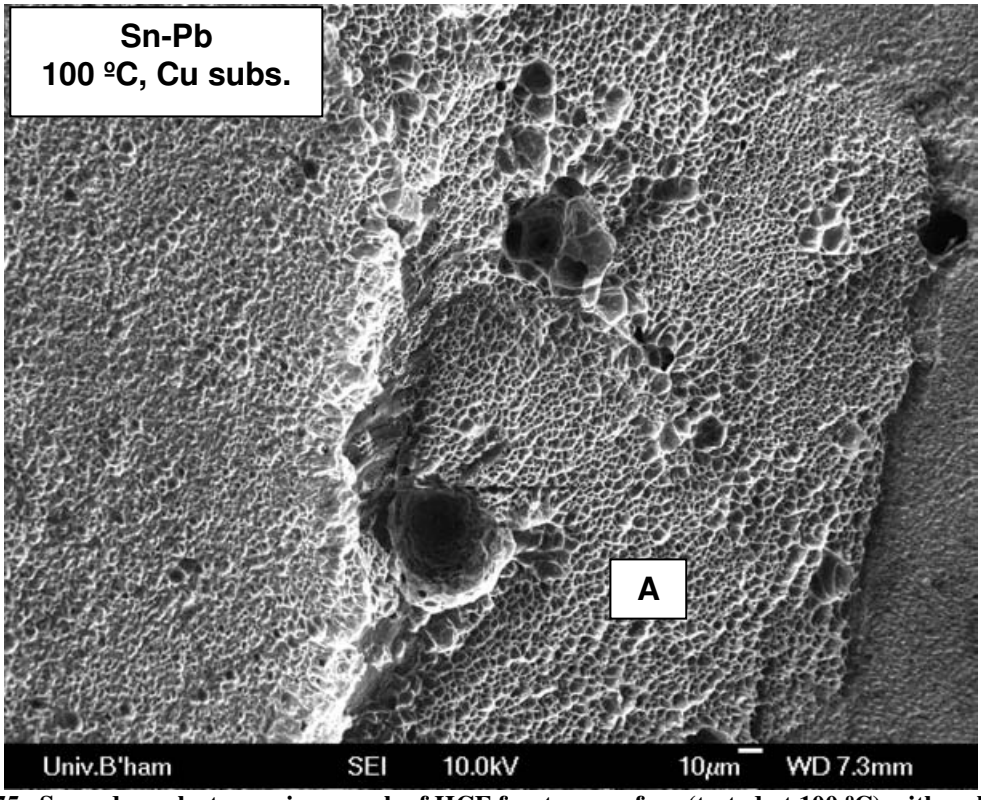

Figure 4.75. Secondary electron micrograph of HCF fracture surface (tested at 100 ºC) with well-defined dimples visible

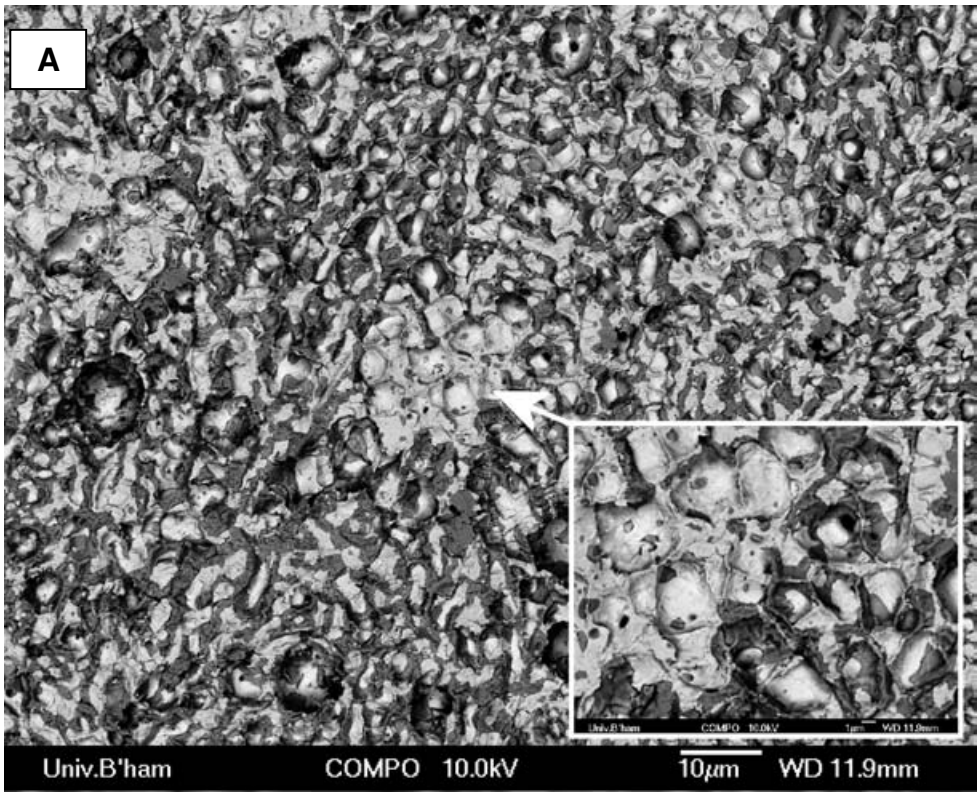

Figure 4.76. Backscattered electron micrograph of zoomed region B from Figure 4.75 Error! Reference source not found. **showing even role of Sn and Pb phases in dimple formation (inset magnified)**

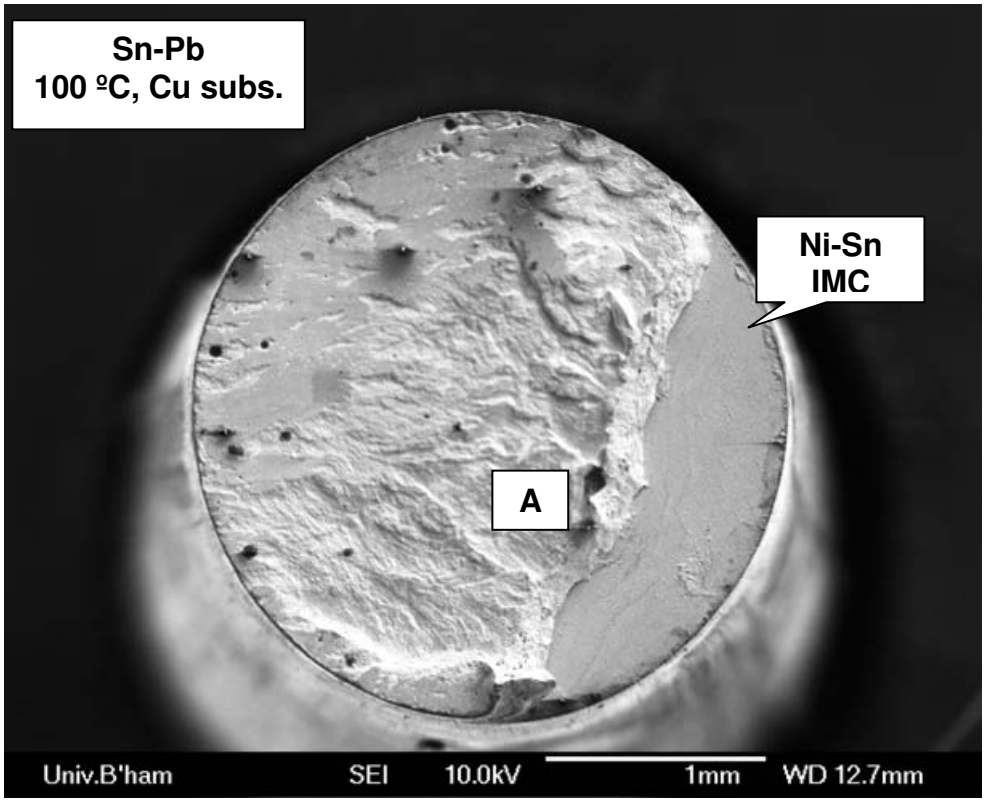

Figure 4.77. Secondary electron micrograph of Sn-Pb HCF fracture surface (tested at 100 ºC) demonstrating bulk failure characteristics

4.6.2 HCF fracture surface features of Sn-Cu-Ni

It has been stated that the majority of fracture paths under high-cycle fatigue in Sn-Cu-Ni were through the bulk of the solder. A case study of this for joint number 161 (25 ºC, Cu substrate) is given in Figure 4.78, which shows micrographs from various sites on the fracture surface. The probable phases of the fracture process (slow fatigue crack growth, fast/unstable crack growth and fast fracture/overstress failure) are indicated along with microstructural evidence for their classifications. The significant void present near the edge of the joint (Figure 4.78, Image A) is a very likely site for fatigue initiation since it represents a stress concentration. A void was again implicated in the fatigue initiation site of joint 301. Joint 302 (Figure 4.79), which was soldered to Ni, also shows failure almost entirely through the bulk solder; this example is representative of the appearance of other Ni-soldered joints. A fractograph from rod 257, which was tested at 100 ºC on a Cu substrate, is shown in Figure 4.80. Its features and those of other fracture surfaces from elevated temperature tests do not appear significantly different from those conducted at room temperature. Bulk failure still dominates, with small areas of clean interfacial IMC/solder separation, although little evidence of cyclic markings is found. This could be due to the lower yield strength of the solder at elevated temperature; sharp surface features will be less likely due to increased plasticity around the crack tip.

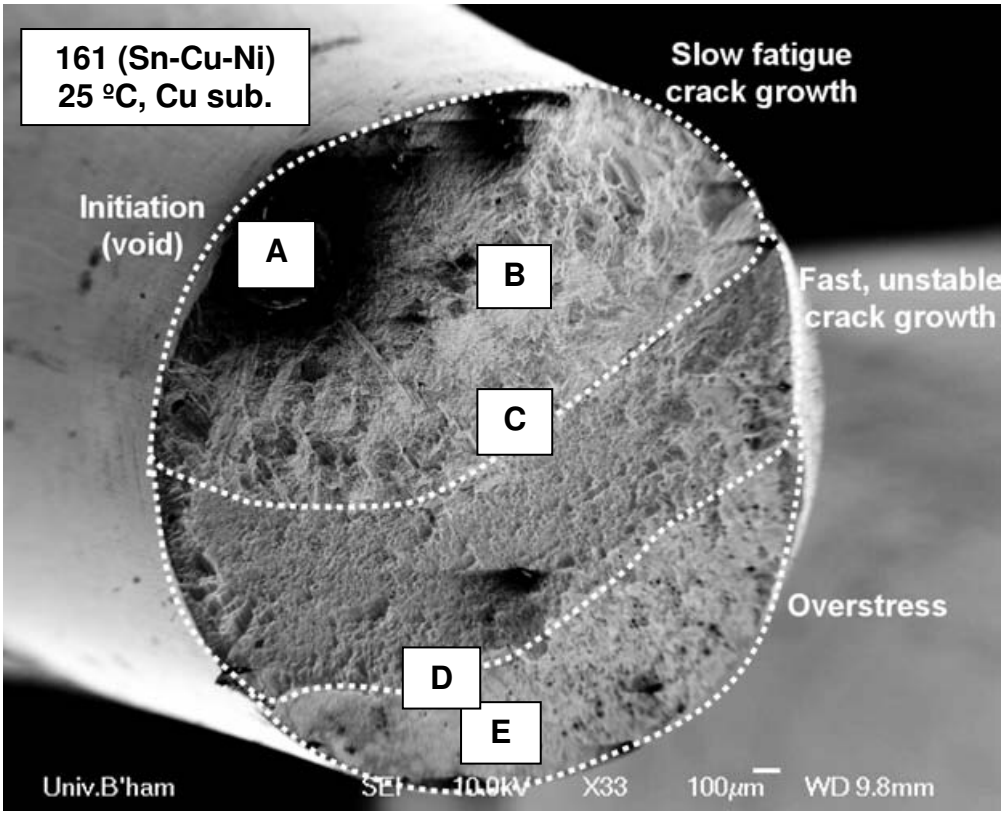

Figure 4.78. Secondary electron image of Sn-Cu-Ni HCF fracture surface of rod 161 (tested at 25 ºC on Cu substrate) showing demarcations of probable stages of failure

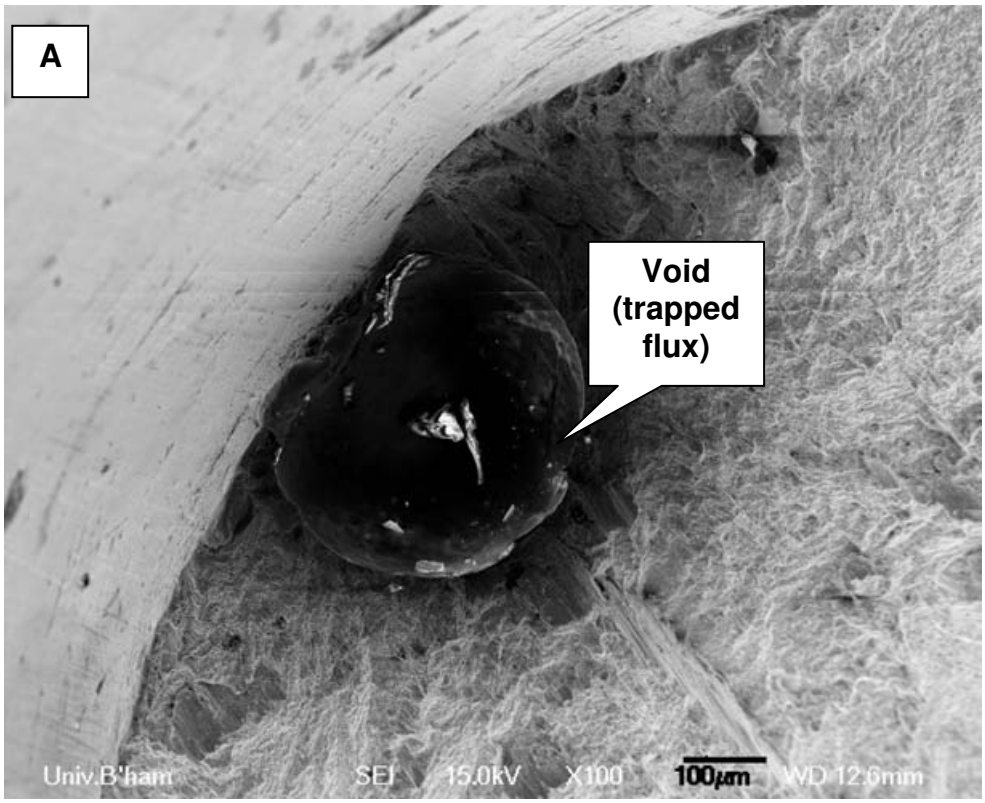

Secondary electron micrograph of zoomed area A from rod 161 showing probable fatigue initiation point – stress concentration around a void (from a trapped flux bubble)

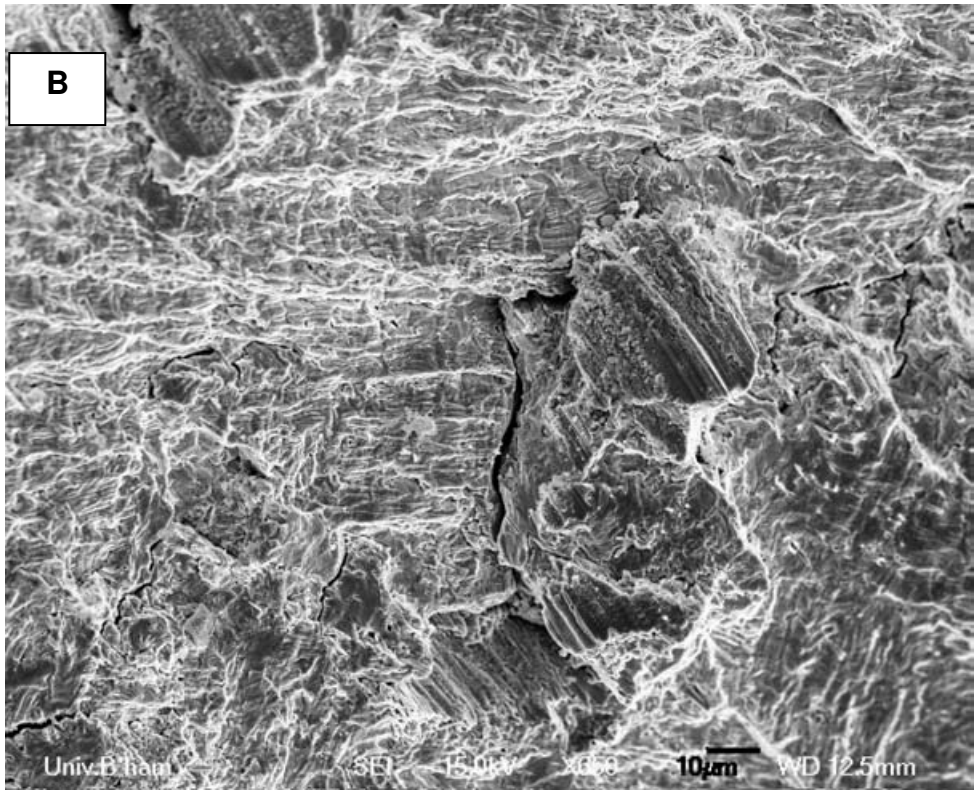

Secondary electron micrograph of zoomed area B from rod 161 showing probable slow fatigue crack growth zone through bulk solder. Rough, three-dimensional morphology and evidence of intergranular or inter-colonial cracking

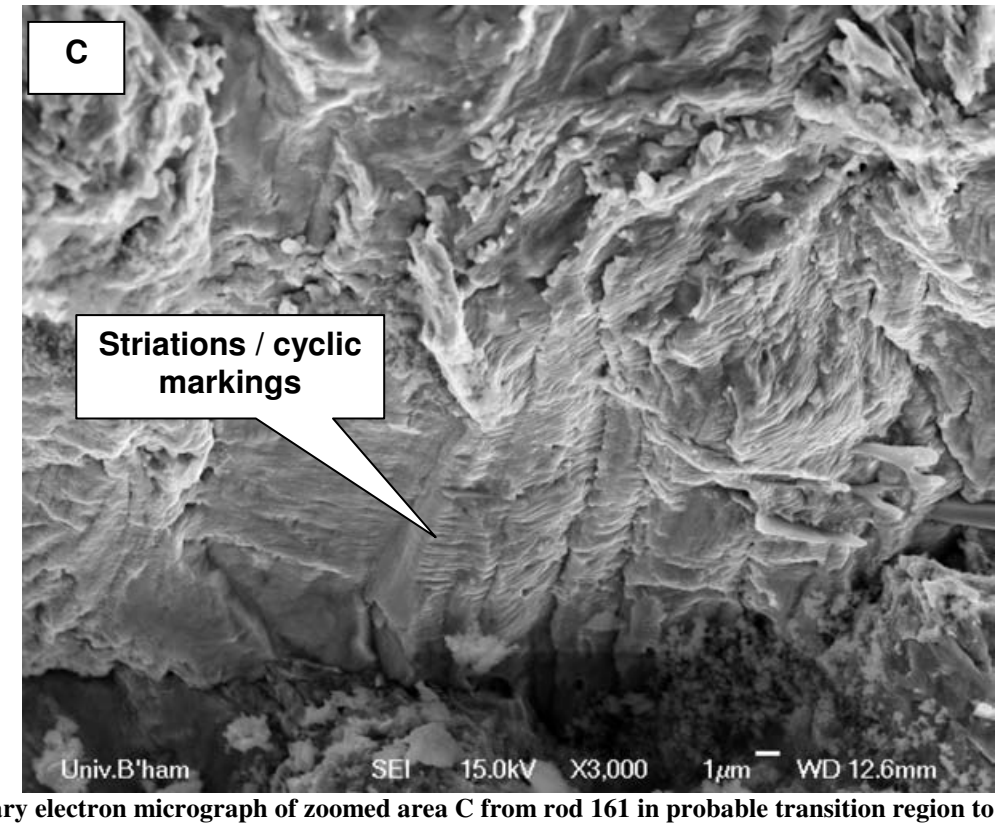

Secondary electron micrograph of zoomed area C from rod 161 in probable transition region to unstable fatigue crack growth showing development of cyclic markings on fracture surface

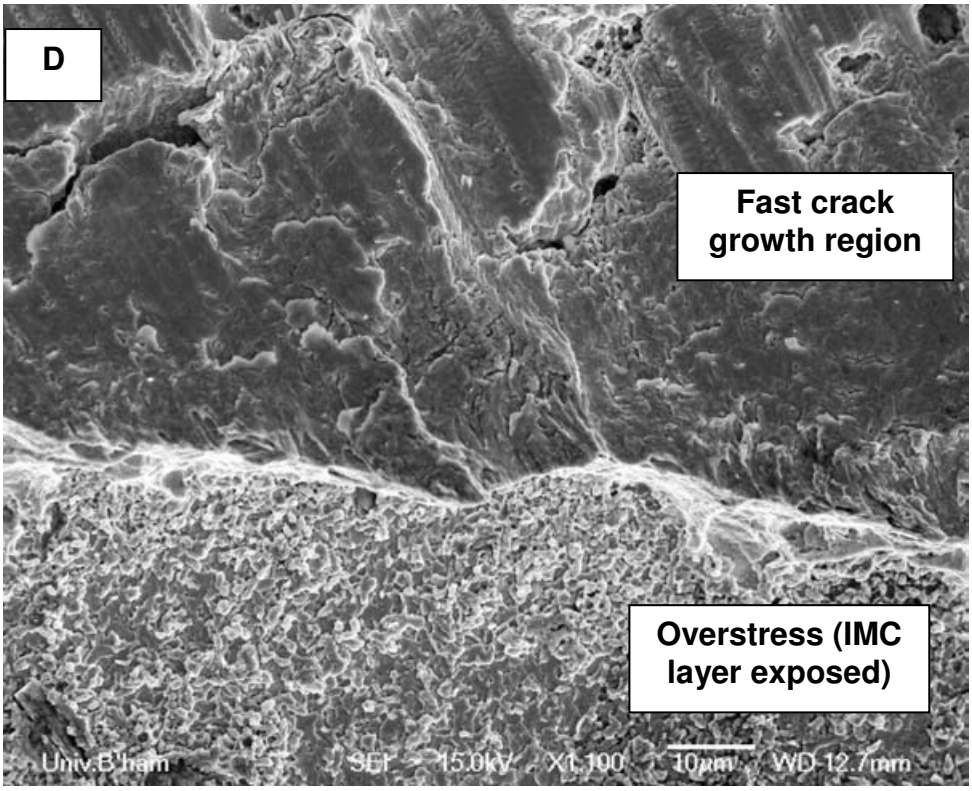

Secondary electron micrograph of zoomed area D from rod 161 showing transition from fast fatigue crack growth to overstress (yield strength of joint exceeded) which resulted in fracture at IMC/solder interface

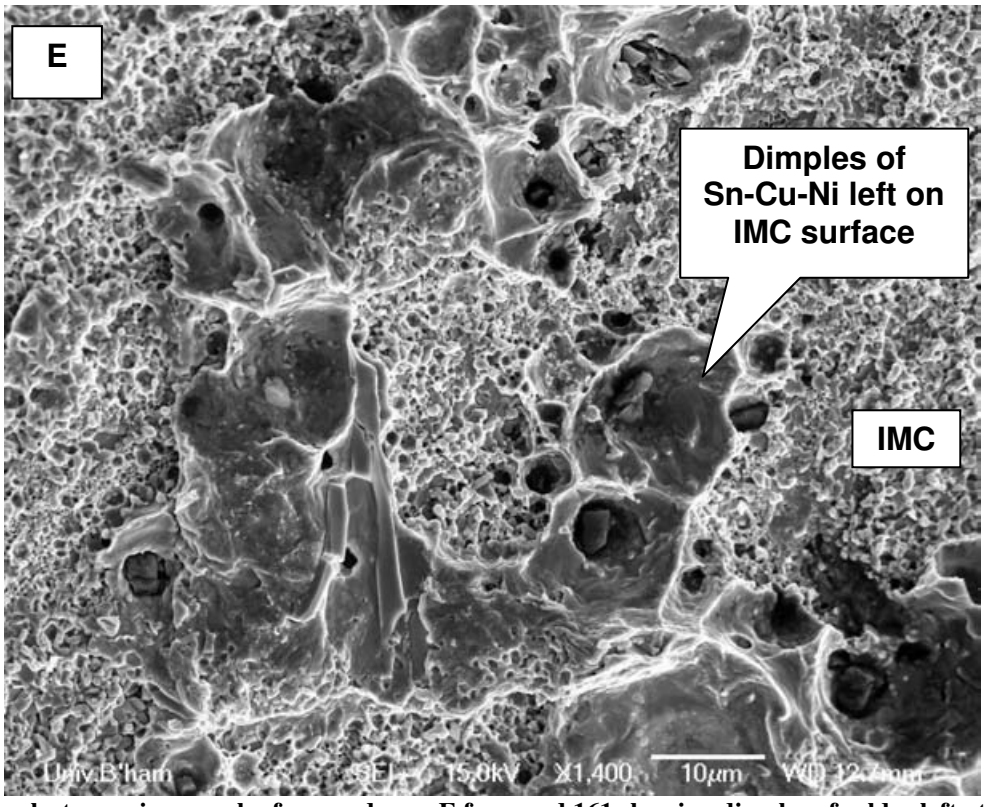

Secondary electron micrograph of zoomed area E from rod 161 showing dimples of solder left attached to IMC layer in overstress failure region

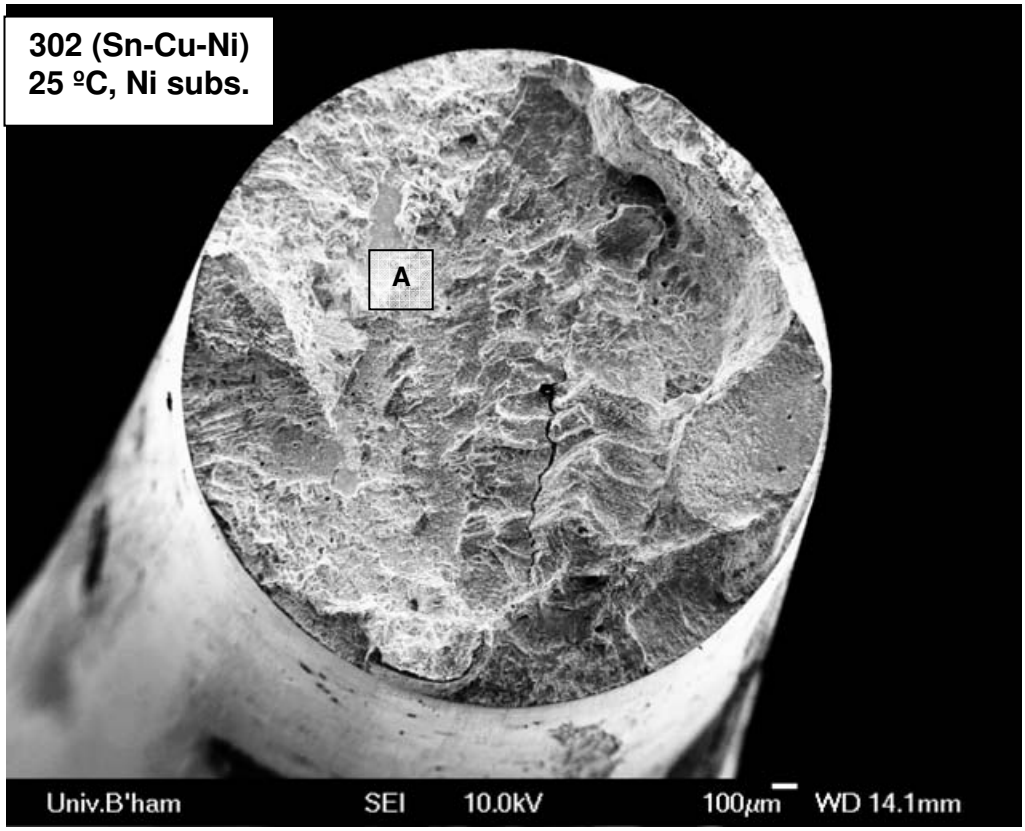

Figure 4.79. Secondary electron micrograph of Sn-Cu-Ni HCF fracture surface (tested at 25 ºC, Ni substrate) showing fracture through bulk solder with no obvious initiation point

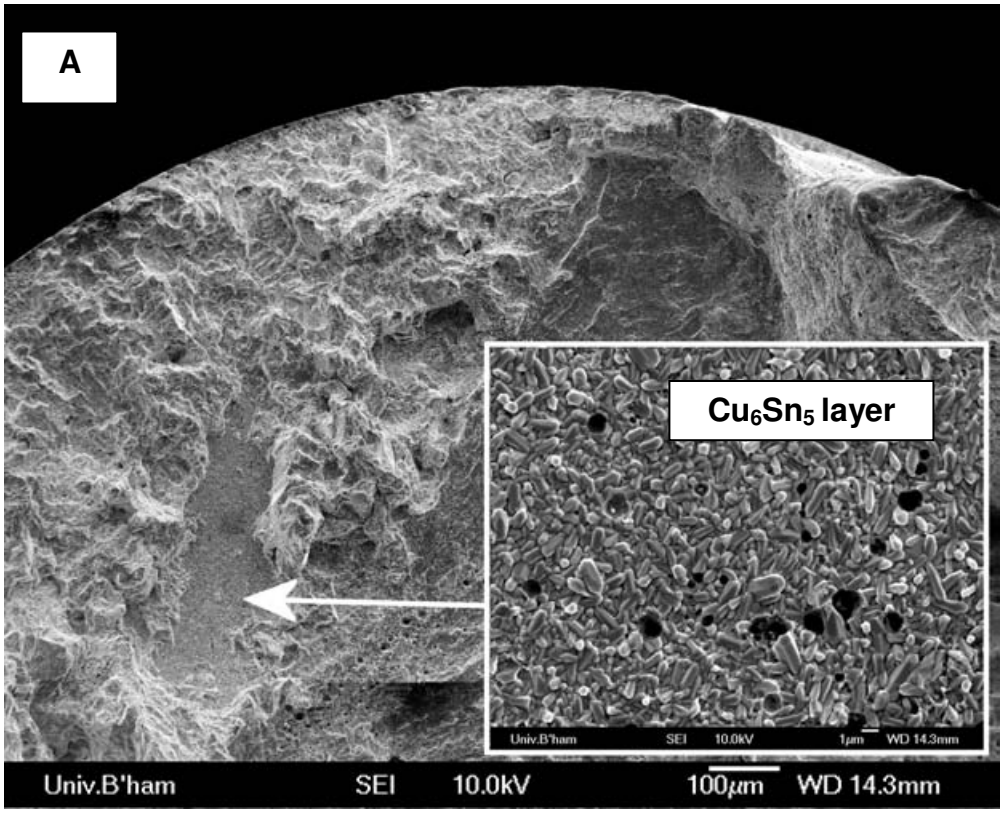

Secondary electron micrograph of zoomed area A from rod 302 showing small region of IMC/solder separation among general bulk failure

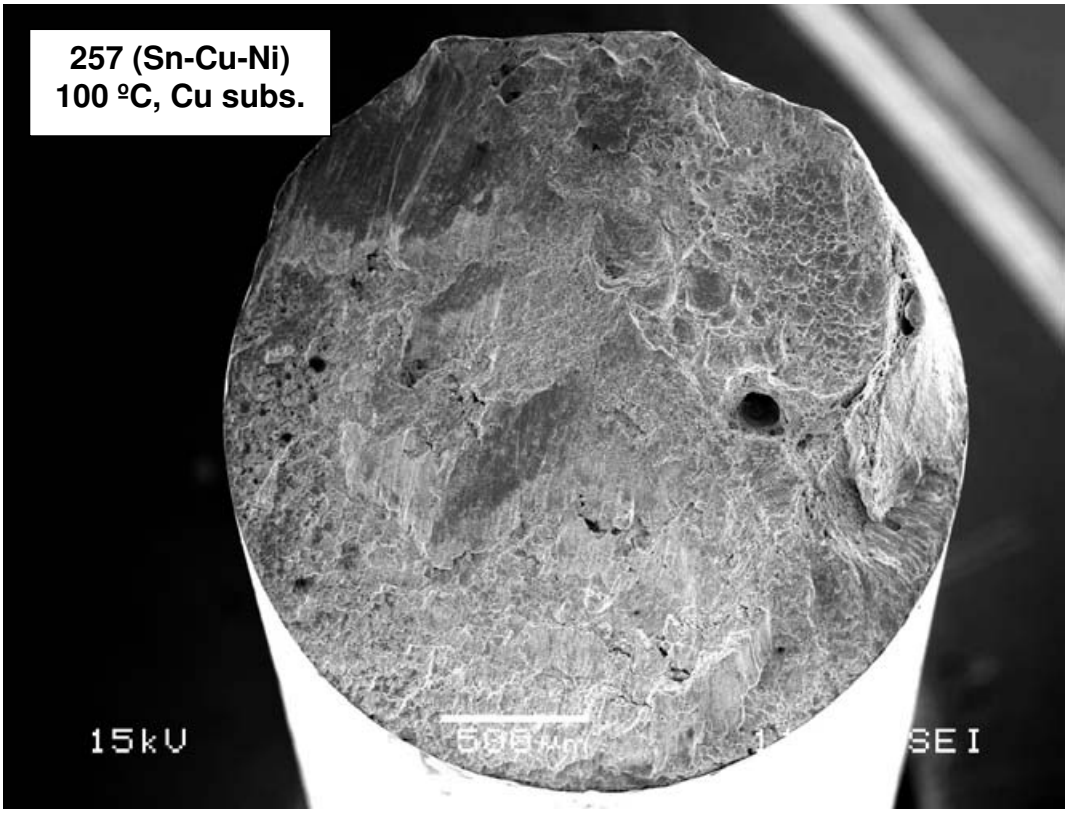

Figure 4.80. Secondary electron micrograph of Sn-Cu-Ni HCF fracture surface of rod 257 (tested at 100 ºC, Cu substrate) showing failure through bulk solder

4.6.3 HCF fracture surface features of SAC305

In the case of joints tested at 25 ºC with Cu substrates the majority of SAC305 joints demonstrate interfacial or near-interfacial fracture. Such an example is shown in Figure 4.81 for rod 45. Fatigue would seem to initiate from the outer edge of the solder joint, close to or at the solder/substrate interface. It then progresses into the joint section between the solder and the Cu_6Sn_5 layer. This process does not appear to leave any cyclic markings or debris on the surfaces and it is evidence from other areas of the fracture surface which leads to the conclusion that this area was formed during steady/slow crack growth. There is a number of small (~100 μm) voids close to the edge of the joint in this area whose stress concentrations probably helped initiate a dominant crack. Around half way across the joint section, the crack path deviates and switches to the opposite interface, where there is evidence of plastic

features such as dimples from overstress, causing a mixture of pure IMC/solder separation and separation leaving remnants or patches of solder still attached to the IMC layer. In between these two areas lies a planar region characterised by wavy 'river lines' [119] in the direction of crack growth which is found on many other SAC305 fracture surfaces in similar locations.

SAC305 joint number 56 is presented as examples of bulk type failure at 25 ºC with Cu substrate (Figure 4.82). It can be seen that even though most of the fracture path is taken through the bulk, it is often found that the final overstress fracture occurs at or near the solder/substrate interface. In these joints, voids are again found to be very likely candidates for initiating fatigue. When examining SAC305 HCF fracture surfaces still at room temperature but with Ni substrates, largely similar features are found to those obtained with Cu substrates, despite there being statistically more bulk failures (Figure 4.64). A notable exception is the discovery of fracture either between the intermetallic layer and the substrate, or possibly between different intermetallic layers themselves (e.g. Ni_3P and $(Ni,Cu)_3Sn_4$). Evidence of this is shown in the Figures for rod 331 (Figure 4.83) where EDX analysis of the fractured surfaces indicates a P content on one surface, only found in the Ni(P) substrate or very thin Ni_3P layer (Figure 4.8).

All the aforementioned fracture behaviour of SAC305 at room temperature is observed when examining fracture surfaces from joints tested at 100 ºC. One difference is the interesting appearance of the fracture surface in the area identified as being responsible for fatigue initiation in rod 185. The grain boundaries of Sn are clearly visible, along with the distribution of fine Ag_3Sn particles along the boundaries and in eutectic Sn + Ag_3Sn regions. The rounded, undulating relief of this region is also noteworthy. It is in contrast to that of the other regions in which the microstructure of the SAC305 alloy is seen, namely that of the

planar fast/unstable crack growth regions identified in (Figure 4.82). Another difference is observed incidence of intergranular cracking in some joints tested at 100 ºC, although since this is predominantly found in the final failure areas, responsible for only a tiny fraction of the joint lifetime, it is thought to be of little consequence.

To summarise, then, high-cycle fatigue failure in SAC305 joints often appears to nucleate from voids, whether internal or close to the edge, although not in all cases. The initial path of the fatigue crack takes either a radial route away from the void or other initiation point through the bulk solder, or a path through or very close to the solder/IMC layer interface (possibly through an IMC/IMC or IMC/substrate interface with Ni substrates). When this fatigue crack has spread across a significant proportion of the joint area (less in the case of high temperature tests) it switches to an interfacial or near-interfacial failure (in the case of a bulk initial path), with a transition region often indicated by a planar, transgranular morphology, or continues along or near the interface. This final region of overstress (whether the stress in the remaining intact area exceeds the yield strength) is often characterised by dimples (formed by coalesced microvoids) or remnants of solder left on the IMC layer.

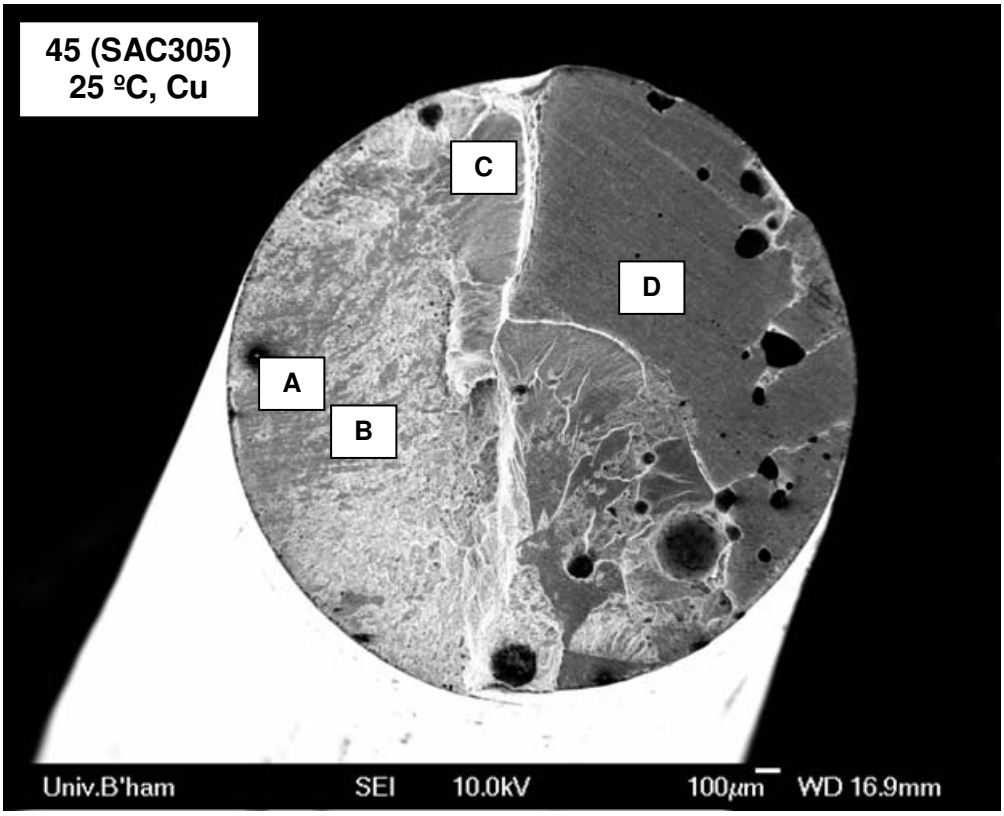

Figure 4.81. Secondary electron micrograph of SAC305 HCF fracture surface (tested at 25 ºC, Cu substrate) showing predominantly interfacial failure

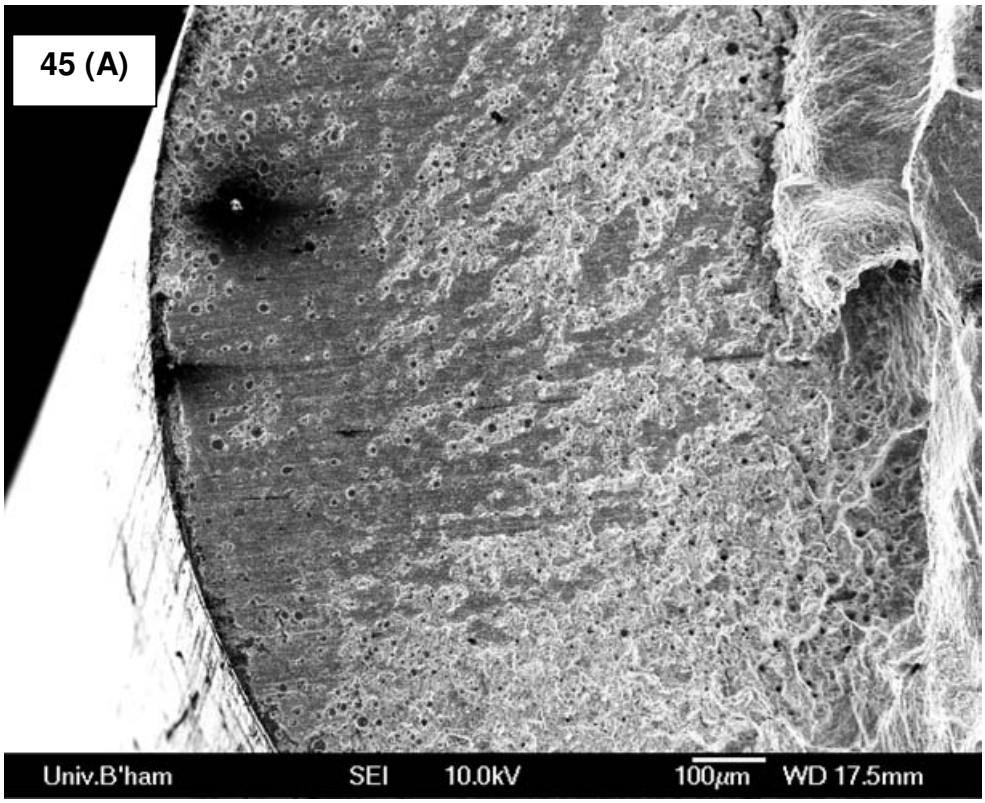

Secondary electron micrograph of zoomed area A from rod 45 showing mixed region of interfacial separation and dimples indicating a probable overstress region causing a fracture path either at or very close to the solder/IMC interface

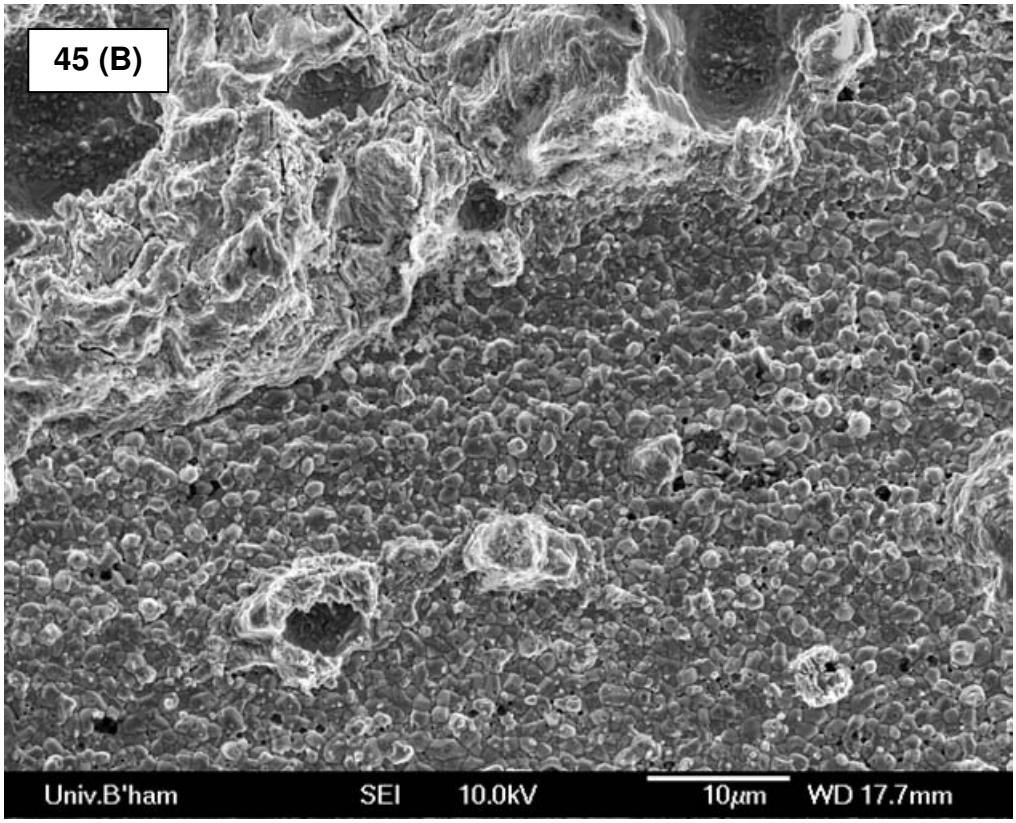

Secondary electron micrograph of zoomed area B from rod 45 showing mixed fracture at IMC and bulk solder in probable overstress region

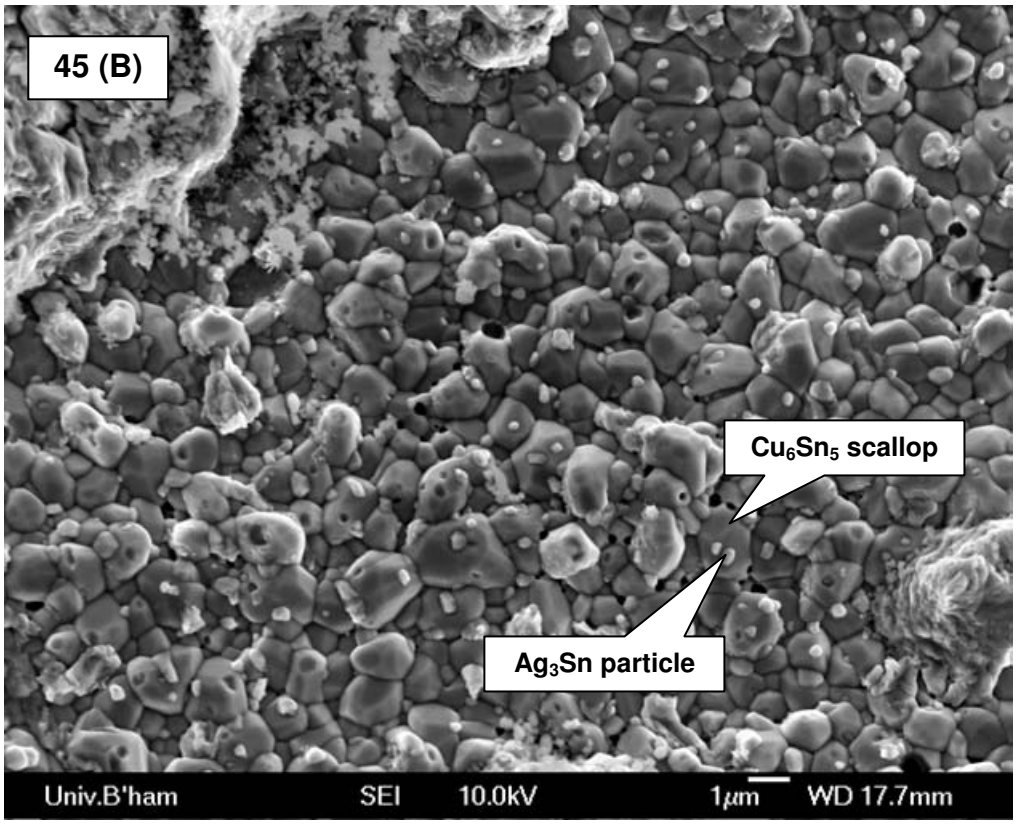

Secondary electron micrograph of zoomed area B from rod 45 showing close-up of fracture at IMC/solder interface

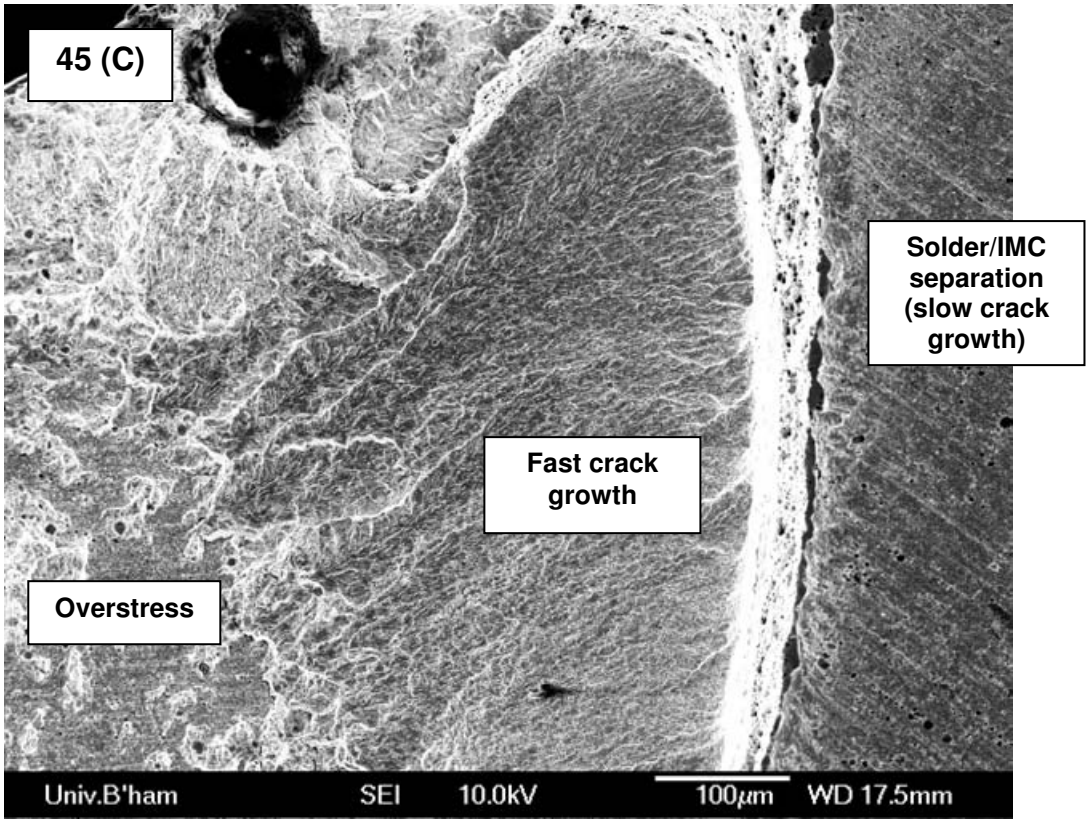

Secondary electron micrograph of area C from rod 45 showing transition from interfacial failure to probable fast crack growth region

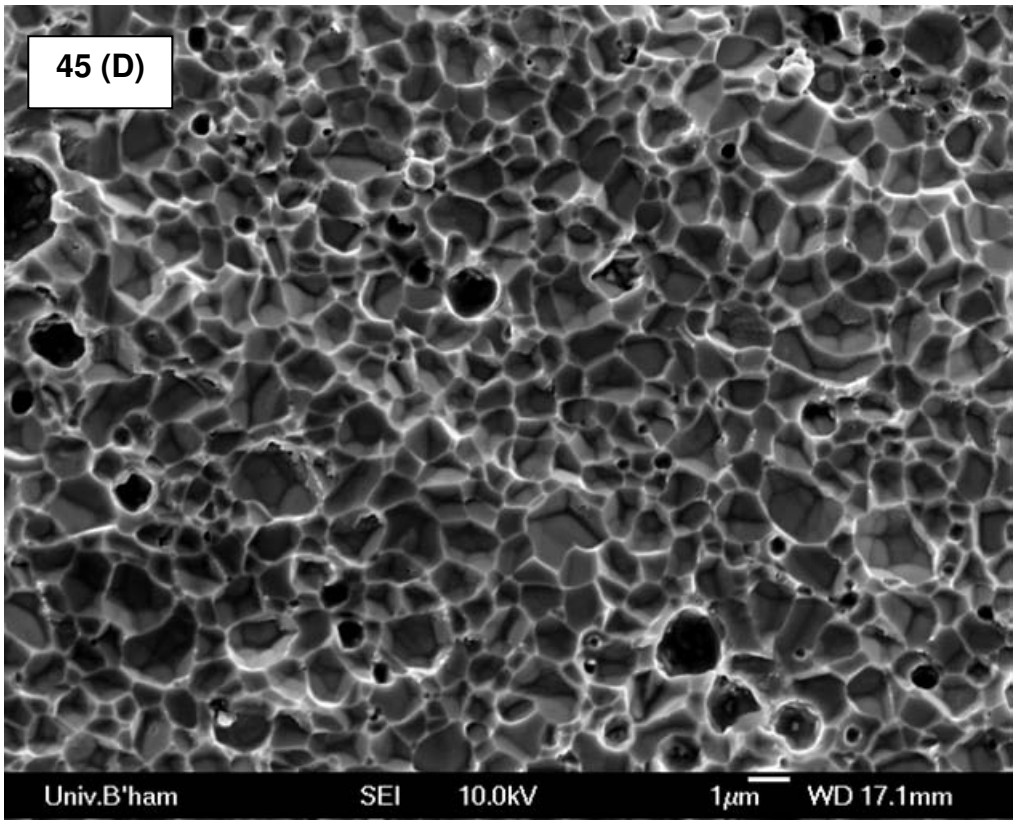

Secondary electron micrograph of area D from rod 45 showing solder bearing imprint from IMC layer of opposing fracture surface – crack has separated the two layers cleanly

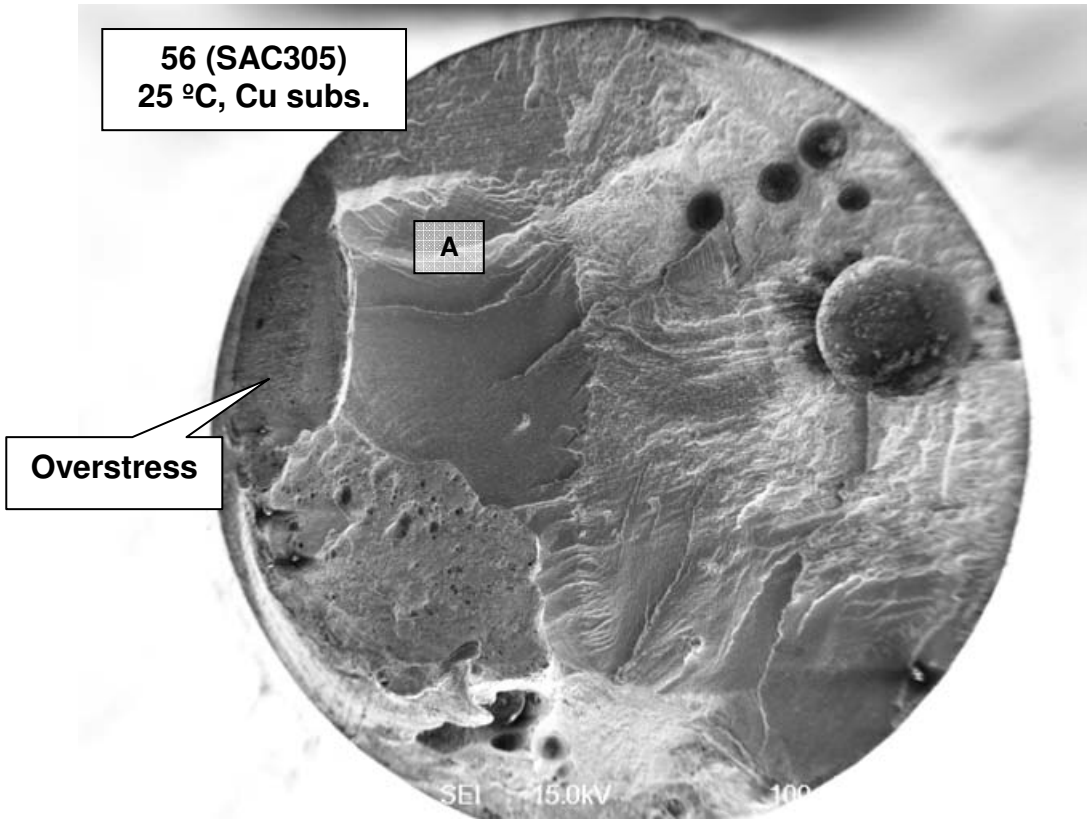

Figure 4.82. Secondary electron micrograph of SAC305 HCF fracture surface from rod 56 (tested at 25 ºC, Cu substrate) showing bulk failure, probably originating from void, and large plane of failure

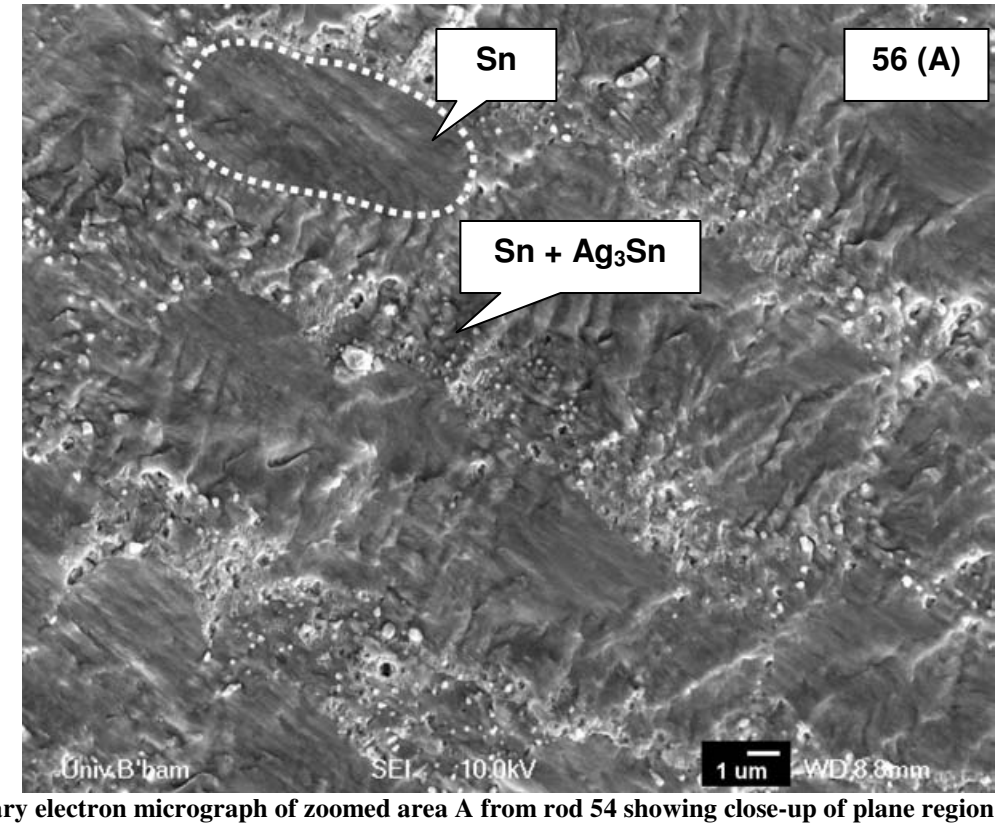

Secondary electron micrograph of zoomed area A from rod 54 showing close-up of plane region of fracture surface. Crack has propagated in transgranular manner, exposing cross-section of Sn and Sn + Ag_3Sn eutectic network structure

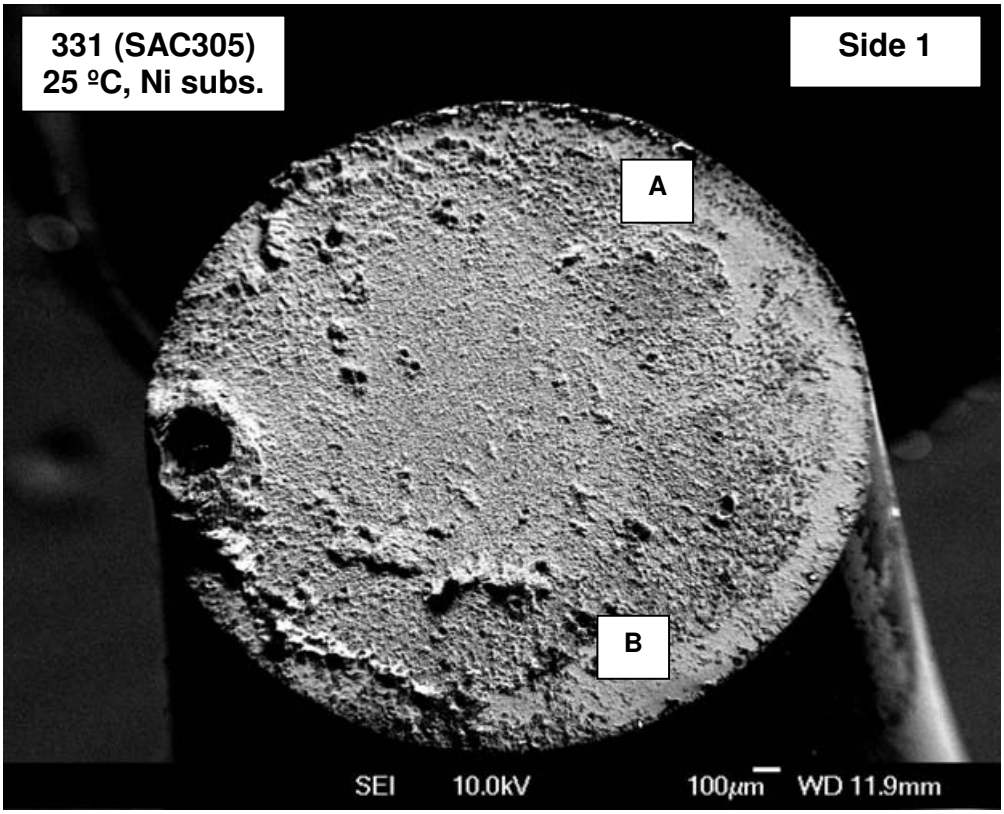

Figure 4.83. Secondary electron micrograph of SA305 HCF fracture surface of rod 331 (tested at 25 ºC, Ni substrate) showing near-interfacial fracture over entire area

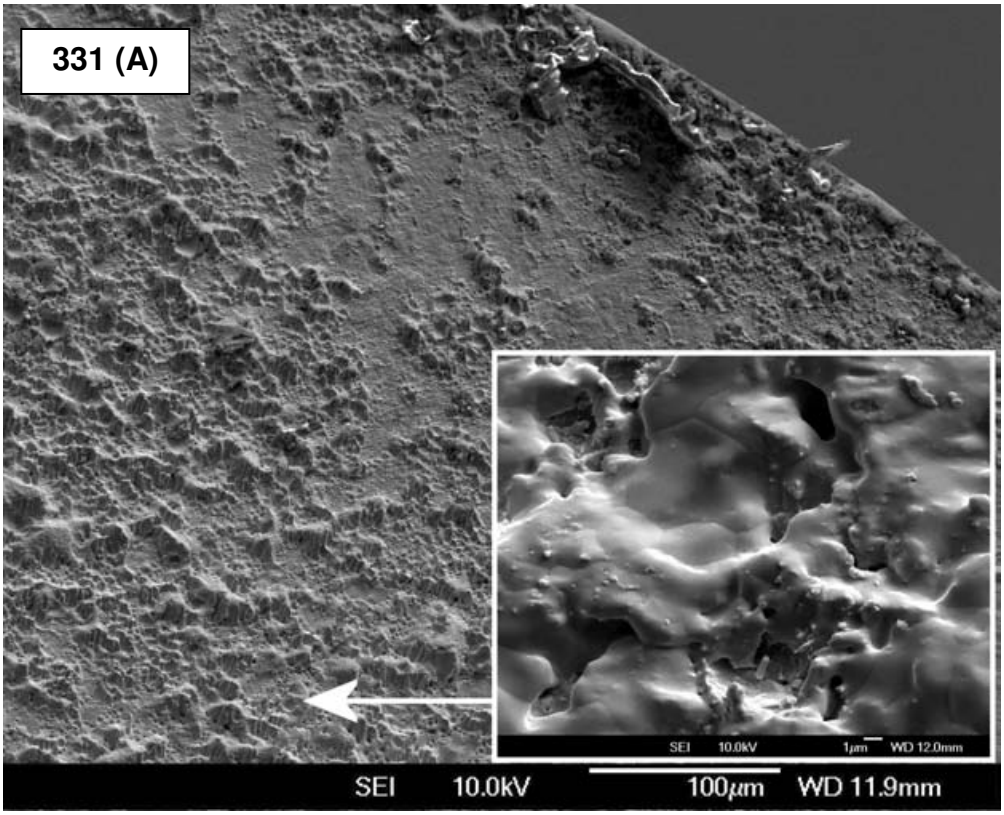

Secondary electron micrograph of zoomed area A from rod 331showing remnants of SAC305 over (Ni,Cu)-Sn IMC layer (inset magnified)

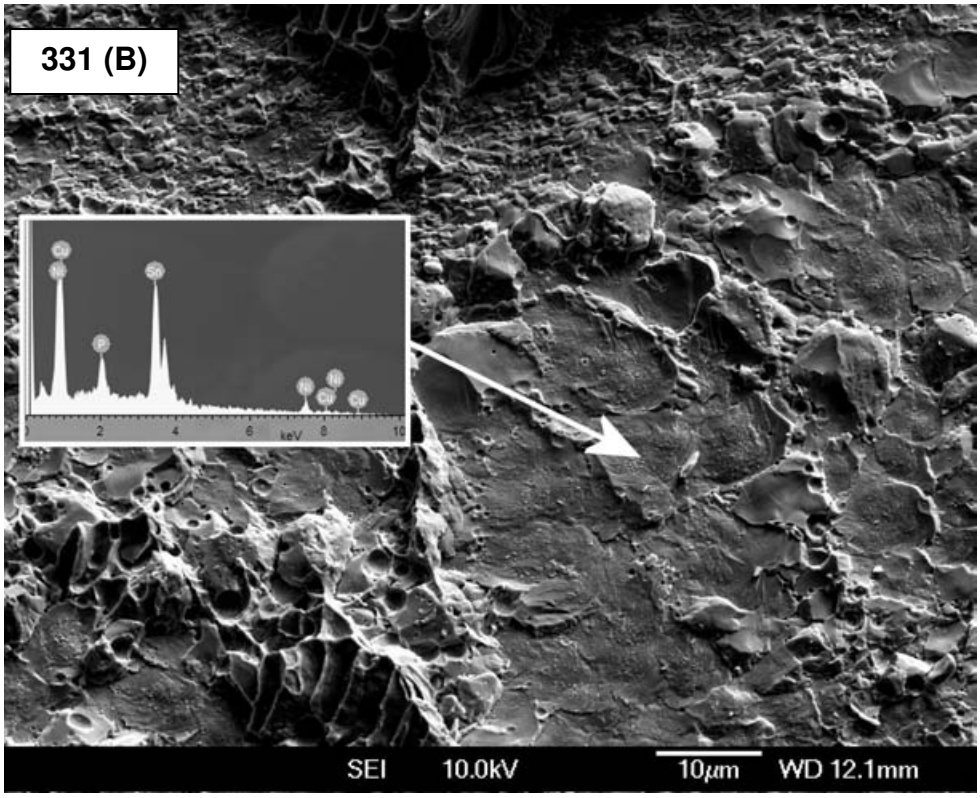

Secondary electron micrograph of zoomed region B from rod 331 (inset EDX spectrum from indicated point) showing significant Ni and P content; flattened surface is likely to be either Ni(P) substrate or thin Ni-P IMC layer revealed by fracture of overlying (Ni,Cu)-Sn IMC layer

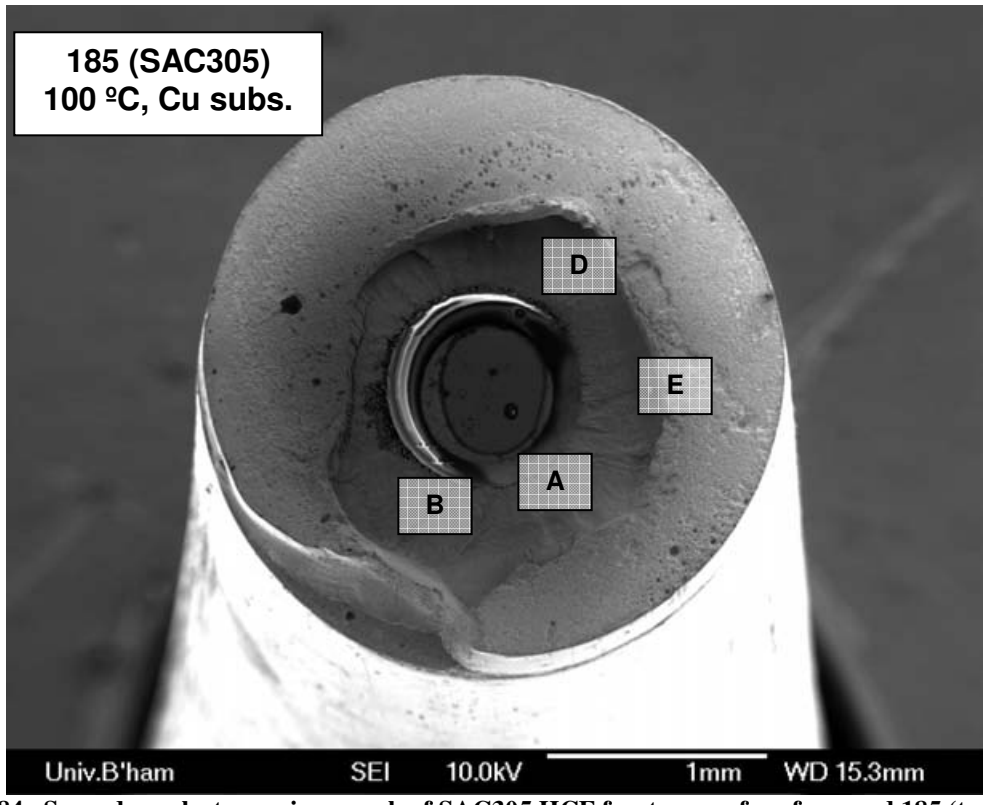

Figure 4.84. Secondary electron micrograph of SAC305 HCF fracture surface from rod 185 (tested at 100 ºC, Cu substrate) showing fatigue failure initiating from large internal void (note: this lifetime of this specimen was very close other, un-voided specimens in its batch)

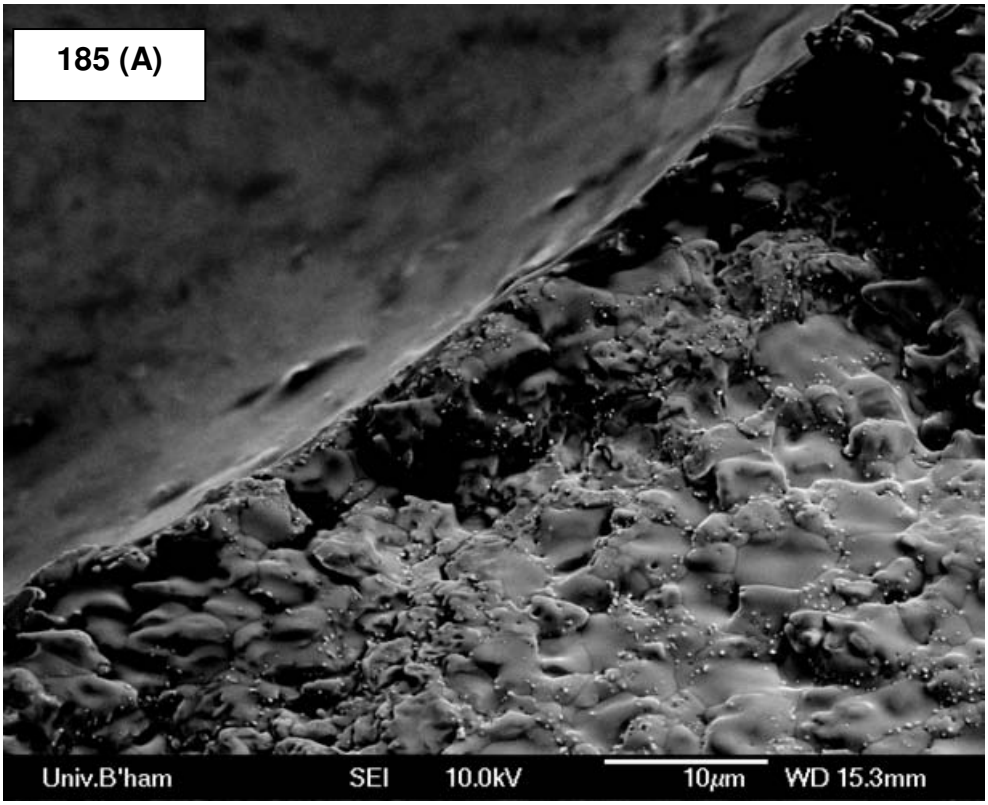

Secondary electron micrograph of zoomed area A from rod 185 showing fatigue initiation area at edge of void. Note transgranular crack path leaving smooth surface

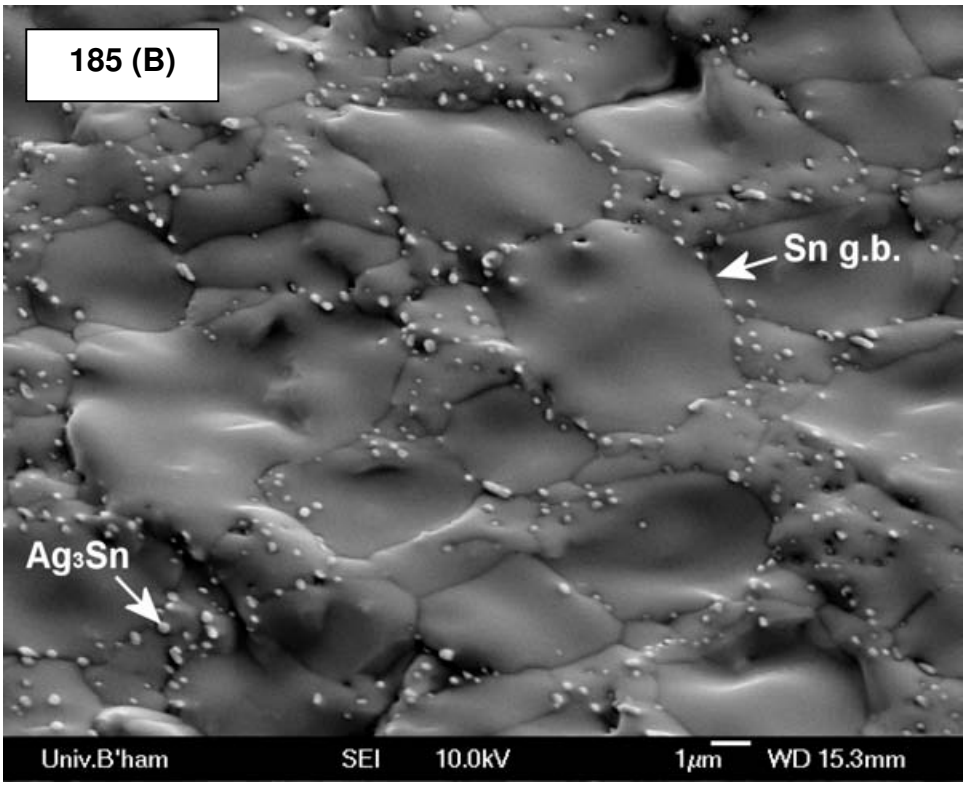

Secondary electron micrograph of zoomed area B from rod 185 showing fracture surface immediately adjacent to internal void where fatigue has initiated from. Crack has revealed grain structure of SAC305 showing fine Ag_3Sn particles residing in eutectic regions and on grain boundaries

Secondary electron micrograph of zoomed area C from rod 185 showing flat transgranular crack growth area. Striations shown of approx. 0.3 μm spacing with eutectic regions disrupting striation pattern but not bowing advancing crack front

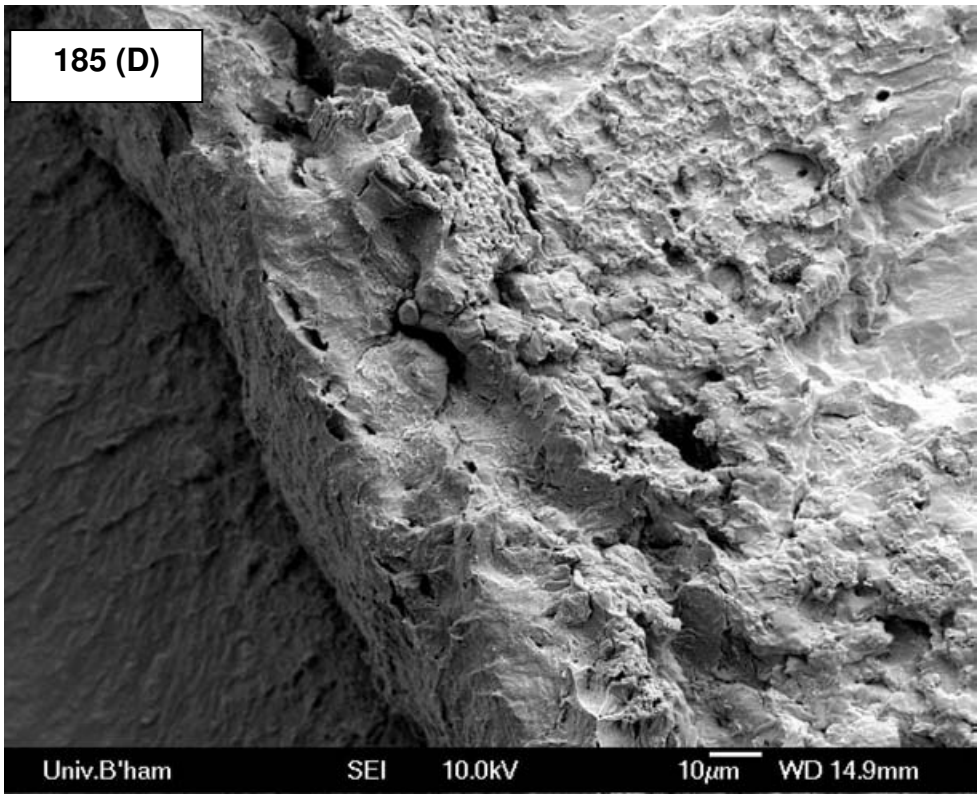

Secondary electron micrograph of zoomed area D from rod 185 showing lip where fracture path emerges from bulk onto interface whereby morphology becomes rougher with evidence of intergranular cracking and tearing

4.6.4 HCF fracture surface features of Innolot

Only room temperature tests with Cu substrates were conducted with this alloy due to its late inclusion in the present work. Despite the large scatter in lifetimes for the same applied stress, the Innolot fracture surfaces conformed to a 'shallow notch' appearance almost without exception (Figure 4.65). Fatigue is shown to initiate from free surfaces, voids or dendritic porosity, and advance in early stages in a transgranular manner, leaving often flat and angular fracture planes behind (Figure 4.85, Figure 4.86). The transition between slow crack growth and overstress regions is not as clear as with the other alloys in the present work. Final fracture due to overstress is shown to overwhelmingly occur between the $(Cu,Ni)_6Sn_5$ layer and the bulk solder. A feature seen exclusively with the Innolot alloy is the large (>10 μm) Ag_3Sn plate-like structures which have grown from the $(Cu,Ni)_6Sn_5$ layer and stay attached during final overstress failure. These intermetallic structures are sometimes found around the notch transition itself. The case study of rod 283 (Figure 4.86) demonstrates unequivocally the fracture path of one Innolot joint from initiation to failure, aided by clear striations whose increasing pitch show the direction of the fatigue crack. The flat, angular appearance of the Innolot fracture surfaces from early stages of crack growth (Figure 4.87) are in contrast to those commonly seen for the other alloys in the present work and are seemingly unrelated to the grain or colony structure of the alloy.

In summary, the high-cycle fatigue fracture surfaces of Innolot are found to be more consistent than those of the other alloys tested, possessing a characteristic macroscopic appearance and clearer fracture surface features.

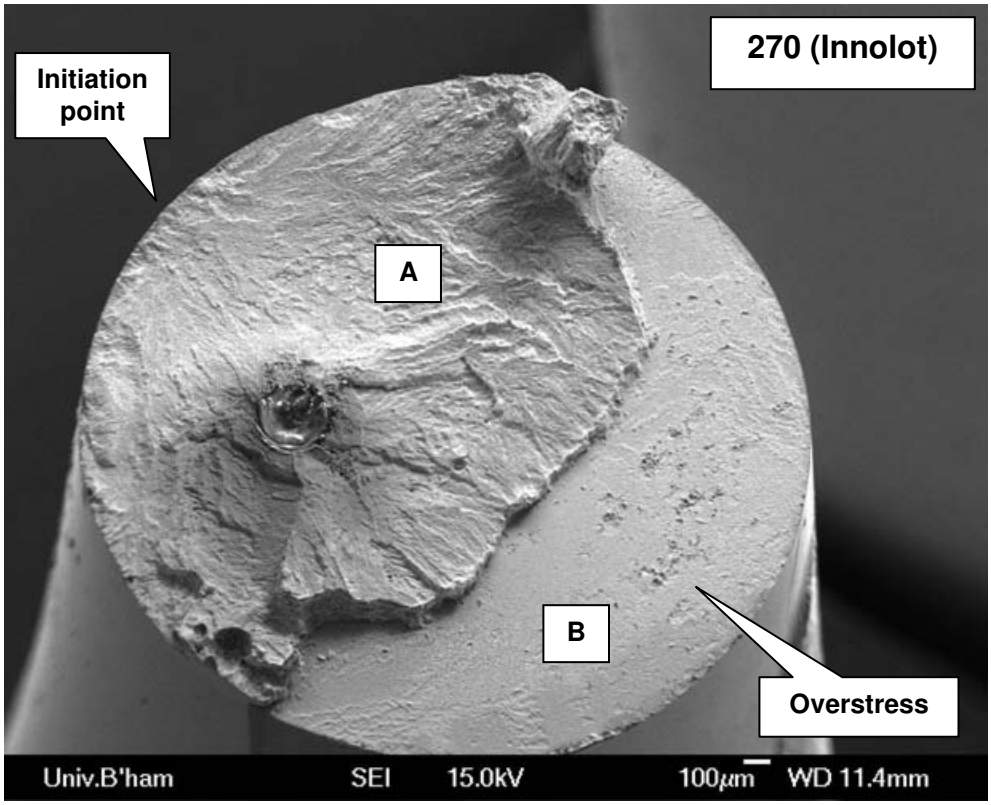

Figure 4.85. Secondary electron micrograph of Innolot HCF fracture surface from rod 270 showing typical shallow notch failure morphology. Small internal void visible in crack growth region but surface markings seem to show fatigue originating from edge rather than this feature

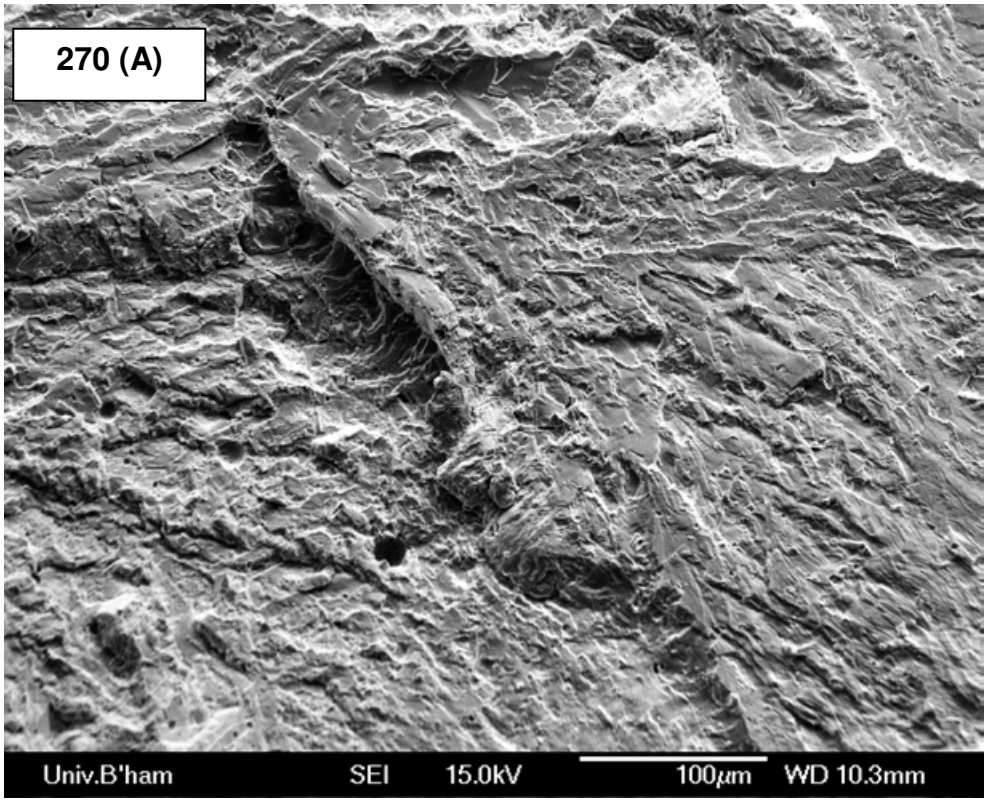

Secondary electron micrograph of zoomed area A from rod 270 showing typical surface appearance of crack growth region

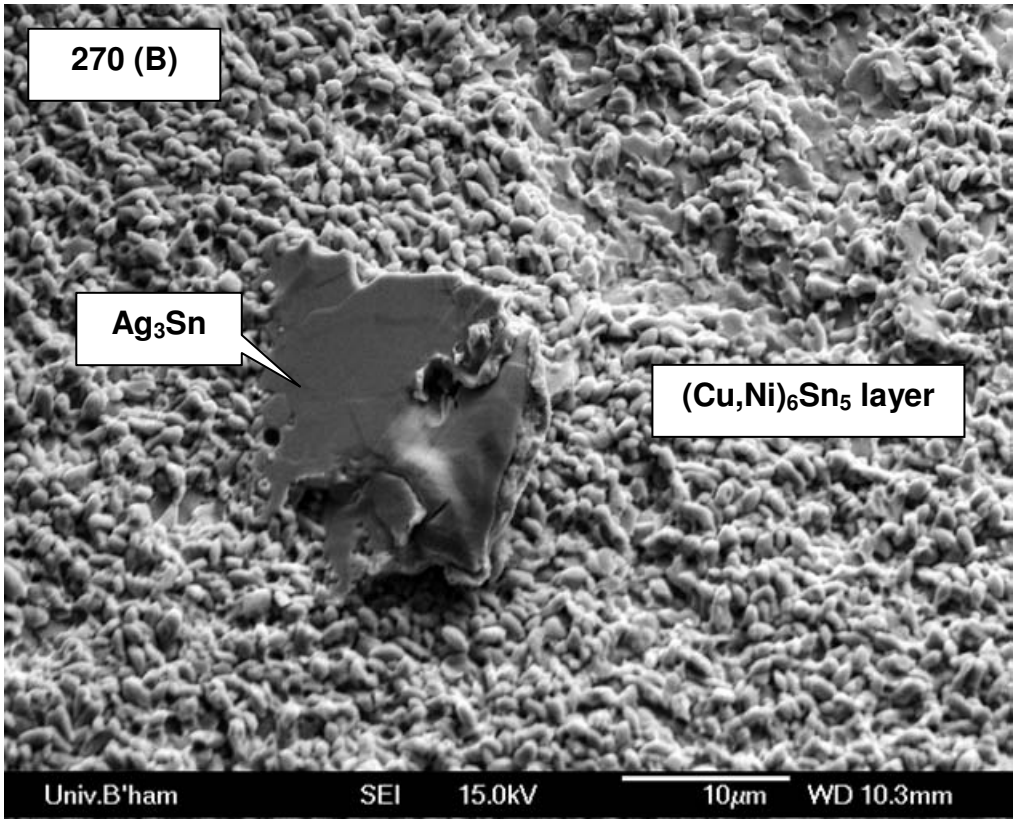

Secondary electron micrograph of zoomed area B from rod 270 showing appearance of overstress region; generally clean separation between IMC layer and solder with protruding Ag_3Sn features

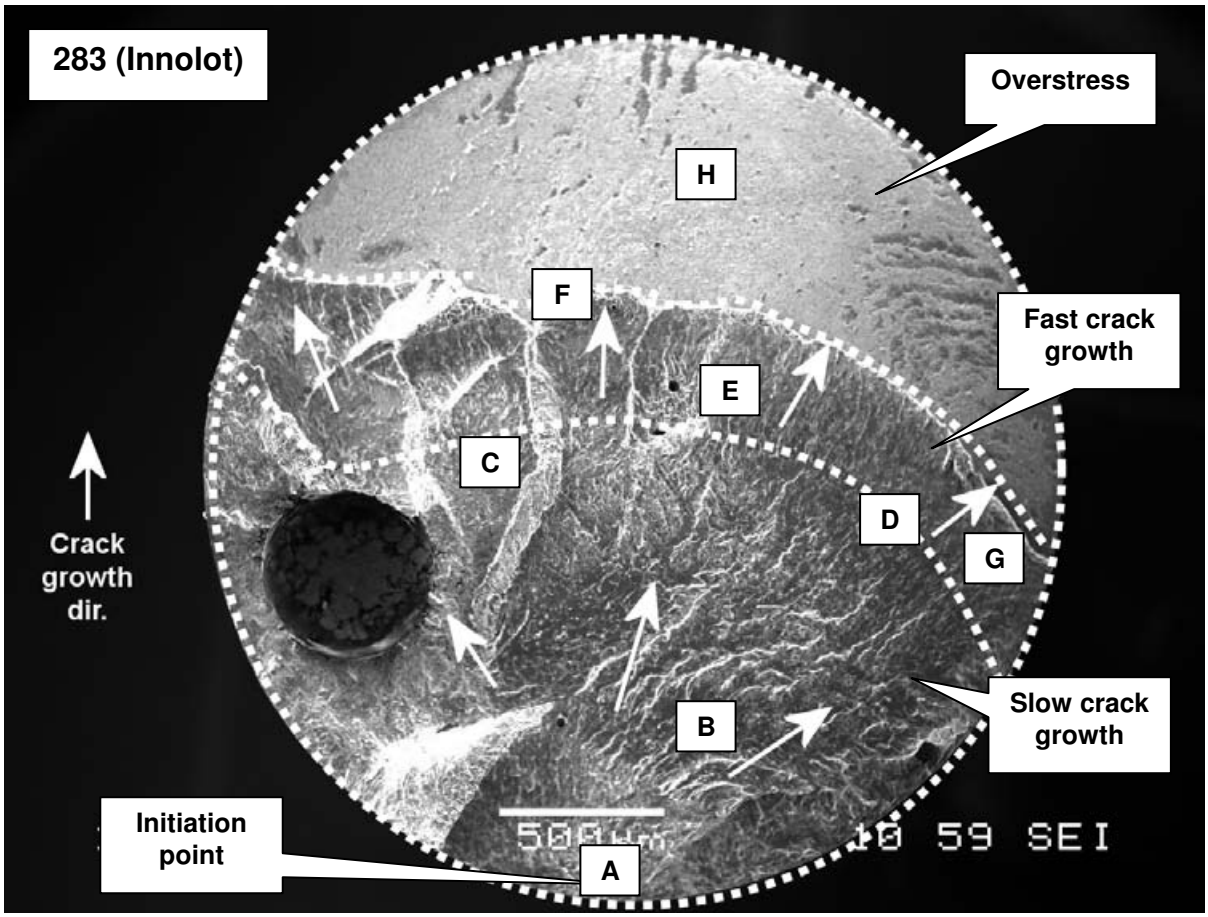

Figure 4.86. Secondary electron micrograph of Innolot HCF fracture surface from rod 283 (shallow notch type failure) showing phases of fatigue failure

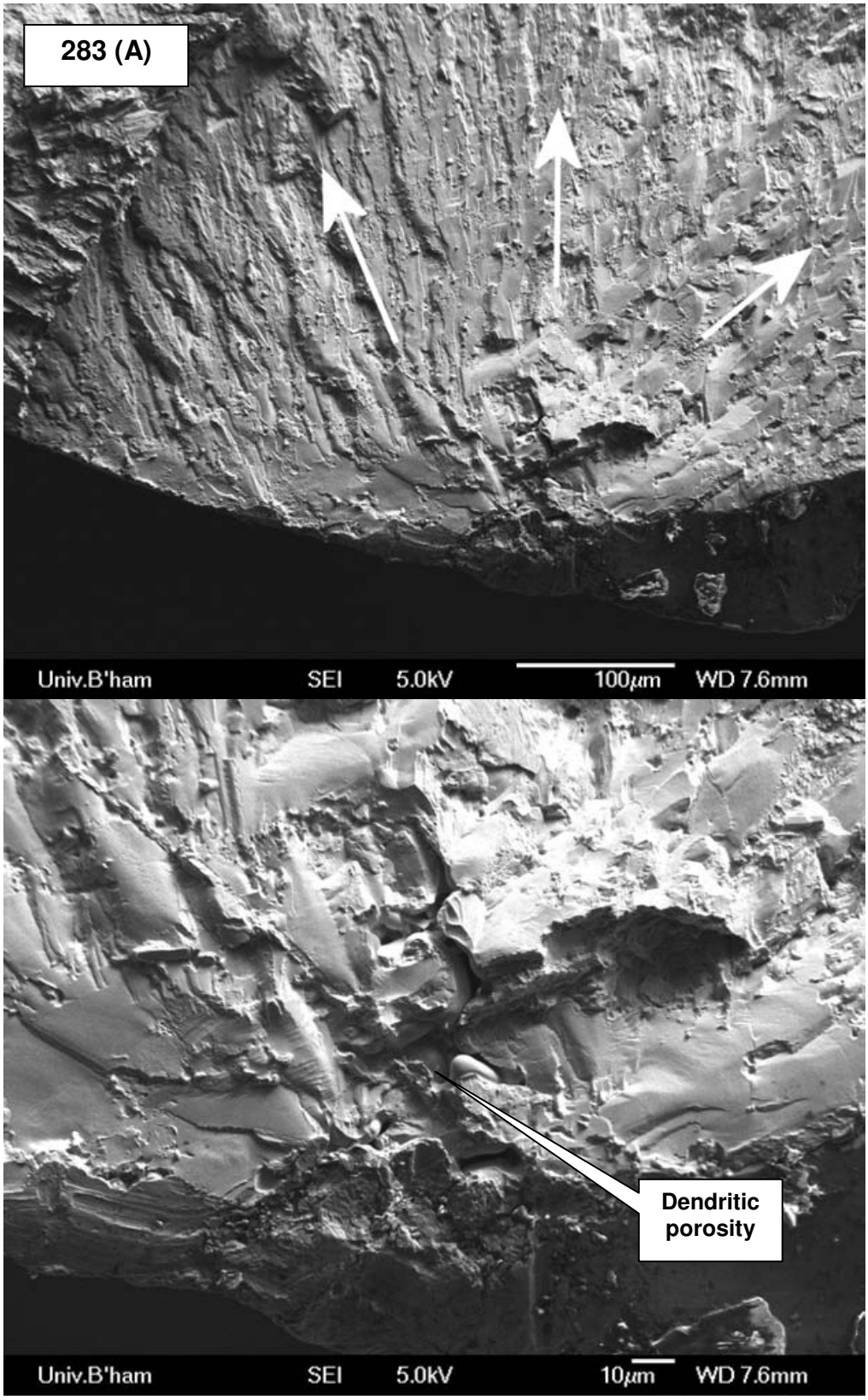

Secondary electron micrographs of zoomed area A from rod 283 showing fatigue initiation point at edge of joint: dendritic porosity (bottom image magnified)

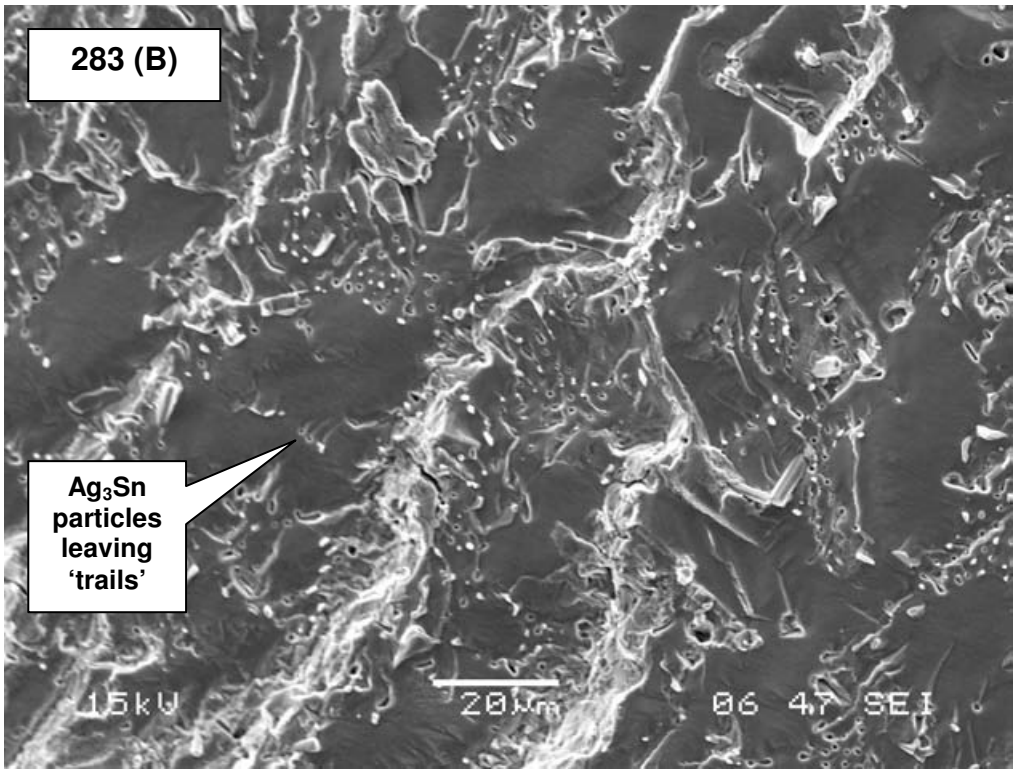

Secondary electron micrograph of zoomed area B from rod 283 showing slow crack growth area consisting of small flat planes of Sn interspersed with ridges and intermetallic particles showing signs small trails behind them, possibly from being dislodged or otherwise disturbed during crack growth

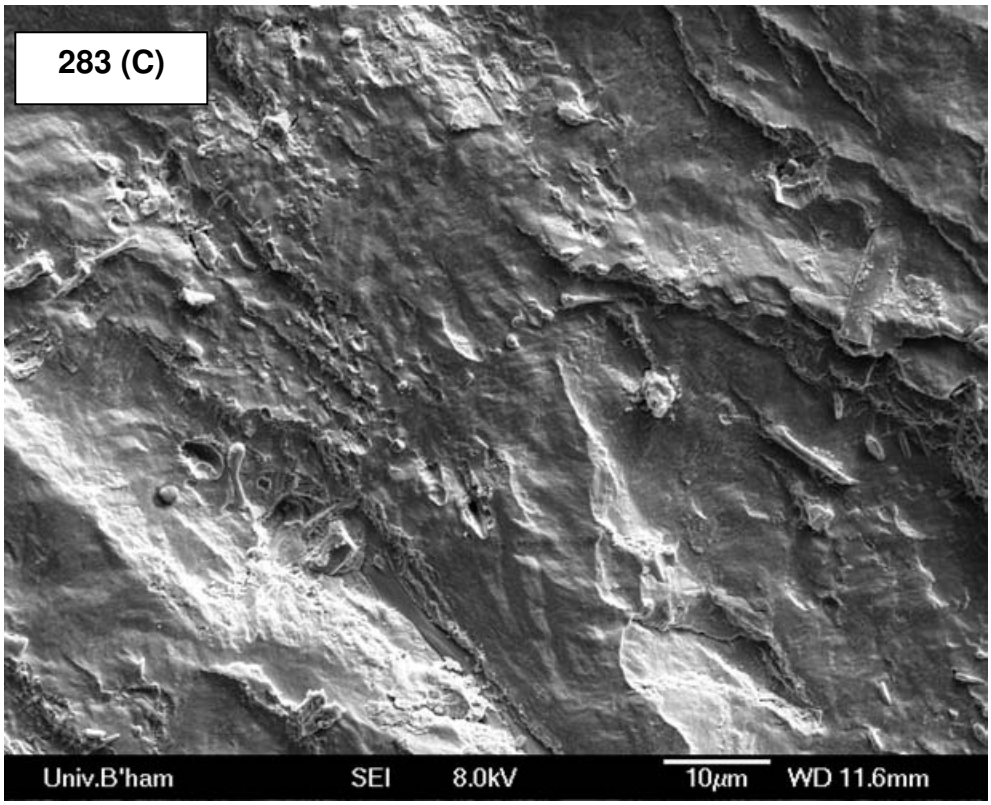

Secondary electron micrograph of zoomed area C from rod 283 showing slow crack growth region

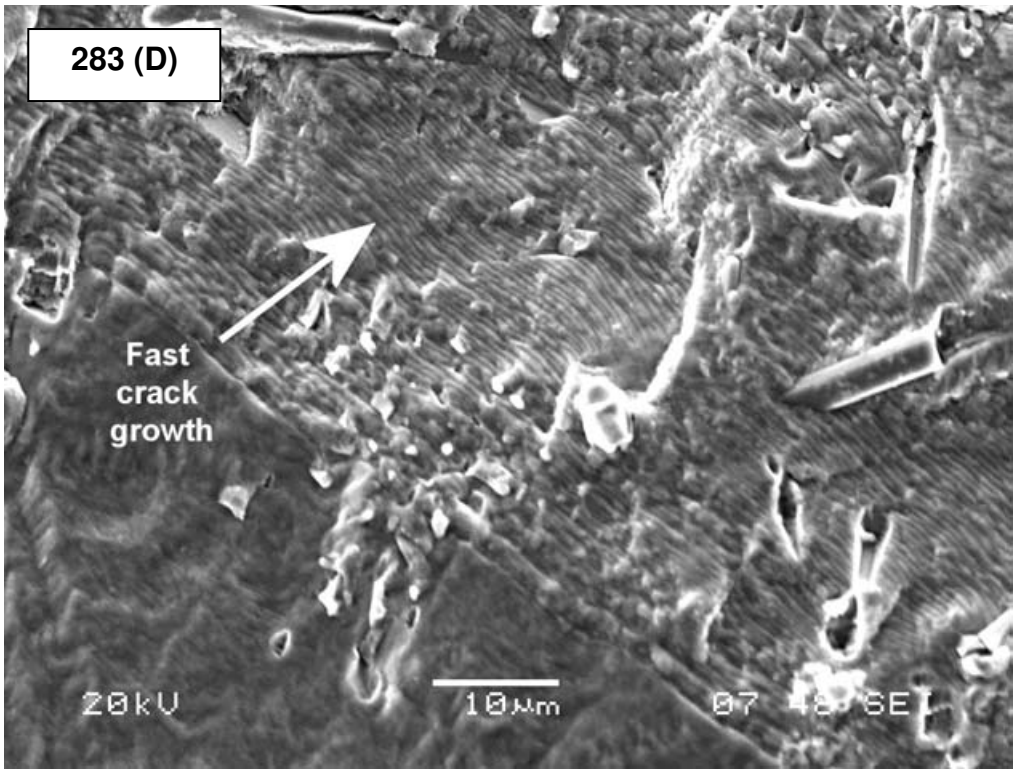

Secondary electron micrograph of zoomed area D from rod 283 showing distinct start of striations indicating fast crack growth

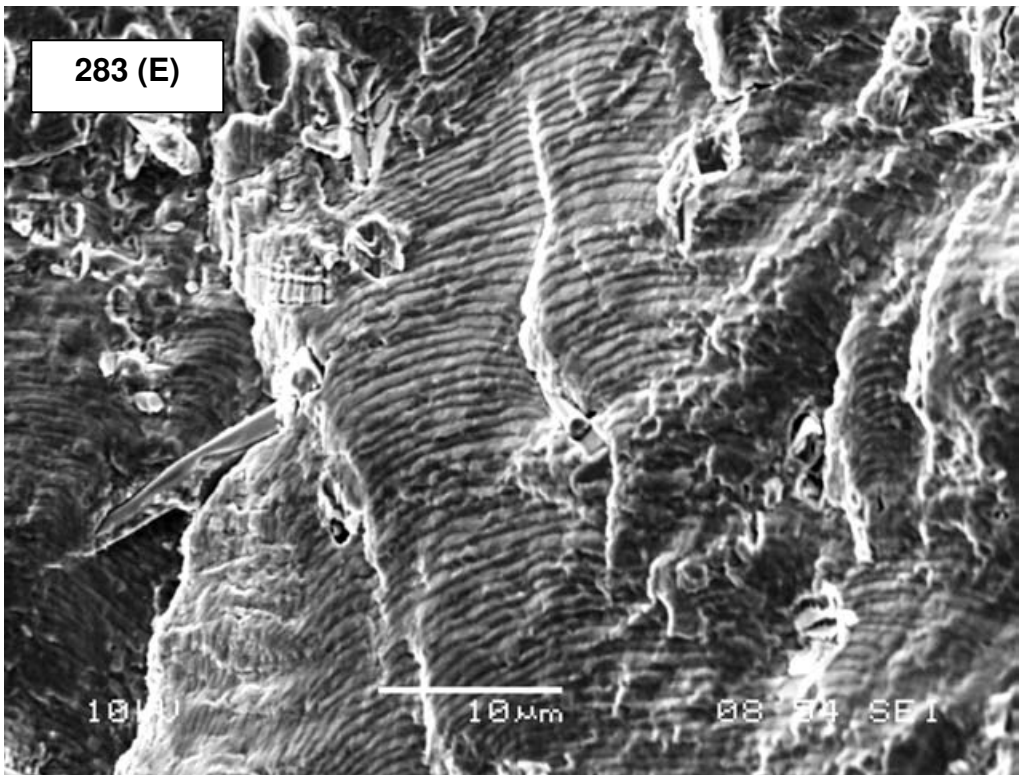

Secondary electron micrograph of zoomed area E from rod 283 showing striations covering many surfaces of fast crack region

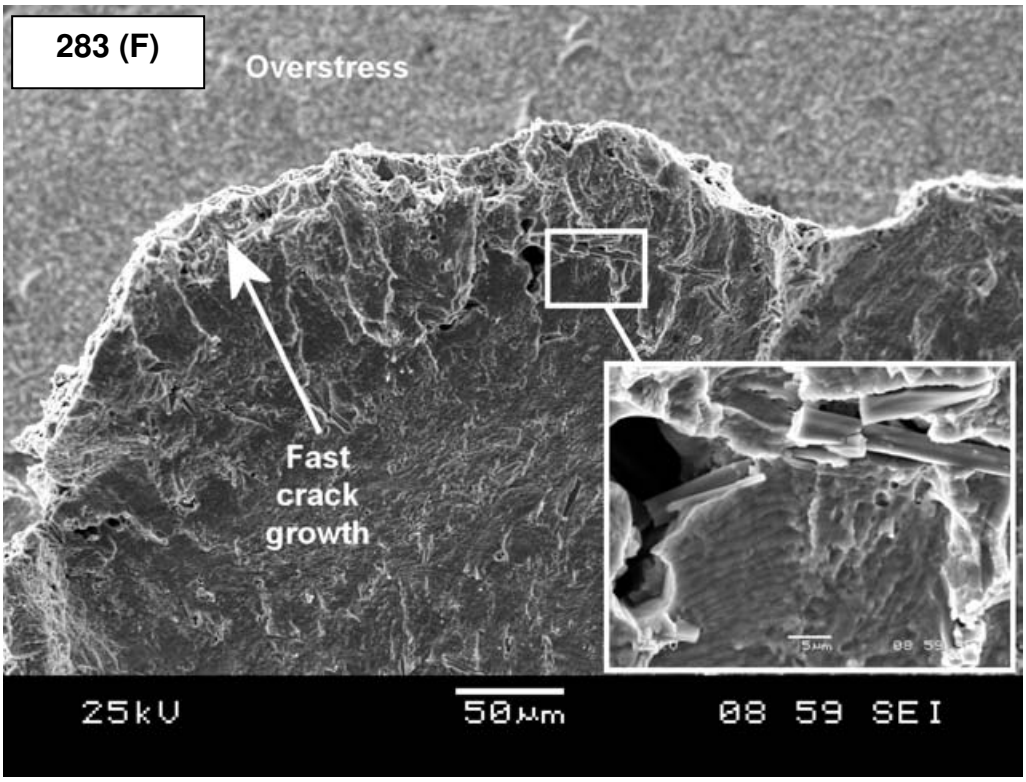

Secondary electron micrograph of zoomed area F from rod 283 showing final stage of fast crack growth before overstress failure occurs at solder/substrate interface

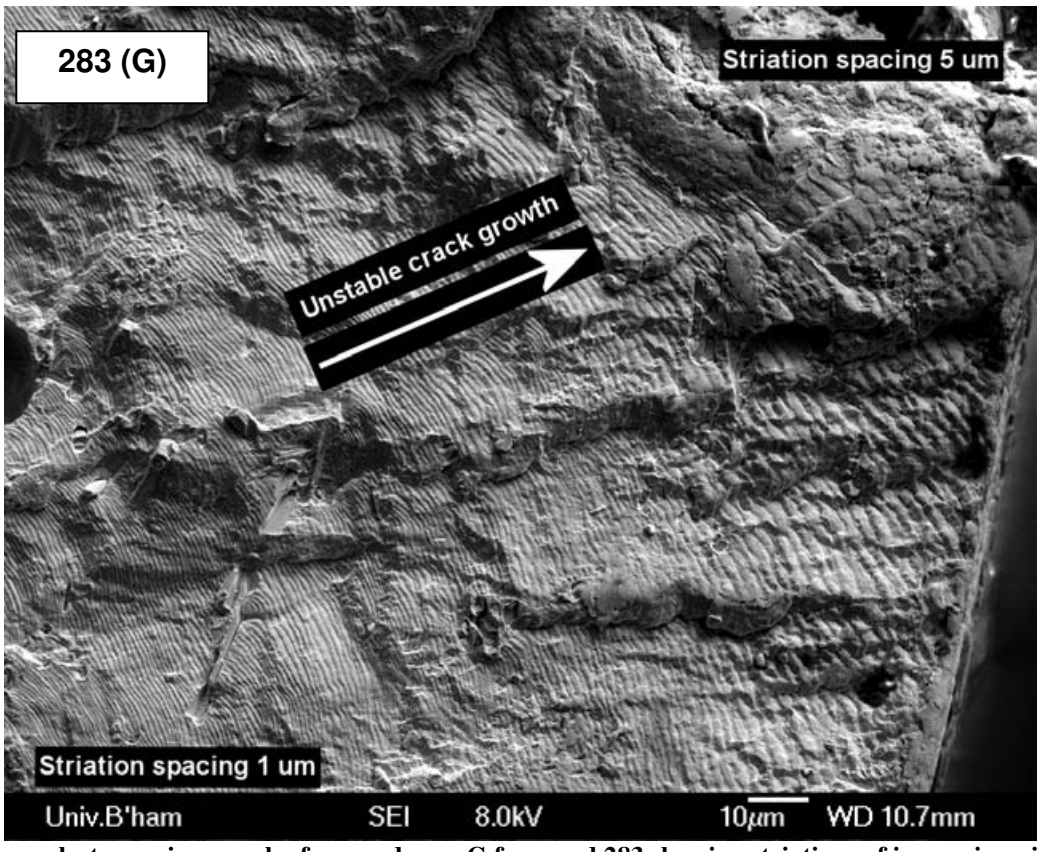

Secondary electron micrograph of zoomed area G from rod 283 showing striations of increasing pitch spreading over surface, clearly indicating direction of crack growth

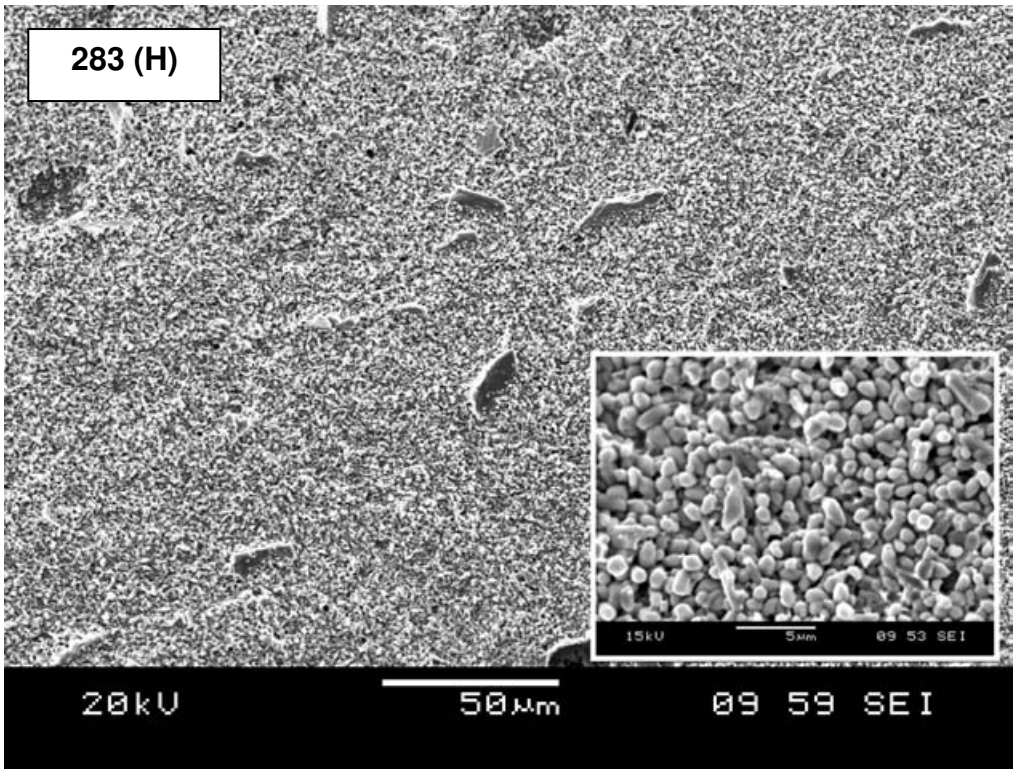

Secondary electron micrograph of zoomed area H from rod 283 showing overstress region consisting of clean separation between solder and $(Cu,Ni)_6Sn_5$ IMC layer (inset magnified)

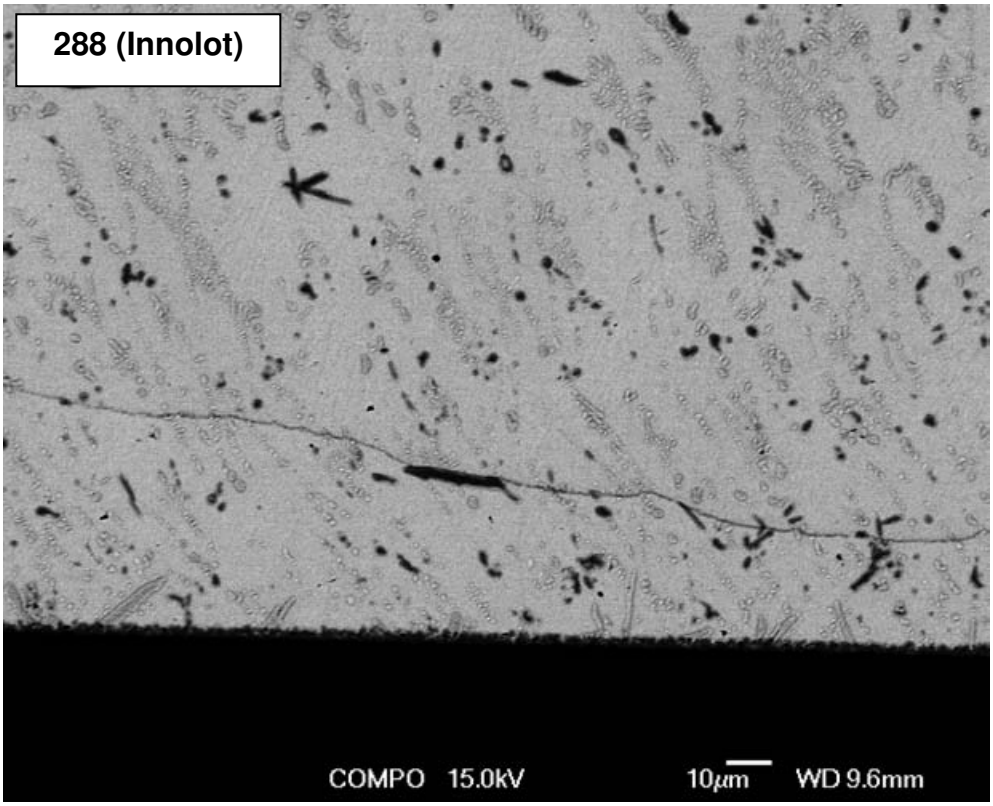

Figure 4.87. Backscattered electron micrograph of joint 288 in cross-section showing flat fatigue crack characteristics

4.7. SAM images and cracking behaviour from resonant decay studies

Each solder specimen that was successfully fatigued to a point just before failure was examined in the SAM as described in Chapter 3 and shown schematically in Figure 4.88. Figures are presented linking the images obtained from the SAM with the micrographs obtained upon cross-sectioning the joints and any prior X-ray transmission evidence of voiding in the specimen.

4.7.1 Sn-Pb fatigue crack progression

Figure 4.89 and Figure 4.90 show the SAM and corresponding crack progression images for three Sn-Pb specimens soldered to Ni substrates and fatigued at 25 ºC. In all cases, wavy crack growth appears to originate from the edge of the specimens near one or two interfaces, then travel deeper into the joint where cracks deviate into the middle of the solder volume. Crack growth does not appear to discriminate between Sn or Pb phases, nor does it appear to follow colony or grain boundaries at any stage. The waviness of the cracks, meaning they do not stay in one vertical plane, hinders the effectiveness of the SAM imaging of the specimens. In most cases, small interfacial voids are instead responsible for most of the acoustic reflections, giving the 'mottled' appearance of the images.

4.7.2 Sn-Cu-Ni fatigue crack progression

Only two Sn-Cu-Ni specimens were successfully fatigued and stopped before failure. In one case, after stopping at $f/f_{initial} = 0.90$, cracks were seen to be initiating from two places – the edges of an internal void and one outer edge of the joint, near the substrate (Figure 4.91). Cracks were not found to have extended further than ~50 μm from their initiation points. The SAM image for this joint (314) did not accurately portray the positions of the cracks. In joint

315 (Figure 4.92) which was halted at $f/f_{initial} = 0.93$, an extensive crack running closely parallel to the solder/IMC interface was found in a position matching that of the SAM image. Extensive secondary cracking was evident and, in places, the crack ran along the solder/IMC interface. In both joints studied the crack shape was angular and deviated frequently, although this did not appear to be related to any microstructural features such as clusters of intermetallic particles or eutectic network boundaries.

4.7.3 SAC387 fatigue crack progression

Joint 214 (Figure 4.93) displayed the clearest SAM image of a crack obtained in the present work. With subsequent cross-sectioning, the crack was found to be propagating purely along the interface between solder and IMC (Cu substrate gave a Cu_6Sn_5 layer). This very planar crack gave a sharp SAM image and allowed the cracked area to be confidently stated as 31 % by image analysis.

4.7.4 SAC305 fatigue crack progression

Figure 4.94 shows the SAM image and cross-sections for joint 344. A strong crack reflection was found with the SAM whose predicted width corresponded well to that found optically upon cross-sectioning. The fatigue crack was found to be running parallel to the solder/IMC interface in general and touching the interface every ~20 μm. Deep into the section at the advancing front of the crack, its depth is only tens of nanometres in places, with a jagged shape. EBSD was applied to the cracked region as shown in Figure 4.95, revealing no difference in grain size or pattern quality adjacent to the crack as compared to the general microstructure. Joint 345 (Figure 4.96) displayed similar characteristics, with a crack extending more than 1000 μm into the section, latterly along the solder/IMC interface. Joint

350 (Figure 4.97) shows reasonable agreement between SAM imaging and crack location, although as the crack increasingly diverts into the bulk of the solder (from its initially interfacial path), it travels out of the focal plane of the SAM. Good cross-polarised light images were obtained from this specimen, which did not reveal any recrystallisation or other orientation differences adjacent to the fatigue crack. Near-interfacial cracking was again seen in specimen 351, although in this case the crack behaviour was complex at the outer edge of the specimen, as opposed to the single crack most often seen.

4.7.5 Innolot fatigue crack progression

A large void was known to be present in joint 357 (Figure 4.98) and, as expected, extensive cracking was detected by the SAM around this void after fatiguing. The wavy nature of the SAM images at different focal depths suggested corresponding cracking at different depths and this too is confirmed. Cracking originates from the waist of the void and spreads outwards across the whole joint width in one particular cross-sectional depth. Crack morphology was generally flat for this joint, with crack widths of several microns. Fatigue cracks in most joints were very thin and sometimes ran in close parallel. Intermetallic particles in the path of fracture appeared to be debonded rather than cracked through. Figure 4.99 shows the SAM images from the remainder of the Innolot joints subject to resonant decay testing. Despite multiple cross-sections being taken through these joints, no signs of cracking were found in any.

4.7.6 Fatigue crack progression summary

The SAM proved to be a useful tool in the study of fatigue-cracked solder specimens; primarily in aiding the cross-sectioning of the joints in relevant locations. It was found that

SAM reflections did not always correspond to internal cracks or voids (especially in the case of the Innolot specimens) although in some cases a good correlation was found; in one case worthy of a quantitative analysis. Pre-critical high-cycle fatigue cracking was observed for all tested alloys.

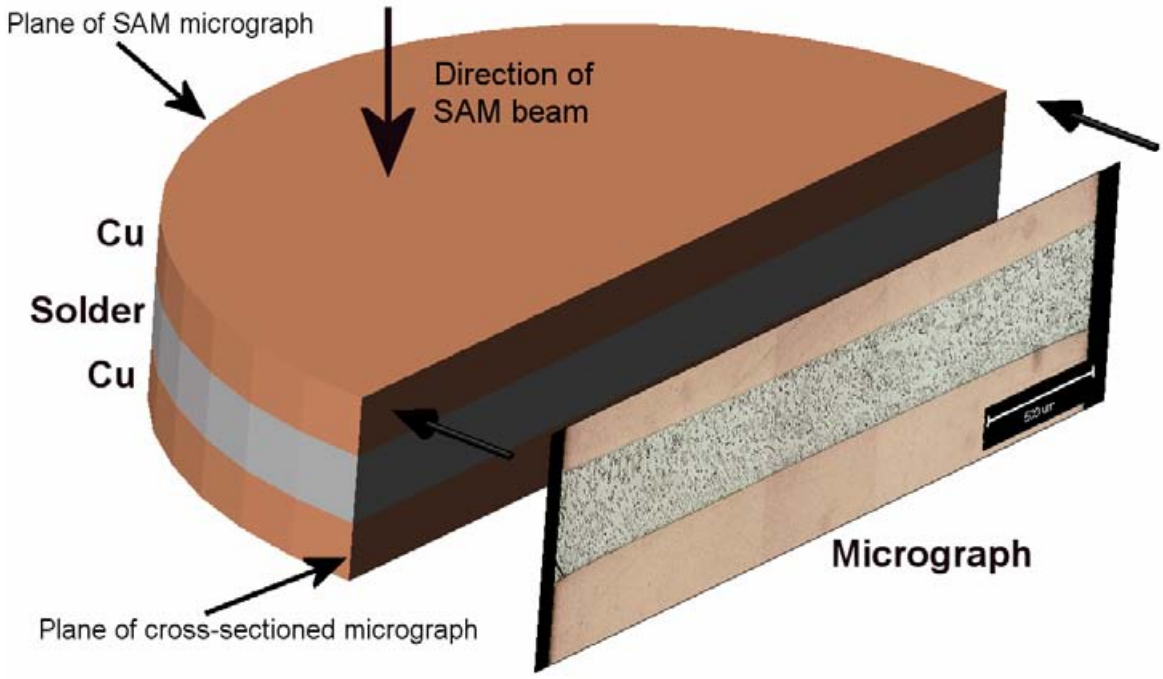

Figure 4.88. Schematic illustration of how micrographs were taken in resonant decay studies

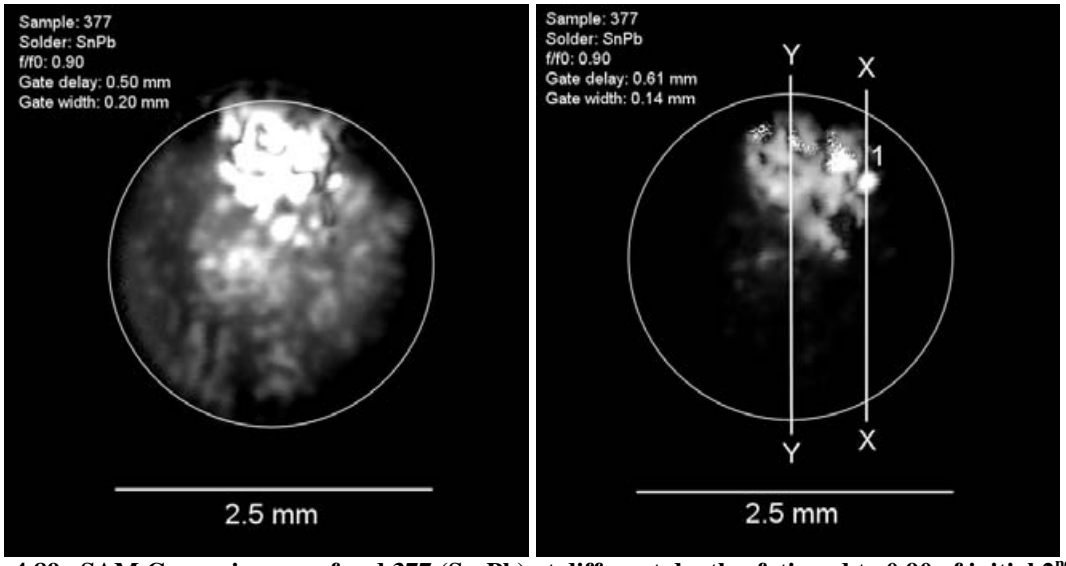

Figure 4.89. SAM C-scan images of rod 377 (Sn-Pb) at different depths, fatigued to 0.90 of initial 2nd resonant frequency. Left scan indicates the presence of undulating cracks due to (fainter) reflections that disappear deeper into the joint section (right)

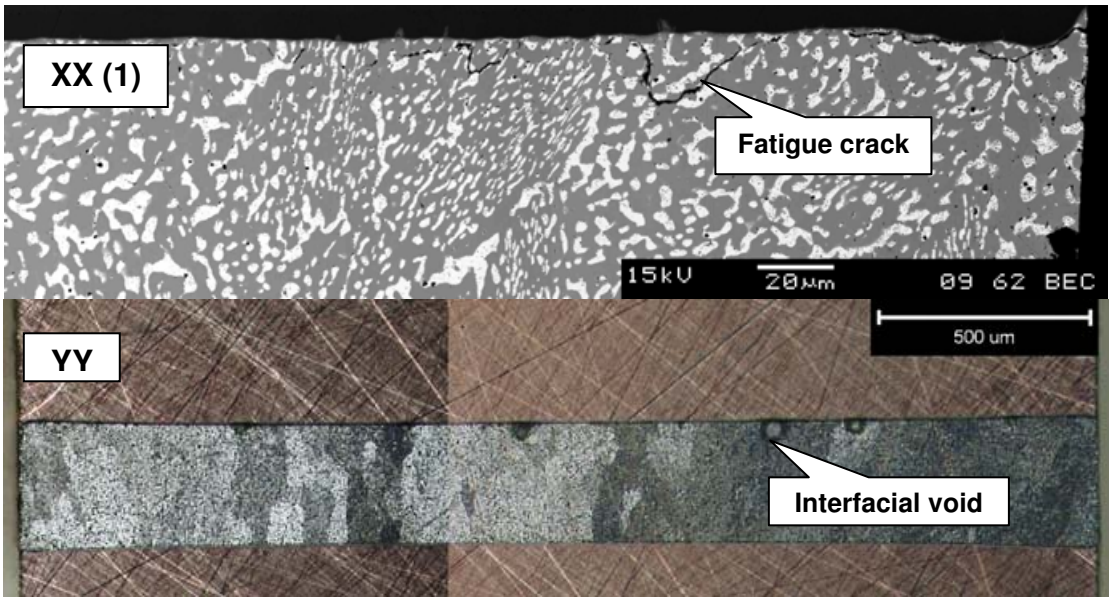

Backscattered electron (top) and optical DIC (bottom) micrographs of cross-sections XX and YY through rod 377 stub. Crack progressing close to upper Ni/solder interface seen in section XX whereas no cracks found in section YY. However multiple, small (<50 µm) interfacial voids observed on upper interface of section YY which could be the source of reflections seen in SAM images.

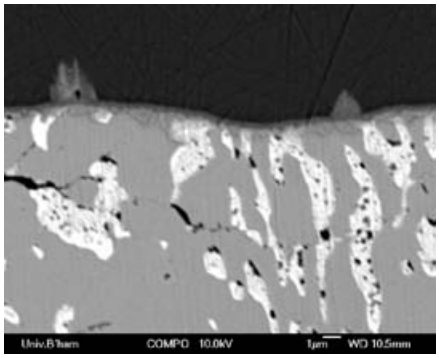

Left: zoomed backscattered electron image from area 1 (XX) showing fine crack progressing through Sn and Pb phases

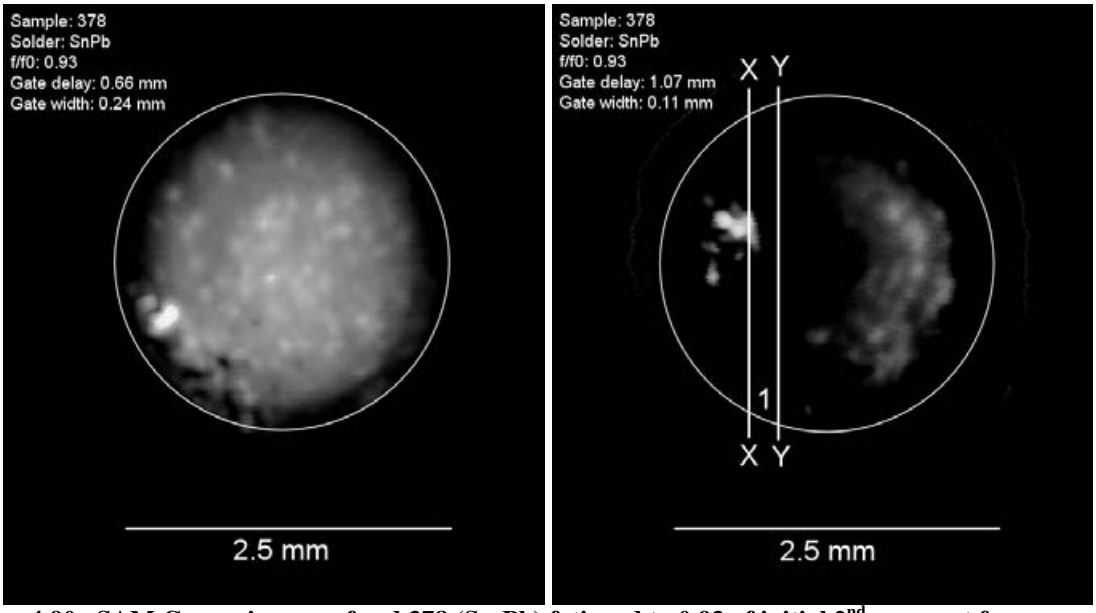

Figure 4.90. SAM C-scan images of rod 378 (Sn-Pb) fatigued to 0.93 of initial 2nd resonant frequency. Images both taken from reverse side of rod stub. 'Mottled' appearance of left image suggests interfacial voiding or small cracks that are highly non-planar.

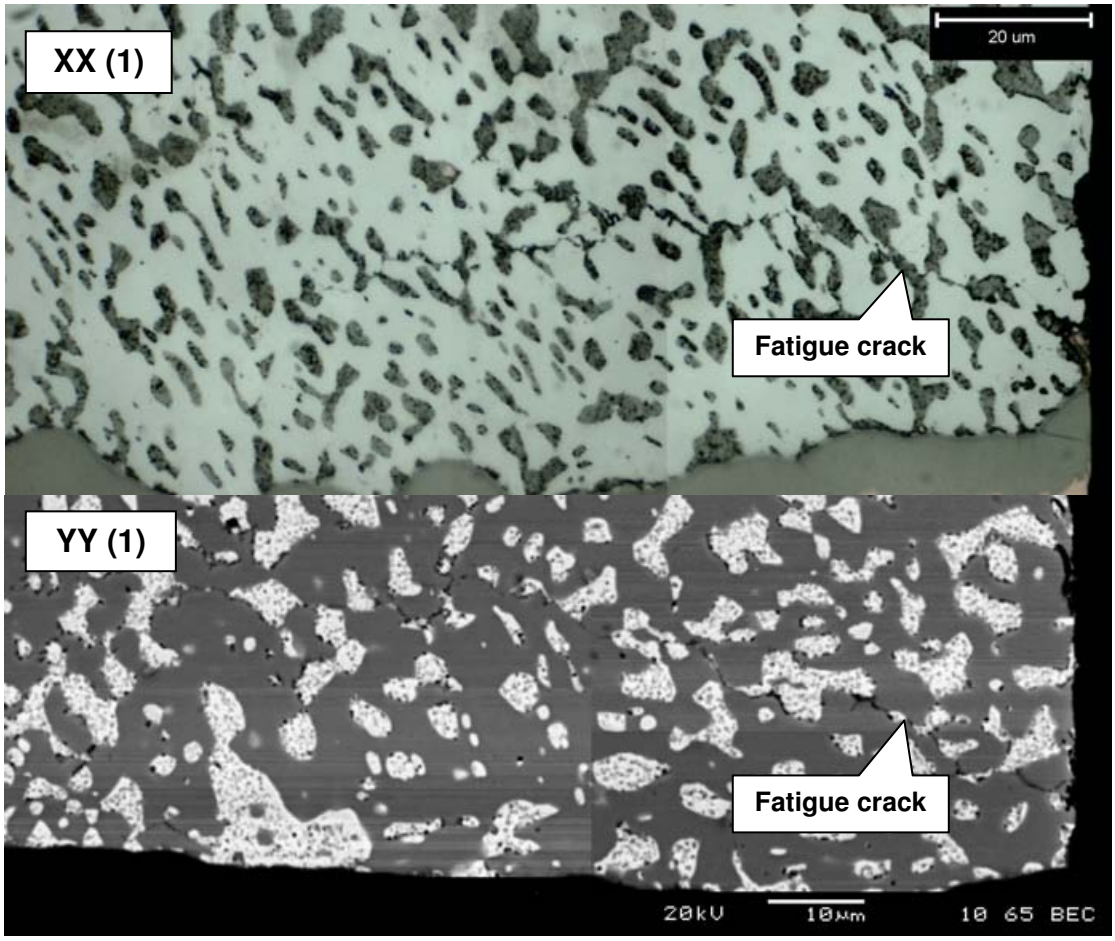

Optical (top) and backscattered electron (bottom) micrographs of sections XX and YY from above SAM image. Fatigue crack of approximately 100 µm length extending from free surface to interior of joint, 20-30 µm from Ni/solder interface.

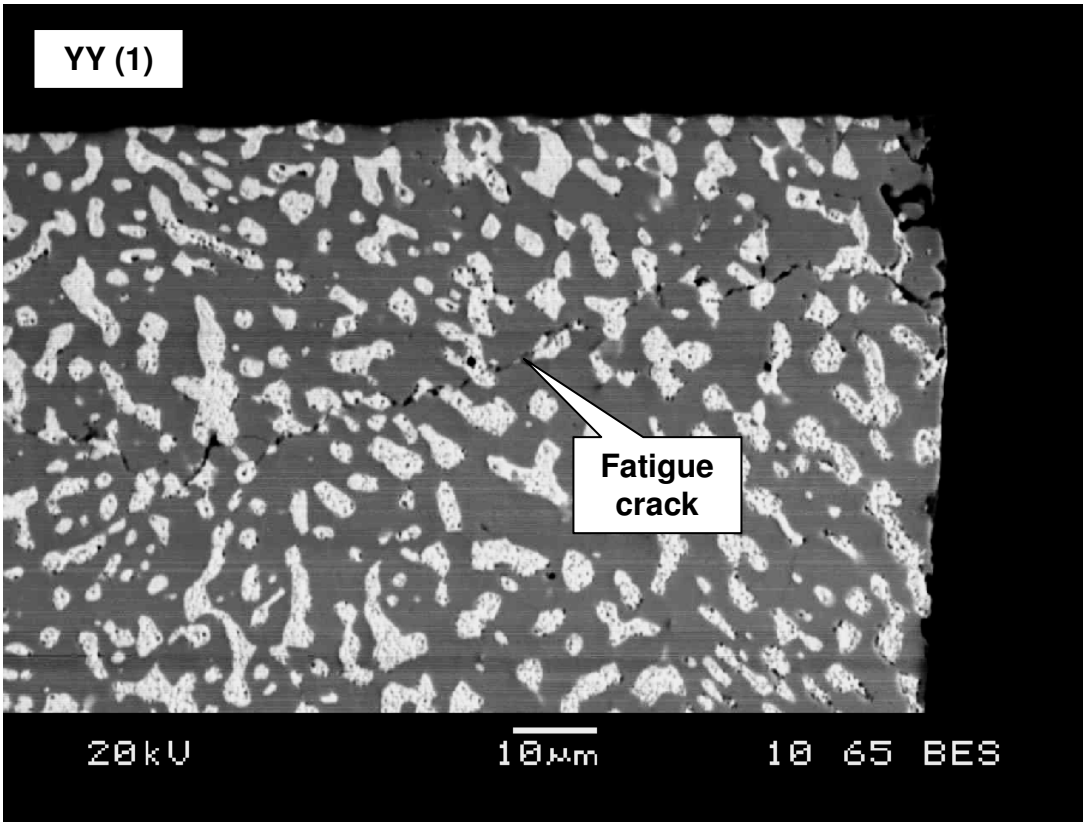

Backscattered electron micrograph of fatigue crack developing near upper interface of joint 378 on same side of section as previous images. Crack extends approx. 250 µm into interior of joint

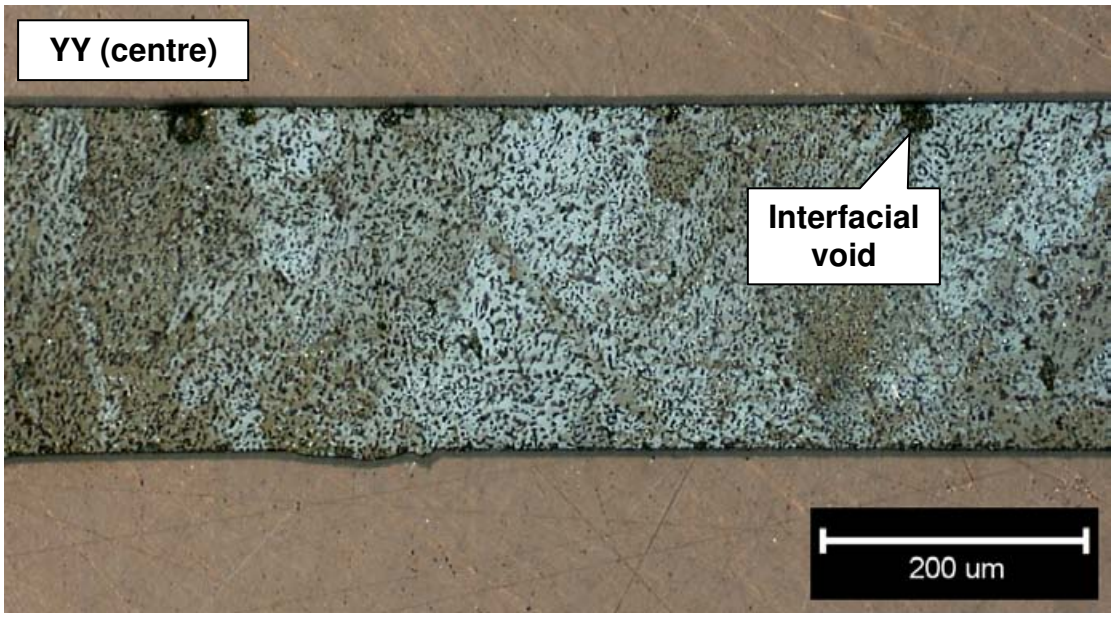

Optical micrograph of centre of section YY from joint 378 (cross-polarised light giving crystal orientation contrast in solder) showing small interfacial voids

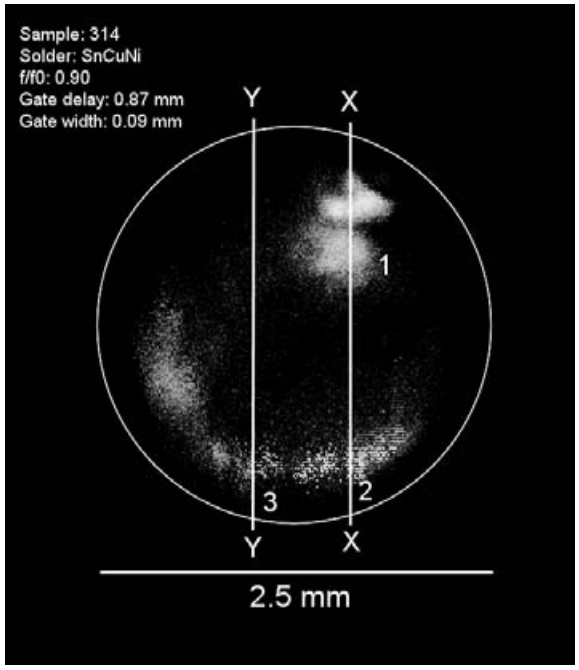

Figure 4.91. SAM C-scan image of joint 314 (Sn-Cu-Ni), fatigued to 0.90 of initial 2nd resonant frequency, showing reflections from cracks (white)

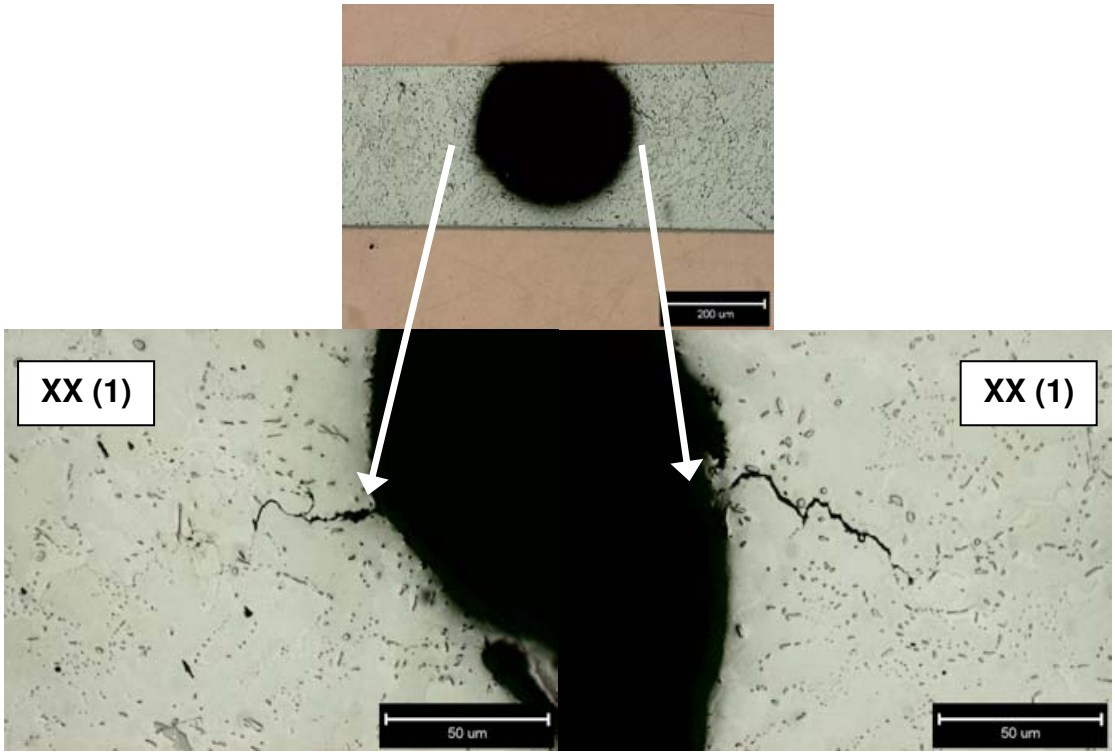

Optical micrographs of fatigue cracks originating from large internal void in section XX of joint 314

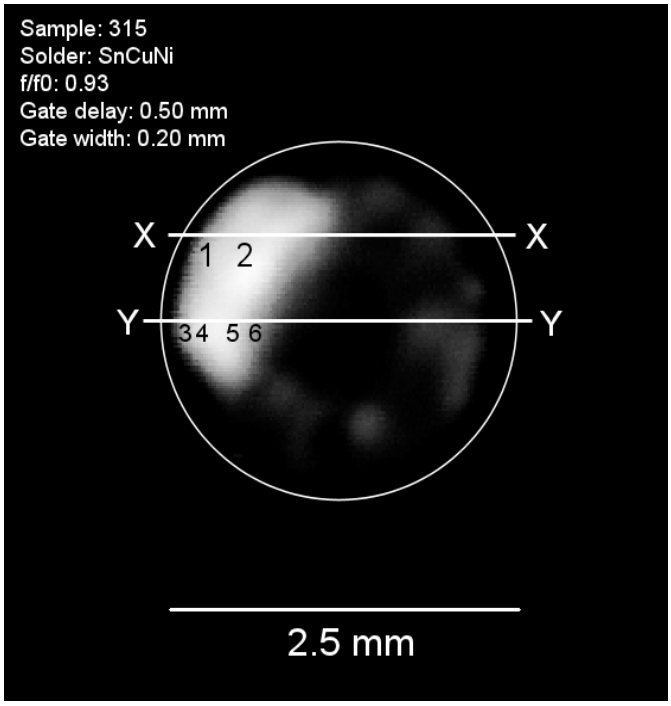

Figure 4.92. SAM C-scan image of joint 315 (Sn-Cu-Ni), fatigued to 0.93 of initial 2nd resonant frequency, showing strong reflection from crack (white) and weaker reflections possibly from voids

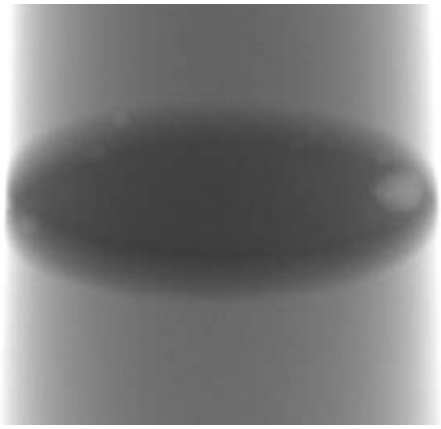

X-ray transmission image of joint 315 before fatigue testing showing a number of small voids close to outer circumference of joint

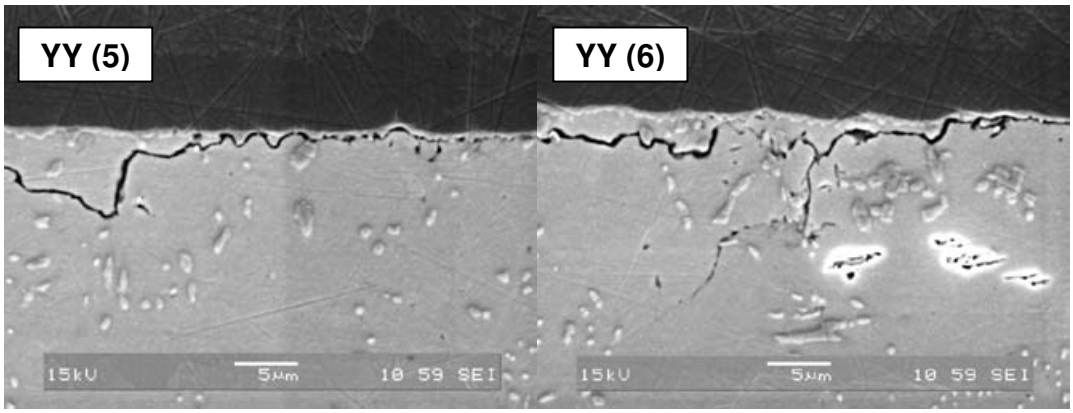

Secondary electron micrographs of areas 5 and 6 from section YY along joint 315 showing alternating path of crack between solder/IMC layer and closely parallel to it

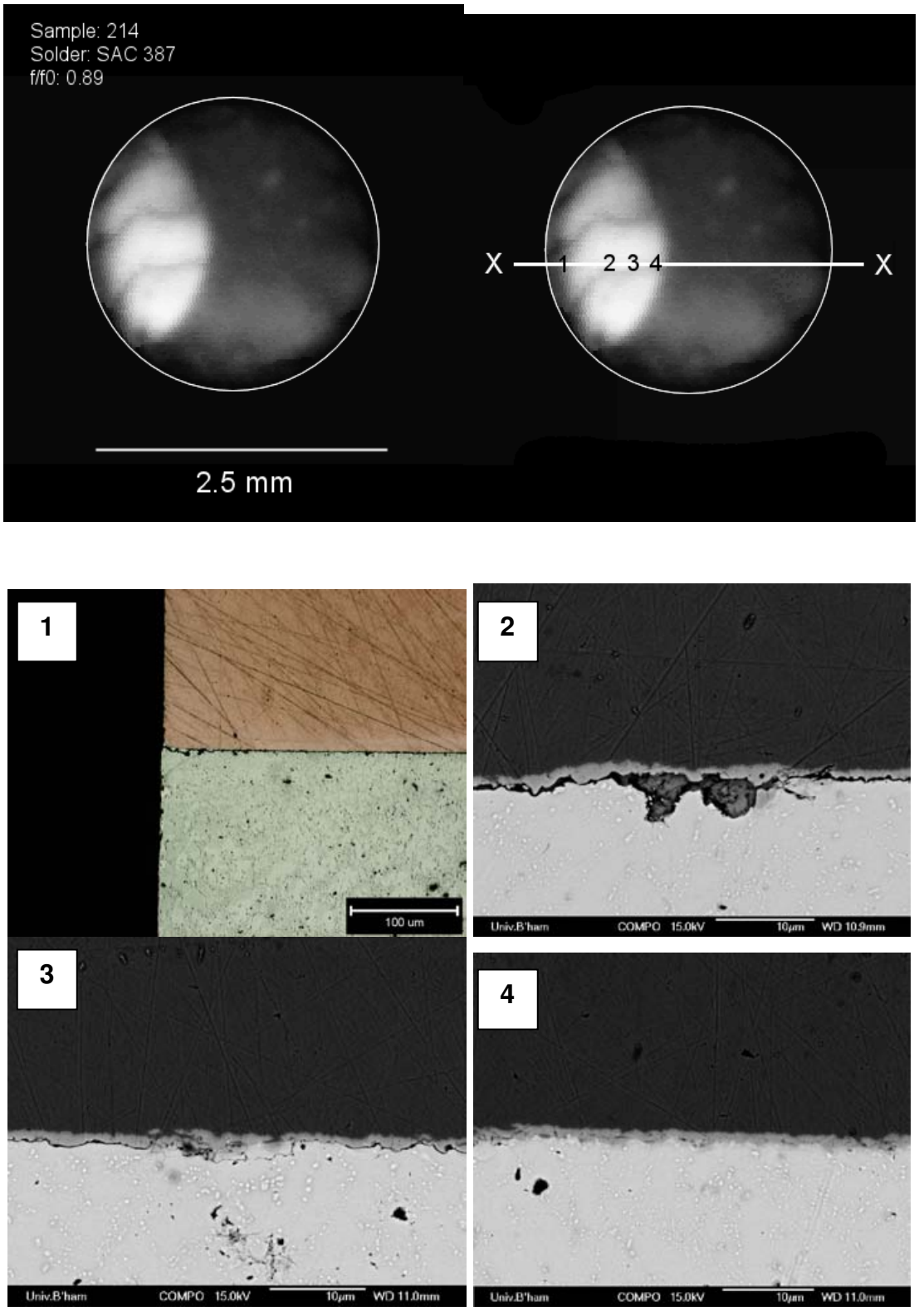

Figure 4.93. (Top left) SAM C-scan image of rod 214, fatigued to 0.89 of initial 2nd resonant frequency, with accompanying micrographs of fatigue crack progress along section XX (top right)

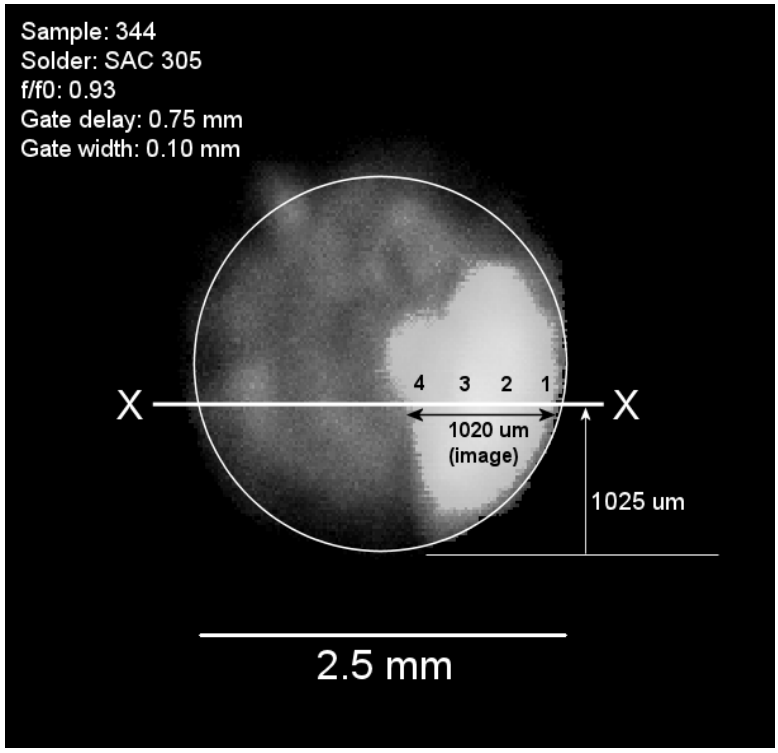

Figure 4.94. SAM C-scan image of rod 344 (SAC305), fatigued to 0.93 of initial 2nd resonant frequency. Strong reflection from right hand side of circle (white area) denotes crack in joint, not deviating more than 100 µm out of plane (see gate width of image). Joint was cross-sectioned along XX. Using chord length (XX) measured optically, amount of material removed is calculated (1025 µm) from circle equations and length of crack indicated by SAM is displayed (1020 µm). Optical measurements from cross-section showed that crack length was in fact ~900 µm

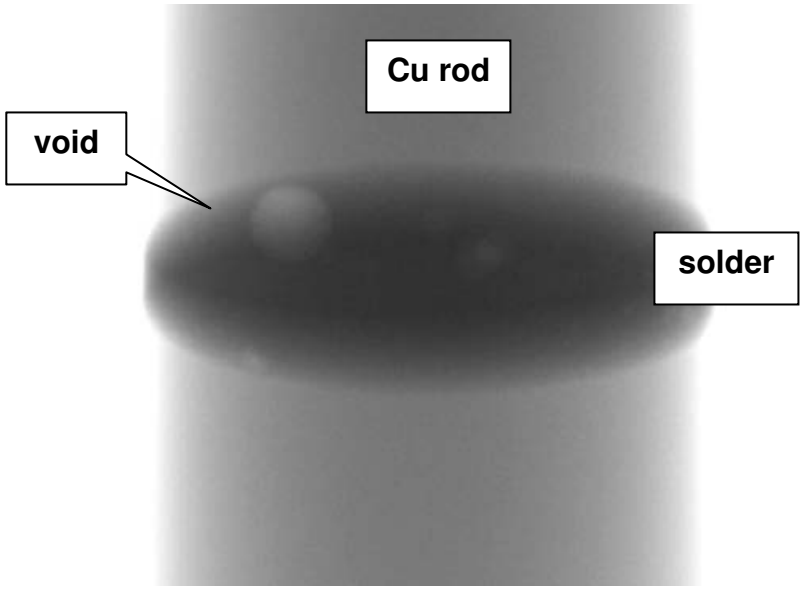

X-ray transmission image at oblique angle through rod 344 before fatigue testing, showing existence of voids

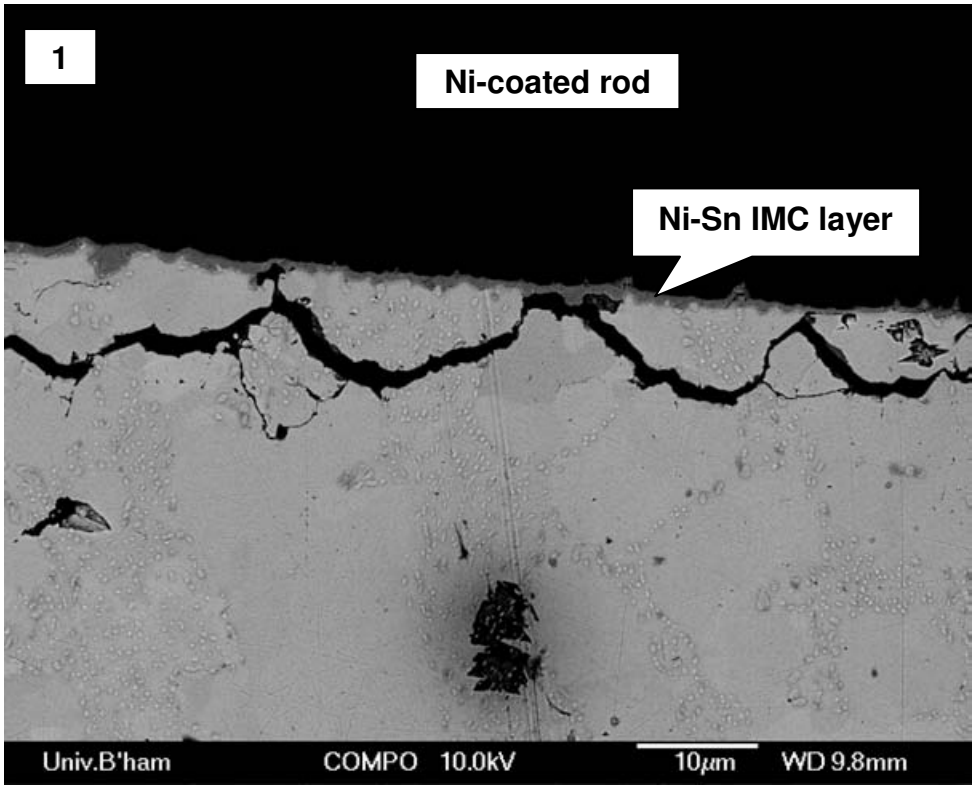

Backscattered electron micrograph of area 1 on section XX through joint 344 showing fatigue crack progressing in a wavy manner alongside the Ni/solder interface, occasionally debonding the IMC layer

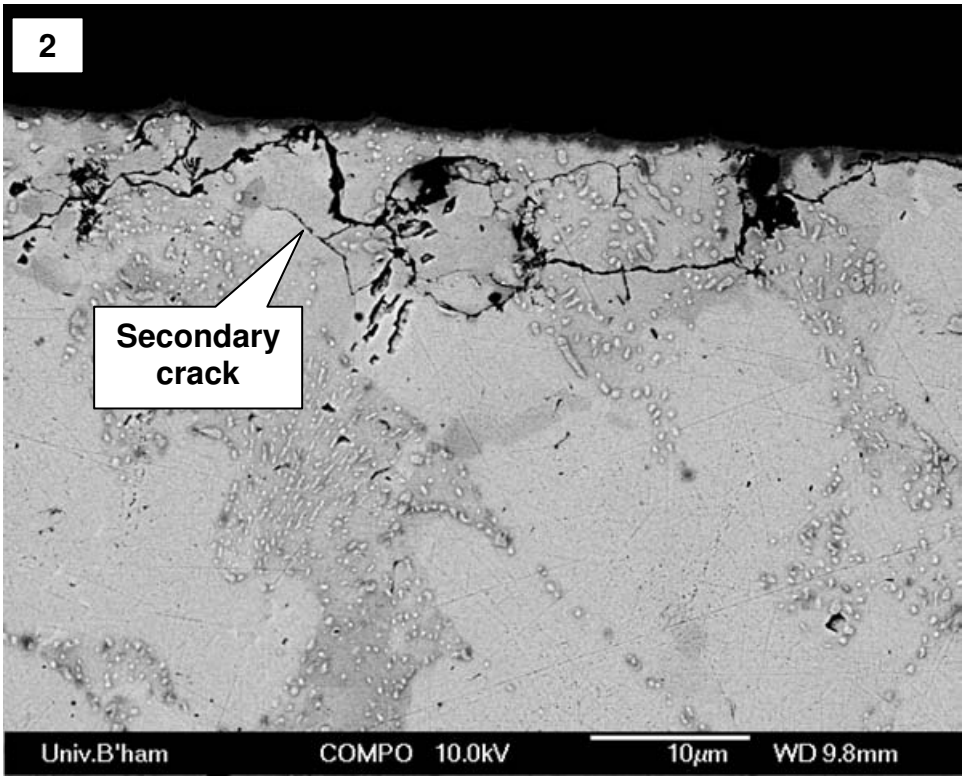

Backscattered electron micrograph of area 2 on section XX through joint 344 showing further fatigue crack growth into the joint and secondary cracking

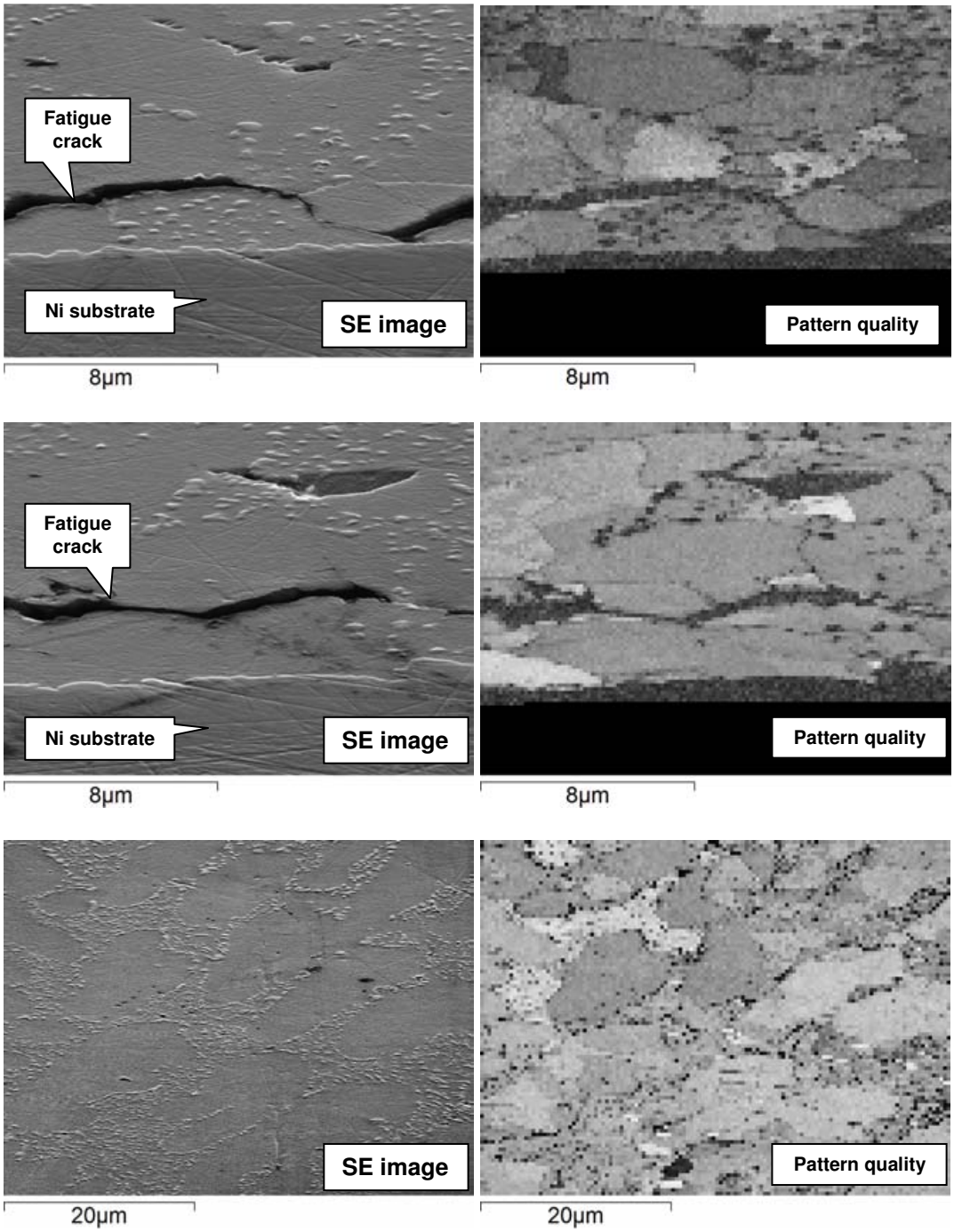

Figure 4.95. Secondary electron images and associated EBSD pattern quality maps for selected areas of SAC305 microstructure found in HCF joint #344. Cracks in upper two microsections are close to the IMC/Ni interface and are caused by fatigue, halted before total failure

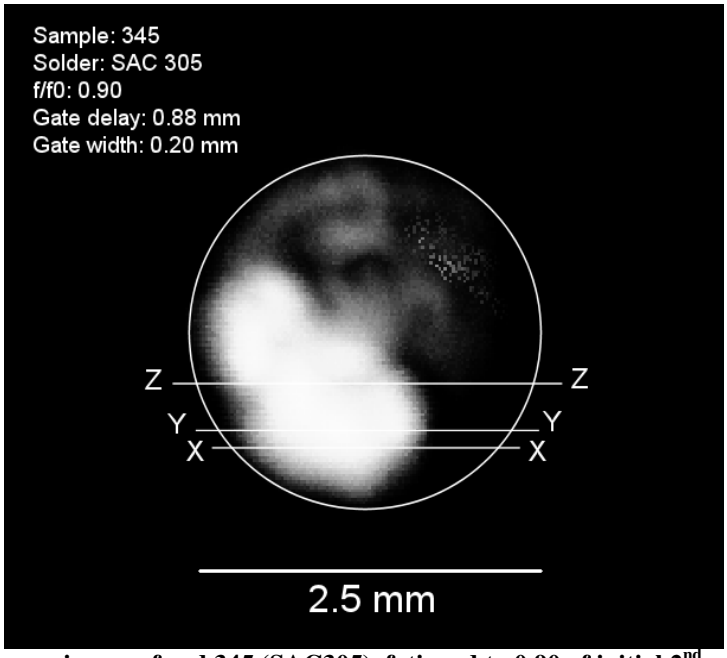

Figure 4.96. SAM C-scan image of rod 345 (SAC305), fatigued to 0.90 of initial 2nd resonant frequency. Strong reflection from crack (white) on left side of joint within 200 µm of nearest rod/solder interface

Optical micrograph of fatigue crack along section XX of joint 345 extending from free surface into joint interior, touching an interfacial void/cavity at one point

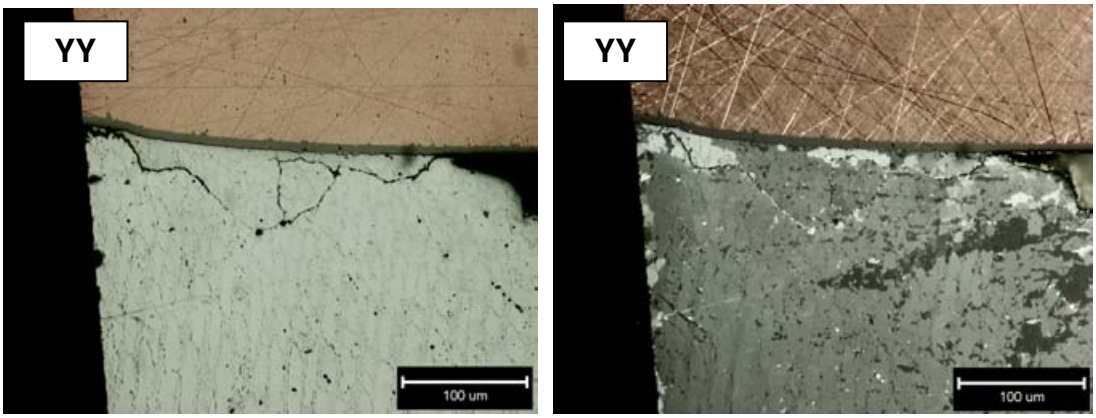

Optical micrographs of section YY through joint 345 (right image uses cross-polarised light for crystal orientation contrast) showing fatigue crack linking free surface of solder with interior cavity

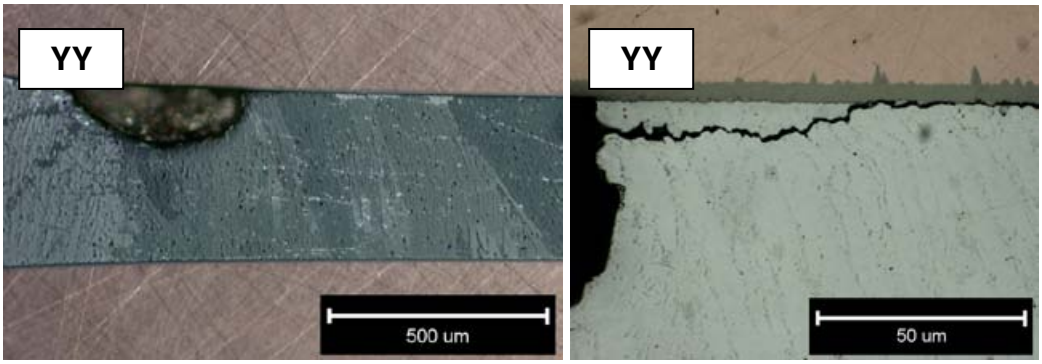

Optical micrographs of section YY through joint 345 showing fatigue crack interaction with cavity adjacent to rod/solder interface

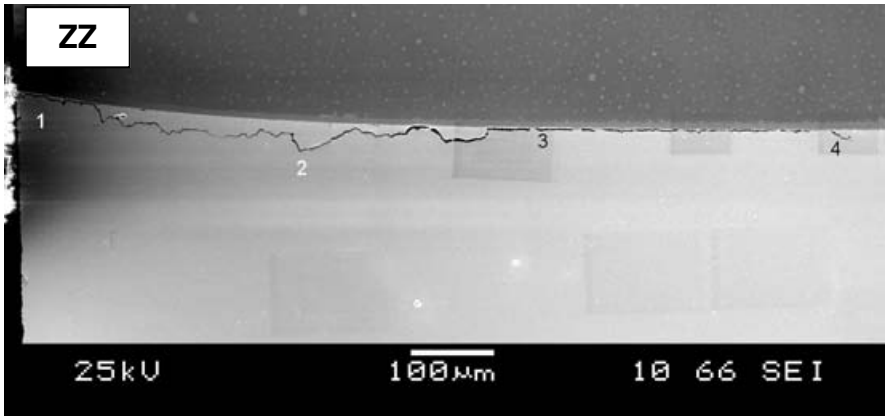

Secondary electron micrograph of section ZZ through joint 345 showing fatigue crack extending ~1000 µm into joint interior, at interface between solder and IMC layer for half its length. Note – image darkening on left is a charging artefact from the SEM

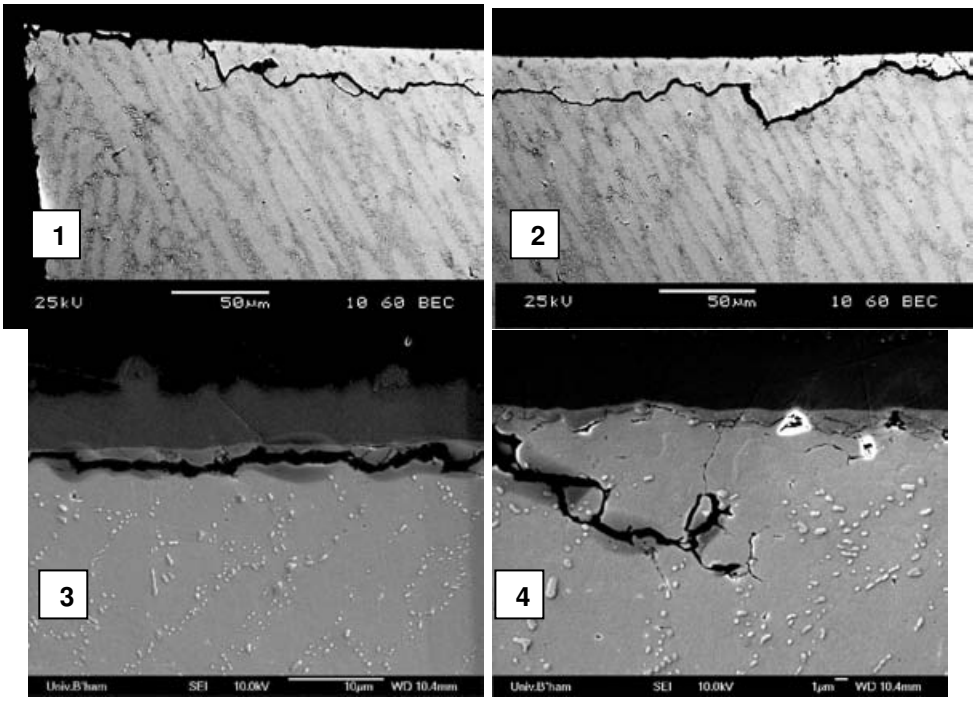

Electron micrographs of zoomed areas 1-4 from above section ZZ though joint 345. Areas 1 and 2 show fatigue crack parallel to IMC layer, area 3 shows cracking between solder/IMC and area 4 shows crack deviation away from interface

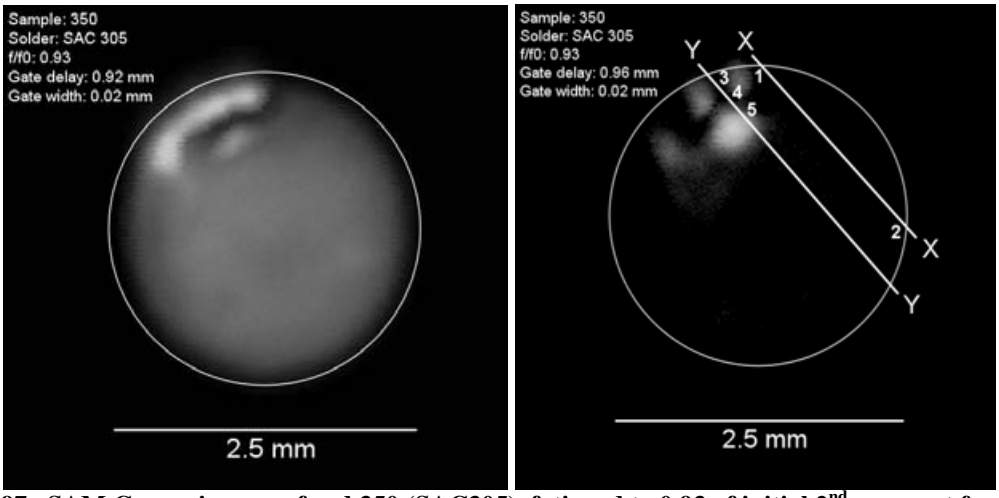

Figure 4.97. SAM C-scan images of rod 350 (SAC305), fatigued to 0.93 of initial 2nd resonant frequency, showing crack (white) at interface between rod and solder. Left image shows features from a 20 µm thick section below the interface, while right image shows features within a further 20 µm deep section

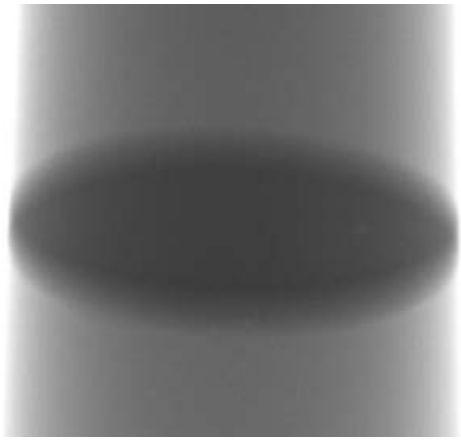

X-ray transmission image of rod 350 before fatigue testing – no voids detected

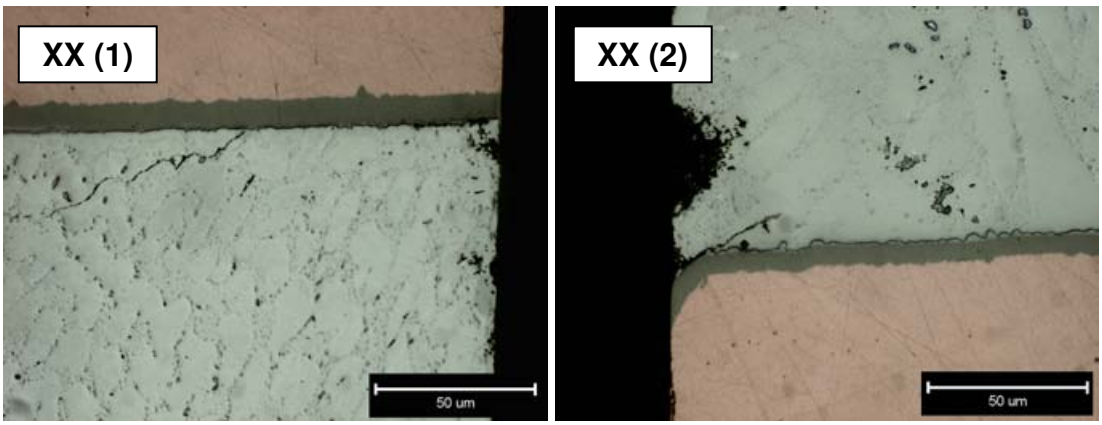

Optical micrographs from section XX of joint 350 – left image shows beginning of main fatigue crack along upper interface while left image shows small fatigue crack by lower interface not detected by the SAM

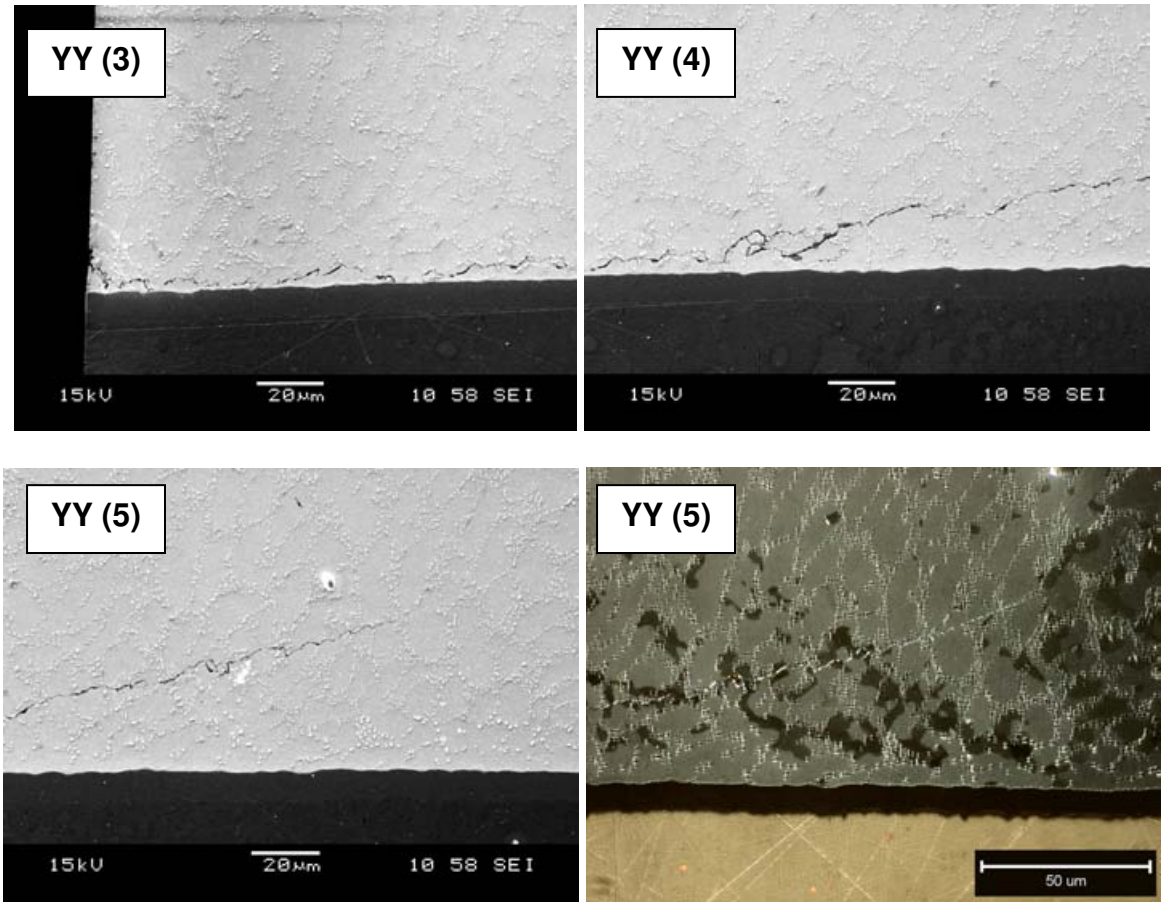

Secondary electron micrographs of fatigue crack propagating in areas 3-5 of section YY of joint 350 plus optical micrograph (lower right) of area 5 using cross-polarised light to give crystal orientation contrast in region surrounding crack

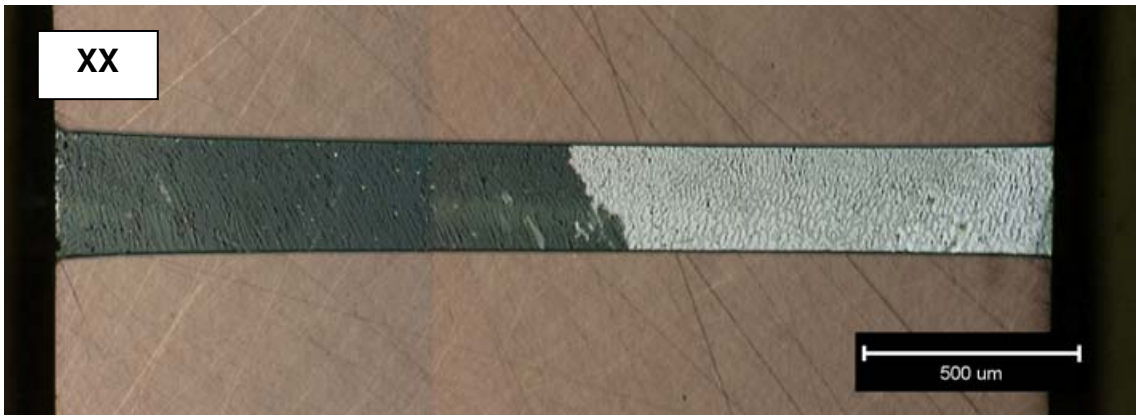

Optical micrograph of entire section XX through joint 350 using cross-polarised light for crystal orientation contrast. Only two major colonies are present throughout section

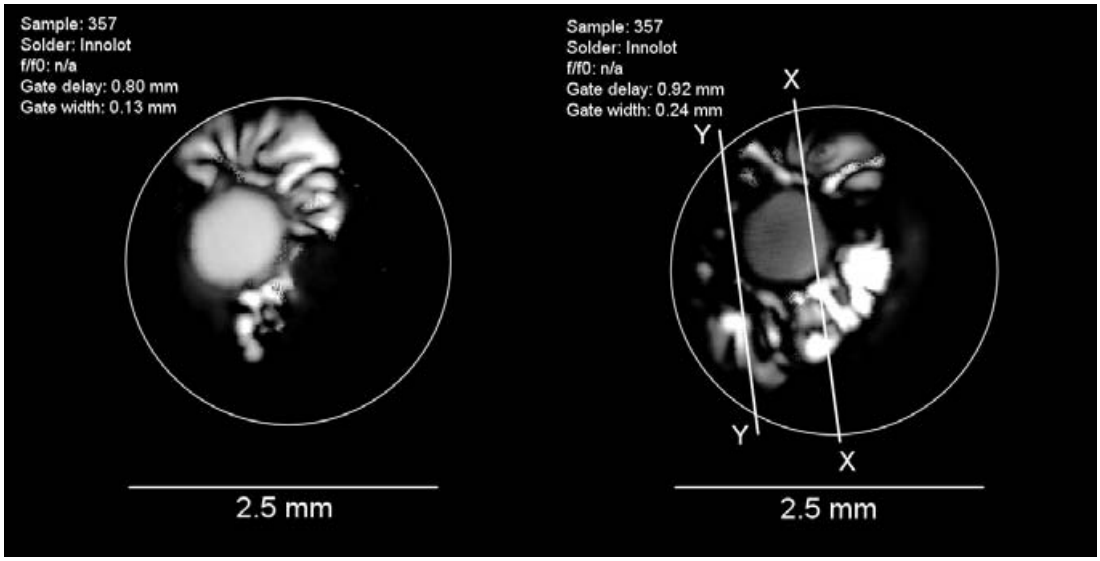

Figure 4.98. SAM C-scan images of joint 357 (Innolot), fatigued until resonant frequencies became indistinct. Large, central void detected before testing by X-ray (below) and confirmed by SAM. Subsequent to fatigue testing, strong reflections from cracks at various depths detected surrounding the void as indicated by white patches on SAM images

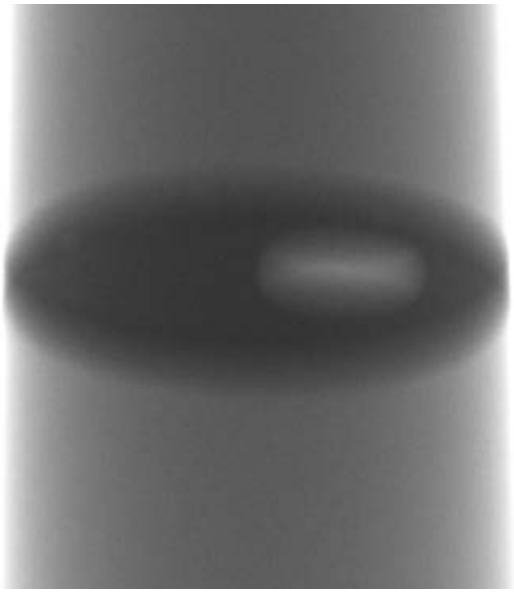

X-ray transmission image of joint 357 prior to fatigue testing, showing large void traversing entire thickness of solder joint

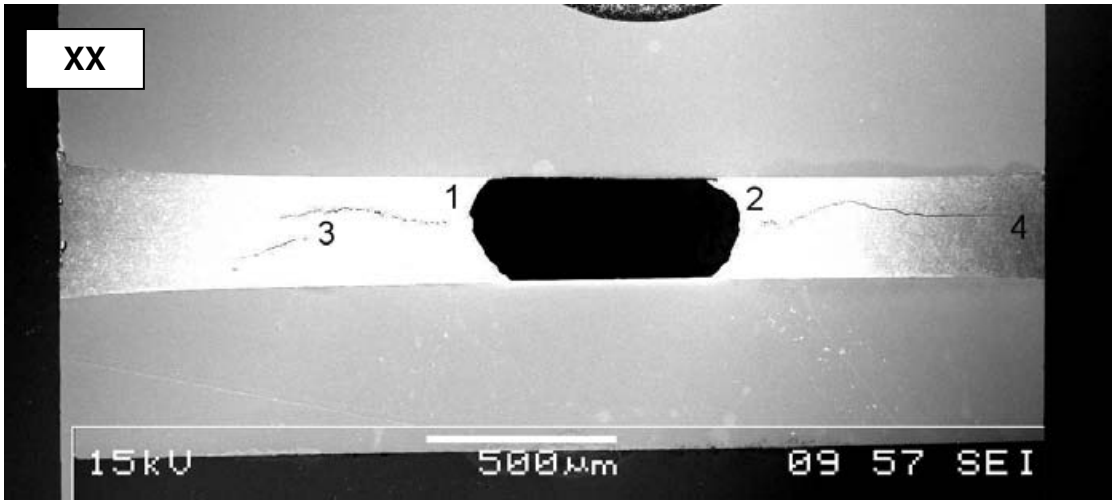

Secondary electron image of section XX through joint 357 showing large central void and fatigue cracks nucleating from its edges

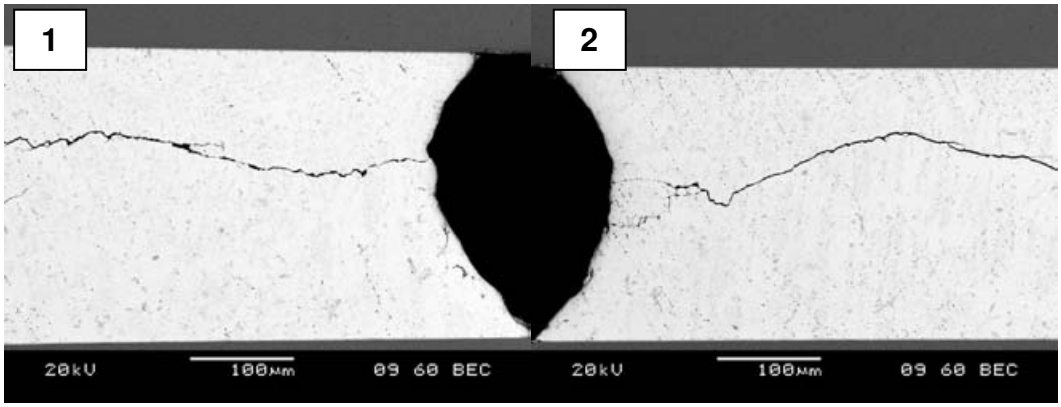

Backscattered electron micrographs of areas 1 and 2 indicated on above section XX image – cracks emanating from waist of large void

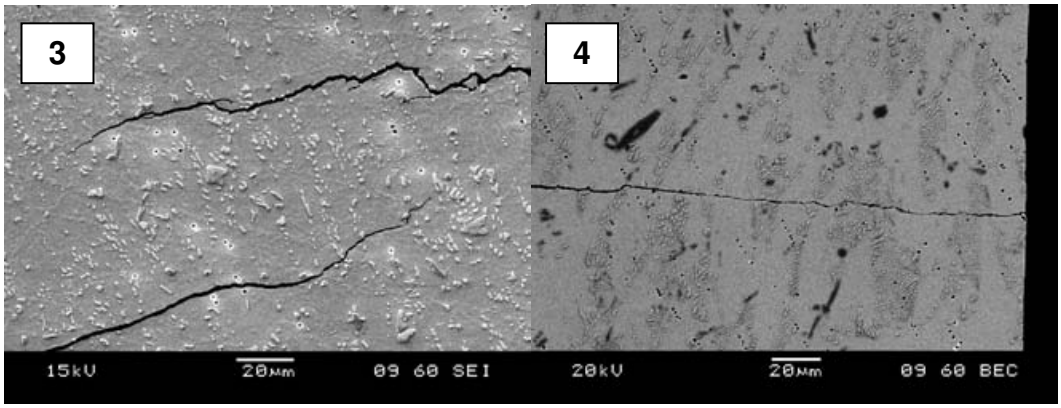

Electron micrographs of areas 3 and 4 indicated on above section XX image – fatigue cracks through central area of solder joint, reaching joint edge in the case of area 4

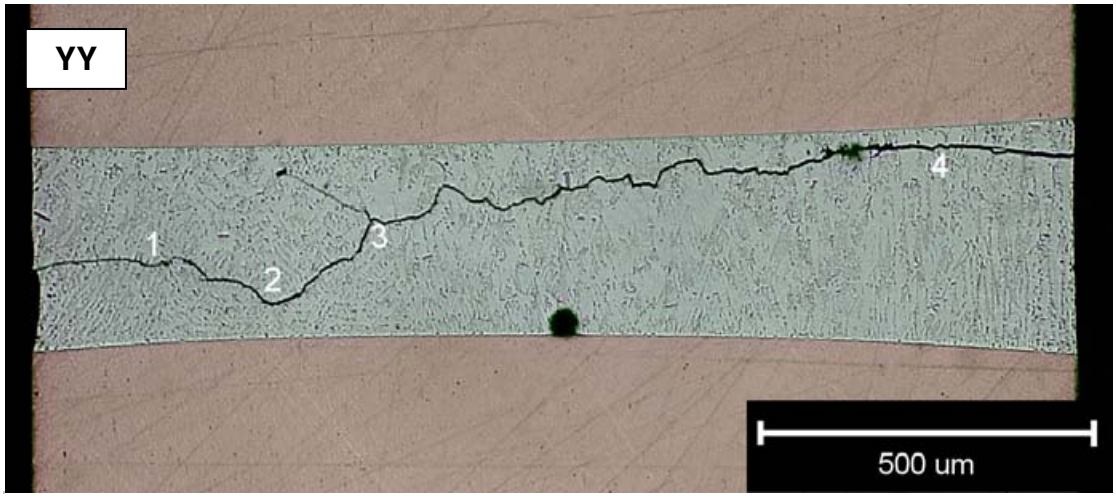

Optical micrograph of section YY through joint 357 showing fatigue crack spanning entire width of joint at this point

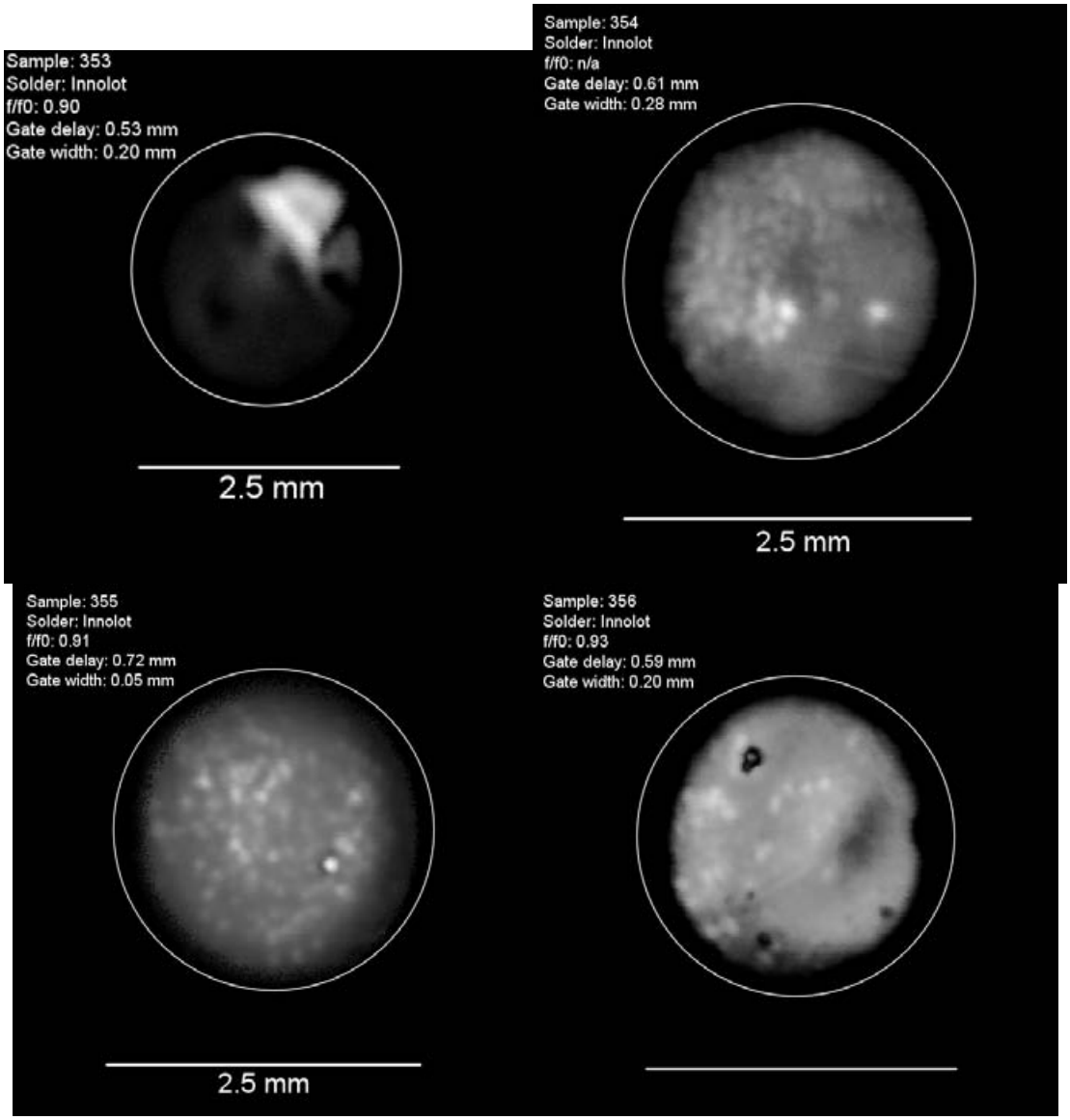

Figure 4.99. SAC C-scan images of four Innolot joints which were fatigued to various states of frequency decay (down to $f/f_{initial} = 0.90$) yet did not show any signs of cracking when cross-sectioned at approximately five different sections

4.8. Damping capacity tests

Figure 4.100 shows an example of the resonant response of a soldered rod over the frequency range 30 Hz – 1 kHz at 25 ºC. Figure 4.101, Figure 4.102, Figure 4.103, Figure 4.104 show the resonant responses of Sn-Pb, Sn-Cu-Ni and SAC305 rods at -50, 25 and 70 or 100 ºC. The expected result is an increase in resonant frequency of a particular rod with a decrease in temperature (due to stiffening) along with a narrowing of the peak shape. However, this was not the case and a clear link between temperature and resonant frequency or peak width was not observed across all solders. Table 3.1 gives calculated Q values from peaks 1 and 2. No consistent effect of temperature on peak width is found. It can be seen from the Figures that poor signal quality was sometimes obtained with scans taken at low or high temperatures. It is thought that the laser vibrometer experienced problems at temperature extremes, possibly due its beam being affected by hot/cold air currents.

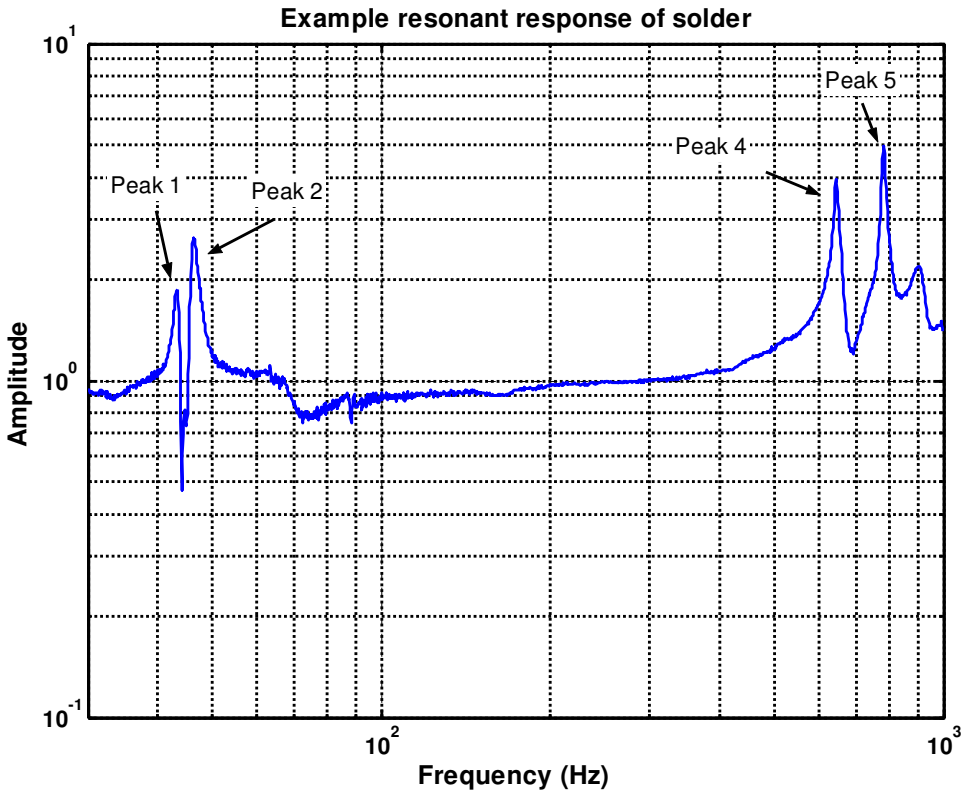

Figure 4.100. Example resonant response of solder joint in rod/holder system at 25 ºC

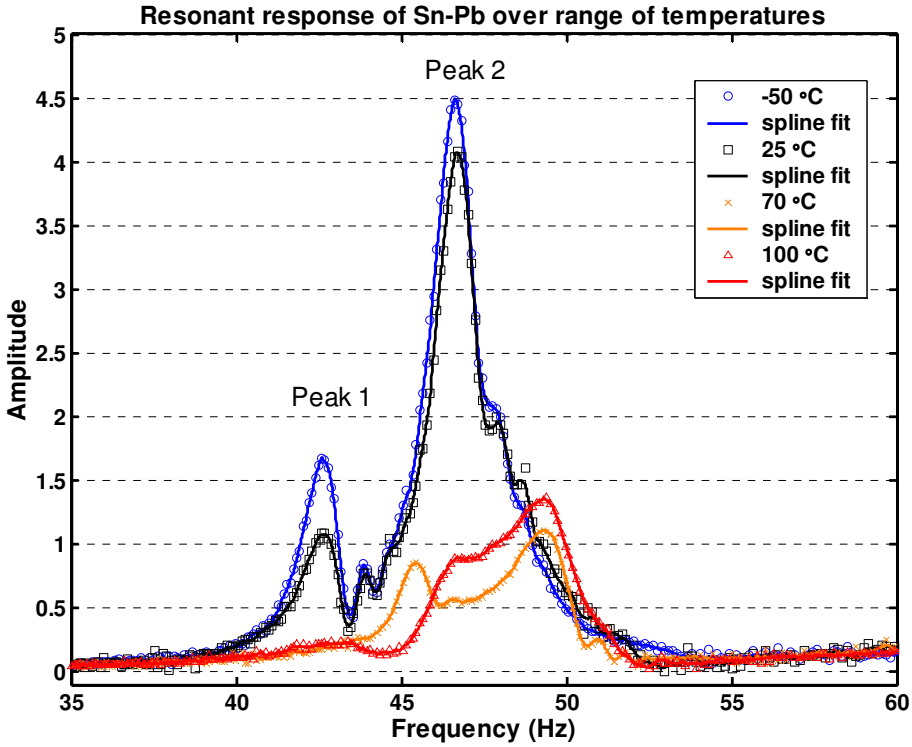

Figure 4.101. Resonant response of rod/holder system containing Sn-Pb joint

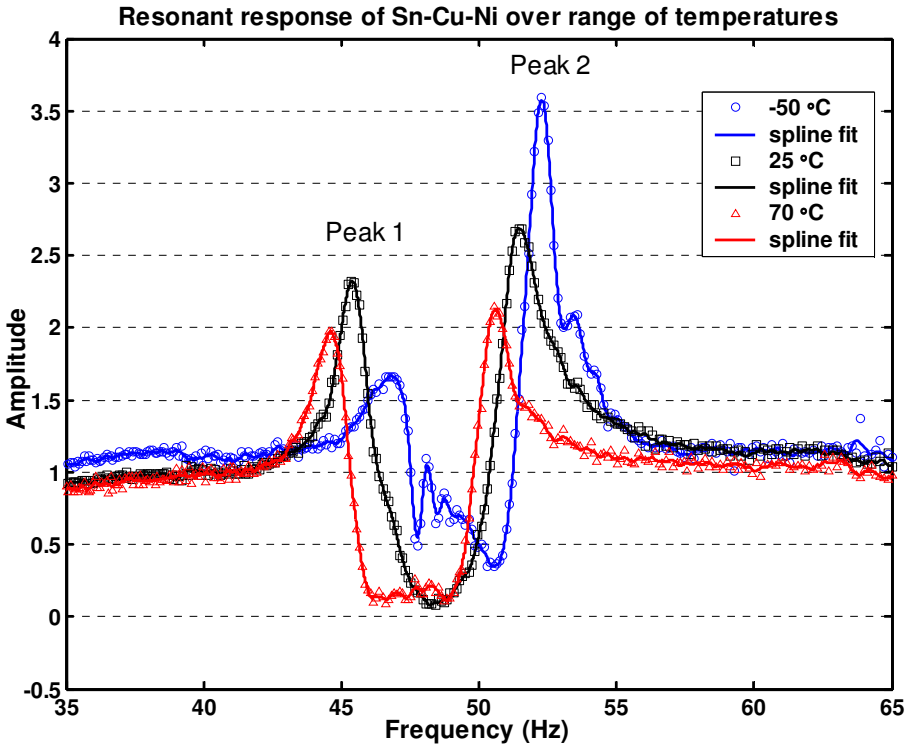

Figure 4.102. Resonant response of rod/holder system containing Sn-Cu-Ni joint

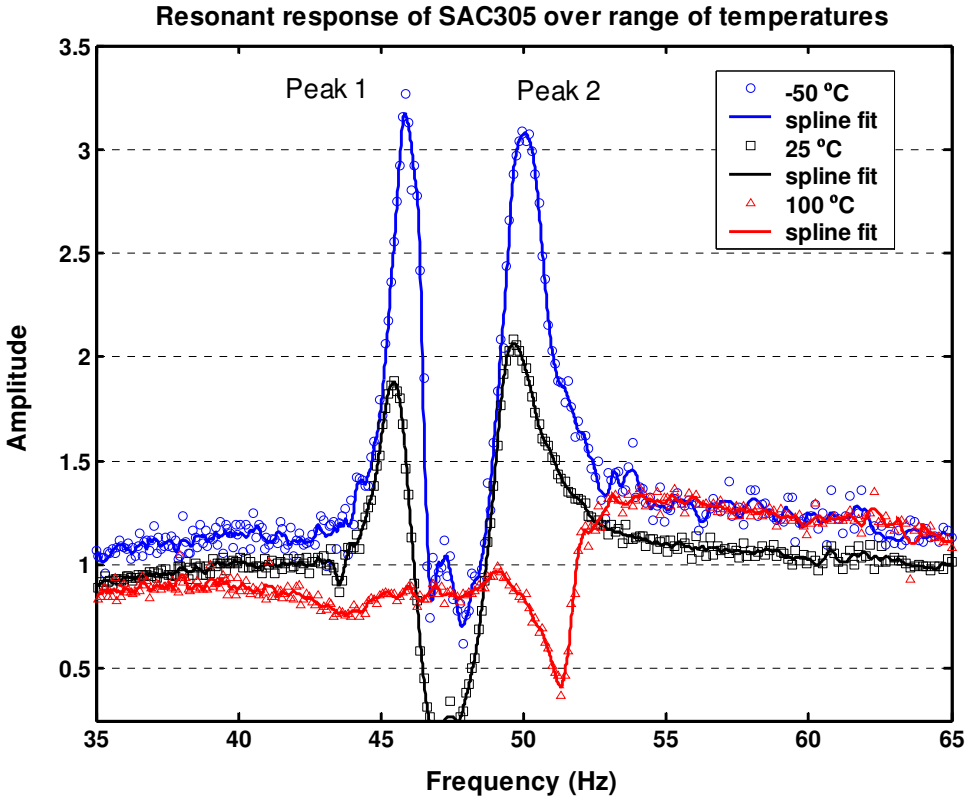

Figure 4.103. Resonant response of rod/holder system containing SAC305 joint

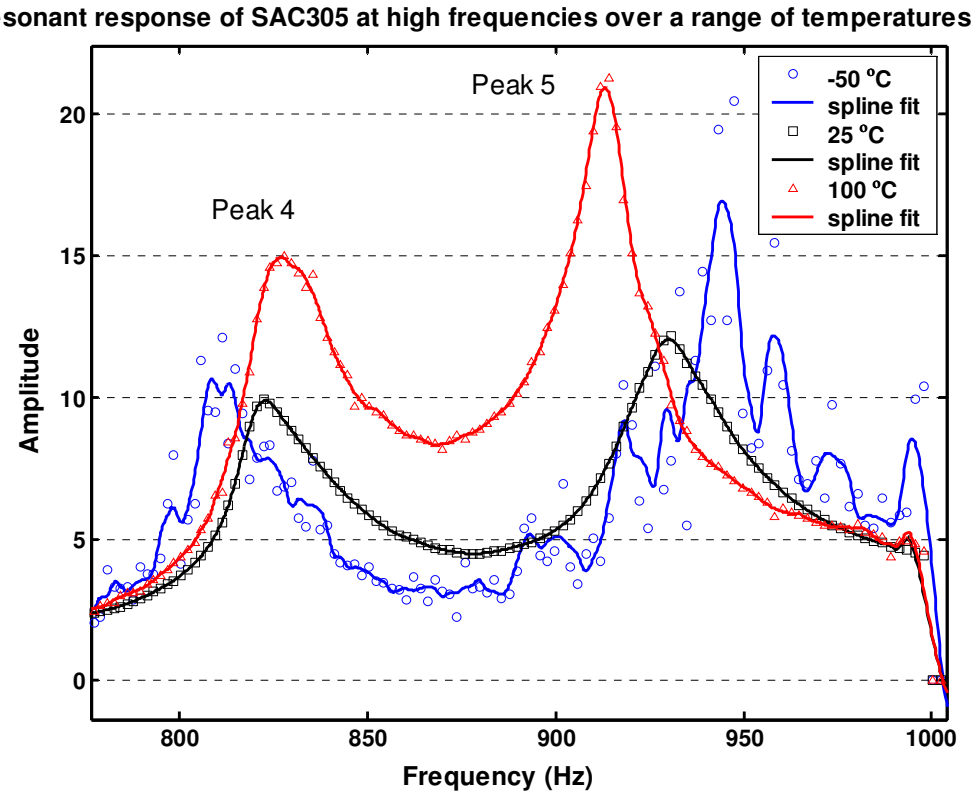

Figure 4.104. Resonant response of rod/holder system at high frequencies containing SAC305 joint

Solder	Temp. ºC	Q factor (peak 1)	Q factor (peak 2)
Sn-Pb	-50	45.3	41.6
	25	41.0	42.8
	70	45.5	30.7
Sn-Cu-Ni	-50	17.5	54.5
	25	37.5	28.8
	70	30.6	38.6
SAC305	-50	41.3	31.7
	25	35.0	22.9
	100	-	-

Table 4-4. Damping Q factors for solders obtained experimentally over a range of temperatures

4.9. Tensile Results

The results of monotonic tensile tests on solder/substrate specimens prepared in exactly the same manner as those for HCF tests (Chapter 3) are presented in Figure 4.105, Figure 4.106 and Figure 4.107. Due to the nature of the clamping system used (roller grips designed for polymer testing), it is recognised that significant amounts of extension are used in the 'settling' of the grips into the soft Cu rods that the solder joints are constructed between. This means that that the extension scale of the graphs will not be accurate, although stresses should be. The grip issue is also responsible for the initial upwards curve in the shape of the plots. Once this initial curve is accounted for, the response of all four solders is fairly linear until abrupt failure.

4.9.1 Tensile Sn-Pb fracture surfaces

Tensile fracture surfaces from three Sn-Pb joints are shown in Figure 4.108. Fracture is always seen to be near or at the solder/substrate interface, although in two cases fracture occurs on opposing interfaces with a shelf separating the two. The details of which interface fracture occurs along are shown to vary, with both the substrate/IMC layer and IMC/solder bonds shown to be involved. Most common however is the tendency to fail in the solder itself but very close (~10 μm) to the interface area, leaving classic void coalescence dimples behind.

4.9.2 Tensile Sn-Cu-Ni fracture surfaces

Tensile fracture surfaces from two Sn-Cu-Ni joints are shown in Figure 4.109. In contrast to Sn-Pb, no dimples of solder were seen. Instead, tensile failure, which occurred in a planar manner across the solder/substrate interface, was confined to either the substrate/IMC layer

or, more commonly, the IMC/solder interface. Very clean separation was seen between the $(Cu,Ni)_6Sn_5$ IMC layer and the bulk solder, revealing the structure of the former and leaving matching imprints in the latter.

4.9.3 Tensile SAC305 fracture surfaces

Tensile fracture surfaces from a Sn-Cu-Ni joint are shown in Figure 4.110. Similarly to Sn-Pb, tensile fracture surfaces for this solder occurs either between substrate and IMC layer, IMC layer and solder, or in the bulk solder very close to the interface by void coalescence. In contrast to Sn-Pb, however, the latter case is more rare and the IMC layer is involved in the majority of the fracture surface. Which fracture route is active does not appear to reflect any geometric considerations; e.g. dimples do not occur preferentially in the centre or outer edge of the circular joint section.

4.9.4 Tensile Innolot fracture surfaces

A representative tensile fracture surface for the Innolot alloy is given in Figure 4.111. The vast majority of failure in this alloy was shown to be between the IMC layer and the bulk solder. In some areas, large Ag_3Sn structures were left behind on the IMC layer, similar to the features described previously in the HCF fractures.

4.9.5 Tensile summary

The tensile strengths of the solders as shown in Figure 4.107 are similar to those found in the literature, with the exception of Sn-Cu-Ni, which demonstrates anomalously high strength compared to the others. An explanation for this result is not forthcoming. The Innolot alloy

– as yet untested in the literature – demonstrates higher strength than the Sn-Pb and SAC alloys, which is to be expected given its Bi addition and greater intermetallic particle content.

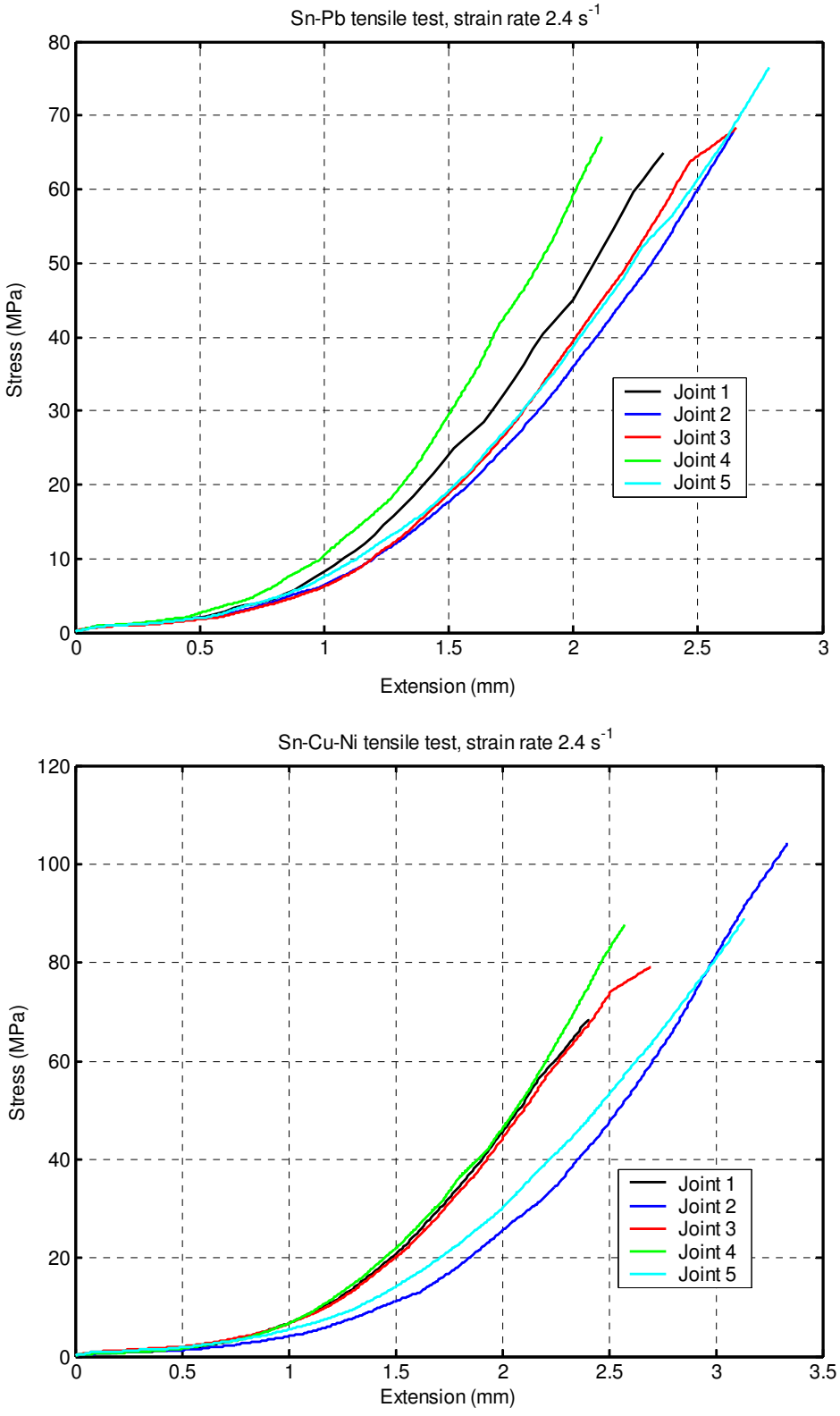

Figure 4.105. Nominal stress vs. extension graphs for Sn-Pb and Sn-Cu-Ni solders. Joints are 2.5 mm diameter by 0.35 mm length solder volumes soldered to Cu substrate and aged for 24 hr at 125 ºC

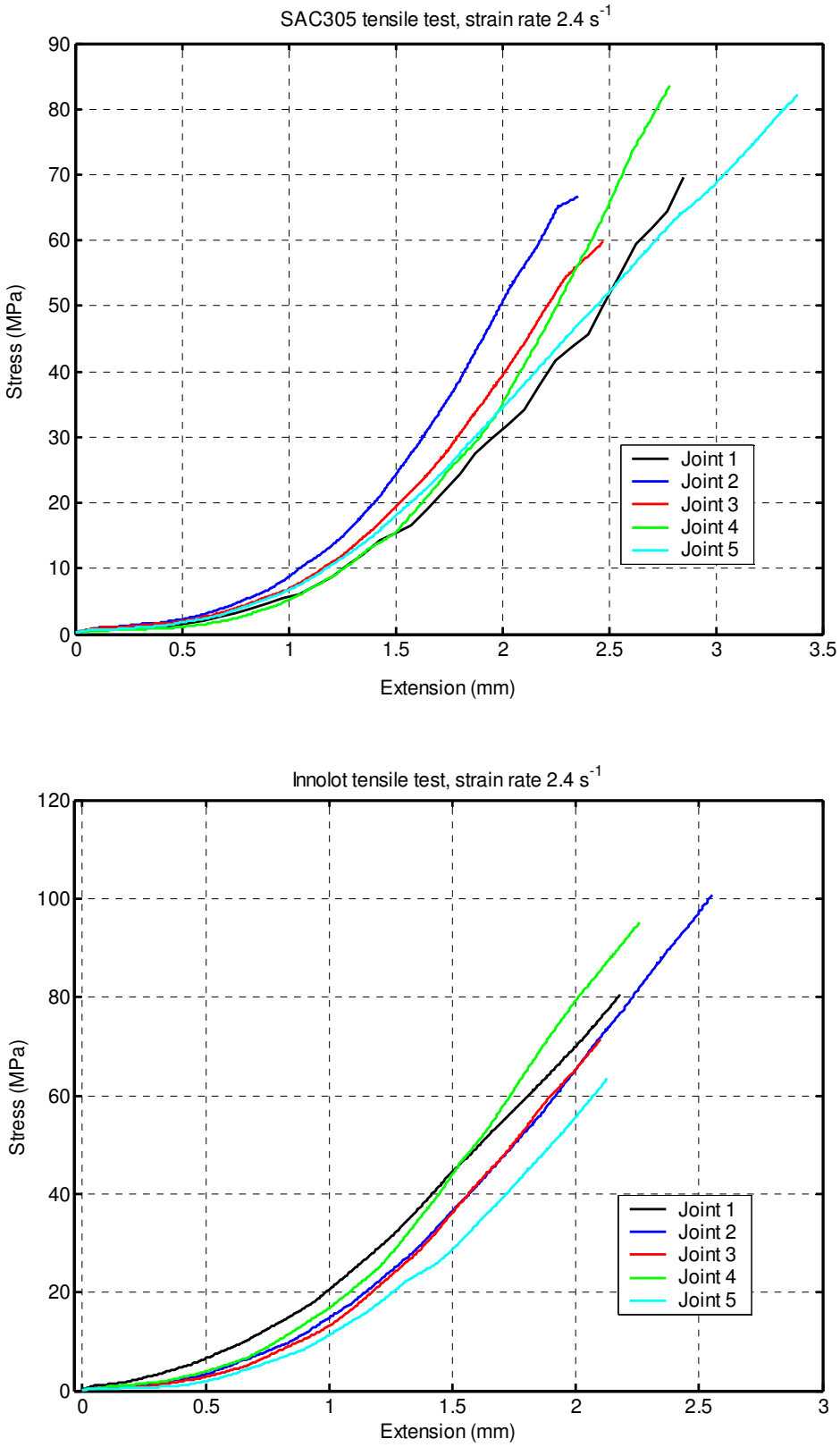

Figure 4.106. Nominal stress vs. extension graphs for SAC305 and Innolot solders. Joints are 2.5 mm diameter by 0.35 mm length solder volumes soldered to Cu substrate and aged for 24 hr at 125 ºC

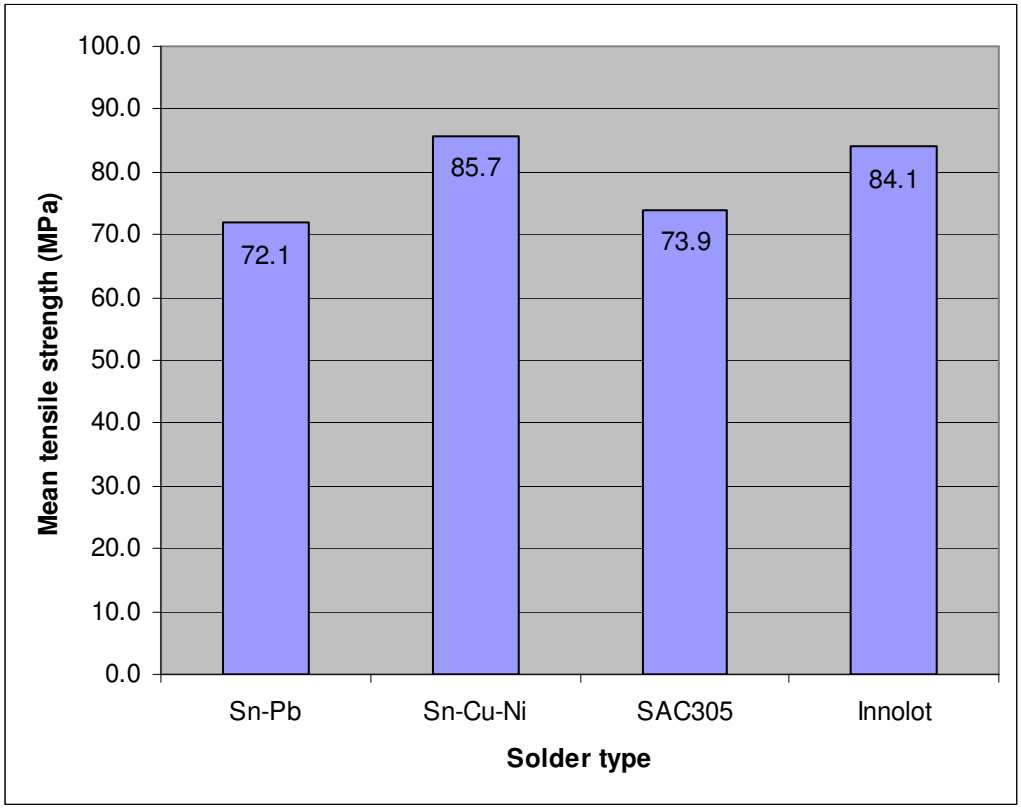

Figure 4.107. Mean tensile strengths from 5 rod specimens tested monotonically in tension at a strain rate of approximately 2.4 s^{-1} at 25 ^{o}C

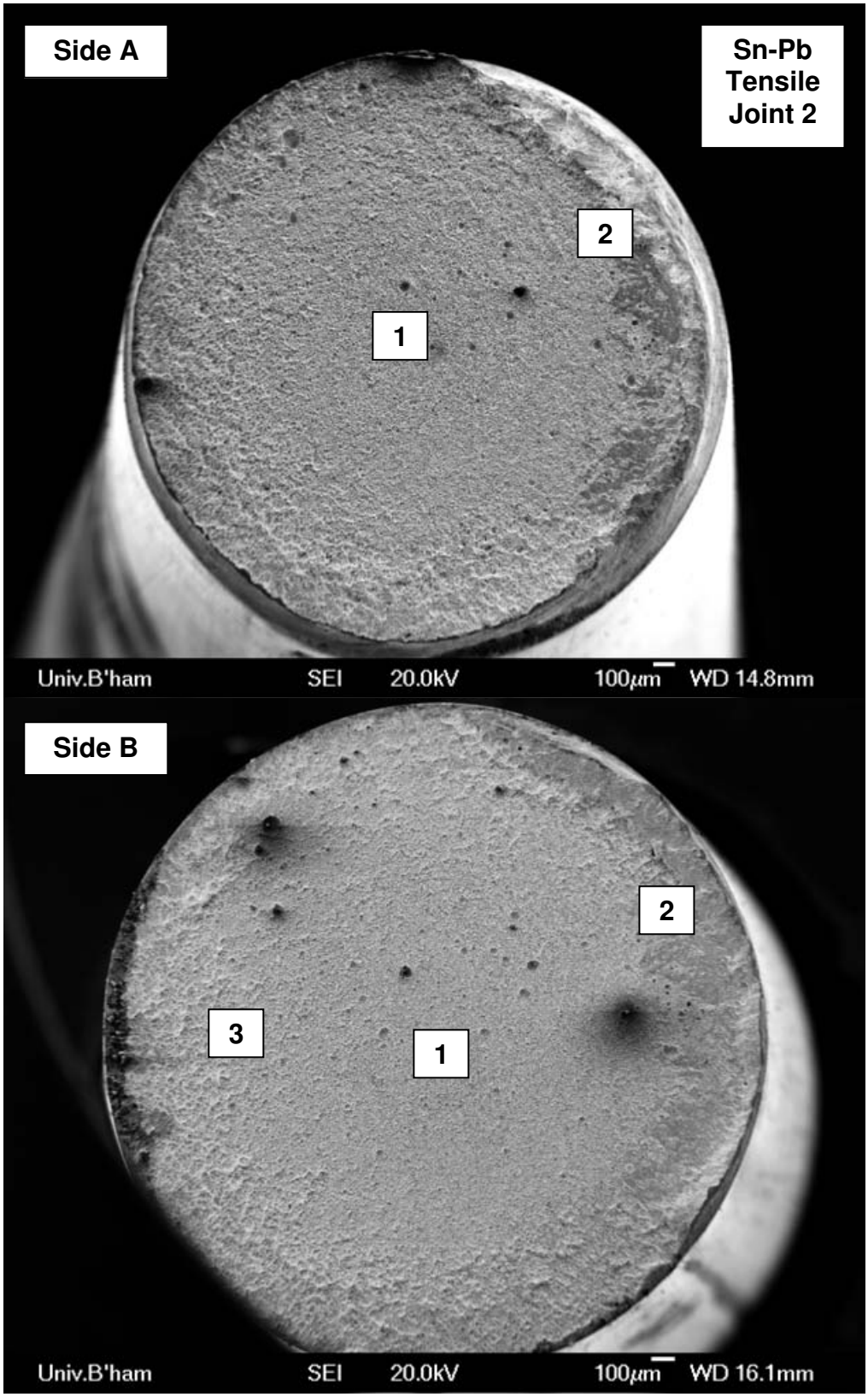

Figure 4.108. Secondary electron micrographs of opposing fracture surfaces of Sn-Pb tensile specimen number 2

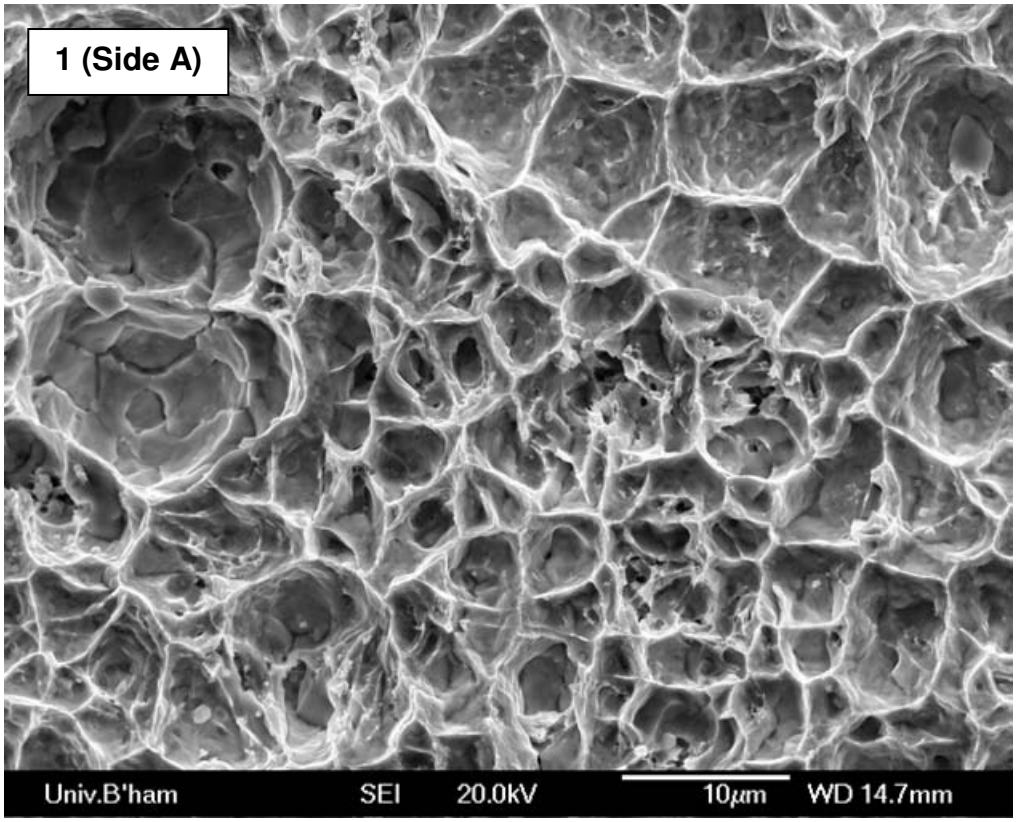

Secondary electron micrograph of area 1 from Sn-Pb tensile fracture surface number 2

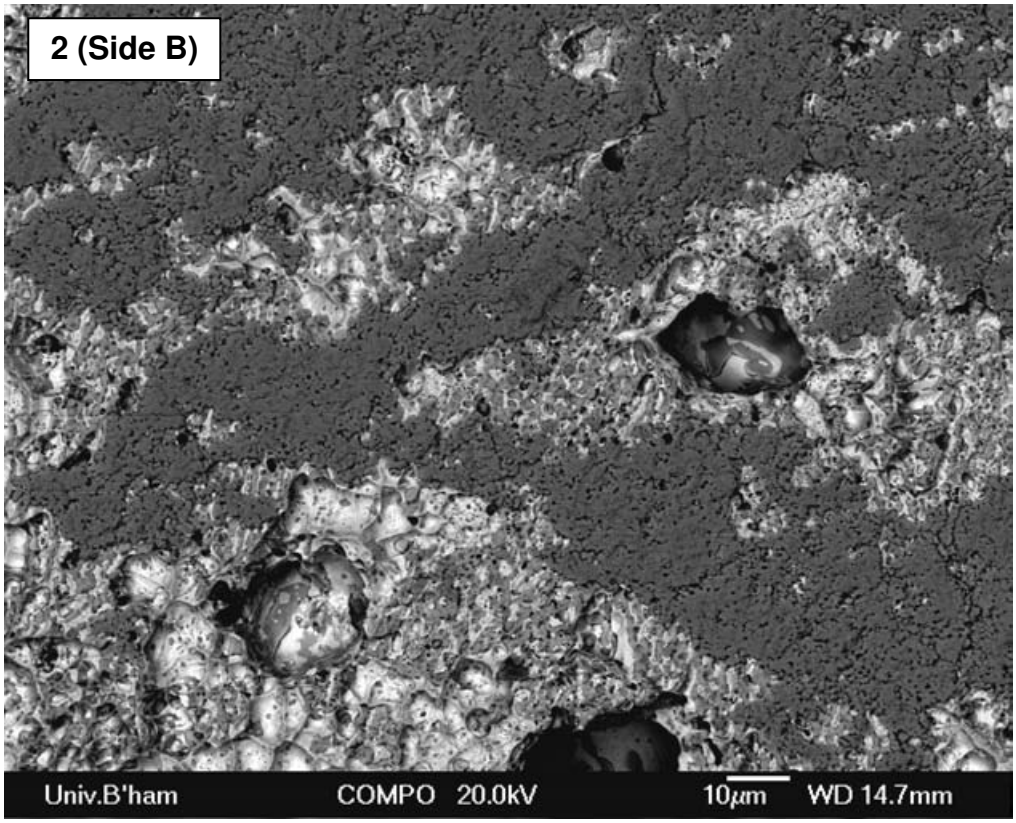

Backscattered electron micrograph of area 2 from Sn-Pb tensile fracture surface (side B) showing regions where Cu_6Sn_5 IMC layer has severed from Cu substrate and stayed attached to bulk of solder volume on the other surface. Atomic number contrast (white = Pb, mid-grey = Sn, dark grey = Cu_6Sn_5)

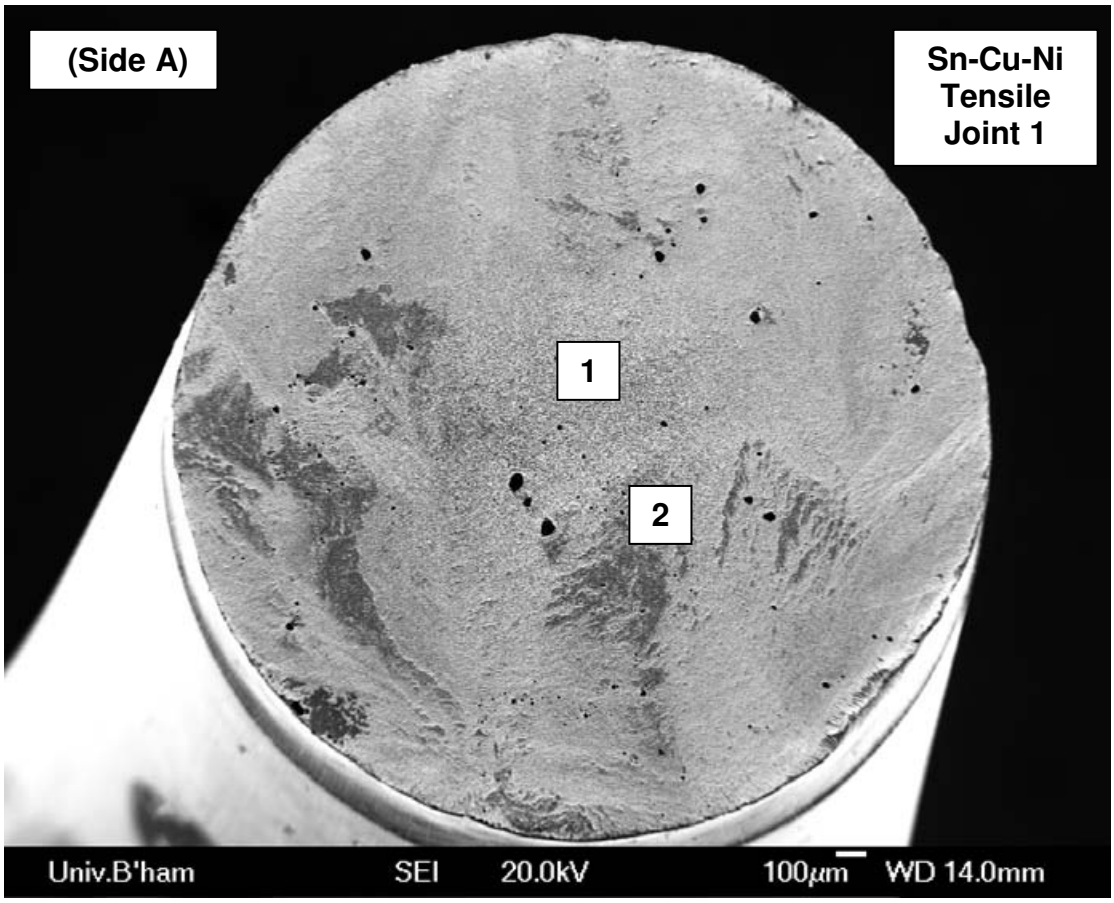

Figure 4.109. Secondary electron micrograph of side A from Sn-Cu-Ni tensile fracture surface number 1 demonstrating entirely planar failure at the solder/substrate interface

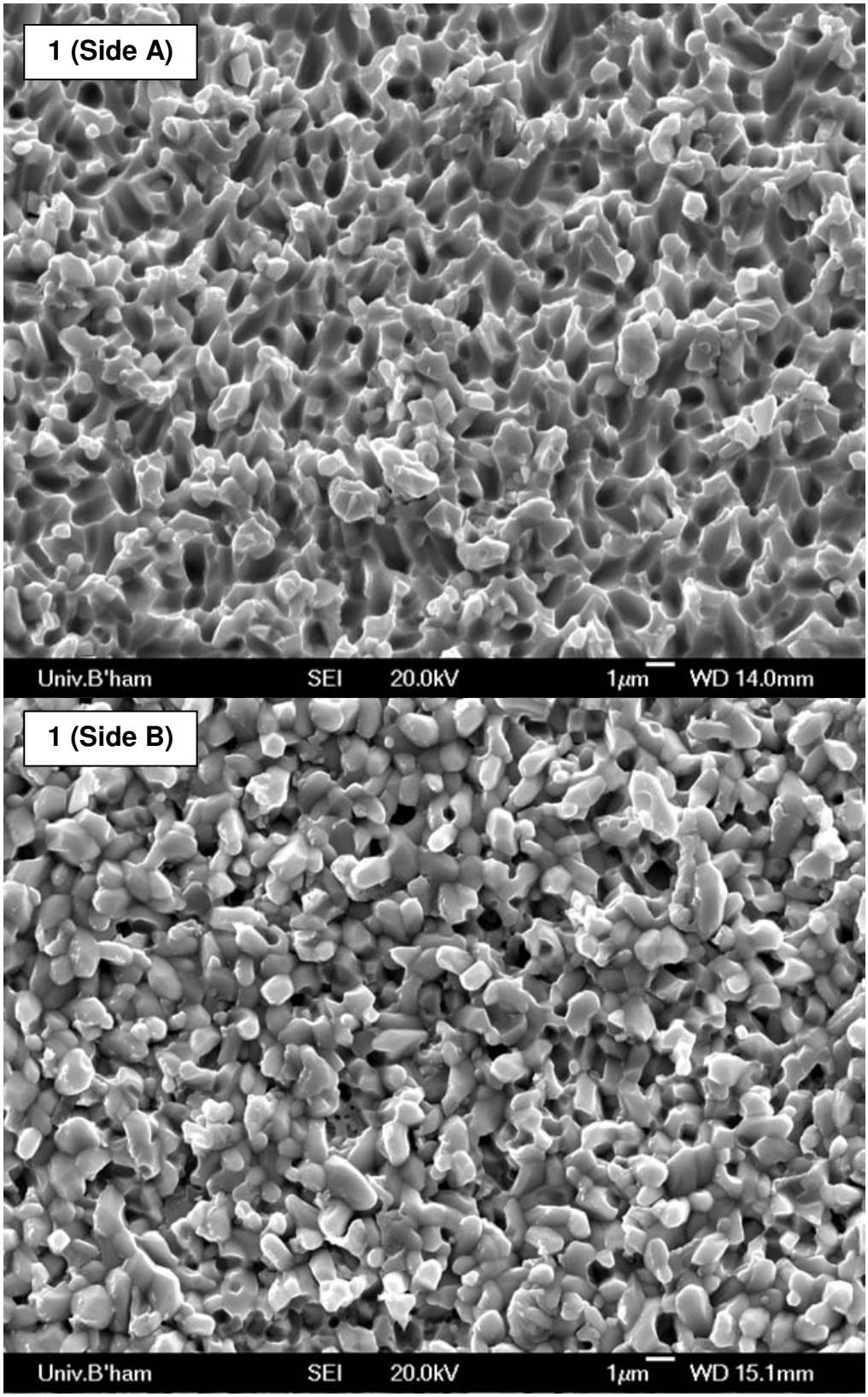

Secondary electron micrographs of area 1 from opposing sides of Sn-Cu-Ni tensile fracture surface from joint number 1 showing clean fracture between Sn matrix and Cu_6Sn_5 IMC layer

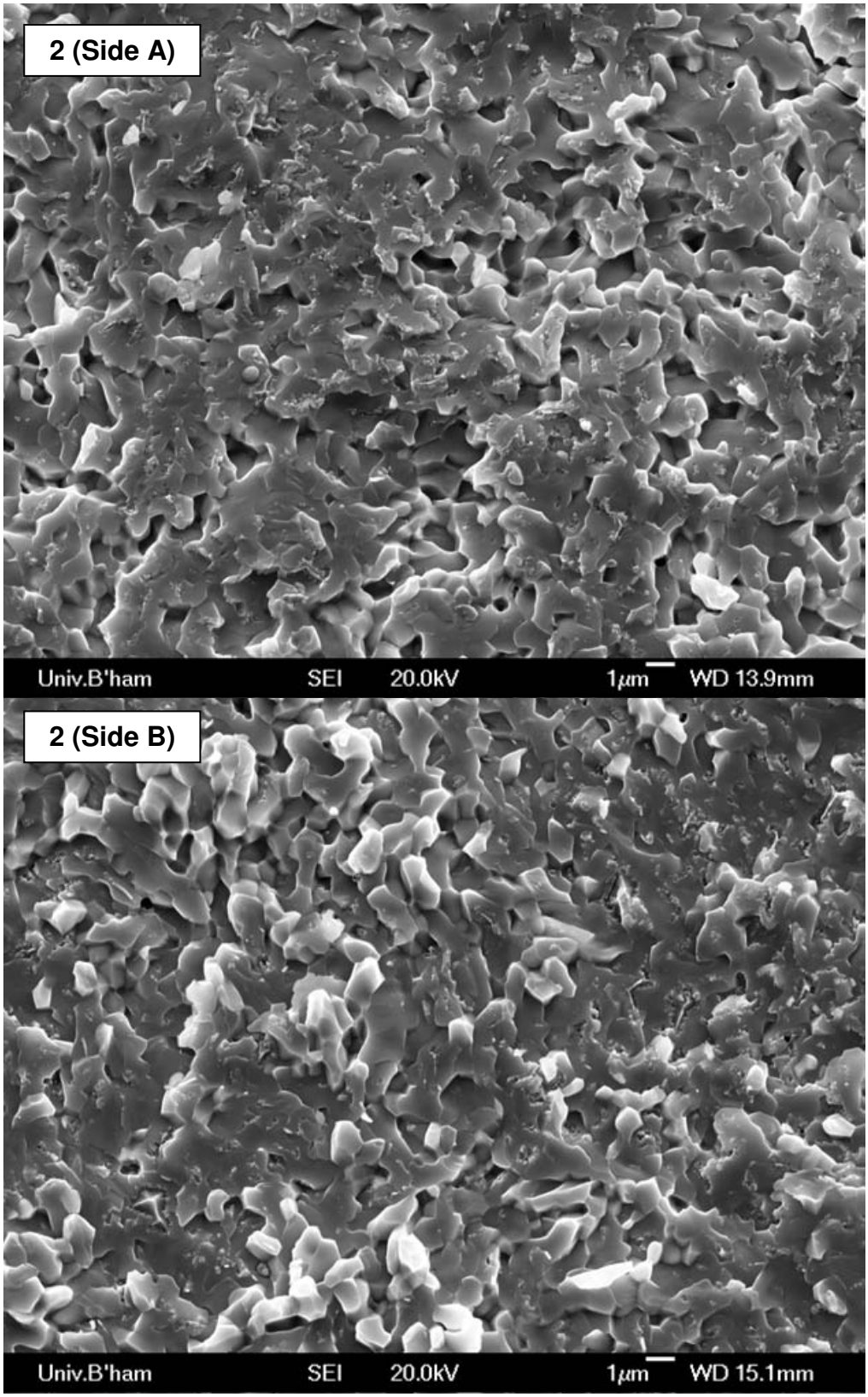

Secondary electron micrographs of area 2 from opposing sides of Sn-Cu-Ni tensile fracture surface from joint number 1 showing separation between Cu substrate and IMC layer

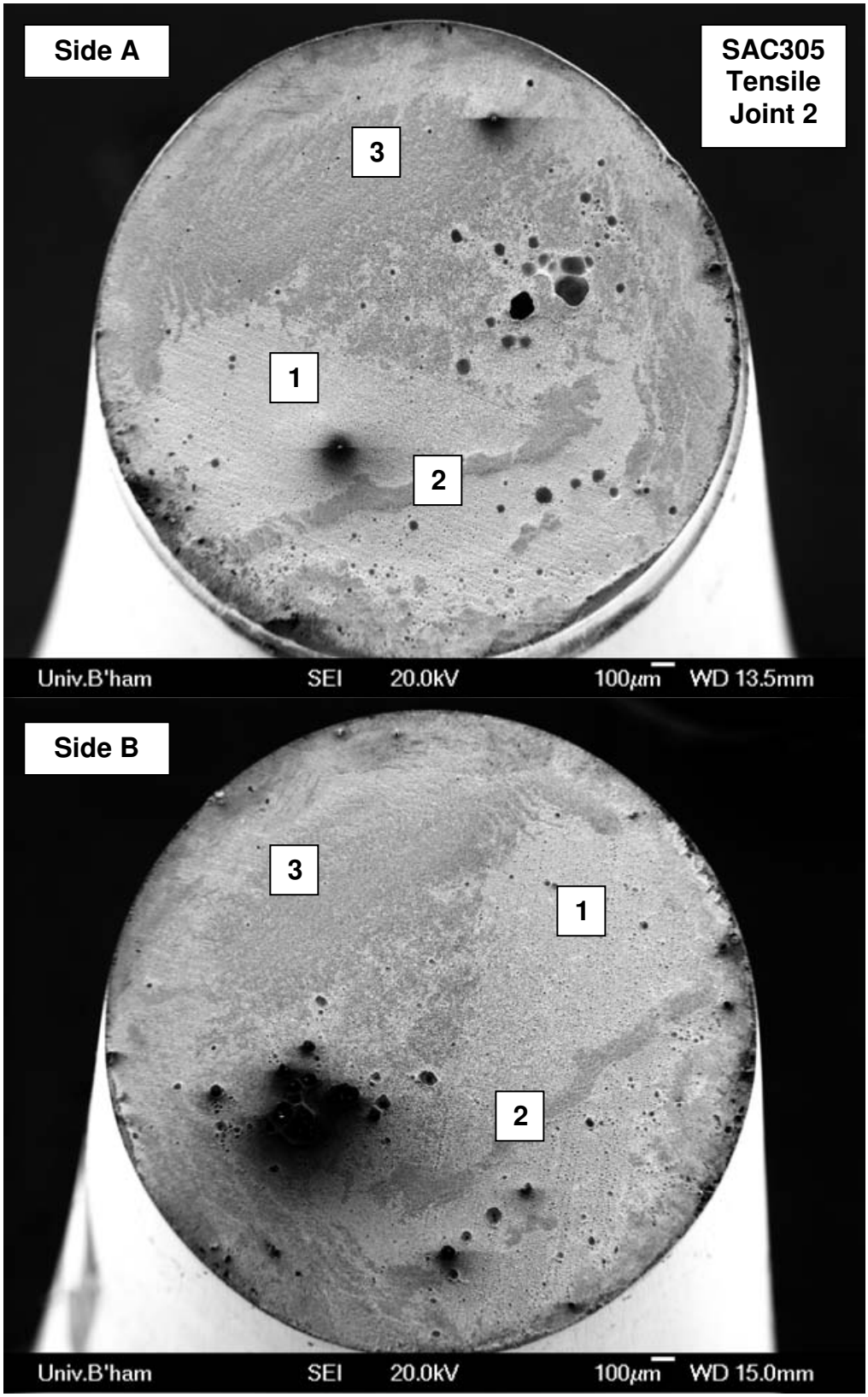

Figure 4.110. Secondary electron micrograph of opposing SAC305 tensile fracture surfaces from joint number 3 demonstrating planar failure at the solder/substrate interface

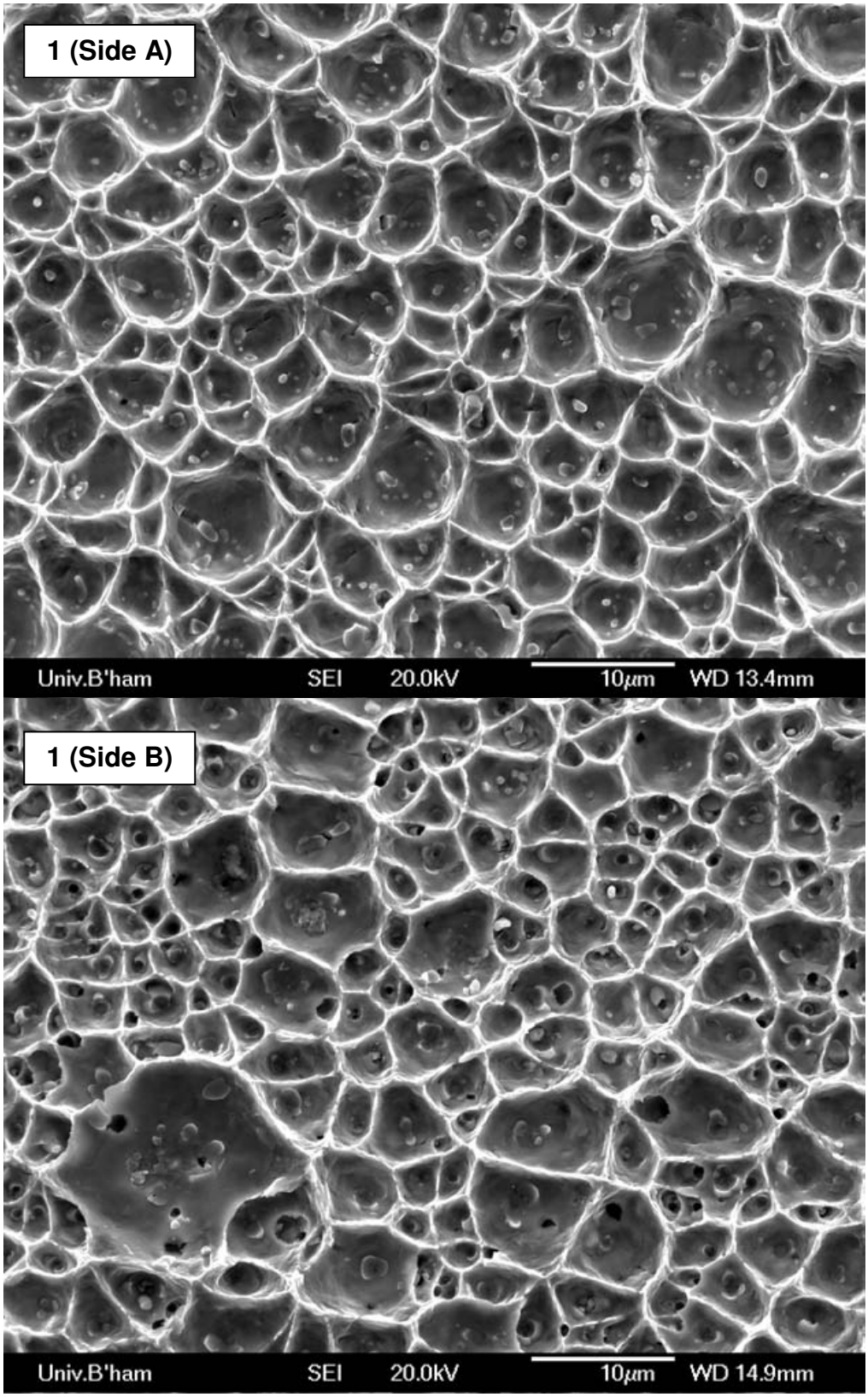

Secondary electron micrographs of area 1 from opposing SAC305 tensile fracture surfaces from joint number 2

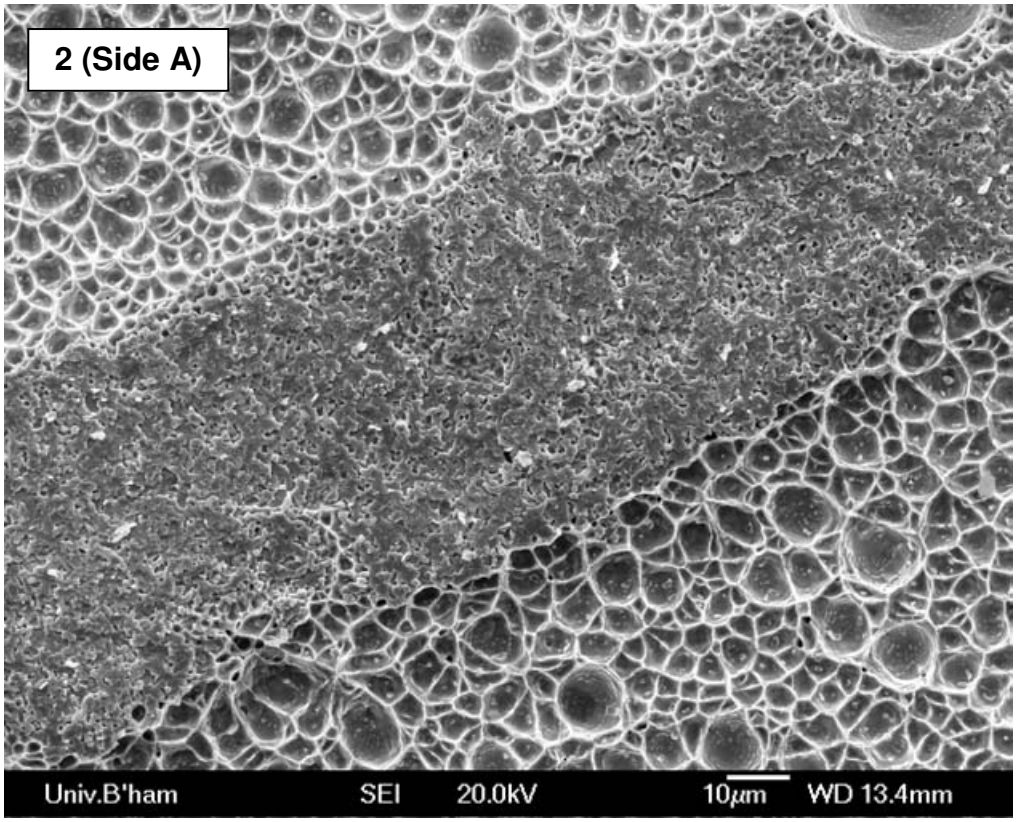

Secondary electron micrograph of area 2 from SAC305 tensile fracture surfaces from joint number 2

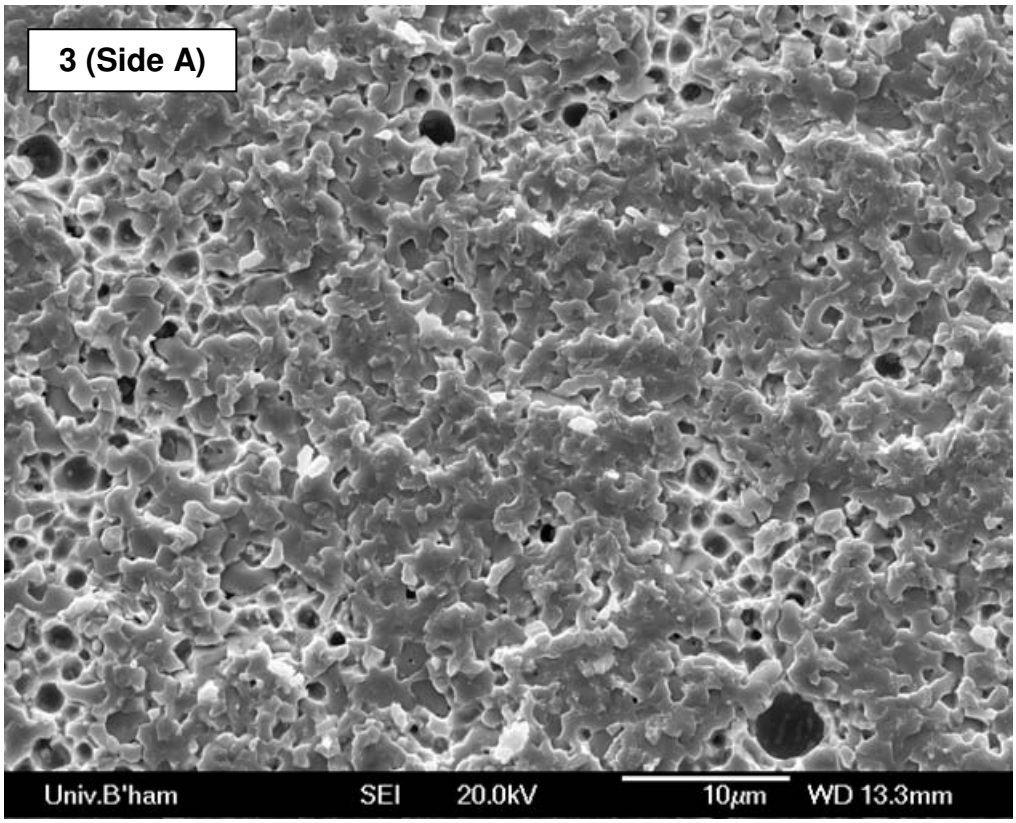

Secondary electron micrograph of area 3 from SAC305 tensile fracture surface from joint number 2

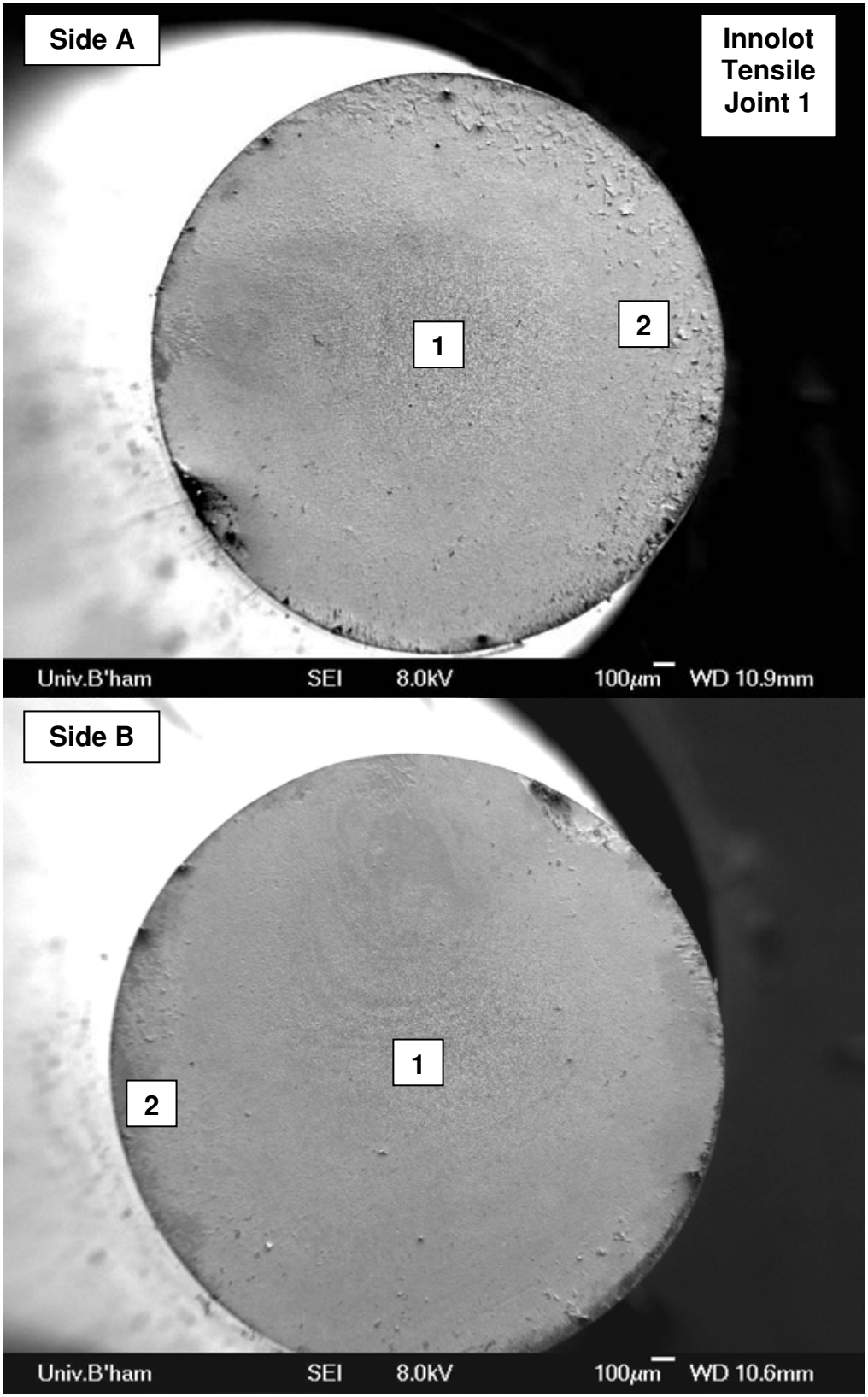

Figure 4.111. Secondary electron micrographs of opposing Innolot tensile fracture surfaces from joint number 1, showing clean interfacial solder/IMC separation across entire area

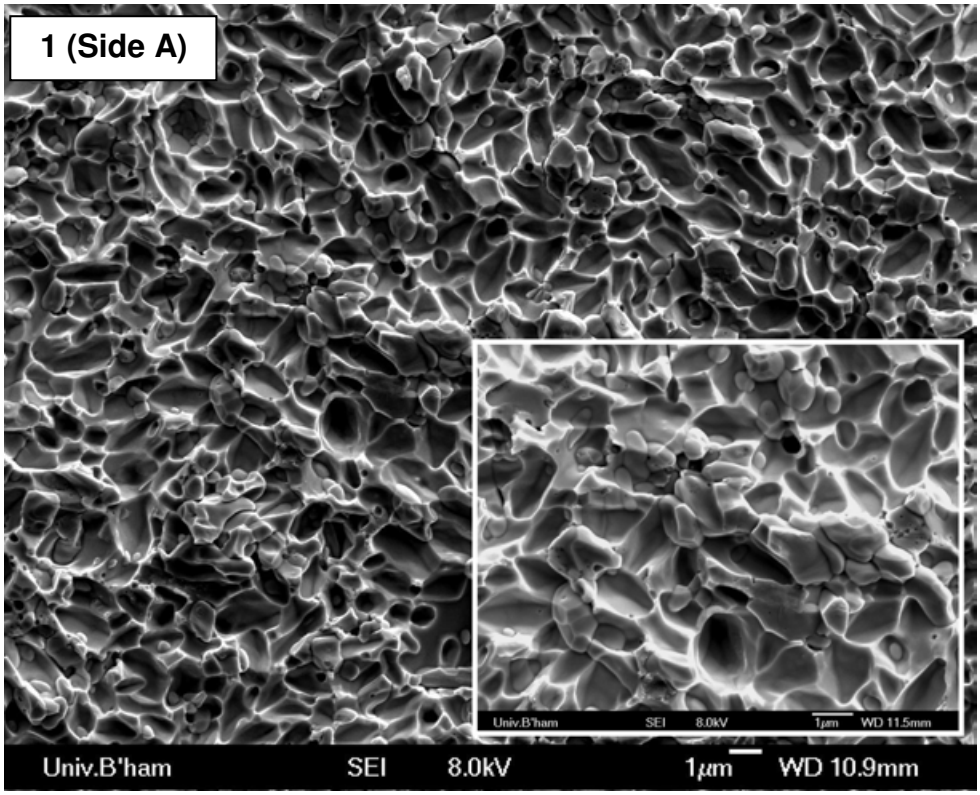

Secondary electron micrograph of area 1 from opposing Innolot tensile fracture surfaces from joint number 1, showing features which represent the large majority of all Innolot tensile fracture surfaces studied – complete separation between $(Cu,Ni)_6Sn_5$ IMC layer and bulk solder

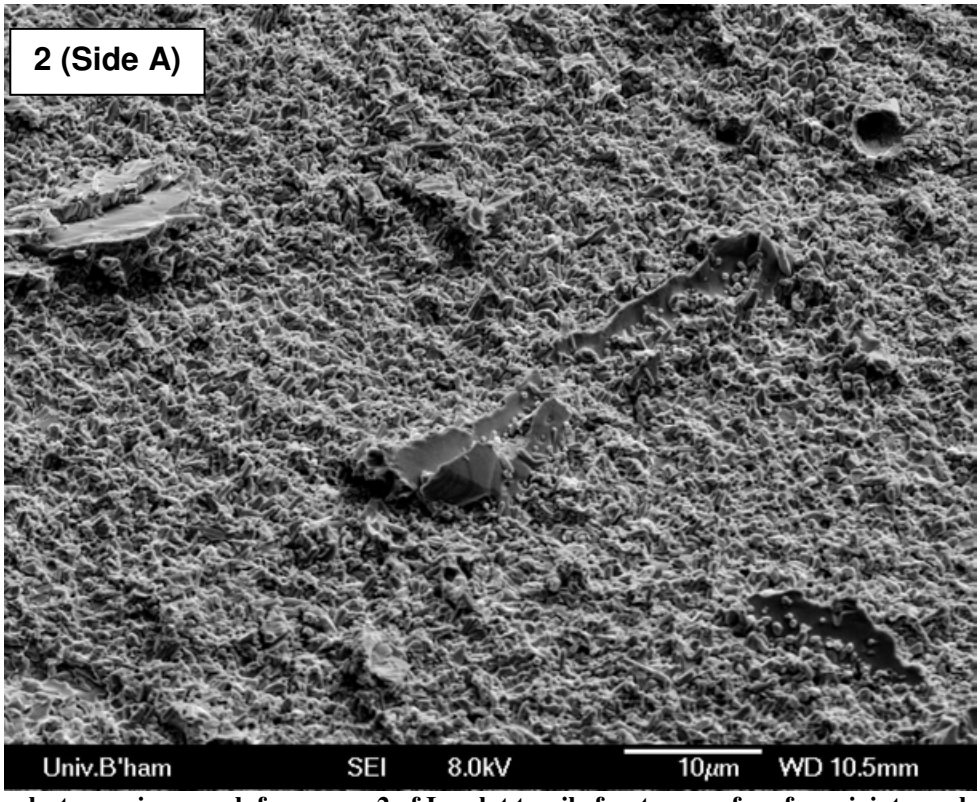

Secondary electron micrograph from area 2 of Innolot tensile fracture surface from joint number 1 showing interfacial failure across entire joing with large (>10 μm) Ag_3Sn remaining attached to $(Cu,Ni)_6Sn_5$ IMC layer

4.1. Summary of results

1. The microstructures of four Pb-free solder alloys and a control Sn-Pb alloy have been characterized when formed in small, cylindrical model joints and the resultant intermetallic layers have been examined. A typical two-phase eutectic microstructure is reported for Sn-Pb and the Pb-free alloys demonstrate a Sn matrix with either dispersed intermetallic particles or pseudo-eutectic regions of Sn + Ag3Sn, consistent with the literature. The microstructure of the Innolot alloy is characterised for the first time and is found to be similar to SAC305 although with more IMC particles and precipitated pure Bi particles in addition to Bi in solid solution. Scallop-type Cu_6Sn_5 / $(Cu,Ni)_6Sn_5$ or Ni_3Sn_4 layers of between 0.72 and 4.16 µm were found, depending on the substrate and solder type.
2. These alloys have been subjected to high-cycle fatigue tests with the methodology laid out in Chapter 3, at room and elevated temperatures. The control Sn-Pb alloy has been shown to significantly outperform all Pb-free alloys in this mode at room temperature, with the possible exception of Innolot, for which there were insufficient results to determine its true performance.
3. The effect of raising test temperature to 100 ºC imparted lifetime reductions and a significant leveling effect on the relative lifetimes of the solders whilst having no effect on their merit order. Observed fracture surfaces were however similar to those obtained at ambient temperature.
4. Specimens soldered to a Ni substrate demonstrated reduced life compared to those soldered to Cu and some statistical differences in fracture behaviour. Statistically, the effect of Ni coating was to reduce the dominance of interfacial failure in all solder types (at the same temperature) although evidence as to why this may be is lacking.

5. The resonant decay of some solder specimens was tracked in order to halt their fatigue tests before final failure occurred. This was successfully accomplished for numerous specimens and cross-sections were taken of these cracks in-situ, showing the cracking behaviour of the alloys and providing a means for evaluating any local microstructural changes resulting from the advancing fatigue crack tip. No evidence of recrystallisation around crack tips was found.
6. High-cycle fatigue fracture surfaces of many specimens were examined in the SEM and, while highly disparate fracture behaviour was observed for all solders, attempts have been made to characterise them. Transgranular cracking was observed in all solders, with no preferential crack paths between the Sn and Pb phases in Sn-Pb or between the pseudo-eutectic regions and Sn in SAC305. Striations were rarely observed. Voids were sometimes found to be the initiation site for fatigue although not in all cases even where large ones were present.
7. Attempts were made to quantify damping capacity of solder specimens at various test temperatures to evaluate whether this could contribute to their performance differences in performance when subjected to vibration. The testing method used proved not to be adequate for this task, since experimental uncertainty masked any effect from intrinsic solder performance; although it could be argued that any such effect was therefore not large enough to observe with a theoretically sound method and possibly insignificant.

5. Discussion

5.1. Experimental method evaluation

The experimental method and test apparatus described in Chapter 3 have demonstrated a way in which solder joints of simple and repeatable geometry can be constructed and tested swiftly using a custom fixture design and an electromechanical shaker. High speeds of testing having been achieved, with eight specimens tested simultaneously. Whilst ideally the solder joints would be of even smaller dimensions, to mimic those found in modern surface-mount electrical components, they have volumes several orders of magnitude less than comparable bulk solder joints tested with conventional machinery by other researchers [20, 27, 85, 92]. They also avoid the variable geometry and thus stress states of solder joints during vibration testing in published works so far [59, 82, 93, 94]. Thanks to these factors, the present work represents probably the first objective study of the high-cycle fatigue of Pb-free solder joints and certainly the first to include tests conducted at elevated temperatures. Part of the discussion on the merits of the present work must be focused on the experimental method, since the quality of the results depends on its validity. The results presented in Figure 3.6 have already demonstrated that, in the frequency range of interest, lateral accelerations of the holders were around 40 dB lower than that of the main, axial, acceleration. This result indicates that the apparatus is achieving a purely tensile/compressive test but this is not sufficient validation by itself. High-speed video images shown in Figure 4.45 give additional assurance that the results presented in these S-N diagrams and the fracture surfaces of solder joints tested therein represent high-cycle fatigue failure produced solely from Mode I loading. The second image in the sequence shows the broken halves of the rod/holder system 0.42 s after separation is first detected; no twisting or bending of the lower half in relation to the upper is visible upon failure or in the preceding

frames of video where cracking is reaching the critical stage. The main evidence supporting the validity of the experimental method is however given in Figure 4.46 - 4.50, which show the fundamental results of the present work – that of stress vs. cycles to failure (S-N) graphs. An important factor to note in these graphs are the quality of the linear fits in log-log space to averaged data points in the majority of cases. These fits elicit confidence in the data without the need to test high numbers of specimens. Since construction of the solder joint specimens is a relatively time-consuming task, this is fortuitous. As is to be expected for a high-cycle fatigue test, the individual specimens show a degree of scatter, which increases numerically with decreasing stress although the coefficient of variation remains similar. The longest lifetime was within 1 – 1.5 orders of magnitude of the smallest for a given stress level, with few exceptions. As a comparison, Mayer et al. [120] report experimental scatters of up to 3 orders of magnitude on cast Mg and Al alloy specimens using a conventional rotating-bend fatigue method.

The disadvantages of the present methodology are as follows. Firstly, as a crack is propagated through a solder specimen, the initial concentricity of the system is diminished since the load will be carried unevenly throughout the specimen (barring the unlikely event of a perfectly concentric crack). This could lead to vibration in multiple directions and a degeneration of the test conditions at the end of joint lifetime. However, the high-speed video evidence does not support this and since high-cycle fatigue is dominated by the time taken to initiate and develop a dominant crack, any such effect would be insignificant when placed in context. Secondly, the joint construction is subject to human influence since although not 'hand-made' as such, joints are hand-polished and not soldered with an automated machine. Only the author prepared the specimens in the present work, which reduces the variation to that of consistency of polishing, although it is recognised that

different people preparing specimens could have an influence in any further work. Time limited the quality of the final polish which could be achieved and it is recognised that surface flaws play a large role in the high-cycle fatigue performance of materials [105] but since all specimens were subject to the same polish and results are averaged, this is not viewed as a serious limitation. Finally, it is recognised that a perfectly uniform Mode I stress state is not achievable, even in a perfect cylindrical geometry, due to the difference in Poisson's ratio and Young's modulus between the Cu rods and the solder joint. However, the variation in principal stresses throughout the solder volume predicted by FEA in Chapter 3 is not large, and almost certainly less than a typical 'real' solder joint, whose shape is essentially that of an uncontrolled three-dimensional casting.

5.2. Order of solders' performance

The merit order of the solders during high-cycle fatigue testing in the present work is contrary to conventional wisdom that higher yield strength correlates with longer high-cycle fatigue lifetimes. The reduction in fatigue lifetimes at elevated temperatures is expected, due to lowered yield strength and increased energy for microplastic deformation; however the unexpected merit order remains. It can be seen from the high-cycle fatigue fracture surfaces presented in Chapter 4 that although the fractographic details of the Pb-free alloys are different from those of Sn-Pb, few differences are seen in the macroscopic fracture path trends (i.e. bulk vs. interfacial), with transgranular crack growth and fatigue initiation from free surfaces or voids being predominant in both cases. An easy explanation of why a comparatively low-strength alloy, Sn-Pb, outperforms the higher-strength SAC305 alloy (which is the most promising Pb-free replacement) in high-cycle fatigue tests is therefore not forthcoming. Also deserving of attention is the difference in performance between solder

joints when using Cu and Ni substrates; this indicates an interaction between the IMC layer and fracture although could be explained as a further manifestation of scatter in the results. The tensile test results presented in Section 4.9 reveal little information helpful to this issue; no differences in strength are seen which mirror the merit order of high-cycle fatigue performance. The tensile strengths as tested in the present work are in fact a combination of the strength of the solder and its interfacial IMC layer, so the only conclusion to draw from them is that the strengths of the bulk solders in the near-interfacial zone and the bond strengths of the IMC layers to the solder are similar, as failure is seen to take place in both. Discussion of a number of theories which could explain the high-cycle fatigue results of the current work are hence presented.

5.3. Initiation control

One theory which could explain the differences in high-cycle fatigue performance of the solder alloys examined in the present work is they contain different quantities of initiation points for fatigue to begin from. High-cycle fatigue is considered to be initiation-controlled; that is; much of a specimen's lifetime is spent in the development of a dominant microcrack, with propagation occurring in the latter stages. In pure metals or nominally 'perfect' test specimens, the classic mechanism for initiation of a fatigue crack is the development of persistent slip bands at the surface which lead to a crack forming. In the present work, pre-existing crack initiators are likely to be present. These take the form of voids, solidification defects and intermetallic particles. Voiding is an acknowledged phenomenon in soldering, principally caused by trapped flux bubbles during the soldering process. IPC (Institute for Printed Circuits) standards IPC-A-610C and IPC-7095 give guidance for acceptable voiding levels in BGA (Ball Grid Array) solder joints. Using X-ray radiography, an average voiding

level of 10 % of the joint area is deemed the limit of acceptability, with any one joint showing 25 % voided area being termed as defective. In the present work these limits would equate to single voids with diameters of ~800 μm and ~1250 μm respectively. Voids of this size were uncommon when using the soldering method in the present work; if a joint contained voids of diameter >1000 μm it typically failed instantaneously and was discounted from the results. In accordance with the reality of soldering practice, smaller voids were tolerated as an inevitable part of the soldering procedure. Although some differences in observed voiding levels between Cu and Ni substrates are reported [13], no significant difference between voiding levels for the Cu and Ni substrates in the present work were detected, although a universal X-ray survey of the specimens was not conducted. Significant differences in voiding levels between the solders were also not found. Fracture surfaces of most specimens showed the presence of small voids but these were not always found to be fatigue initiation points. Part of the scatter in the results must therefore be assumed to originate from voids lying in different locations in the joints.

Since all solder joints are small castings, solidification defects are expected, especially in non-eutectic alloys. Variation from eutectic compositions is shown to increase solder solidification defects [121]. Dendritic cavities were detected in two of the alloys in the present work (Sn-Cu-Ni and Innolot) although some such defects may have been polished off during joint preparation since they will generally occur at the surface [122]. One might expect the Sn-Pb alloy to contain less fatigue initiators, since 1. It is a well-characterised eutectic whose two phases are mutually soluble and 2. It does not contain any intermetallic particles. In contrast, the SAC305 alloy is known to be hypo-eutectic (even if the exact eutectic composition is disputed) and variations in cooling conditions are known to cause a range of solidification behaviour in it [11-13, 34, 123]. It also contains two types of

intermetallic particles whose shapes (in the un-aged condition) are often angular and whose interfaces with the matrix could provide initiation sites. While the exact sources of fatigue initiation were often hard to locate in the present fracture surfaces (unless voids were involved), it is intuitive to suggest the SAC305 alloy, due to its more heterogeneous microstructure, presents far more potential fatigue sites than Sn-Pb, thus providing a reason to explain the two alloys' performance disparity. The Sn-Cu-Ni alloy is likely to lie between SAC305 and Sn-Pb in terms of potential initiation sites, with no Ag_3Sn particles present and essentially a binary (rather than ternary) eutectic composition, with only trace Ni content.

5.1. Inherent crack propagation resistance

If one considers that cracks start early in the fatigue life of a specimen then their crack propagation resistance, or fracture toughness, becomes very important. In studying the crack propagation of Sn-37Pb solder in high detail Ding et al. found that ageing of the microstructure promotes transgranular propagation rather than intergranular [124]. This was found to be due to dislocations emanating from the crack tip and forming cell or sub-grain structures in order to reduce their energy. Nano-cracks and voids resulted from the build-up of dislocations, eventually coalescing to join the main crack. This was in contrast to the un-aged (and finer) microstructure, where the grain boundaries were responsible for deformation from dislocation climb. The microstructure of the aged specimens (the exact treatment being unreported) shown by Ding was in line with those reported in the present work, which were subject to a moderate ageing treatment. Hence when considering present cracking behaviour in Sn-Pb, the grain size is probably of low relevance as the self-arrangement of dislocations into cell structures in the crack tip zone will instead be the controlling factor. The high stacking fault energy of Sn (meaning highly mobile vacancies and dislocations) is cited as a

factor in this behaviour. The only pure crack propagation studies of Pb-free studies thus far have been conducted by Zhao et al. [75, 125] who find that Sn-Ag-Cu demonstrates superior crack growth resistance to that of Sn-Pb. The micro mechanisms of cracking are as yet unreported for Sn-Ag-Cu alloys although it can be theorised that, given a similar grain size to Sn-Pb, the intermetallic-reinforced Sn-Ag-Cu will probably present additional barriers to crack growth from the need to shear or bypass particles.

5.4. Damping capacity

The damping capacity (alternatively referred to as the internal friction) of a material is its ability to scatter energy inelastically through a variety of internal mechanisms, with higher damping capacity meaning reduced amplitude of mechanical vibrations. Since the specimens in the present work form part of the dynamic testing system themselves, with a dead weight suspended from them as opposed to them being strain-controlled by a machine, the theory that damping capacity differences could alter the vibration response of the specimens under test is an attractive one, especially when varying temperatures are considered. Any such difference would alter the effective driving force (ΔK) for a fatigue crack. This is not of academic interest only to this particular testing method, since solder joints in real life also connect masses, albeit smaller, to PCBs. The results from the present work are not of sufficient quality to draw conclusions on whether such a disparity between the Pb and Pb-free solders exists, or to what extent the damping capacity changes at elevated temperatures. It is thought that this is because the solder joints in the present work form a physically small part of the overall dynamic system when compared to the long Cu rod, the weight and fixture system. In other words, any difference between the solders is lost among the experimental noise from the elastic responses of other parts of the test system (most likely the Cu rods). In

the absence of experimental data, it can be discussed whether or not any such differences would be large by reference to published academic work on the subject. It is known that the elastic moduli of metals decrease sharply and their damping capacities increase at $T_h > 0.5$ [126] (at which all alloys in the present work reside at room temperature) and viscoelastic processes may become more prominent (ones which cause a phase lag in the stress-strain response due to a time-dependent component of *E*). Table 5.1 shows a summary of the frequency-dependent energy scattering methods which are held responsible for viscoelastic behaviour in metallic solids [126], and their temperature and frequency ranges of greatest relevance.

Mechanism	Temperature	Frequency	Applicability
Thermoelastic phenomenon	All	1 Hz - 1 kHz	Possible
Valency Electron movement	Very low	High	Remote
Viscosity of grain boundaries	Med - High	Low	Low
Movement of solute atoms (Snoëk effect)	Med	Low	Low - main effect in interstitial solid solutions
Dislocation relaxation (Bordoni effect)	Varies	MHz range	Remote

Table 5.1. Frequency dependent energy scattering methods in metals and their applicability to the present work

For the specific case of high-T_h metals (i.e. solders) being vibrated at relatively high frequencies, only the thermoelastic effect is potentially relevant. Zener [127] determined this effect, caused by non-reversible thermal currents at intermediate frequencies, to have a relaxation time, τ, equal to $\frac{h^2}{\pi^2 D_t}$ where h = specimen thickness and D_t is the thermal diffusion coefficient for the material. Using dimensions from the present work and reference D_t figures for Sn-Pb [128] this would give a relaxation peak in the 10^6 Hz range, well outside the present frequency of cycling. This is due to the low thermal conductivity of Sn and Pb. The differences in thermal diffusion between Sn and Pb are not significant enough to bring this internal friction peak into the relevant range, so the chances of it influencing the present results are very slim.

The mechanisms described give specific peaks in the internal friction spectrum related to frequency (and temperature) but these peaks are overlaid on a high background spectrum of general energy dissipation at $T_h > 0.5$, caused by complex, temperature-dependent mechanisms involving atomic vacancies, state changes, diffusion and dislocations [126]. The damping capacity (δ) of pure Sn and Pb has been studied at ambient temperature by Cook and Lakes [129] where it was found that both metals had very similar δ values of around 0.015 at the frequency of interest in the present work (600 Hz). This would appear to rule out a difference in the damping capacities of Sn-Pb and SAC305 at room temperature if only the intrinsic properties of their constituents are considered, although there remains the (low) possibility of a grain boundary or solid solution rearrangement effect causing a different response in Sn-Pb. As almost all internal friction processes are temperature dependent, the possibility of the 100 ºC results in the present work being affected by such a process remains. In summary, although the method used to determine damping capacity in the present work is valid, the contribution of other elastic members in the system has masked any differences. It would appear that there is a low probability of any specific internal friction peaks existing in any of the alloys at the temperatures and frequencies in question, although at different frequencies in real-life situations, differences between Pb and Pb-free alloys could become apparent, as hinted at by the work of Song et al. [27] described in Chapter 2.

5.2. Creep interactions

It was established in Chapter 2 that since Sn-based solders reside at homologous temperatures of approximately 0.6 at room temperature, creep mechanisms of lattice and dislocation core diffusion are active. The wide disparity in results was also discussed, blamed partly on different testing regimes. It is therefore difficult to conduct an assessment of whether creep is a controlling factor in the present work since there is no one report

containing the same alloys, temperatures, dimensions and strain rates in the literature. Vianco et al. [130, 131] have performed creep compression tests on the Sn-3.9Ag-0.6Cu alloy at suitable temperatures and stresses. The same post-solder heat treatment of a 24 hr dwell at 125 ºC (as in the present work) was applied. Their results, along with those of two selected other studies, are shown in Table 5.2 along with the predicted creep extension of a solder joint during one half-cycle of stress (0 to 30 MPa) in the present work when using the published creep data.

Study	Creep rate		Equivalent extension per cycle in present work (m)	
	Room temp.	~ 100 ºC	Room temp.	~ 100 ºC
Vianco et al. [130, 131] (Sn-3.9Ag-0.6Cu)	1×10^{-5}	1×10^{-4}	4×10^{-12}	3×10^{-11}
Kerr and Chawla [77] (Sn-3.5Ag)	1×10^{-7}	1×10^{-3}	3×10^{-13}	3×10^{-9}
Shohji et al. [21] (Sn-37Pb)	1×10^{-4}	1×10^{-3}	3×10^{-11}	3×10^{-9}

Table 5.2. Tensile extension due to creep in the present work calculated from results in the literature

It can seen that, taking the least conservative figures from the published results, the time available for creep limits the global extension to no more than a few nanometres per half cycle in the worst case scenario of 100 ºC. It is recognised that the reported creep figures are minimum strain rates and as such the initial creep could be an order of magnitude higher, but essentially these figures suggest that the contribution of creep to local strain at the tip of a fatigue crack would be small in the present work. This is despite the high homologous temperatures and stress levels involved and is due to the high speed of testing. This conclusion is backed up by the fatigue crack results of Zhao et al. [75, 125] which suggest that creep is not a dominant process in Sn-Pb or Sn-Ag-Cu solders when fatigued at rates of at least 10 Hz. The one instance in their work which suggests a creep interaction for Sn-Ag-Cu is in the case of an R ratio of 0.7 – i.e. a high mean stress. This is not the case in the present work (R = -1) where the mean stress is zero and fully reversed. Evidence from

fracture surfaces presented in Chapter 4 demonstrates that crack growth is transgranular in all alloys in the present work. Neither grain boundary cavitation, cited by Suresh [105] as a sign of creep in fatigue, nor intergranular failure, cited by Skelton [132] as a similar indicator in many engineering metals, are found to be present here.

5.3. Thermodynamic / recrystallisation effects

The recrystallisation of Sn occurs around room temperature [8]. Any limited work hardening of Sn-based alloys from plastic deformation is quickly dissipated through recrystallisation and subsequent softening. It could be postulated that a thermodynamically-induced microstructural change due to local crack tip plasticity could cause a difference in local fracture toughness between Sn-Pb and Pb-free alloys. Recrystallisation tends to increase ductility and decrease strength [42] although in some precipitation-hardening alloys the fracture toughness can decrease [133]; this is not likely with the present, Sn-based alloys. Relevant differences between Sn-Pb and Pb-free alloys are the solid solution of Pb in Sn (for Sn-Pb), which probably raises the energy required for recrystallisation, the homologous temperature difference (which does the converse for Sn-Pb) and a difference in grain size. Mechanical work is known to trigger microstructural coarsening in eutectic Sn-Pb [5] – this was not found in terms of either local grain/lamella growth or colony orientation changes around cracks in the Sn-Pb HCF specimens which were cross-sectioned at an advanced fatigue stage. In the SAC305 HCF specimens also cross-sectioned before final failure, no significant evidence of recrystallisation was found around cracks through optical microscopy. EBSD mapping of sectioned specimens proved to be problematic because of the requirement for an excellent surface polish with the soft materials in question. However, the results that were obtained from one specimen where acceptable pattern quality was achieved show that

there was no detected microstructural change around an advancing fatigue crack in SAC305 (Figure 4.92). This is judged by the lack of either changes in grain dimensions near the crack tip, or significant EBSD pattern quality fluctuations in the vicinity. Recrystallised grains would be expected to be relatively strain-free and therefore give a stronger (whiter) pattern quality [134]. In summary, the evidence collected in the present work indicates that no thermodynamically driven microstructural change is taking place local to a high-cycle fatigue crack in either Sn-Pb or SAC305 solders. This finding rules out a dynamic effect on the fracture toughness of the specimens being present. It is also in alignment with the findings of Zhao et al. [75, 125] who did not see evidence of recrystallisation during fatigue crack growth experiments in Pb and Pb-free solders at higher testing frequencies.

5.4. Other mechanisms

When testing micro-sized specimens such as in the present work, the crystallographic texture of the joints may become an issue since they could consist of relatively few colonies or even one colony (orientation) throughout the entire joint. The greater surface-volume ratio of micro-sized joints also means faster cooling than with bulk specimens, with more directional cooling behaviour as a result. Coupled with the aforementioned anisotropy of Sn, it is not inconceivable that large regions of uniform orientation would cause a high scatter in results due to the wide variation in availability of slip planes oriented normal to the tensile axis. However, while examples of very large colonies were observed (Figure 4.97), in general all solders demonstrated a polycrystalline texture which indicates that the dimensions and cooling rates in the present work are such that this effect is minimised. In addition, one would expect the averaging of data to overcome the effect unless particular orientations were more favourable – an effect which would need dedicated research.

The presence of two distinct failure routes throughout the results – one through the bulk solder and one close to the solder/substrate interface – could indicate that two separate failure mechanisms are occurring. This hypothesis is backed by the effect that changing the interfacial metallurgy has on the fatigue life of the specimens. However, when examining the detail of the interfacial failures, it is apparent the neither the substrate/IMC nor IMC/solder interfaces themselves are predominantly the path for failure. Failure is instead commonly observed approximately 10 μm away, parallel to the substrate, in all solders tested. In isolated regions of some fracture surfaces failure along one of the interfaces is observed but there is no indication that this area is responsible for initiating failure in many instances. The location of the interfacial-type fracture paths could indicate that the near-interfacial region is microstructurally weaker than the remainder of the solder joint. Two possible mechanisms could facilitate this effect. One is that the stress state of the present joint geometry is such that a maximum stress in the *z*-direction is reached just inside the solder/substrate boundaries, possibly influenced by the elastic properties of the intermetallic layer. The FE analysis presented in Figure 3.8 and Figure 3.9 does not concur with this, however, with stress gradients small through the *z*-plane (joint thickness). It is possible that the higher moduli of the intermetallic compound layers, reported in Table 2.3, result in localised strain increases in the adjacent solder region but it does not seem intuitive that any such effect would manifest itself ~10x the IMC layer thickness in distance away. The other possible mechanism is one of local compositional change in the near-interfacial region. This would be in the form of Sn depletion for Sn-Pb, since only the Sn constituent forms interfacial compounds, or Cu depletion in the Pb-free solders as it diffuses into the interfacial compounds, whether on Cu or Ni substrates. In both cases, the depleted region is likely to be weaker than the bulk solder. However, there is no evidence from the many micrographs of this region to suggest

that there is such a change in microstructure and the near-interfacial cracks do not demonstrate any microstructural preference.

5.5. Summary

A comprehensive picture of the high-cycle fatigue performance of Sn-Pb and Pb-free solders has been built up by the present work in a way which has not been attempted before. Valid S-N diagrams have been constructed at ambient and elevated temperatures showing the intrinsic difference in HCF life between Sn-Pb and Pb-free solders rather than a solder-component-PCB system. The results of the present work do however contain phenomena which are difficult to explain in a unified manner. The high-cycle fatigue performance difference between Sn-Cu-Ni and SAC305, for example, is easily accounted for by the greater yield stress of the latter (at least in the literature if not in the anomalous tensile results presented here) – similarly; the reduction in lifetimes of all solders at elevated temperatures is expected from reference to many other metallurgical studies. However the high performance of the Sn-Pb solder in comparison to the Pb-free alloys is unexpected, since its properties are thought only to be advantageous in high strain range situations [135]. The complex effect of soldering to a Ni substrate, i.e. to the benefit of the Pb-free alloys but to the detriment of Sn-Pb, also lacks an easy explanation given that failure is not shown to occur at the intermetallic layer itself. It is probable that the interfacial intermetallic layer influences the local properties of the solder matrix, whether by strain or by compositional variance and that this effect is lessened with Ni substrates, tipping a balance between crack path preference from the interfacial region towards the bulk slightly. The large variations in gradient on the S-N diagram between the solders at room temperature also suggest that the relationship between

cycles to dominant fatigue crack initiation and applied stress is not consistent between the solders, if one considers the initiation phase to account for the majority of fatigue life. The resonant frequency decay study of the solder joints has established that a slow accumulation of damage, probably in the form of micro-cracking, occurs throughout the first 90 % of the specimens' lives, with large-scale crack propagation taking place at an accelerating rate in the final 10 % of life. The cracking rate of all solders (with the exception of Innolot) in this final phase appears to be very similar. The technique of assessing resonant frequencies in the present work is not sensitive enough, however, to draw conclusions concerning any differences in damage accumulation during the initial stages of life, at least with the limited number of specimens available. It is thought by the author that the results from the resonant decay work, along with the greater proliferation of microcrack nucleation sites (e.g. solidification defects and intermetallic particles) in the Pb-free alloys Sn-Cu-Ni and SAC305 mean that ease of fatigue initiation is responsible for the differences between them and the baseline Sn-Pb solder. It is thought unlikely that this fatigue initiation difference comes simply from increased propensity for voiding. An in-depth study of crystallographic orientation and defect effects in the vicinity of initiation areas was not feasible in the present work but would provide more insight into the situation. Whilst differences in microstructure and crack propagation behaviour between Sn-Pb and Pb-free solders have been highlighted, the only studies to date in this area conclude that, when initiated by a notch, the bulk crack growth rate of Sn-Pb is greater than that of SAC305 [75, 125]. Thus it would be counter-intuitive to suggest that intrinsic crack growth resistance is responsible for the large lifetime variations observed in the present work without further investigation. Creep interactions and thermodynamic effects have been researched but found to be only remotely likely to influence the results. The damping capacity of the solders interacting with the results due to

the particular way in which they have been tested in the present work has not been ruled out, due to inconclusive experiments, but published work suggests there is little difference to be found between the responses of Sn and Pb which could account for the fatigue performance differences found here.

Insufficient time was available to investigate fully the high-cycle fatigue performance of the Innolot 6-part Pb-free alloy. From the limited data set available, it would appear to out-perform all solders, at least in the very-high-cycle regime. This performance is however accompanied by a high degree of scatter in the results, despite very similar fracture surface appearances across all specimens. The data also suggest it may have an even shallower S-N gradient than Sn-Pb, meaning that its durability in the ultra-high cycle regime ($>10^8$ cycles) could be significantly greater than that of any of the other solders in the study. Its resonant decay behaviour is anomalous when compared to the other solders, resulting in no macro cracks being found even after stiffness decay of the specimens. It is the only solder in the study with solid solution hardening elements and it could be theorised that the ordering of these (substitutional) atoms under vibration is altered by a Snoëk-type thermoelastic effect. More research into this alloy would be of much benefit, since it promises performance greatly in excess of 'standard' SAC alloys under cyclic elastic straining, if the large scatter can be investigated and mitigated. Its use in high-reliability sectors of the industry would only be viable once it could be guaranteed that it would not come into contact with existing Sn-Pb products or processes, however, due to the risks outlined in Chapter 2.

5.6. Further work

Obvious extensions to the present work would include a test matrix comprising all solders thus far included, at both elevated and sub-zero temperatures with Cu and Ni substrates. Extending the work to low temperatures (e.g. -55 ºC) would be of interest to all the high-reliability sectors; i.e. aerospace, military and automotive, since these could be encountered frequently. It would also improve the understanding of the effect temperature has on the high-cycle fatigue of solders. Investigating the full high-cycle fatigue behaviour spectrum of the Innolot alloy would prove interesting for the development of modified SAC alloys with improved performance since it promises much in this area. Another major area of interest is the effect of prior thermal ageing and/or cycling on the high-cycle fatigue of solders. The microstructural changes in Sn-Pb during ageing are generally more pronounced than those of the Pb-free alloys but it remains to be seen whether this has an influence on their crack initiation and propagation properties. Ageing would also bring the role of the intermetallic interface layer to the fore, since its growth and morphology are thought to influence the difficulty of crack propagation along it [65]. The testing of specimens at alternative frequencies would be possible with the existing experimental set-up and could provide insight into any internal friction effects, although the choice of frequencies would be limited to some extent by the resonant response of the system outlined in Chapter 3.

Although the SAM proved an adequate tool for the locating of cracks in un-broken fatigue specimens, another possible technique – X-ray tomography – would give a true three-dimensional view of the internal cracking. Additionally, the method used to obtain almost-broken specimens was extremely laborious and would benefit from a degree of automation. Finally, testing of more specimens at each stress level would provide more confidence in the

data and enable a more thorough statistical approach to be applied, including the fit of data to normal or Weibull distributions, for example.

6. Conclusions

1. It is possible to test small, model solder joints in the high-cycle fatigue regime without the use of specialised equipment. The present work demonstrates this concept and method with good results.
2. High-cycle fatigue performance of Pb-free alloys at room temperature is significantly poorer than that of Sn-Pb solder. The difference is lessened by use of Ni substrates rather than Cu although it is not clear why this is the case. Fatigue initiation at the more numerous microstructural flaws in the Pb-free solders is suspected to be the cause of this difference. The near-interfacial crack resistance of all the solders is modified by the different IMC layers encountered with Ni substrates; in a relatively detrimental way for Sn-Pb.
3. Basquin coefficients of solders vary widely at room temperature, with the high-cycle fatigue lifetime of Sn-Pb being the most sensitive to stress.
4. At 100 ºC the Basquin coefficients of all tested solders are very similar and their performance is reduced and less disparate, although their merit orders are unchanged.
5. The Innolot 6-part alloy offers the potential for long mean lifetimes but demonstrates a high degree of scatter. More work is needed on this alloy to establish whether it offers benefits over the SAC family of alloys in high-cycle fatigue.
6. Current results do not extend to the very-high-cycle fatigue regime but suggest that differences between Pb and Pb-free solders will be even greater, which could have implications for long-terms electronics and solder connection reliability in applications exposed to vibration, especially on Cu substrates.
7. All solders except Innolot experience similar damage/cracking characteristics when their high-cycle fatigue lifetimes are normalised, as shown by resonant decay studies.

8. It is difficult to achieve the necessary surface finish for EBSD with solders although the technique would be useful for studying their microstructures and crystallography, especially in the region around fatigue cracks.

7. Appendices

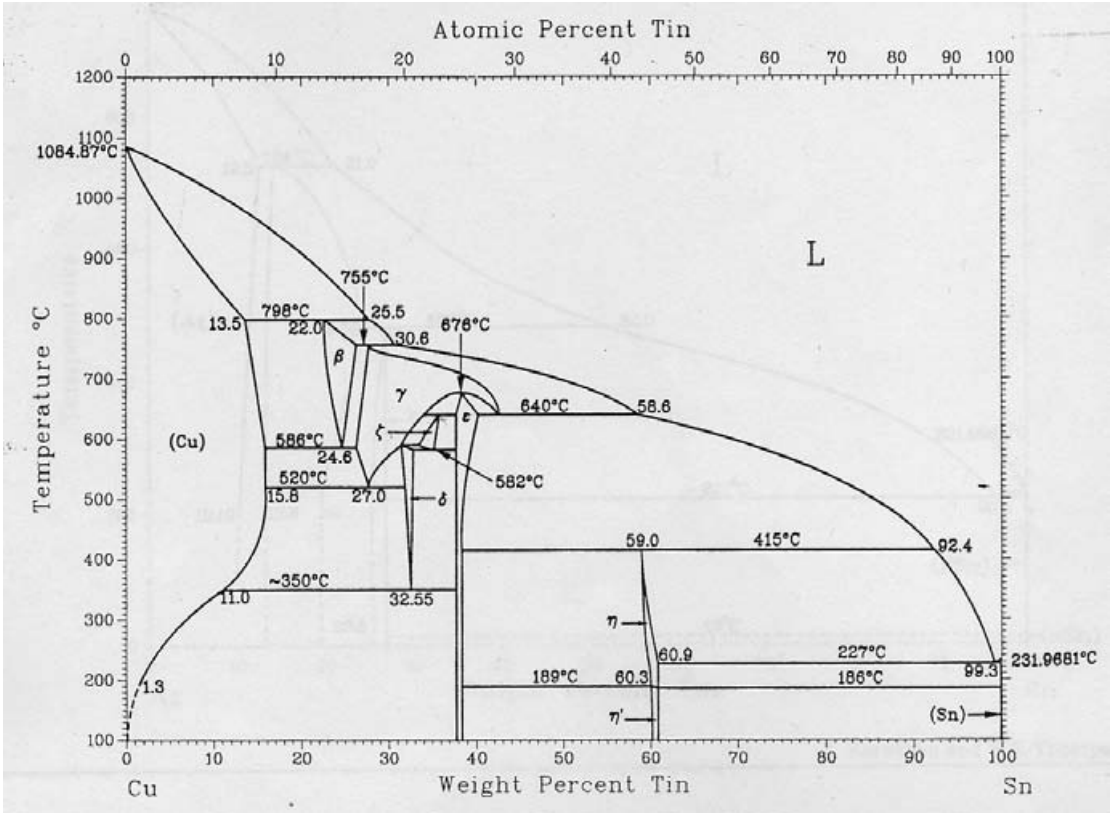

Appendix 7.1. Cu-Sn phase diagram (reproduced from [17])

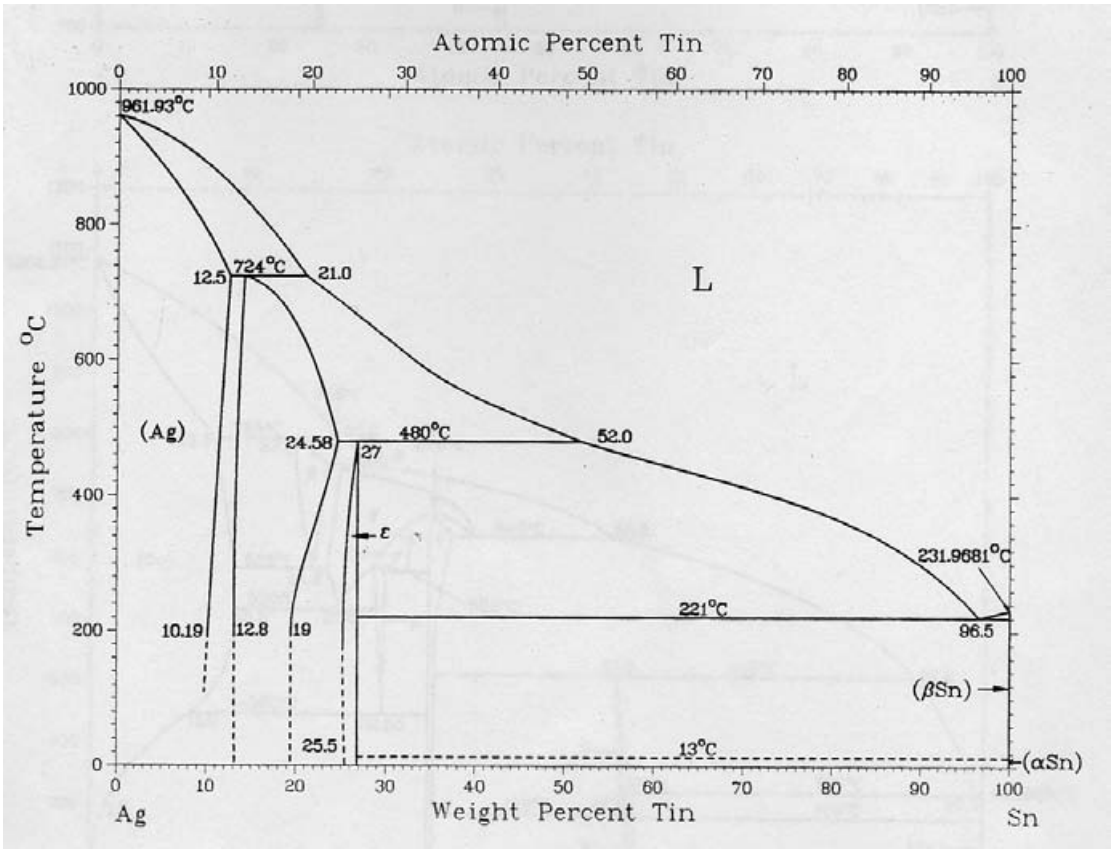

Appendix 7.2. Ag-Sn phase diagram (reproduced from [17])

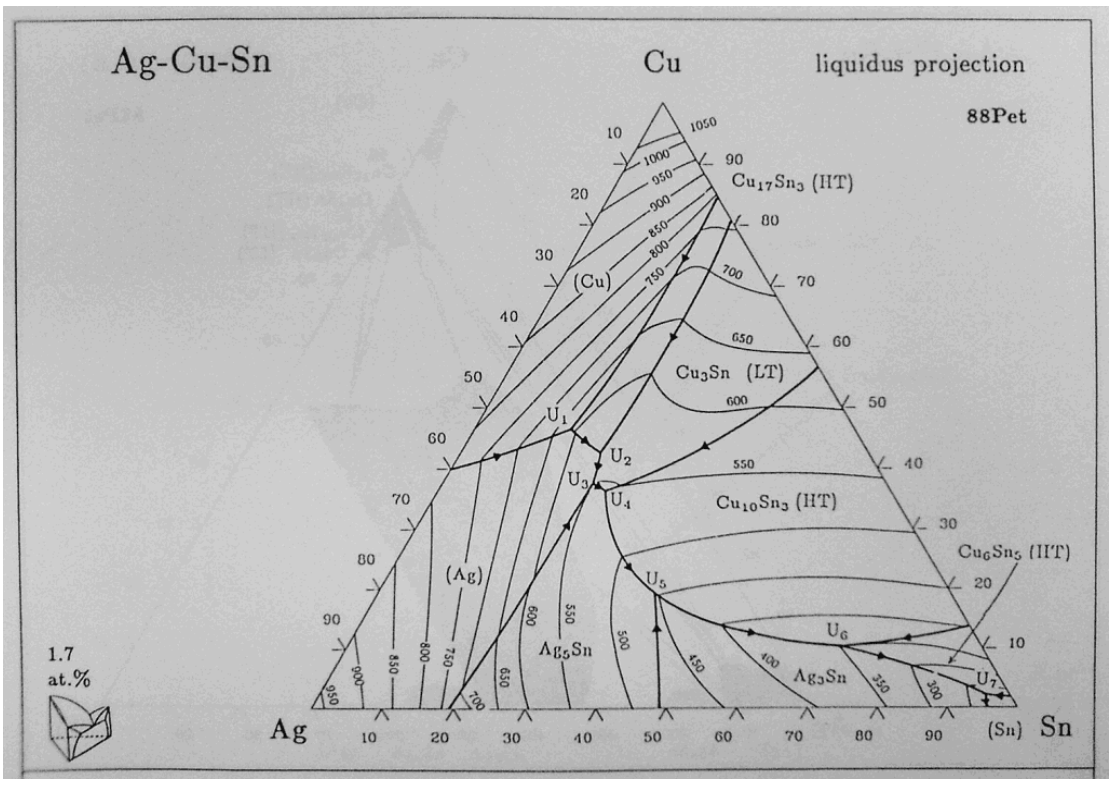

Appendix 7.3. Isotherm from ternary Ag-Cu-Sn phase diagram (reproduced from [136])

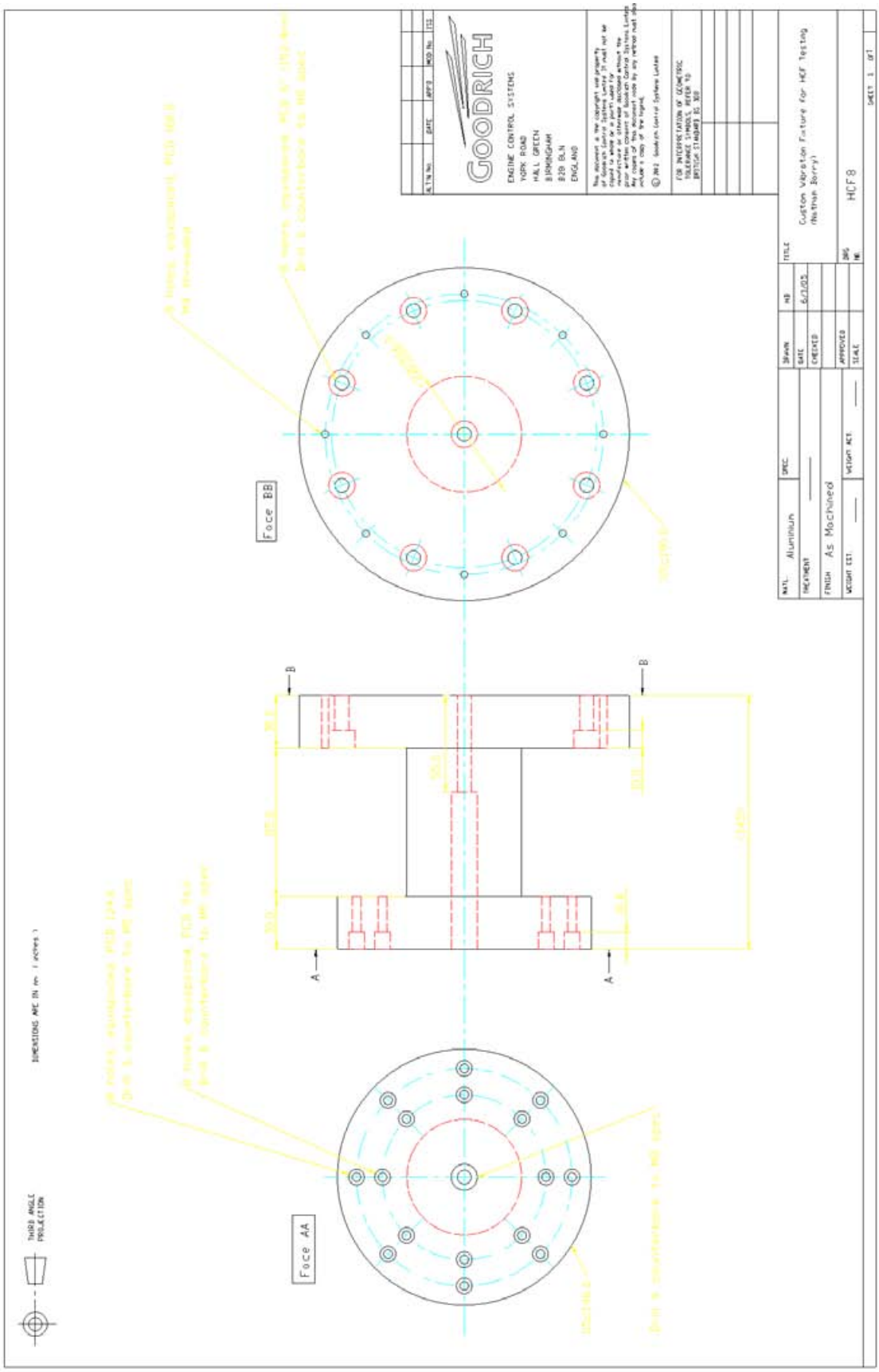

Appendix 7.4. Design of custom HCF vibration table fixture

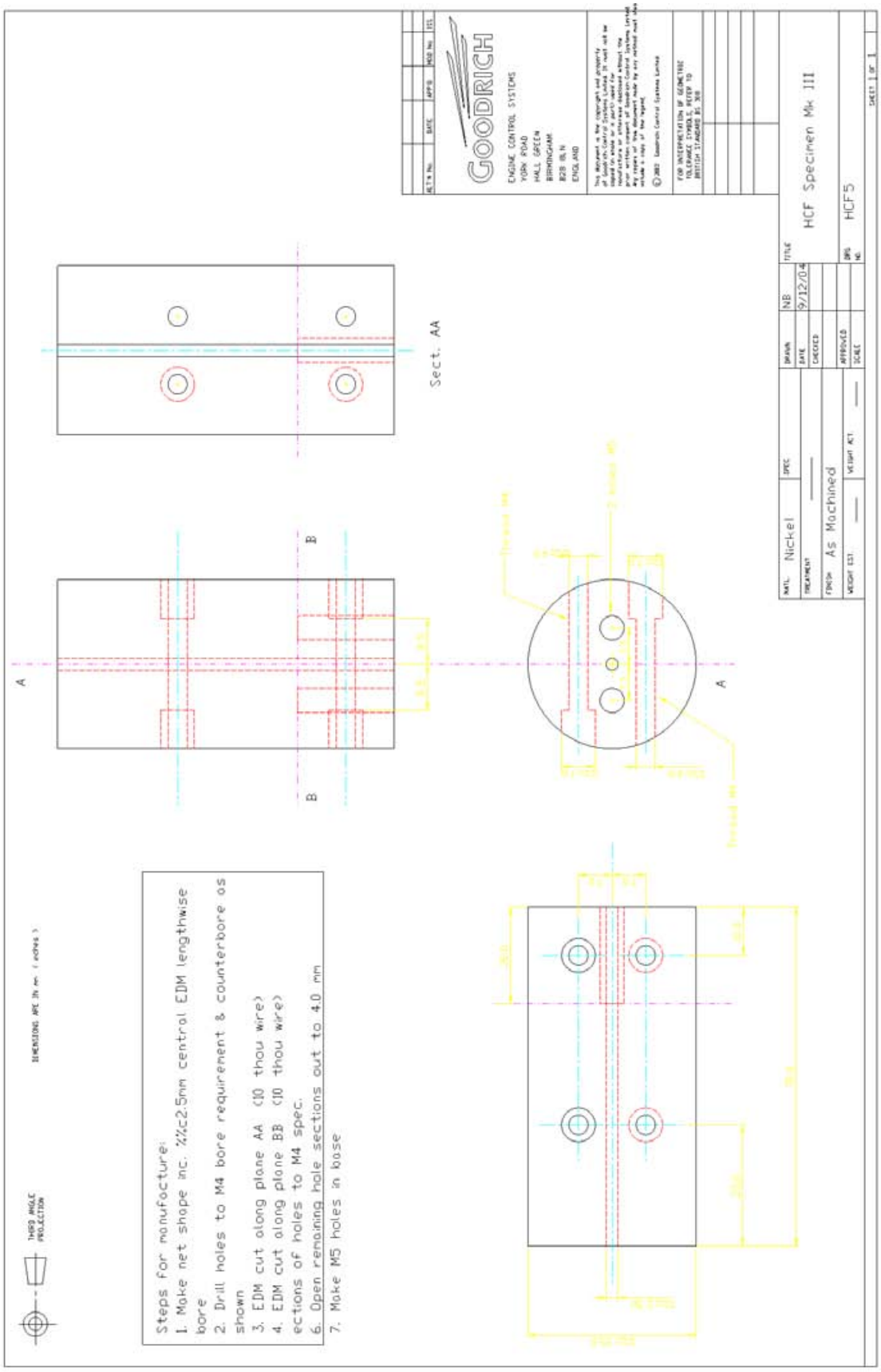

Appendix 7.5. Design of stainless steel cylinders used in HCF fixture

8. References

1. *Directive 2002/95/EC of the European Parliament and of the Council of January 2003 on the restriction of the use of certain hazardous substances in electrical and electronic equipment*. 2003. p. 19-23.
2. *Directive 2002/96/EC of the European Parliament and of the Council of 27 January 2003 on waste electrical and electronic equipment (WEEE)*. 2003. p. 24-28.
3. Miric, A.Z. and A. Grusd, *Lead-free alloys.* Soldering & Surface Mount Technology, 1997. **10**(1): p. 19-25.
4. ASM, *Welding, Brazing and Soldering*. 10 ed. Metals Handbook. Vol. 6. 1990, Washington DC: ASM International Press.
5. Frear, D.R., W.B. Jones, and K.R. Kinsman, *Solder Mechanics - A State of the Art Assessment*. 1990, Pennsylvania: The Minerals, Metals & Materials Society.
6. Plumbridge, W.J., R.J. Matela, and A. Westwater, *Structural Integrity and Reliability in Electronics*. 2003, Dordrecht, Netherlands: Kluwer Academic Publishers.
7. Smithells, C.J., *Smithells Metals Reference Book*. 7 ed, ed. E.A. Brandes and G.B. Brook. 1992, Oxford: Butterworth-Heinemann Ltd.
8. Hedges, E.S., *Tin and its alloys*. 1960, London: Edward Arnold Publishers Ltd.
9. Carapella, L.A. and R. Hultgren, *The ferromagnetic nature of the beta phase in the copper-manganese-tin system.* Transactions of the American Institute of Mining, Metallurgical and Petroleum Engineers, 1942. **147**: p. 232-242.
10. International, A., *Properties and Selection: Nonferrous Alloys and Special-Purpose Materials*. 10 ed. Metals Handbook. Vol. 2. 1990, Washington DC: ASM International Press.
11. Snugovsky, L., et al., *The solid solubility of Ag and Cu in the Sn phase of eutectic and near-eutectic Sn-Ag-Cu solder alloys.* Journal of Electronic Materials, 2004. **33**(11): p. 1313-1315.
12. Moon, K.W., et al., *Experimental and Thermodynamic Assessment of Sn-Ag-Cu Solder Alloys.* Journal of Electronic Materials, 2000. **29**(10): p. 1122-1134.
13. Harrison, M.R., J.H. Vincent, and S. H.A.H., *Lead-free reflow soldering for electronics assembly.* Soldering & Surface Mount Technology, 2001. **13**(3): p. 21-38.
14. Ganesan, S. and M. Pecht, *Lead-free Electronics*. 2004, Maryland: CALCE EPSC Press.
15. Ciocci, R., *Handling the migration to lead-free.* IEEE Transactions on Components and Packaging Technologies, 2001. **24**(3): p. 536-538.
16. Ciocci, R. and M. Pecht, *Learning from the migration to lead-free solder.* Soldering & Surface Mount Technology, 2006. **18**(3): p. 14-18.
17. ASM, *Binary Alloy Phase Diagrams*. Vol. 2. 1990, Washington DC: ASM International Press Ltd.
18. Vianco, P.T. and J.A. Rejent, *Properties of Ternary Sn-Ag-Bi Solder Alloys: Part I - Thermal Properties and Microstructural Analysis.* Journal of Electronic Materials, 1999. **28**(10): p. 1127-1137.
19. Vianco, P.T. and J.A. Rejent, *Properties of Ternary Sn-Ag-Bi Solder Alloys: Part II - Wettability and Mechanical Properties Analyses.* Journal of Electronic Materials, 1999. **28**(10): p. 1138-1143.

20. Kanchanomai, C., Y. Miyashita, and Y. Mutoh, *Low-Cycle Fatigue Behavior of Sn-Ag, Sn-Ag-Cu, and Sn-Ag-Cu-Bi Lead-Free Solders.* Journal of Electronic Materials, 2002. **31**(5): p. 456-464.
21. Shohji, I., et al., *Tensile properties of Sn-Ag based lead-free solders and strain rate sensitivity.* Materials Science and Engineering A, 2004. **366**: p. 50-55.
22. Villars, P., A. Prince, and H. Okamoto, *Handbook of Ternary Alloy Phase Diagrams*. Vol. 5. 1995: ASM International.
23. Gickler, A., C. Willi, and M. Loomans, *Contamination of lead-free solders.* Surface Mount Technology, 1997. **11**(11): p. 44-48.
24. Choi, S., et al., *Effects of Pb contamination on the eutectic Sn-Ag solder joint.* Soldering & Surface Mount Technology, 2001. **13**(2): p. 26-29.
25. Kariya, Y. and M. Otsuka, *Effect of Bismuth on the Isothermal Fatigue Properties of Sn-3.5mass%Ag Solder Alloy.* Journal of Electronic Materials, 1998. **27**(7): p. 866-870.
26. Zeng, K. and K.N. Tu, *Six cases of reliability study of Pb-free solder joints in electronic packaging technology.* Materials Science and Engineering R, 2002. **38**: p. 55-105.
27. Song, J.M., et al., *Resonant Vibration Behaviour of Lead-Free Solder.* Jounal of Electronic Materials, 2003. **32**(12): p. 1501-1508.
28. Li, G.Y., et al., *Effects of Sb addition on tensile strength of Sn-3.5Ag-0.7Cu solder alloy and joint.* Thin Solid Films, 2006. **504**: p. 421-425.
29. Lee, H.T., et al., *Reliability of Sn-Ag-Sb lead-free solder joints.* Materials Science and Engineering A, 2005. **407**: p. 36-44.
30. Harris, P.G. and K.S. Chaggar, *The role of intermetallic compounds in lead-free soldering.* Soldering & Surface Mount Technology, 1998. **10**(3): p. 38-52.
31. Loomans, M.E. and M.E. Fine, *Tin-Silver-Copper Eutectic Temperature and Composition.* TMS Metallurgical and Materials Transactions A, 2000. **31**(4).
32. Miller, C.M., I.E. Anderson, and J.F. Smith, *A viable tin-lead solder substitute: Sn-Ag-Cu.* Journal of Electronic Materials, 1994. **23**(7): p. 595-601.
33. Huang, B., A. Dasgupta, and N.C. Lee. *Effect of SnAgCu Composition on Reflow behavior*. in *IPC and Soldertec Global 2nd International Conference on Lead Free Electronics: "Towards Implementation of the RoHS Directive"*. 2004. Amsterdam, Netherlands.
34. Kang, S.K., et al., *Ag_3Sn Plate Formation in the Solidification of Near-Ternary Eutectic Sn-Ag-Cu.* Journal of Materials, 2003. **55**(6): p. 61-65.
35. Nurmi, S., et al., *The effect of solder paste composition on the reliability of SnAgCu joints.* Microelectronics Reliability, 2004. **44**: p. 485-494.
36. Stam, F.A., Davitt, E., *Effects of thermomechanical cycling on lead and lead-free (SnPb and SnAgCu) surface mount solder joints.* Microelectronics Reliability, 2001. **41**: p. 1815-1822.
37. Lehman, L.P., et al. *Microstructure and Damage Evolution in Sn-Ag-Cu Solder Joints*. in *Electronic Components and Technology Conference*. 2005: IEEE.
38. Kim, K.S., S.H. Huh, and K. Sugunuma, *Effects of fourth alloying additive on microstructures and tensile properties of Sn-Ag-Cu alloy and joints with Cu.* Microelectronics Reliability, 2003. **43**: p. 259-267.
39. Wade, N., et al., *Effects of Cu, Ag and Sb on the Creep-Rupture Strength of Lead-Free Solder Alloys.* Journal of Electronic Materials, 2001. **30**(9): p. 1228-1231.

40. Lee, J.G. and K.N. Subramanian, *Microstructural features contributing to enhanced behaviour of Sn-Ag based solder joints.* Soldering & Surface Mount Technology, 2005. **17**(1): p. 33-39.
41. Villain, J., O.S. Brueller, and T. Qasim, *Creep behaviour of lead free and lead containing solder materials at high homologous temperatures with regard to small solder volumes.* Sensors and Actuators A, 2002. **99**: p. 194-197.
42. Dieter, G.E., *Mechanical Metallurgy*. International Student Edition ed. 1961, Philadelphia, USA: McGraw-Hill.
43. Haswell, P.L., *Durability Assessment and Microstructural Observations Of Selected Solder Alloys*, in *Department of Mechanical Engineering*. 2001, University of Maryland: Maryland.
44. Guo, F., et al., *Evaluation of creep behaviour of near-eutectic Sn-Ag solders containing small amount of alloy additions.* Materials Science and Engineering A, 2003. **351**: p. 190-199.
45. Yoon, J.W., et al., *Intermetallic compound layer growth at the interface between Sn-Cu-Ni solder and Cu substrate.* Journal of Alloys and Compounds, 2004. **381**: p. 151-157.
46. Frear, D.R., et al., *Pb-Free Solders for Flip-Chip Interconnects.* Journal of Materials, 2001. **53**(6): p. 28-33.
47. Pang, H.L.J., B.S. Xiong, and T.H. Low, *Low cycle fatigue study of lead-free 99.3Sn-0.7Cu solder alloy.* International Journal of Fatigue, 2004. **26**: p. 865-872.
48. Warwick, M., *Implementing Lead Free Soldering - European Consortium Research*. 1999, IDEALS: Hemel Hempstead.
49. Nihon, C. *something to do with Sn-Cu-Ni*. in *IPC*. 2006. Malmo.
50. Luo, W.C., et al., *Solid-state reactions between Ni and Sn-Ag-Cu solders with different Cu concentrations.* Materials Science and Engineering A, 2005. **396**: p. 385-391.
51. Nishikawa, H., J.Y. Piao, and T. Takemoto, *Interfacial Reaction between Sn-0.7Cu(-Ni) Solder and Cu Substrate.* Journal of Electronic Materials, 2006. **35**(5): p. 1127-1131.
52. Lee, C.B., et al., *Intermetallic compound layer formation between Sn-3.5 mass%Ag BGA solder ball and (Cu, immersion Au/electroless Ni-P/Cu) substrate.* Journal of Materials Science, 2003. **14**: p. 487-493.
53. Han, H., Y.C. Sohn, and J. Yu, *Interfacial Reactions between Cu_xNi_y Alloy Underbump Metallurgy and Sn-Ag-$_z$Cu Solders.* Journal of Electronic Materials, 2007. **36**(5): p. 578-586.
54. Dariavach, N., et al., *Intermetallic Growth Kinetics for Sn-Ag, Sn-Cu and Sn-Ag-Cu Lead-Free Solders on Cu, Ni and Fe-42Ni Substrates.* Journal of Electronic Materials, 2007. **35**(7).
55. Borgesen, P. and D.W. Henderson, *White Paper: "Fragility of Pb-Free Solder Joints"*. 2004, Universal Instruments Corporation: Binghampton, NY.
56. Kato, H., K. Matsubara, and K. Kageyama, *Decrease in fatigue life of Sn-3.8wt%Ag-1.2%wtCu alloy solder joints due to thermal cycling.* Materials Science and Technology, 2003. **19**: p. 1403-1409.
57. Shangguan, D., *Analysis of crack growth in solder joints.* Soldering & Surface Mount Technology, 1999. **11**(3): p. 27-32.
58. Zeng, K., et al., *Kirkendall void formation in eutectic SnPb solder joints on bare Cu and its effect on joint reliability.* Journal of Applied Physics, 2005. **97**(024508).

59. Tu, P.L., Y.C. Chan, and J.K.L. Lai, *Effect of Intermetallic Compounds on Vibration Fatigue of μ-BGA Solder Joint.* IEEE Transactions on Advanced Packaging, 2001. **24**(2).
60. Sharif, A., M.N. Islam, and Y.C. Chan, *Interfacial reactions of BGA SN-3.5%Ag-0.5%Cu and Sn-3.5%Ag solders during high-temperature aging with Ni/Au metallization.* Materials Science and Engineering B, 2004. **113**: p. 184-189.
61. Larsson, A.K., L. Stenberg, and S. Lidin, *The superstructure of domain-twinned η'-Cu6Sn5.* Acta Crystallographica B, 1994. **50**(6): p. 636-643.
62. Burkhardt, W. and K. Schubert, *Uber messingartige Phasen mit AS-verwandter Struktur.* Zeitschrift Fuer Metallkunde, 1959. **50**: p. 444-452.
63. Nowtony, H. and K. Schubert, *Die Kristallstrucktur von Ni3Sn4.* Naturwissenschaften, 1944. **32**(76).
64. Tsai, I., et al., *Mechanical Properties of Intermetallic Compounds on Lead-Free Solder by Moire Techniques.* Journal of Electronic Materials, 2006. **35**(5): p. 1059-1066.
65. Varghese, J. and A. Dasgupta. *A qualitative understanding of interfacial failure during flexural loading of printed wiring assemblies*. in *ASME Mechnical Engineering Congress and Exposition*. 2006. Chicago, Illinois.
66. Suo, Z. and J.W. Hutchinson, *Sandwich Test Specimens For Measuring Interface Crack Toughness.* Materials Science and Engineering A, 1989. **107**: p. 135-143.
67. Lin, D.C., et al., *An investigation of nanoparticles addition on solidification kinetics and microstructure development of tin-lead solder.* Materials Science and Engineering A, 2003. **360**: p. 285-292.
68. Jang, G.Y., J.W. Lee, and J.G. Duh, *The Nanonindentation Characteristics of Cu6Sn5, Cu3Sn, and Ni3Sn4 Intermetallic Compounds in the Solder Bump.* Journal of Electronic Materials, 2004. **33**(10): p. 1103-1110.
69. Deng, X., et al., *Young's Modulus of (Cu, Ag)-Sn intermetallics measured by nanoindentation.* Materials Science and Engineering A, 2004. **364**: p. 240-243.
70. Lucas, J.P., et al., *Mechanical Properties of Intermetallic Compounds Associated with Pb-Free Solder Joints Using Nanoindentation.* Journal of Electronic Materials, 2003. **32**(12): p. 1375-1383.
71. Li, G.Y., *Characteristics of intermetallics and micromechanical properties during thermal ageing of Sn–Ag–Cu flip-chip solder interconnects.* Materials Science and Engineering A, 2005. **391**(1-2): p. 95-103.
72. Pratt, R.E., E.I. Stromswold, and D.J. Quesnel, *Effect of Solid-State Intermetallic Growth on the Fracture Toughness of Cu/63Sn-37Pb Solder Joints.* IEEE Transactions on Components, Packaging and Manufacturing Technology Part A, 1996. **19**(1): p. 134-141.
73. Balakrisnan, B., et al., *Fracture Toughness of Cu-Sn Intermetallic Thin Films.* Journal of Electronic Materials, 2003. **32**(8): p. 166-171.
74. Calvert, J.R. and R.A. Farrar, *An Engineering Data Book.* 1999, Basingstoke: Palgrave.
75. Zhao, J., Y. Miyashita, and Y. Mutoh, *Fatigue crack growth behavior of 96.5Sn-3.5Ag lead-free solder.* International Journal of Fatigue, 2001. **23**: p. 723-731.
76. Choi, S., et al., *Creep Properties of Sn-Ag Solder Joints Containing Intermetallic Particles.* Journal of Materials, 2001. **53**(6): p. 22-26.
77. Kerr, M. and N. Chawla, *Creep deformation behaviour of Sn-3.5Ag solder/Cu couple at small length scales.* Acta Materialia, 2004. **52**: p. 4527-4535.

78. Kim, K.S., S.H. Huh, and K. Sugunuma, *Effects of intermetallic compounds on properties of Sn-Ag-Cu lead-free soldered joints.* Journal of Alloys and Compounds, 2003. **352**: p. 226-236.
79. Ding, Y., C. Wang, and L. Mingyu, *Scanning Electron Microscope In-Situ Investigation of Fracture Behavior in 96.5Sn3.5Ag Lead-Free Solder.* Jounal of Electronic Materials, 2005. **34**(10): p. 1324-1335.
80. Steinberg, D.S., *Vibration analysis for electronic equipment*. 2nd ed. 1988, Chicester: John Wiley & Sons.
81. Guo, Q., M. Zhao, and H.F. Wang, *SMT solder joint's semi-experimental fatigue model.* Mechanics Research Communications 32, 2005. **32**: p. 351-358.
82. Kim, Y., H. Noguchi, and M. Amagai, *Vibration fatigue reliability of BGA-IC package with Pb-free solder and Pb-Sn solder.* Microelectronics Reliability, 2006. **46**: p. 459-466.
83. Basaran, C., H. Tang, and S. Nie, *Experimental damage mechanics of microelectronic solder joints under fatigue loading.* Mechanics of Materials, 2004. **36**: p. 1111-1121.
84. Kanchanomai, C. and Y. Mutoh, *Effect of temperature on isothermal low cycle fatigue properties of Sn-Ag eutectic solder.* Materials Science and Engineering A, 2004. **381**: p. 113-120.
85. Pang, H.L.J., B.S. Xiong, and T.H. Low, *Low cycle fatigue models for lead-free solders.* Thin Solid Films, 2004. **462-463**: p. 408-412.
86. Zhang, Q., A. Dasgupta, and P.L. Haswell. *Viscoplastic constitutive properties and energy partitioning model of lead-free Sn3.9Ag0.6Cu solder alloy*. in *53rd Electronic Components and Technology Conference*. 2003. New Orleans, Louisiana: IEEE.
87. Lee, W.W., L.T. Nguyen, and G.S. Selvaduray, *Solder joint fatigue models: review and applicability to chip scale packages.* Microelectronics Reliability, 2000. **40**(231-244).
88. Liu, X.W. and W.J. Plumbridge, *Thermomechanical fatigue of Sn-37 wt.% Pb model solder joints.* Materials Science and Engineering A, 2003. **362**: p. 309-321.
89. Mutoh, Y. and J. Zhao. *Fatigue crack growth behavior in 63Sn-37Pb and 95Pb-5Sn solder materials*. in *APACK '99*. 1999. Singapore.
90. Basaran, C. and R. Chandaroy, *Mechanics of Pb40/Sn60 near-eutectic solder alloys subjected to vibrations.* Applied Mathematical Modelling, 1998. **22**: p. 601-627.
91. Zhao, Y., Basaran, C., Cartwright, A., Dishongh, T., *Thermomechanical behavior of micron scale solder joints under dynamic loads.* Mechanics of Materials, 2000. **32**: p. 161-173.
92. Kanchanomai, C., W. Limtrakarn, and Y. Mutoh, *Fatigue crack growth behavior in Sn-Pb eutectic solder/copper joint under mode I loading.* Mechanics of Materials, 2005. **37**: p. 1166-1174.
93. Wang, H.F., M. Zhao, and Q. Guo, *Vibration fatigue experiments of SMT solder joint.* Microelectronics Reliability, 2004. **44**: p. 1143-1156.
94. Che, F.X., et al. *Vibration Fatigue Test and Analysis for Flip Chip Solder Joints* in *5th Electronics Packaging Technology Conference*. 2003. Singapore: IEEE.
95. Liu, X., et al., *Experimental study and life prediction on high cycle vibration fatigue in BGA packages.* Microelectronics Reliability, 2006. **46**(7): p. 1128-1138.
96. Farahmand, B., *Fatigue and Fracture Mechanics of High Risk Parts*. 1997, New York, USA: Chapman & Hall.

97. Osterman, M. and A. Dasgupta, *Life expectancies of Pb-free SAC solder interconnects in electronic hardware.* Journal of Materials Science: Materials in Electronics, 2007. **18**: p. 229-236.
98. Lalanne, M., P. Berthier, and J. Der Hagopian, *Mechanical Vibrations for Engineers*. 1983, Chichester: John Wiley and Sons.
99. Salawu, O.S. and C. Williams, *Review of full-scale dynamic testing of bridge structures.* Engineering Structures, 1995. **17**(2): p. 113-121.
100. Sinou, J.J. and A.W. Lees, *The influence of cracks in rotating shafts.* Journal of Sound and Vibration, 2005. **285**(4-5): p. 1015-1037.
101. George, T.J., et al., *Development of a novel vibration-based fatigue testing methodology.* International Journal of Fatigue, 2004. **26**: p. 477-486.
102. Bedewi, N.E. and D.N. Kung, *Effect of fatigue loading on the modal properties of composite structures and its utilization for prediction of residual life.* Composite Structures, 1997. **37**(3/4): p. 357-371.
103. Giannoccaro, N.I., et al., *Fatigue damage evaluation of notched specimens through resonance and anti-resonance data.* Engineering Failure Analysis, 2006. **13**(3): p. 340-352.
104. Chuang, C.M., T.S. Lui, and L.H. Chen, *The Characteristics of Vibration Fracture of Pb-Sn and Lead-Free Sn-Zn Eutectic Solders.* Journal of Electronic Materials, 2001. **30**(9): p. 1232-1240.
105. Suresh, S., *Fatigue of materials*. 1991, Cambridge: Cambridge University Press.
106. Robinson, W.H., *Lead-rubber hysteretic bearings suitable for protecting structures during earthquakes.* Earthquake Engineering & Structural Dynamics, 2006. **10**(4): p. 593-604.
107. Graff, K.F., *A history of ultrasonics.* Physical Acoustics, 1981. **15**: p. 1-97.
108. Briggs, A., *An introduction to scanning acoustic microscopy*. 1985, Oxford: Oxford University Press.
109. McCluskey, P., M. Munamarty, and M. Pecht, *Popcorning in PBGA Packages During IR Reflow Soldering.* Microelectronics International, 1997. **14**(1): p. 20-23.
110. Nousiaianen, O. and R. Rautioaho, *Solder joint reliability in AgPt-metallized LTCC modules.* Soldering & Surface Mount Technology, 2005. **17**(3): p. 32-42.
111. Chuang, R.W. and C.C. Lee, *High-temperature non-eutectic indium-tin joints fabricated by a fluxless process.* Thin Solid Films, 2002. **414**(2): p. 175-179.
112. Rolls-Royce, *The Jet Engine*. 2005: St. Ives Westerham Ltd.
113. Watt, I.M., *The principles and practise of electron microscopy*. 2nd ed. 1997, Cambridge: Cambridge University Press.
114. Huang, M.L., et al., *Morphology and Growth Kinetics of Intermetallic Compounds in Solid-State Interfacial Reaction of Electroless Ni-P with Sn-based Lead-Free Solders.* Journal of Electronic Materials, 2006. **35**(1): p. 181-188.
115. Wu, C.M.L. and M.L. Huang, *Creep Behavior of Eutectic Sn-Cu Lead-Free Solder Alloy.* Journal of Electronic Materials, 2002. **31**(5): p. 442-448.
116. Yoon, J.-W., et al., *Reliability investigation and interfacial reaction of ball-grid-array packages using the lead-free Sn-Cu solder.* Journal of Electronic Materials, 2004. **33**(10): p. 1190-1199.
117. Ye, L., et al., *Microstructure investigation of Sn-0.5Cu-3.5Ag and Sn-3.5Ag-0.5Cu-0.5B lead-free solders.* Soldering & Surface Mount Technology, 2001. **13**(3): p. 16-20.

118. Ho, C., et al., *Effect of Cu concentration on the reactions between Sn-Ag-Cu solders and Ni.* Journal of Electronic Materials, 2002. **31**(6): p. 584-590.
119. Hull, D., *Fractography*. 1 ed. 1999, Cambridge: Cambridge University Press.
120. Mayer, H., et al., *Endurance limit and threshold stress intensity of die case magnesium and aluminium alloys at elevated temperatures.* International Journal of Fatigue, 2005. **27**: p. 1076-1088.
121. Wable, G., et al., *Solidification shrinkage defects in electronic solders.* JOM Journal of the Minerals, Metals and Materials Society, 2005. **57**(6): p. 38-42.
122. Ueshima, M., M. Nodera, and T. Tajika. *Mechanism of Shrinkage Cavities and Method for Restricting them in SnAgCu Alloy System*. in *IPC/Soldertec Global 4th International Electronics Conference and Exhibition*. 2006. Malmo, Sweden: IPC.
123. Snugovsky, L., et al., *Some aspects of nucleation and growth in Pb-free Sn-Ag-Cu solder.* Materials Science and Engineering, 2005. **21**(1): p. 53-60.
124. Ding, Y., et al., *In-situ observation on microfracture behavior ahead of the crack tip in 63Sn37Pb solder alloy.* Metallurgical and Materials Transactions A, 2006. **37**(3): p. 1017-1025.
125. Zhao, J., et al., *Fatigue crack-growth behavior of Sn-Ag-Cu and Sn-Ag-Cu-Bi lead-free solders.* Journal of Electronic Materials, 2002. **31**(8): p. 879-886.
126. Puskar, A., *Internal Friction of Materials*. 2001, Cambridge: Cambridge International Science Publishing.
127. Zener, C., *Elasticity and Anelasticity*. 1948, Chicago: University of Chicago Press.
128. ASM, *Metals Handbook: Properties and Selection: Nonferrous Alloys and Special-Purpose Materials*. 10 ed. Metals Handbook. Vol. 2. 1990, Washington DC: ASM International Press.
129. Cook, L.S. and R.S. Lakes, *Damping at high homologous temperature in pure Cd, In, Pb, and Sn.* Scripta Metallurgica et Materialia, 1995. **32**(5): p. 773-777.
130. Vianco, P., J. Rejent, and A. Kilgo, *Creep behavior of the ternary 95.5Sn-3.9Ag-0.6Cu solder—Part I: As-cast condition.* Journal of Electronic Materials, 2004. **33**(11): p. 1389-1400.
131. Vianco, P., J. Rejent, and A. Kilgo, *Creep behavior of the ternary 95.5Sn-3.9Ag-0.6Cu solder: Part II—Aged condition.* Journal of Electronic Materials, 2004. **33**(12): p. 1473-1484.
132. Skelton, R.P., *Fatigue at High Temperatures*. 1985, London: Applied Science Publishers.
133. Deshpande, N.U., et al., *Relationship Between Fracture Toughness, Fracture Path and Microstructure of 7050 Aluminum Alloy: Part I. Quantitative Characterization.* Metallurgical and Materials Transactions A, 1998. **29A**: p. 1191-1198.
134. Schwartz, A.J., M. Kumar, and B.L. Adams, *Electron Backscatter Diffraction in Materials Science*. 2000, New York: Springer.
135. Plumbridge, W.J., *Long term mechanical reliability with lead-free solders.* Soldering & Surface Mount Technology, 2004. **16**(2): p. 13-20.
136. Villars, P., A. Prince, and H. Okamoto, *Handbook of Ternary Alloy Phase Diagrams*. Vol. 3. 1995: ASM International.